②

WRDC-TR-89-2126

STRUCTURAL TESTING AND ANALYTICAL RESEARCH
OF TURBINE COMPONENTS

M. Swaminadham
Aerospace Mechanics Division
University of Dayton Research Institute
Dayton, OH 45469

October 1989

Final Report for Period September 1985 - June 1989

Approved for public release; distribution unlimited

DTIC
ELECTE
JUN 28 1990
S B D

AERO PROPULSION AND POWER LABORATORY
WRIGHT RESEARCH DEVELOPMENT CENTER
AIR FORCE SYSTEMS COMMAND
WRIGHT-PATTERSON AIR FORCE BASE, OHIO 45433-6563

NOTICE

WHEN GOVERNMENT DRAWINGS, SPECIFICATIONS, OR OTHER DATA ARE USED FOR ANY PURPOSE OTHER THAN IN CONNECTION WITH A DEFINITELY GOVERNMENT-RELATED PROCUREMENT, THE UNITED STATES GOVERNMENT INCURS NO RESPONSIBILITY OR ANY OBLIGATION WHATSOEVER. THE FACT THAT THE GOVERNMENT MAY HAVE FORMULATED OR IN ANY WAY SUPPLIED THE SAID DRAWINGS, SPECIFICATIONS, OR OTHER DATA, IS NOT TO BE REGARDED BY IMPLICATION, OR OTHERWISE IN ANY MANNER CONSTRUED, AS LICENSING THE HOLDER, OR ANY OTHER PERSON OR CORPORATION; OR AS CONVEYING ANY RIGHTS OR PERMISSION TO MANUFACTURE, USE, OR SELL ANY PATENTED INVENTION THAT MAY IN ANY WAY BE RELATED THERETO.

THIS REPORT HAS BEEN REVIEWED BY THE OFFICE OF PUBLIC AFFAIRS (ASD/PA) AND IS RELEASABLE TO THE NATIONAL TECHNICAL INFORMATION SERVICE (NTIS). AT NTIS IT WILL BE AVAILABLE TO THE GENERAL PUBLIC INCLUDING FOREIGN NATIONS.

THIS TECHNICAL REPORT HAS BEEN REVIEWED AND IS APPROVED FOR PUBLICATION.

JOHN D. REED, Aerospace Engineer
Propulsion Integration
Engine Integration & Assessment Branch
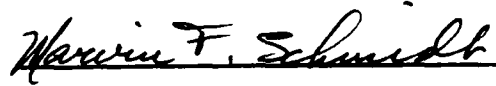
MARVIN F. SCHMIDT, Chief
Engine Integration & Assessment Branch

FOR THE COMMANDER

JAMES S. PETTY, PhD
Acting Deputy for Technology
Turbine Engine Division
Aero Propulsion & Power Laboratory

IF YOUR ADDRESS HAS CHANGED, IF YOU WISH TO BE REMOVED FROM OUR MAILING LIST, OR IF THE ADDRESSEE IS NO LONGER EMPLOYED BY YOUR ORGANIZATION PLEASE NOTIFY WRDC/POTA , WRIGHT-PATTERSON AFB, OH 45433- 6563 TO HELP MAINTAIN A CURRENT MAILING LIST.

COPIES OF THIS REPORT SHOULD NOT BE RETURNED UNLESS RETURN IS REQUIRED BY SECURITY CONSIDERATIONS, CONTRACTUAL OBLIGATIONS, OR NOTICE ON A SPECIFIC DOCUMENT.

REPORT DOCUMENTATION PAGE		Form Approved OMB No. 0704-0188

1a. REPORT SECURITY CLASSIFICATION UNCLASSIFIED		1b. RESTRICTIVE MARKINGS	
2a. SECURITY CLASSIFICATION AUTHORITY N/A		3. DISTRIBUTION/AVAILABILITY OF REPORT Approved for public release; distribution is unlimited.	
2b. DECLASSIFICATION/DOWNGRADING SCHEDULE N/A			
4. PERFORMING ORGANIZATION REPORT NUMBER(S) UDR-TR-89-60		5. MONITORING ORGANIZATION REPORT NUMBER(S) WRDC-TR-89-2126	
6a. NAME OF PERFORMING ORGANIZATION University of Dayton Research Institute	6b OFFICE SYMBOL (If applicable)	7a NAME OF MONITORING ORGANIZATION Aero Propulsion & Power Laboratory (WRDC/POTC) Wright Research & Development Center	
6c. ADDRESS (City, State, and ZIP Code) 300 College Park Avenue Dayton, OH 45469		7b. ADDRESS (City, State, and ZIP Code) WRDC/POTC, WPAFB, OH 45433-6563	
8a. NAME OF FUNDING/SPONSORING ORGANIZATION	8b. OFFICE SYMBOL (If applicable)	9. PROCUREMENT INSTRUMENT IDENTIFICATION NUMBER Contract No. F33615-85-C-2585	

8c. ADDRESS (City, State, and ZIP Code)	10. SOURCE OF FUNDING NUMBERS			
	PROGRAM ELEMENT NO.	PROJECT NO.	TASK NO	WORK UNIT ACCESSION NO
	62203F	3066	12	21

11. TITLE (Include Security Classification)

STRUCTURAL TESTING AND ANALYTICAL RESEARCH OF TURBINE COMPONENTS

12. PERSONAL AUTHOR(S)
M. Swaminadham

13a. TYPE OF REPORT Final	13b. TIME COVERED FROM 9/85 TO 6/89	14. DATE OF REPORT (Year, Month, Day) 1989 October 2	15. PAGE COUNT 307

16. SUPPLEMENTARY NOTATION
N/A

17. COSATI CODES			18. SUBJECT TERMS (Continue on reverse if necessary and identify by block number)
FIELD	GROUP	SUB-GROUP	Vibrations; Critical Speeds; Turbine and Compressor Blades; and Bladed-Disk Dynamics; Plane-of-Light Probes; Noncontact Stress Measurement System (NSMS), Gridwire System; Mistuning (Continue on Reverse Side)

19. ABSTRACT (Continue on reverse if necessary and identify by block number)

Finite-element based deterministic and probabilistic analytical methods were applied for the normal mode and forced response characterization of simple-to-complex turbine and compressor components. Noncontacting blade deflection instrumentation--four fiber optic plane-of-light sensors and dual Z-Grid wire systems were designed, built and tested for measuring blade tip deflections of rotating disks. Differential double pulse inferometry was applied for the mode shape definition of rotating bladed disk, and the full-field modal fringe patterns were quantitatively interpreted by the sine extrapolation technique. A joint effort with AEDC for the concurrent evaluation of the UTRC and UDRI non-interference blade measurement systems for measuring integral order vibration of a flexible disk was completed. Critical speeds and maximum blade tip deflections of a test disk from the two instrumentation systems were compared, and good agreement for the two test series results was seen. The results from the integrated NSMS - Z-Grid instrumentation
(Continue on Reverse Side)

20. DISTRIBUTION/AVAILABILITY OF ABSTRACT ☒ UNCLASSIFIED/UNLIMITED ☐ SAME AS RPT ☐ DTIC USERS	21. ABSTRACT SECURITY CLASSIFICATION UNCLASSIFIED	
22a NAME OF RESPONSIBLE INDIVIDUAL John D. Reed	22b. TELEPHONE (Include Area Code) (513) 255-5308	22c. OFFICE SYMBOL WRDC/POTC

DD Form 1473, JUN 86   Previous editions are obsolete.

A

18. SUBJECT TERMS: Data Acquisition and Analysis, Sensitivity and Probabilistic Finite-element Analysis.

19. ABSTRACT: tests were also compared. The UDRI developed NSMS analysis software programs analyzed the optical probe array data and extracted blade-to-blade deflections and compared them with the interferometric data. Directions for future turbine dynamics measurement techniques were also provided.

FOREWORD

This report describes the work performed during 1 September 1985 through 30 June 1989 under the Air Force Contract No. F33615-85-C-2585 to the University of Dayton Research Institute. The work was conducted both at the Unviersity of Dayton and at the Innovative Structural Research Laboratory of the Aero Propulsion and Power Laboratory, WRDC. The primary focus was to develop and apply analytical and experimental methods to understand the dynamic behavior of rotating turbine blades and bladed disks.

The Air Force program monitors were Messrs. John D. Reed and William A. Stange of POTC and their technical direction and support to this program are duly acknowledged. The author appreciated the day-to-day support and encouragement received from the Project Engineer Mr. Robert J. Dominic (now retired) and the Principal Investigator, Mr. Michael L. Drake of the University of Dayton. Several individuals had made significant contributions to the success of the program and the author acknowledges:

> Mr. Robert J. Dominic for the plane-of-light sensor and Z-grid design and data analysis;

> Dr. Robert A. Brockman and Mr. Frank Lung for the turbine probabilistic analysis;

> Mr. Michael Gutman, Mr. Robert Blanchard, Mr. George T. Collins and Mr. James M. Aulds for the electronic design of the noncontact measurement systems;

> Mr. Thomas W. Held for the data analysis software development;

> Mr. Dennis Davis for conducting rotating tests; and

> Ms. Jo Glover for typing the manuscript.

The author acknowledges the support of Mr. Dale Whitford, Supervisor of the Aerospace Mechanics Division.

TABLE OF CONTENTS

TABLE OF CONTENTS (Continued)

TABLE OF CONTENTS (Continued)

LIST OF ILLUSTRATIONS

LIST OF ILLUSTRATIONS (Continued)

LIST OF ILLUSTRATIONS (Continued)

LIST OF ILLUSTRATIONS (Continued)

LIST OF ILLUSTRATIONS (Continued)

xiii

LIST OF ILLUSTRATIONS (Continued)

LIST OF TABLES

SECTION I
INTRODUCTION

The advent of new material and manufacturing techniques has resulted in the use of thin, light weight, and integrally machined engine components for aircraft propulsion. These components operate under high centrifugal and thermal load conditions and under severe vibratory environment. Surge, stall, and flutter are some of the flow related vibration excitation mechanisms while the rotor balance, misalignment, and bearing induced instability are mechanical sources of vibrations. If turbine and compressor blades and disks operate under vibratory conditions for an extended period of time they fail due to fatigue at critical locations. Hence the study of flexible turbine blades and bladed disk system vibrations is an important task in the evolution of a design strategy to ensure structural integrity of turbine engine structural components.

Two approaches, analytical and experimental, need constant upgrading to meet the design and test requirements of the critical turbine components. The geometric intricacy, material and geometry properties uncertainty, and the nonlinear response of these components limit the deterministic analysis application. The upgraded analysis will have to consider these effects. Also, strain gage-slip ring or strain gage-telemetry measurement methods have provided the stress and vibration data at selected points on turbine and compressor blades in operation. Laser interferometry has been used for the full-field vibration data in laboratory conditions. However, these measurement methods suffer from disadvantages such as limited data, short time operation, long downtime for sensor repair and installation, and limited accessibility.

Two aspects are readily discernable from this discussion. First, we need to develop reliable and large vibration data acquisition systems for the continuous monitoring of several blades of the many critical stages of turbine and compressor rotors. Second, the new analytical methods will have to consider the

1

statistical variations in turbine engine material and geometric properties.

1.1 PROGRAM THRUSTS

Recognizing the present gaps in the existing turbine engine design technology, this research program identified and set forth multifold thrusts in developing new measurement devices and upgrading the analysis techniques. The analytical and experimental methods developed were fundamental, laboratory oriented, and possess potential for application on prototype engine components.

The research and development thrusts from this program were:

1. Develop new noncontacting vibration measurement systems for rotating bladed disk assemblies,

2. Develop finite element based deterministic and probabilistic analytical methods to determine the dynamic response of turbine blades and bladed disk systems,

3. Apply and evaluate of the analysis and measurement systems to define the vibratory response of rotating turbine disks.

1.2 PROGRAM SUMMARY

During the period 1 September 1985 to 31 May 1989, the work on the Structural Testing and Analysis Research of Turbine Engine Components was done at the Innovative Structural Research Laboratory (ISRL) of the Aero Propulsion and Power Laboratory, Wright-Patterson Air Force Base, and also at the University of Dayton Research Institute (UDRI).

A four-channel fiber optic plane-of-light digital data acquisition and data display system was designed, fabricated, and demonstrated for tip deflection measurements on rotating blades. This system is laboratory suited, equipped to compensate for shaft speed changes during one revolution, and has a fast turnaround capability.

A novel two-channel digital Z-grid (grid wire) instrumentation system was designed, fabricated, and tested to measure an instrumented blade tip deflection of a rotating bladed disk. Both the plane-of-light and Z-grid wire measurement systems were integrated such that the data acquisition was achieved through a common device.

Suitable data analysis software programs were developed to generate time and frequency spectra from the test data and to extract the blade tip deflection of all blades from the optical system data and one blade from the grid wire system data. A quantitative fringe interpretation method for the differential double pulse interferometry was also developed and applied to define full-field vibration patterns of a flexible rotating bladed disk.

A joint effort with Arnold Engineering Development Center (AEDC) and United Technologies Research Center (UTRC) to excite a rotating bladed disk in a backward traveling wave and compare the performance of the AEDC/UTRC and ISRL/UDRI four-channel optical systems concurrently was successfully completed.

A broad range of finite element based deterministic and probabilistic analysis methods was developed and applied to the normal mode, frequency response, and sensitivity calculations of simple-to-intricate turbine components. The UDRI developed PROTEC computer code conducts sensitivity and probabilistic calculations for the turbine structures.

Results from this research effort have been documented in seven interim reports and presented in technical papers at several conferences during the period of this program.

1.3 ORGANIZATION OF THE FINAL REPORT

The work performed to achieve the goals of this research program was described in detail in 22 bimonthly and 7 interim technical reports. However, only brief descriptions of important contributions to this project are included in the final report.

The following references and reports give detailed information for specific projects:

1. "Turbine Blade Data Acquisition System - Technical Reference Manual," by Michael J. Gutman (1).

2. "Turbine Blade Data Acquisition System - User's Guide," by Michael J. Gutman (2).

3. "Turbine Blade Data Acquisition System - Software Reference," by Michael J. Gutman et al. (3).

4. "Z-Grid Signal Conditioning System - User's Guide and Technical Reference," by J. Michael Aulds et al. (4).

5. "Probabilistic Finite Element Analysis of Dynamic Structural Response," by R. A. Brockman et al. (5).

6. "Evaluation of Plane-of-Light Noninterference Stress Measurement Systems for Measuring Bladed Disk Vibrations," by M. Swaminadham and Robert J. Dominic (6).

7. "Data Analysis Guide for the Noncontacting Blade Deflection Measurement System," by Thomas W. Held (7).

An outline of the contents of this report follows.

SECTION I outlines the need for noninterference stress and deflection measurement methods development for rotating turbine components. It also provides documentation format for the final report.

SECTION II describes the finite element model generation and modal analysis methods for flat, twisted, and circular plates, and bladed disk assemblies. Cases of numerical investigation on the tuned and mistuned bladed disk frequency response are detailed. A procedure and its application to suppress singularities in the analysis of advanced compressor blades and bladed disk assemblies to save cost and computational effort has been described.

SECTION III deals with the stochastic variations in turbine structural element material and geometric properties and develops a rationale for deriving the frequency and mode shape sensitivities. Geometric model generation, sensitivity and probabilistic

calculation, and output presentation are coded in the PROTEC computer program. This section illustrates the application of PROTEC for the deterministic and probabilistic analyses of simple-to-complex structural components.

SECTIONS IV and V deal with the important aspects of the design, development, and test tasks of the plane-of-light and Z-grid instrumentation systems. The development of four optical sensors and their integration with a 10-MHz clock to digitize and store the optical probe signals are described. The principles involved in the digital design and grid wire layout of the Z-grid system for measuring tangential and axial displacement components of one single blade of a rotating disk are also described here. Features common to both optical and grid wire systems are mentioned, and the steps to acquire and display blade data via a common front end and control monitor are explained.

SECTION VI discusses speed compensation and data analysis software procedures for the stationary and traveling wave analysis of vibrating bladed disks. The steps to resolve axial and tangential components of a blade tip deflection are described. Fringe interpretation for double pulse interferograms and the derivation of scaling factors for the three disk mode shapes are described in this section.

SECTION VII deals with the hardware design and disk instrumentation to excite and measure response from two disks in stationary and traveling wave resonances. Excitation magnets and sensor probe location details are illustrated. Details of the three test series conducted with UTRC are provided. Problems of triple pulse interferometry and nonlinear disk response are addressed. Time average mode shape interferograms for static bladed disks are furnished.

SECTION VIII summarizes the analytical and experimental frequencies, critical speeds, and mode shapes. Discrepancy in analytical predictions and measurements is discussed. Resonance speed, mode shape, and phase changes due to a stationary harmonic and static force fields are explained. The wave buildup and the amplitude collapse in the linear and nonlinear disk response

5

regimes are provided. Tables in this section compare the UDRI analysis predictions with the optical and grid wire system measurements. In addition, AEDC and UDRI NSMS evaluation tests and results are also provided.

Section IX presents the conclusions based on the analytical, experimental, and instrumentation development effort on vibrations of rotating turbine engine components. Recommendations to the Air Force for the future turbine dynamics research is also provided.

SECTION II
VIBRATION ANALYSIS BY DETERMINISTIC APPROACH

A broad analytical capability for performing deterministic dynamic analysis of turbine engine components has been developed. Components ranging from flat plate to complex integral bladed disk assemblies were analytically modeled and analyzed for normal mode and forced response calculations. Wide use of the general purpose finite element codes to model turbine, compressor structural components was accomplished. MAGNA (Material and Geometrical Non-Linear Analysis (8)), SAP (Structural Analysis Program (9)), and COSMIC NASTRAN (10) computer programs have been implemented on CDC Cyber, VAX and CRAY/XMP computer systems and the pre- and post-processing capabilities of these codes are interchangeably used for analytical modeling and results-plotting purposes.

Application of these codes for the dynamic analysis of turbine blades and bladed disks is described below.

2.1 FINITE ELEMENT MODEL

Based on a linear elastic analysis, the finite element approximation begins from the constitutive relationship:

$$\sigma_{ij} = E_{ijkl}\, \epsilon_{kl} \tag{1}$$

Because of the symmetry of the stress tensor, σ_{ij} and of the strain tensor, ϵ_{ij}, the property of σ_{ij} being a potential function of ϵ_{ij} and of the isotropy of the material, equation (1) reduces to

$$\sigma_{ij} = \frac{E}{1+\nu} \left(\epsilon_{ij} + \frac{\nu}{1-2\nu}\, \sigma_{ij}\, \epsilon_{kl} \right) \tag{2}$$

For small displacements, the linear strain tensor is given by

$$\epsilon_{ij} = \frac{1}{2} (u_{i,j} + u_{j,i}) \tag{3}$$

where u_i defines the displacement vector. The principle of virtual

7

work requires for the stresses and inertial forces the relationship

$$\int_V \sigma_{ij} \, \delta\epsilon_{ij} \, dV = -e \int_V \ddot{u}_k \, \delta u_k \, dV \tag{4}$$

which yields by completion with the virtual work done by the nodal force of a finite element, the equations of motion

$$M^j \, \ddot{\phi}^j + k^j \, \phi^j = s^j \tag{5}$$

where s^j is the nodal force vector, ϕ^j is the modal displacement vector and M^j and k^j are the element mass and stiffness matrice, respectively.

For a complex structure comprising $j = 1, 2, \ldots n$ finite elements the description follows by adding the n equations (5) in appropriate manner to give

$$M \, \ddot{\phi} + k \, \phi = S \tag{6}$$

and which yields by introducing the boundary conditions and the assumption of harmonic vibrations, $\phi = \hat{\phi} \cos \omega t$

$$(-\omega^2 M^* + k^*) \, \hat{\phi} = 0 \tag{7}$$

The solution of the eigenvalue problem gives the natural frequency (radians) and the corresponding eigenvectors ϕ which determine the mode shapes of vibrating structural components.

2.2 VIBRATION ANALYSIS OF TWISTED BLADES AND CIRCULAR DISKS BY FINITE ELEMENT METHODS

A general purpose in-house finite element computer program (MAGNA) has been used to analyze the dynamic characteristics of the basic components of bladed disk structures. Cantilevered flat and twisted plates and centrally clamped circular plates having the same geometry and material properties as those tested in the ISRL

were analyzed for eigenvalues and eigenfunctions. The blade was assumed to have a linear twist angle about its centroidal axis. Pre- and post-processing capabilities of the MAGNA program have been used to evaluate several natural frequencies and mode shapes of the test objects. Results from the flat and pretwisted cantilevered plate and centrally clamped circular plate analyses are presented in Tables 1 and 2 respectively. Mode shapes of twisted plates using MAGNA's contour plotting features depicting constant amplitude vibrations are presented in Figure 1. Circular plates dynamic deformed shapes as shown in Figure 2 were generated by the MAGNA's geometry plot (G-plot) capability. These display features enhanced our understanding of the blade-alone and disk-alone eigenfunctions.

2.3 BLADED DISK VIBRATIONS

Finite element analysis method has been applied to integrate circular disk and blades into one assembly and to evaluate the natural frequencies and mode shapes of a 12-in.-diameter, 12-bladed disk assembly. SAP finite element code has been implemented on the CDC computer, and several annular disks were modeled using thin shell plate elements. Several frequencies obtained through SAP agreed well with MAGNA's results and experimental values. However, the SAP IV program provided output in written data only and did not have plotting capability. To interpret the SAP results qualitatively, a computer program has been written to convert SAP-output into a format accepted by the plotting program used by the MAGNA code. This feature allowed us to plot model geometry and vibration contours of the bladed disk.

A comparison of analytical and experimental frequencies of a bladed disk is shown in Table 3. Finite element model and the natural modes of a 12-in.-diameter bladed disk analyzed by SAP IV and plotted using MAGNA's plotting capabilities are shown in Figures 3a and 3b.

TABLE 1
NATURAL FREQUENCIES (HZ) OF FLAT AND PRETWISTED PLATES

Geometry and Material Properties
  Length x width x thickness: 2 x 2 x 5/64 in.

Maximum twist angle at the tip: 45°

Young's Modulus: 30×10^6 psi
Poisson's ratio : 0.3
Density   : 0.000735 lb-m/in^3

Mode	Flat Plate	Twisted Plate
1B	735	774
1T	1641	3446
2B	4351	4630
3B	5784	6725
2T	6129	8342
4B	9894	10338

B - Bending,   T - Torsion

TABLE 2
NATURAL FREQUENCIES (HZ) OF CIRCULAR PLATES

Geometry and material properties
  Outer radius: 6 in. and 4 in.
  Inner radius: 0.5 in.
  Thickness   : 5/64 in.

Young's Modulus: 30×10^6 psi
Poisson's ratio : 0.3
Density   : 0.000735 lb-m/in^3

Mode (n, s)	MAGNA 4" Dia.	LEISSA (11) 4" Dia.	BLEVINS (12)
1 (1, 0)	199.6	168.5	168.1
2 (0, 0)	238.4	215.5	215.4
3 (2, 0)	281.1	281.0	280.8
4 (3, 0)	–	594.3	594.5
5 (4, 0)	–	1305.2	1304.8

n - nodal dia,   s - nodal circle
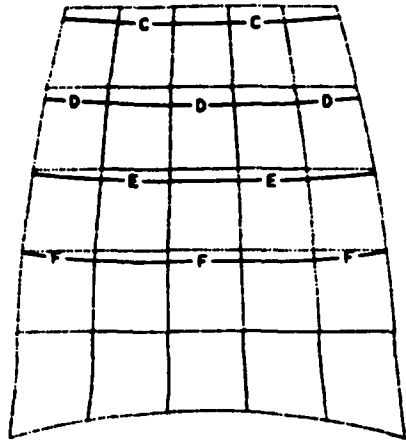
666 Hz
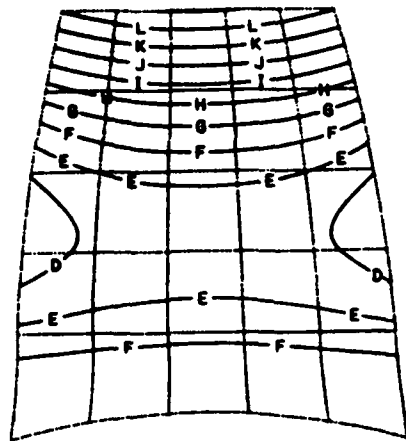
3,480 Hz
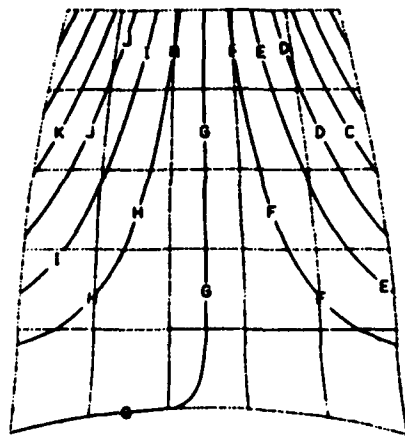
4,181 Hz

Figure 1.   Natural Modes of Twisted Plates.

11
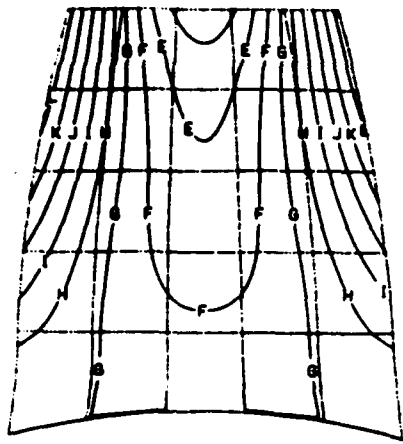
5,730 Hz
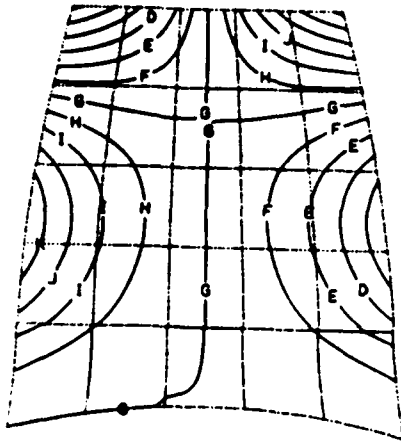
8,051 Hz
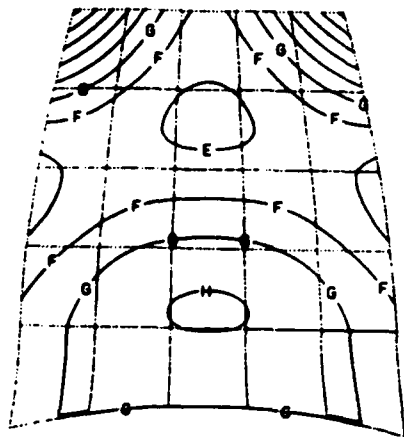
10,421 Hz

Figure 1(cont'd).   Natural Modes of Twisted Plates.

12

Nodal Dia.

76.92 Hz

98.52 Hz

120.19 Hz
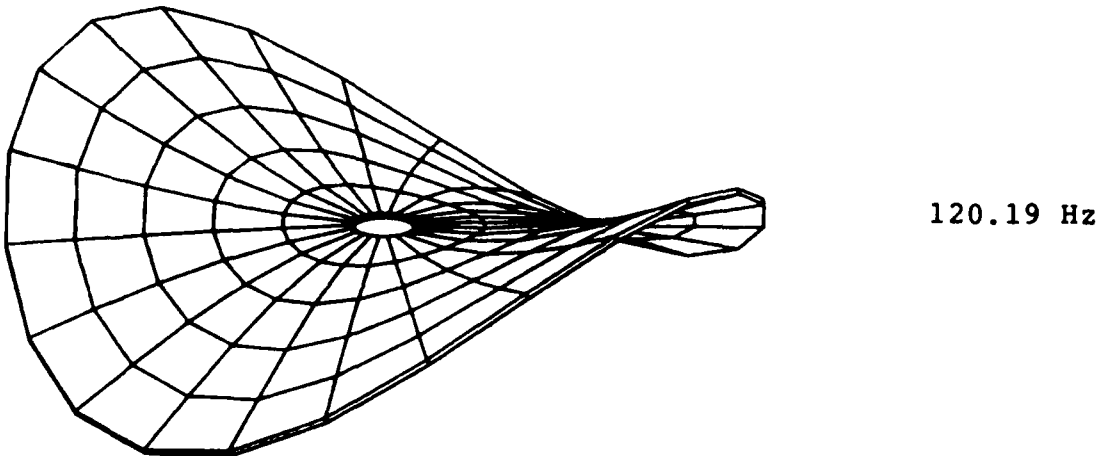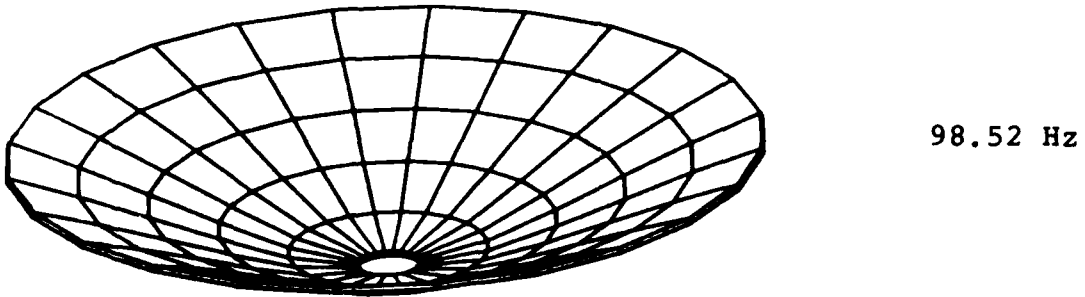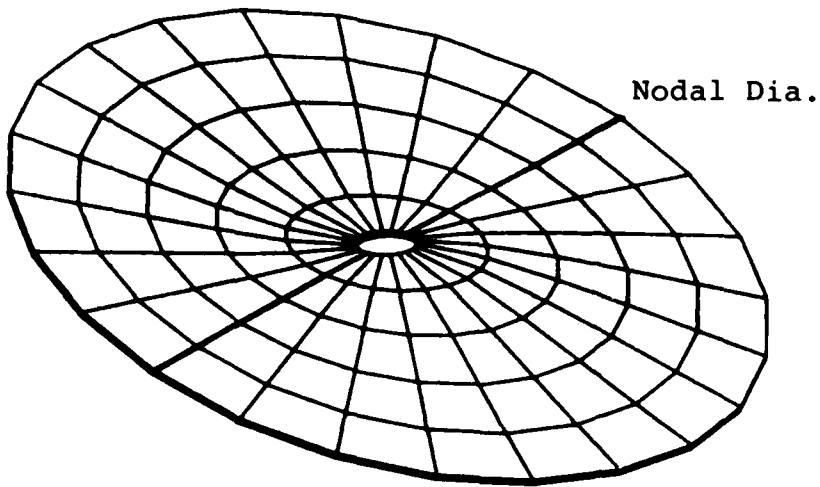
Figure 2.   Natural Modes of Circular Plates.

TABLE 3

NATURAL FREQUENCIES (HZ) OF A 12-IN.-DIAMETER, 12-BLADED DISK

Mode (n,s)	Analytical (SAP)	Experimental (Holography)
(1,0)	73.3/74.1	68.4/68.8
(0,0)	91.9	84.5
(2,0)	106.3/107.7	104.9/108.0
(3,0)	199.8/203.8	193.1/193.5
(4,0)	292.1/299.0	269.6/271.1
(0,1)	367	-

n - nodal diameter, s - nodal circle

2.3.1 Centrifugal Force Effect on Disk Modal Characteristics

Rotational speeds have considerable effect in increasing resonance frequencies of rotating blades and bladed disks of turbine engines. Solutions of the equations of motion of rotating bladed disks enabled us to study the centrifugal force effect on natural frequencies and mode shapes. Some details of the analytical basis are described here.

The equations of motion of a rotating blade disk (13) are

$$[M] \{\ddot{u}\} + [B] \{\dot{u}\} + [[K] - \Omega^2[M_1]] \{u\} = \{P\} \qquad (8)$$

where
$$\{\dot{u}\} = \begin{matrix} U_x \\ U_y \\ U_z \end{matrix} \qquad (9)$$

14

Inner Dia = 1/2 inch
Outer Dia = 8 inch
Blade Length = 2 inch
Overall Disk Dia = 12 inch
Thickness = 0.078 inch
Material: Steel
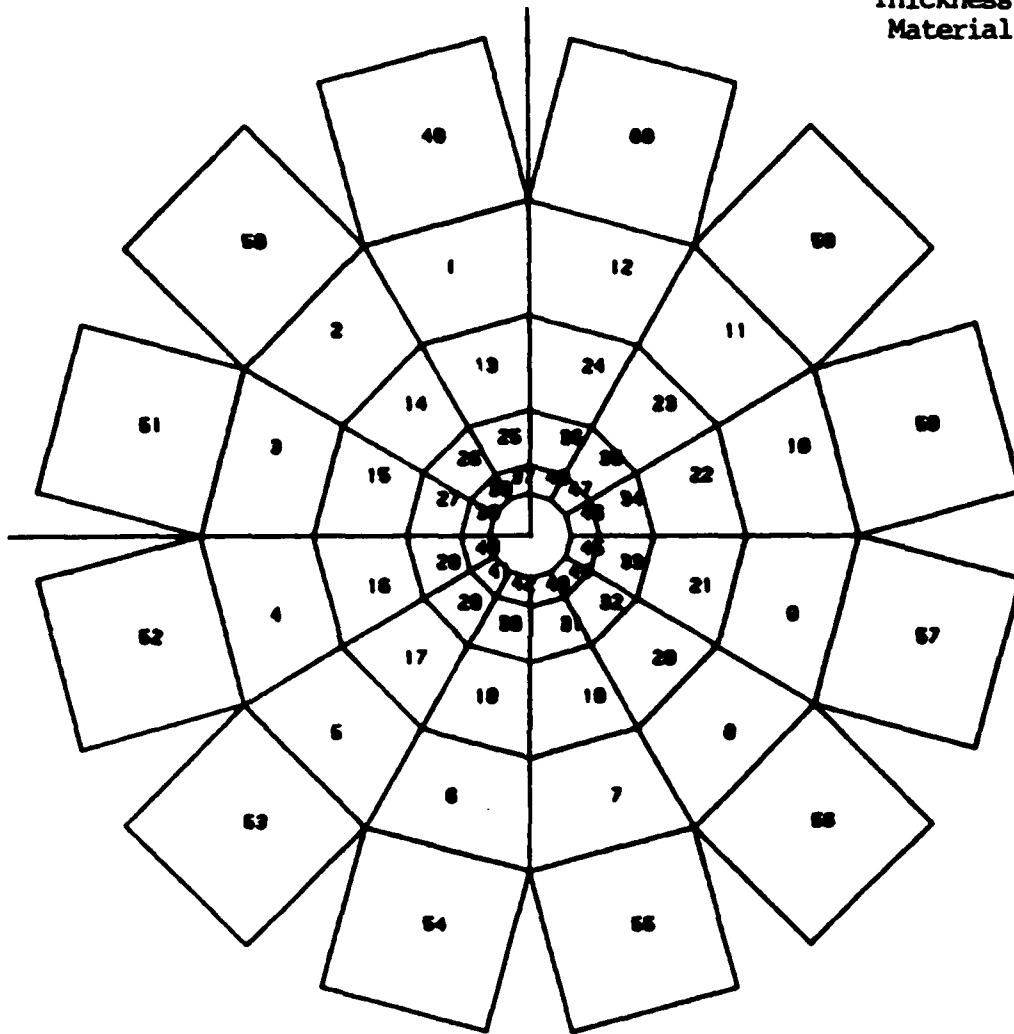
Figure 3a. Finite Element Model of a 12-Inch-Diameter Disk.

1 D Cos Θ, 73.3 Hz
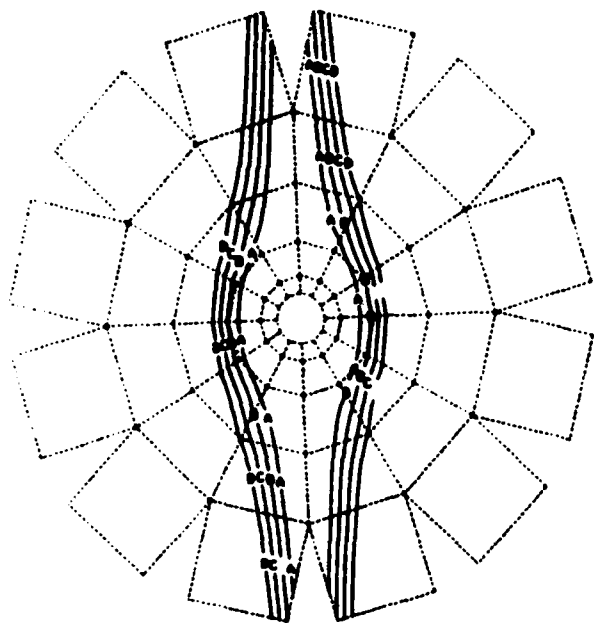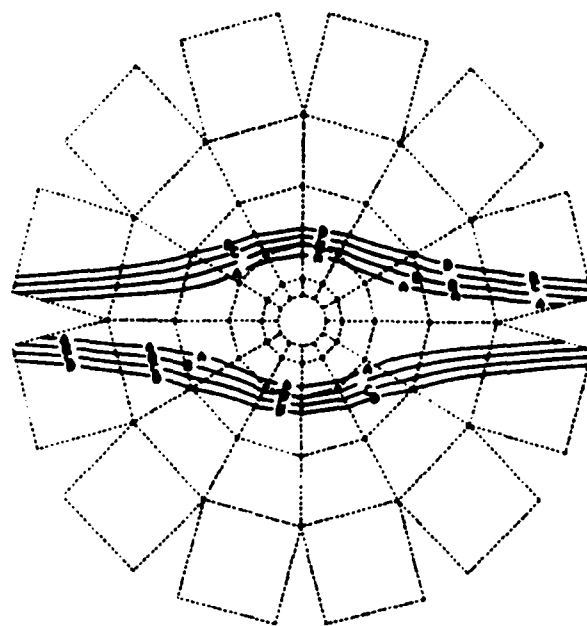
1 D Sin Θ, 74.1 Hz
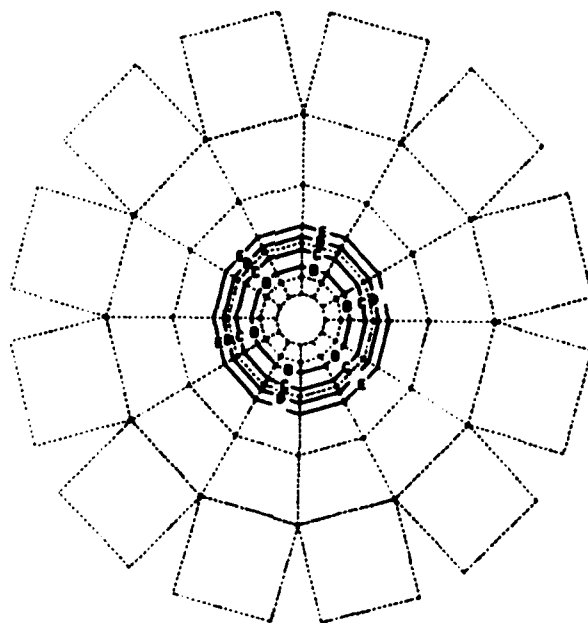
O C MODE, 91.89 Hz

Figure 3b.   Mode Shapes of 12-Inch-Diameter Disk (SAP).

2 D Sin Θ, 106.3 Hz

2 D Cos Θ, 107.7 Hz

3 D Sin Θ, 199.8 Hz
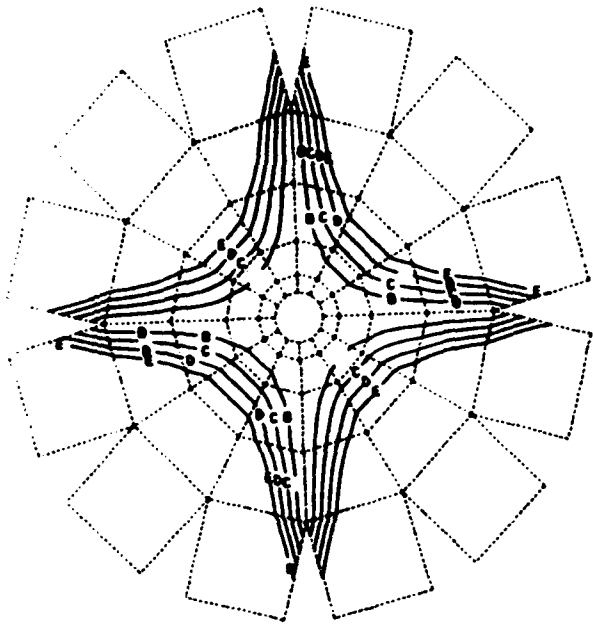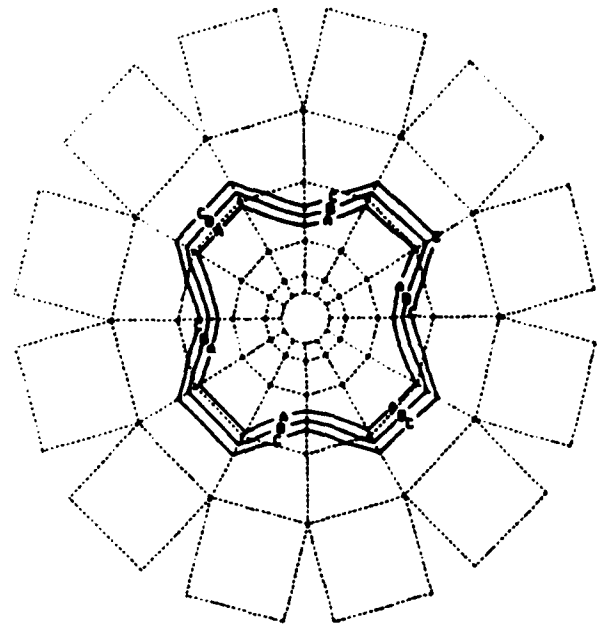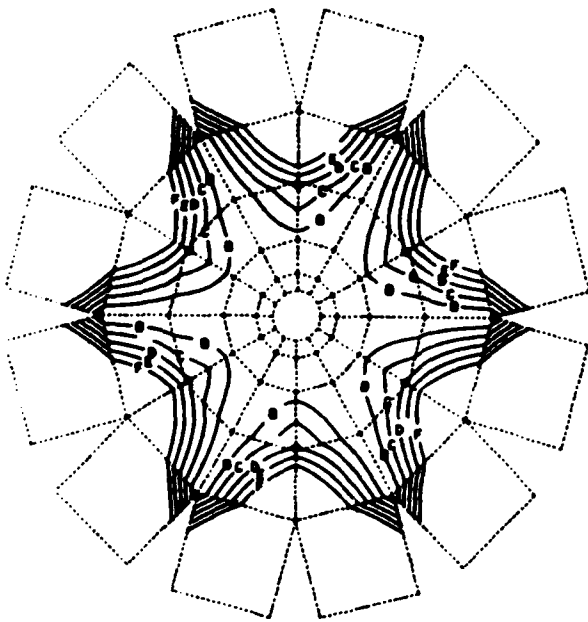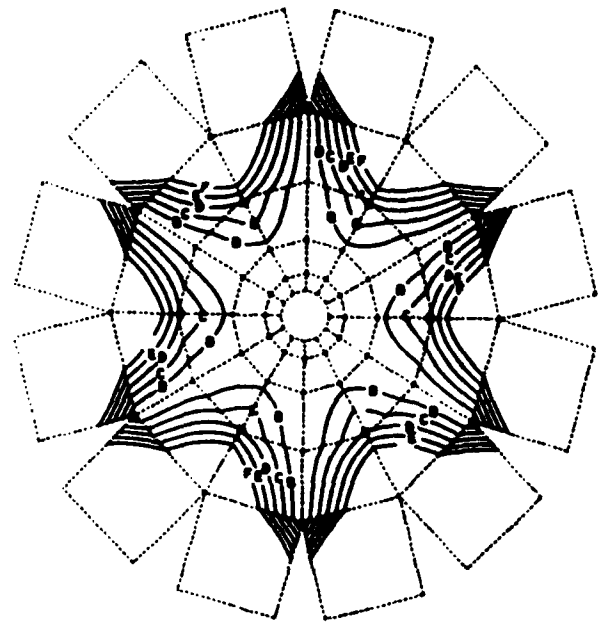
3 D Cos Θ, 203.8 Hz

Figure 3b(cont'd). Mode Shapes of 12-Inch-Diameter Disk (SAP).

$$[M] = [M]^{Global} = [T_{GB}]^T \begin{bmatrix} m & o & o \\ o & m & o \\ o & & m \end{bmatrix} [T_{GB}] \qquad (10)$$

$$[B] = [B]^{Global} = [T_{GB}]^T \begin{bmatrix} o & o & o \\ o & o & -m \\ o & m & o \end{bmatrix} [T_{GB}] \qquad (11)$$

$$[K] = [K]^{Global} \qquad (12)$$

$$\text{and } [M_1] = [M_1]^{Global} = [T_{GB}]^T \begin{bmatrix} o & o & o \\ o & m & o \\ o & o & m \end{bmatrix} [T_{GB}] \qquad (13)$$

A special feature of $[M_1]$ matrix, associated with Ω is that it contributes to stiffness in the plane orthogonal to the rotational axis. Elements of the stiffness matrix (Equation 12), were generated from four node quadrilateral plate elements with five d.o.f. per node (three in plane translations and two rotations). Appropriate boundary conditions were,

at the inner radius, $\{u\} = \{u^1\} = 0$ $\qquad (14)$

and at the free ends, $\{u^{11}\} = \{U^{111}\} = 0.$ $\qquad (15)$

When nonstructural concentrated mass ($\overline{M}$) was used at a grid point to mistune a bladed disk, a contribution to the kinetic energy was added. The expression for T was appropriately changed. The form of mass matrix for concentrated mass ($\overline{M}$) is

$$[\overline{M}] = \left[\begin{array}{ccc:ccc} \overline{M} & 0 & 0 & 0 & \overline{ZM} & -\overline{YM} \\ & \overline{M} & 0 & -\overline{ZM} & 0 & \overline{XM} \\ & & \overline{M} & \overline{YM} & -\overline{XM} & 0 \\ \hdashline & & & \overline{I}_{xx} & -\overline{I}_{xy} & \overline{I}_{xz} \\ & \text{Sym} & & & \overline{I}_{yy} & -\overline{I}_{yz} \\ & & & & & \overline{I}_{zz} \end{array} \right] \qquad (16)$$

18

2.3.2 Frequency Response of a Bladed Disk

The equation of motion of a bladed disk system with no damping is

$$[M] \{\ddot{u}\} + [K] \{u\} = \{P\} \tag{17}$$

Here, $\{u\}$ are the displacements and $\{P\}$ are the loads acting on the system. For normal mode analysis, the above equation gets uncoupled, and each mode is represented by one equation of motion.

$$\text{Let } u_i = \sum_{j=1}^{N} \phi_{ij}\xi_j \tag{18}$$

or
$$\{u\} = [\phi] \{\xi\} \tag{19}$$

Equation (17) now becomes

$$[M] [\phi] \{\ddot{\xi}\} + [K] [\phi] \{\xi\} = \{P\} \tag{20}$$

$$[\phi]^T[M] [\phi] \{\ddot{\xi}\} + [\phi]^T[K] [\phi] \{\xi\} = [\phi]_j^T\{P\} \tag{21}$$

and letting
$$\omega_j^2 = \frac{1}{\mu_j} (\phi_j)^T[K] \{\phi_j\} \tag{22}$$

and
$$\mu_j = (\phi_j)^T[M] \{\phi_j\} \tag{23}$$

Equation (21) becomes

$$[\mu_j] \{\ddot{\xi}_j\} + [\omega_j^2\mu_j] \{\xi_j\} = (\phi_j)^T\{P\} \tag{24}$$

where j denotes the mode number
    i denotes the displacement coordinate

To obtain displacement in frequency domain, Laplace transformation with $S = \delta/\delta t$ is used to get

$$\{u\} = [\phi] \quad \frac{1}{\mu_j (s^2 + \omega_j^2)} \quad [\phi]^T\{P_j\} \tag{25}$$

19

Analogous to experimental technique, wherein a sinusoidal forcing function sequentially sweeps through all the modes of a bladed disk, a numerical simulation of a sinusoidal forcing function of the following form was implemented.

$$P(\omega) = A(\omega)e^{i\phi(\omega)}$$
$$P(\omega) = A\omega e^{i\omega}$$
$$P(\omega) = A[\cos\omega + i\sin\omega] \tag{26}$$

2.3.3 Effects of Speed and Concentrated Masses-A Numerical Study

A 12-in.-diameter, 12-bladed disk was considered for analysis. A reasonable number of 4 node quadrilateral plate elements with five degrees of freedom per node was used in the analysis solution format (COSMIC NASTRAN Rigid Format 13) to evaluate twin modal frequencies of the bladed disk.

Natural frequencies and mode shapes of a bladed disk with the following dimensions were determined for several speeds.

Inner diameter of the disk	= 1 in.
Outer diameter of the disk	= 8 in.
Blade length	= 2 in.
Overall outer diameter of bladed disk	= 12 in.
Blade width	= 2 in.
Angle of twist at the tip of blade	= 45°
Number of blades	= 12
Thickness (constant)	= 5/64 in.
Young's Modulus	= 30x10^6 psi
Poisson's ratio	= 0.3
Density	= 0.000735 lb-m/in^3

Concentrated mass, $\overline{M}_1$ = 3.90 grams, $\overline{M}_2$ = 7.8 grams.

From Table 4, it is obvious that the centrifugal force effect on a tuned system increased its natural frequencies. Repeated (double and equal) frequencies were present for every diametral (circumferential) mode except for zero circular (radial) mode. Mode shape corresponding to the second of each pair of frequencies was rotated by an angle governed by $\pi/2n$, where n is

20

the number of diametral mode. For example, in 1D mode, nodal
diameters were orthogonal to each other, while in 2D mode, nodal
diameters are rotated by 45 degrees and so on. Contour lines
corresponding to normal displacements were symmetrical with respect
to x-y axes. Mode shapes for a tuned system are presented in
Figure 4.

TABLE 4
ROTATIONAL SPEEDS VS. NATURAL FREQUENCIES (HZ)
OF A TUNED BLADED DISK

Speed	Modes				
(rpm)	1D	OC	2D	3D	4D
0	76.5	92.1	110.2	200.3	276.9
	76.5		110.2	200.3	276.9
1000	78.6	93.5	112.5	202.0	278.3
	78.6		112.9	203.6	281.3
1700	82.2	95.8	116.7	205.1	280.8
	82.2		117.2	206.8	283.1
2000	84.3	97.2	119.2	206.9	282.3
	84.3		119.6	208.6	285.3
4000	104.0	110.4	142.8	225.8	298.0
	104.0		143.3	227.3	300.0
5000	116.6	119.1	158.2	238.8	309.2
	116.6		158.6	240.3	312.0
6000	130.1	128.7	175.3	253.9	322.3
	130.1		175.6	255.4	325.0

Mistuning due to concentrated masses at specific
locations on the disk was studied. Changes in frequencies are
presented in Table 5. With mistuning of this nature, repeated
roots will degenerate into two modes. The dependency and extent of
this degeneration depends on the magnitude and the relative
positions of mistuning masses. When only one mass at the outermost
radius was used to deliberately mistune the disk, one of the roots
lowered in frequency while the other remained essentially the same.
This effect was seen in all diametral modes. Rotational speeds
stiffen the disk and increase the numerical value of the resonant
frequencies.

21
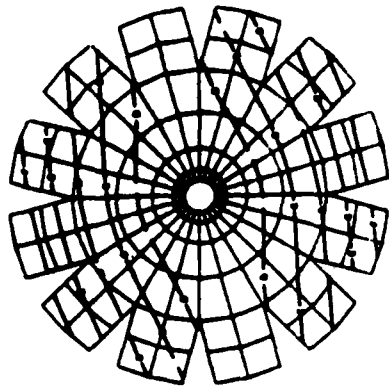
1D CosΘ MODE , 76.5 Hz
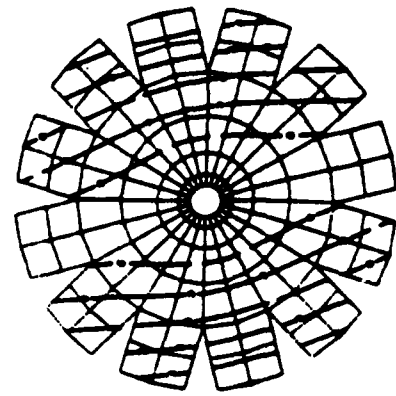
1D SinΘ MODE , 76.5 Hz
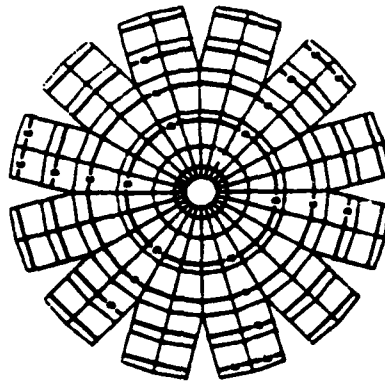
O C MODE ,92.1 Hz
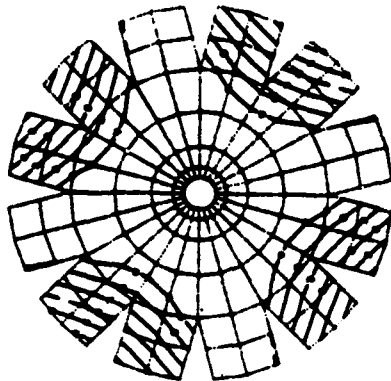
2 D Cos Θ MODE, 110.17 Hz
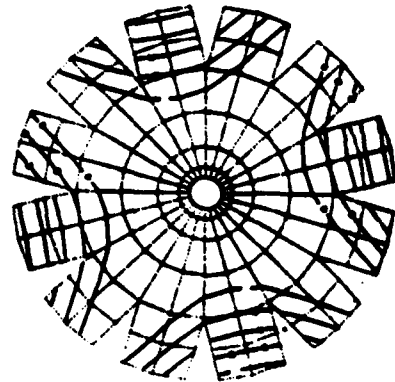
2 D SinΘ MODE, 110.17 Hz
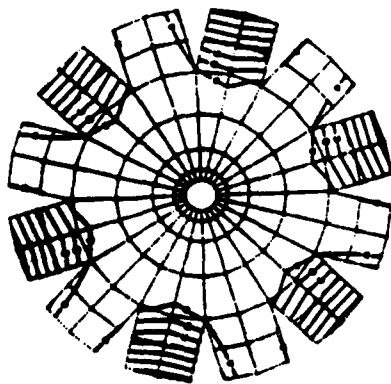
3 D CosΘ MODE,200.3 Hz
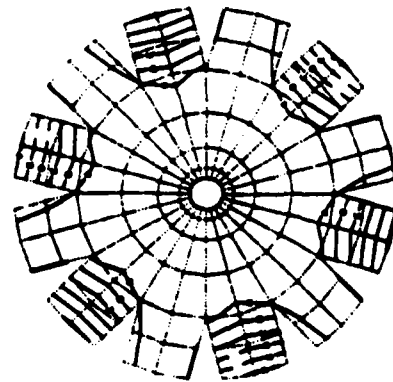
3 D SinΘ MODE , 200.3 Hz

Figure 4.   12-Inch-Diameter Tuned Disk Mode Shapes.

TABLE 5
MISTUNED DISK SPEED VS. NATURAL FREQUENCIES (HZ)
CONCENTRATED MASS $\bar{M}_1$ OF 7.8 GRAMS
AT GRID POINT 257

Speed (rpm)	Modes				
	1D	OC	2D	3D	4D
0	54.2	86.6	100.0	161.6	236.2
	76.6		110.5	200.3	279.3
1000	57.3	88.2	102.2	164.4	
	78.6		112.9	202.1	
1700	62.7	91.1	106.3	169.4	
	82.2		117.4	205.5	
2000	65.6	92.7	108.7	172.2	244.6
	84.3		119.9	207.4	284.9
3000	77.1	99.4	119.1	184.1	254.5
	93.0		131.0	216.0	291.9
5000	104.4	117.0	148.1	215.3	282.3
	116.4		160.8	241.8	312.9
6000	118.6	130.2	165.3	233.2	299.0
	127.7		178.5	256.9	326.5

With a single mass of 7.8 grams, equivalent of one blade mass (same trend was evidenced for half the mass), and for the case of 1D mode, mode that corresponds to lower frequency had distorted shape. The mode corresponding to the unaltered frequency remained symmetrical with the nodal line passing through the mistuning mass. The nodal diameter was attached to concentrated mass, and the mass does not participate in mode formation. This trend is true for all diametral modes with a single concentrated mass. Circular modes were also disfigured in the sense that the disk half containing the concentrated mass had less displacement compared to the other half. Also, the center of the circular contour lines moved away from the geometric center of the disk. In 2D, 3D, etc., modes, one of the split modes was altered while the other remained unaltered. In the unaltered modal configuration, nodal diameters pass through the mistuning concentrated mass. The results for a mistuned mass of 3.9 grams are presented in Table 6.

23

With the increase of speed, mode shapes corresponding to the lower and unaltered frequencies behaved as before except that both frequencies raised in proportion to the speed of rotation and the displacements were less. Mode shapes for a case of $\bar{M}_1$ = 7.8 grams and N = 2,000 rpm are presented in Figure 5. The centrifugal effect of the concentrated mass reduces the resonant displacements in one of the split modes.

A study with two equal concentrated masses at 180° and also at 90° to each other was conducted, and the effect of these two masses was to lower both frequencies of the diametral and circular modes as shown in Table 7. The mode shapes remained symmetrical in the first case, but in the latter case, nodal lines did not attach themselves to concentrated masses.

TABLE 6
MISTUNED BLADED DISK SPEED
VS. NATURAL FREQUENCIES (HZ)

CONCENTRATED MASS $\bar{M}_1$ OF 3.9 GRAMS
AT GRID POINT 257

Speed	Modes				
(rpm)	1D	OC	2D	3D	4D
0	64.5	88.1	101.8	170.7	241.1
	76.6		110.5	200.3	279.3
1000	67.0	89.6	104.1	173.0	243.0
	78.6		112.9	202.1	280.7
1700	71.4	92.3	108.2	177.1	246.5
	82.2		117.3	205.3	283.3
2000	76.6	95.5	113.4	182.1	250.8
	86.7		122.6	209.4	286.6
3000	84.0	100.2	121.0	189.6	257.3
	93.0		130.4	215.5	291.6
5000	109.3	117.7	150.0	218.0	282.8
	116.6		159.7	240.0	312.2
6000	122.8	130.3	167.3	235.1	298.7
	128.6		177.0	255.4	325.5
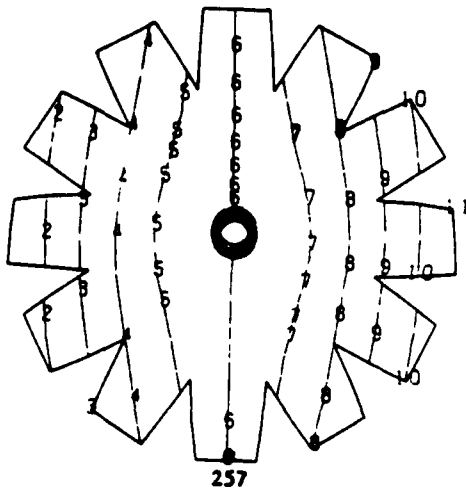
1 D Cosθ MODE , 84.3 Hz
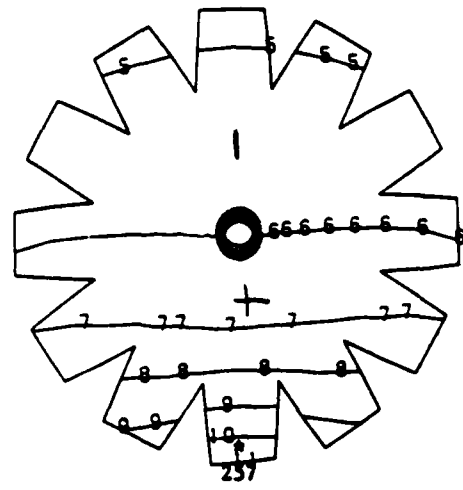
1 D Sinθ MODE , 65.6 Hz
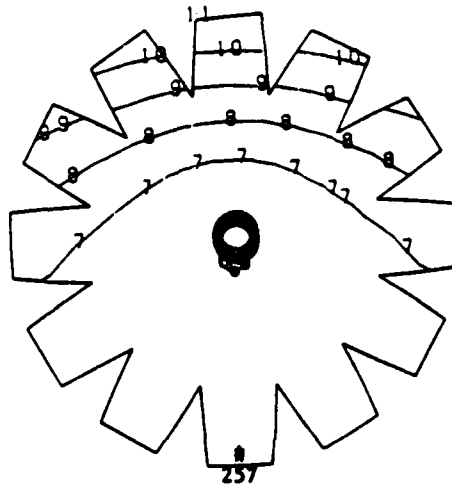
0 C MODE , 92.7 Hz
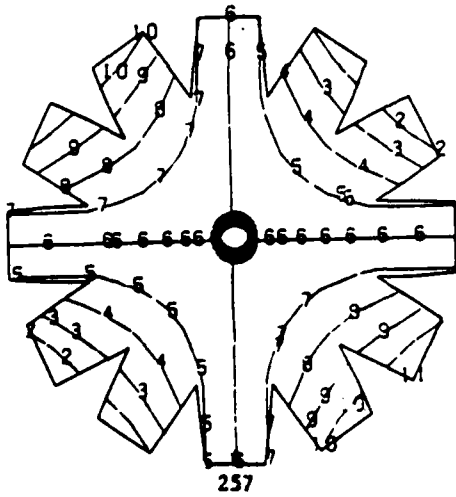
2 D Cosθ MODE , 119.9 Hz
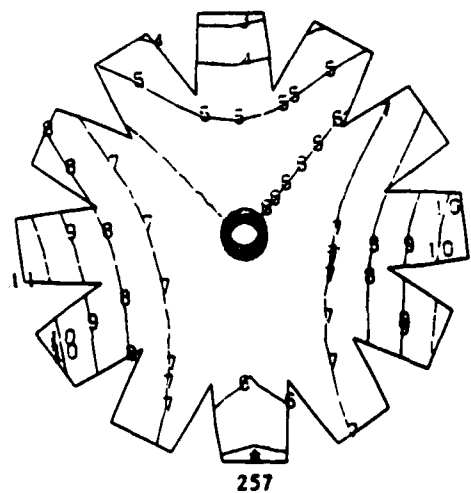
2 D Sinθ MODE , 108.7 Hz

Figure 5.   Mistuned Rotating Disk Mode Shapes.

25

Vibration-amplitudes for the grid points 257, 188, and 170 were evaluated as a function of excitation frequency in a simulated sine dwell test. Variations in amplitudes for small increments of frequencies in close proximity to resonances, for the 1D, OC, 2D and 3D modes, are presented in Figure 6. Modal damping values were estimated from these graphs, by the halfpower point bandwidth method. Resonances were widely separated even for split modes, and no response contribution from other modes was evident. Phase differences in responses for the grid points 257 and 170 which were spatially offset by 90° are seen in diametral modes. Modal damping values are quite small and correspond to hysteresis damping of the disk material. The results from a study on bladed disk mistuning, rotational effects and frequency response can be found in reference (14).

TABLE 7
MISTUNED BLADED DISK DYNAMICS
CONCENTRATED MASS $\overline{M}_1$ AND $\overline{M}_2$, EACH OF 3.9 GRAMS
AT GRID POINTS 257 AND 230 AT 90°

Speed	Modes				
(rpm)	1D	OC	2D	3D	4D
0	64.1	86.8	92.6	159.2	229.4
	64.8		110.5	177.9	266.5
1000	66.7	88.2	95.1	161.6	231.3
	67.2		113.0	180.1	268.6
1700	71.3	90.9	99.7	166.0	231.8
	71.4		117.4	184.0	272.4
2000	76.5	94.1	105.2	171.5	239.1
	76.7		122.9	188.9	277.1
3000	83.5	98.8	113.2	179.5	245.7
	84.3		130.9	196.2	284.2
5000	108.0	116.9	143.1	209.7	271.6
	110.5		160.8	224.1	311.3
6000	125.0	120.1	160.6	227.6	287.8
	128.6		178.5	241.0	326.1

26
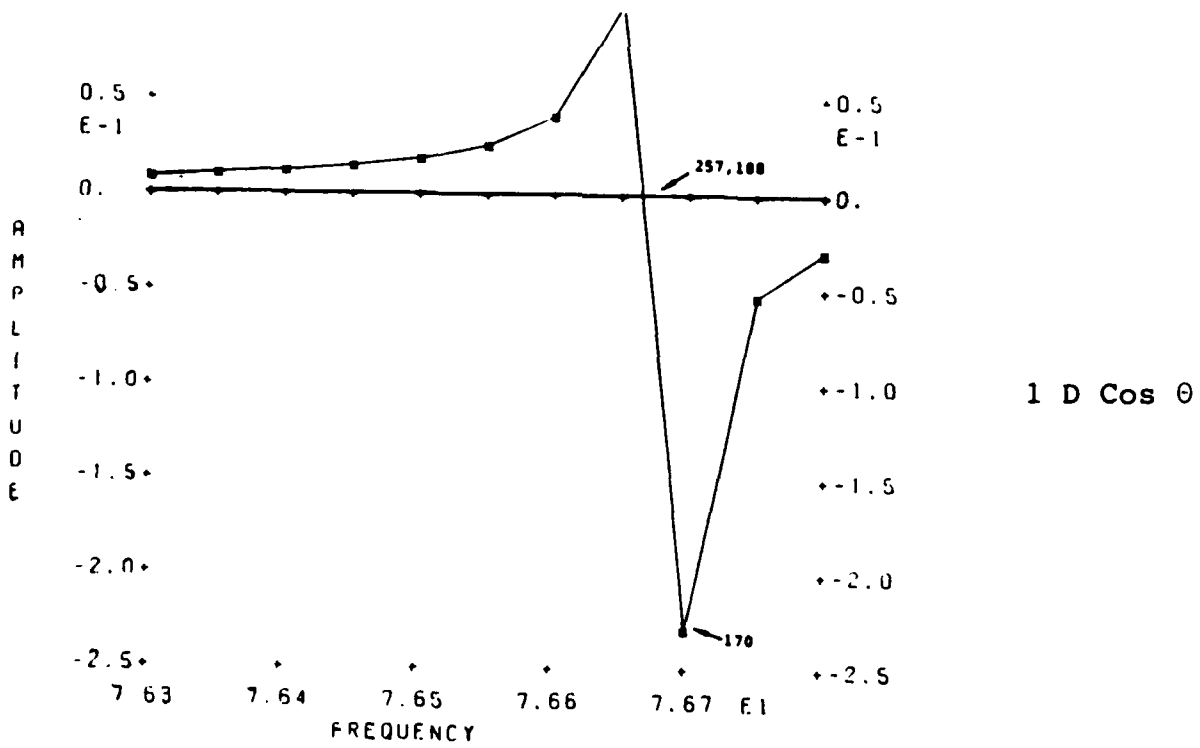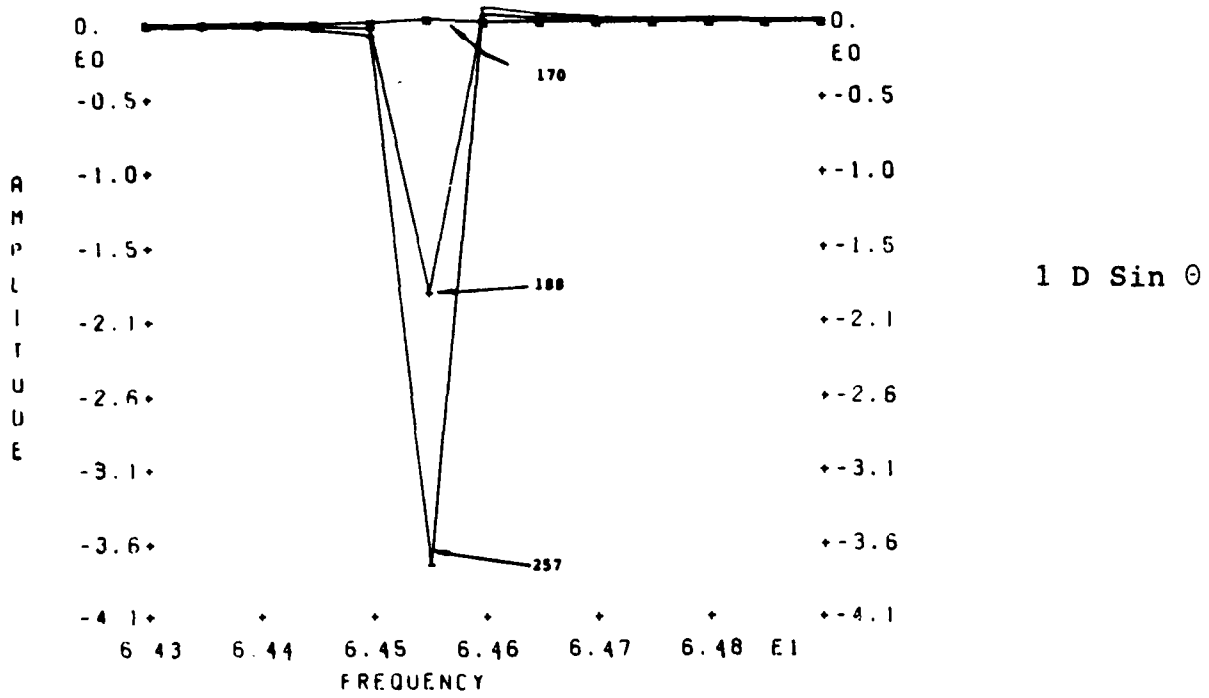
Figure 6. Modal Response of Mistuned Disk Near Resonance.

0.
E0

H
M
P
L
I
T
U
D
E.

170

188

257

-0.5+

-1.1+

-1.6+

-2.1+   +   +   +   +   +   +   +   +
   8.801   8.803   8.805   8.807   8.809   8.811   8.813   8.815

+0.
E0

+-0.5

+-1.1

+-1.6

+-2.1
E1

O C MODE
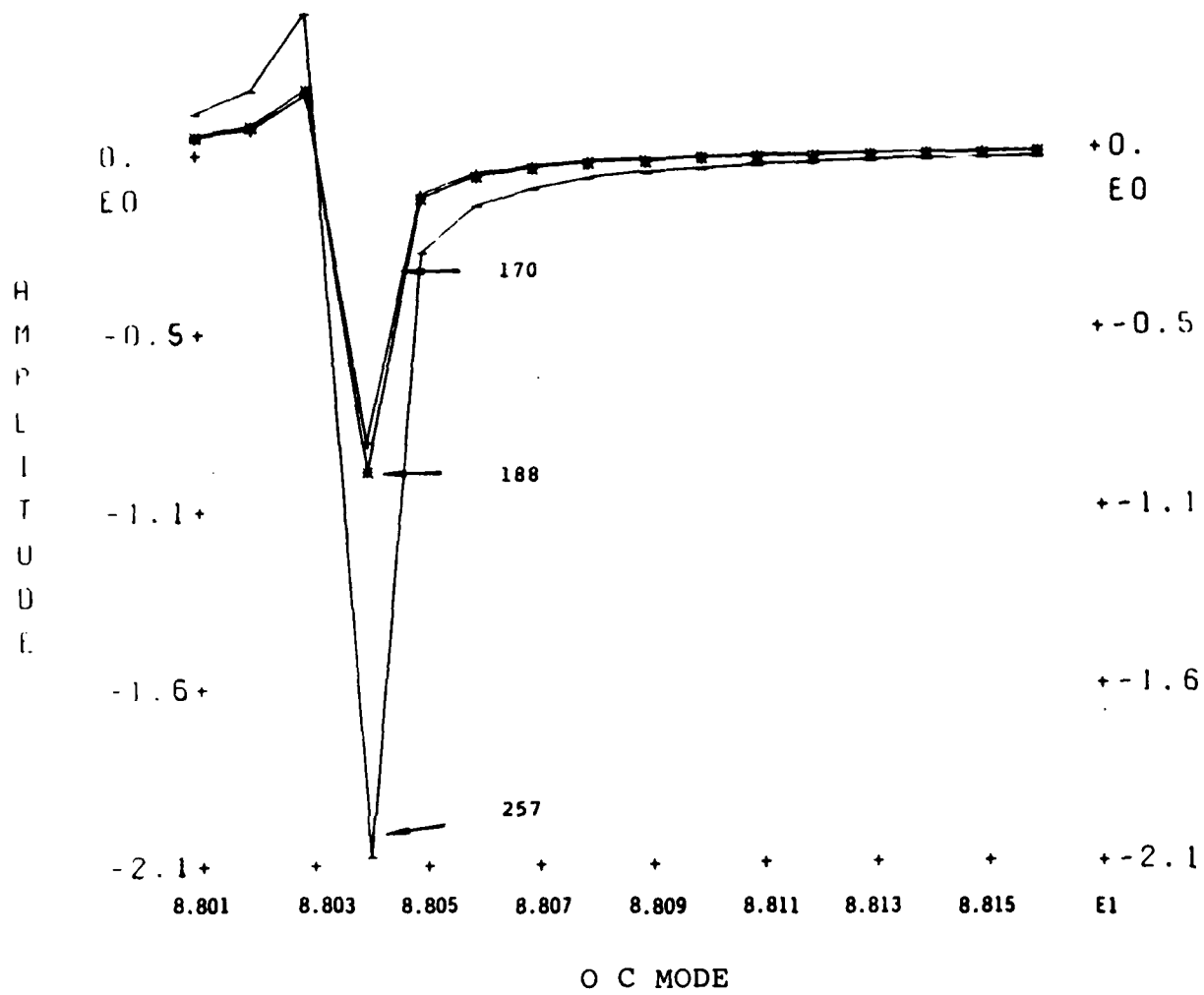
Figure 6(cont'd).   Modal Response of Mistuned Disk Near Resonance.
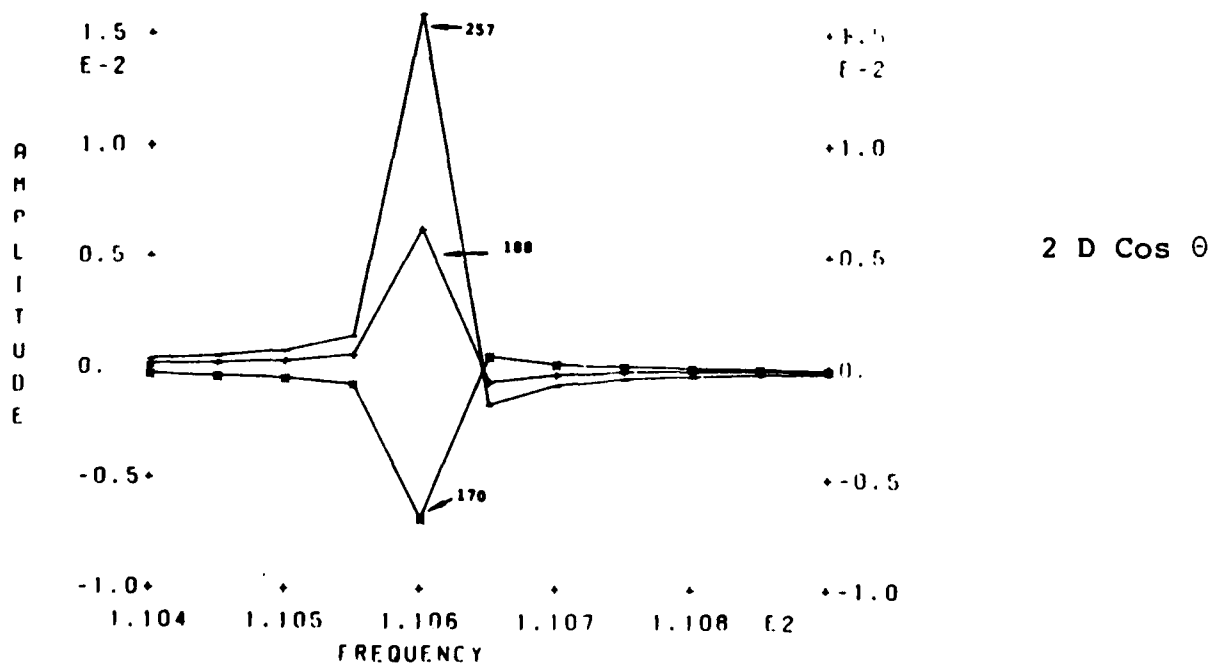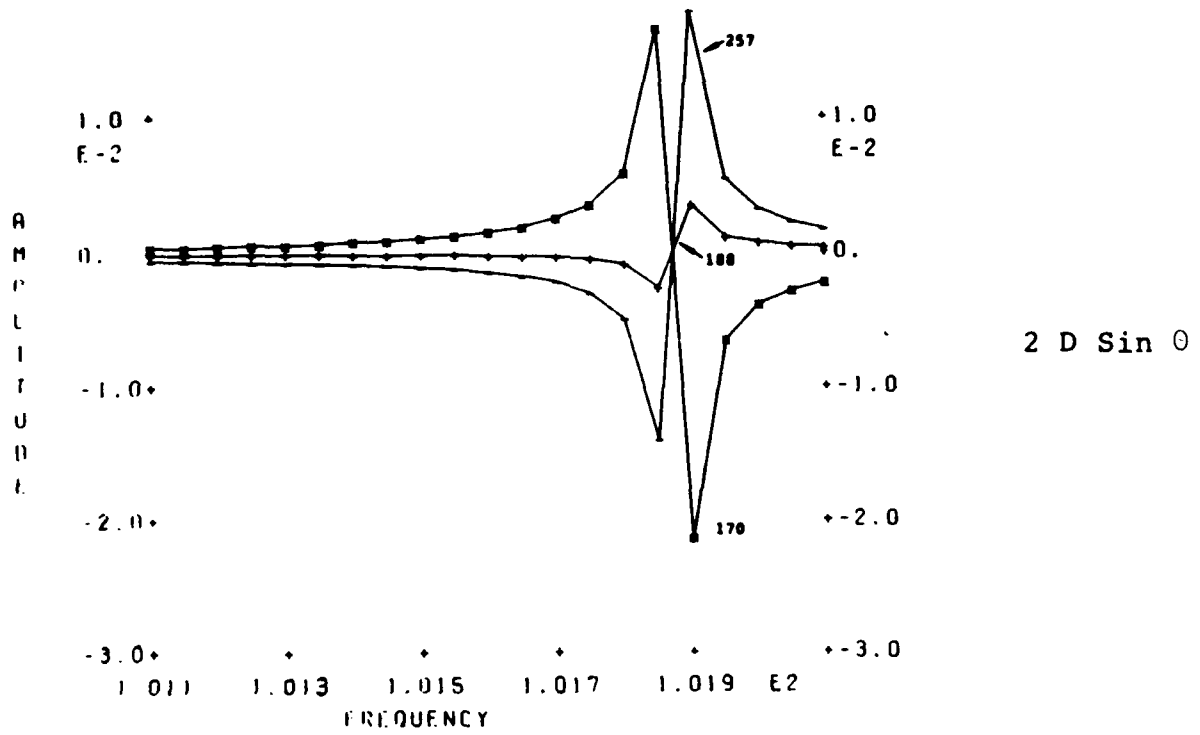
Figure 6(cont'd).   Modal Response of Mistuned Disk Near Resonance.

29

2.4 ADVANCED COMPRESSOR BLADE VIBRATIONS

Two finite-element programs were used to study the resonant characteristics of an advanced compressor blade. SAP IV with quadrilateral elements allowed tuning of the blade model to represent its half-plate and half-shell geometric appearance. The COSMIC NASTRAN program with triangular plate elements was also used to analyze blade vibrations. An added feature of NASTRAN was its accommodation of rotational effects. SAP analysis provided a close agreement with the experimental determination of several lower order modes.

The titanium blades of an axial flow compressor disk had a transonic airfoil cross section, were integrally machined with the disk, and had an aspect ratio of 1.255. These blades had a meridional chord curved at the base which gradually leaned out at the tip. Leading edge sweep of the blade tip was obtained by increasing the chord length in the midspan region. Nonradial stacking of the centroids of the cross sections towards the tip and reflex curvature in the meridional plane of the leading edge were used to limit excessive stresses on one side of the airfoil surface. All these features of the blade profile were obtained from the geometry file supplied by the PW and also from the reference (15). Variations in chord length, thickness, stagger angle and the stacking centroids can easily be observed in Figure 7.

2.4.1 SAP Analysis

The SAP IV program was employed with plate and shell elements to analyze the blade for natural frequencies and mode shapes. The model for the UDRI SAP IV analysis is shown in Figure 8. The SAP IV analytical model had 143 nodal points and 120 quadrilateral plate/shell elements, with grid points 131 through 143 completely restrained to simulate the fixed root condition of the blade. Each nodal (grid) point had six degrees of freedom and the analysis method can selectively free or restrain the rotations X', Y', and Z' independently to simulate the plate or shell element characteristics. The bending properties of the plate and shell

30
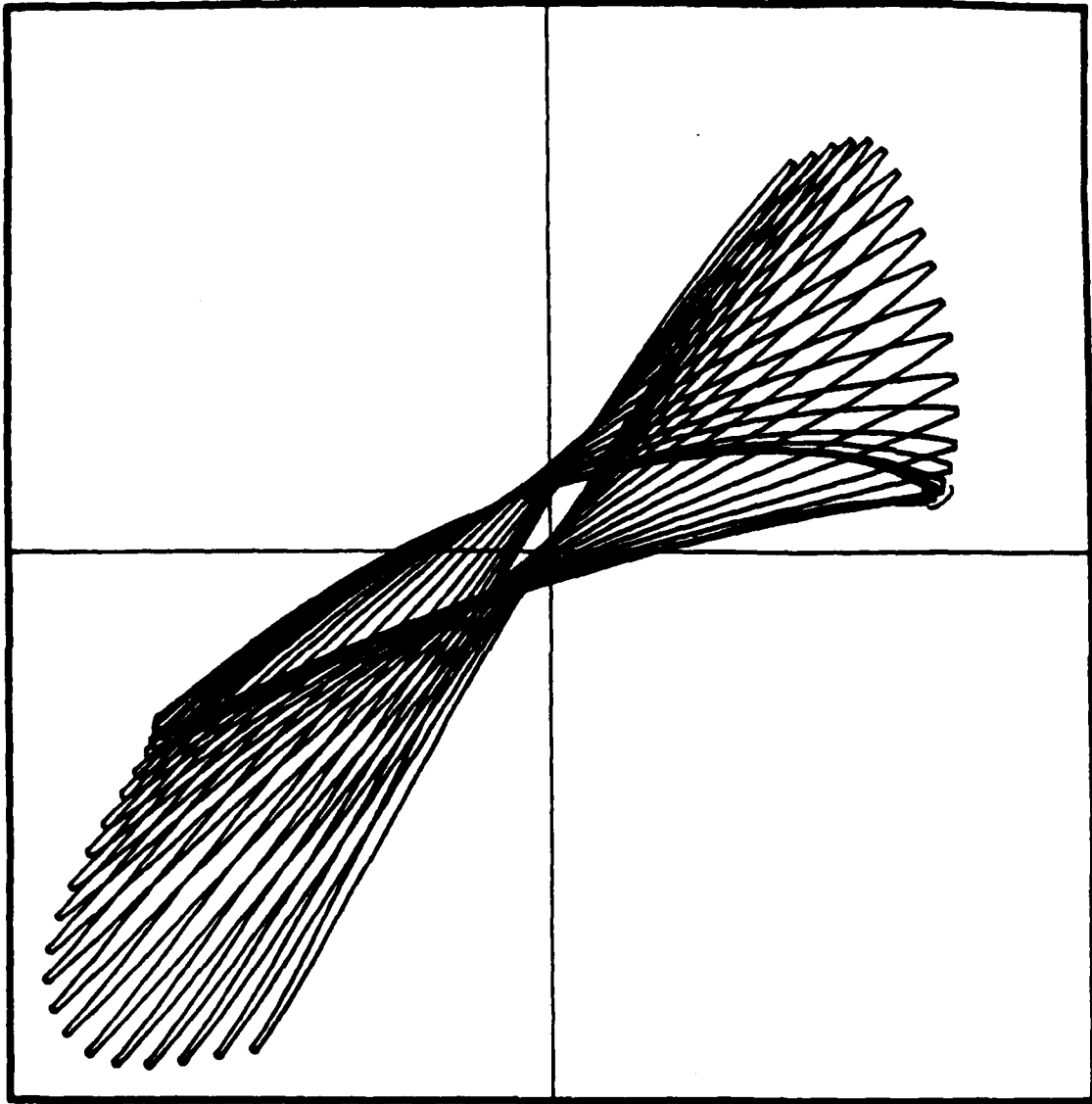
Figure 7. Variable Geometry Compressor Blade
Cross Section.
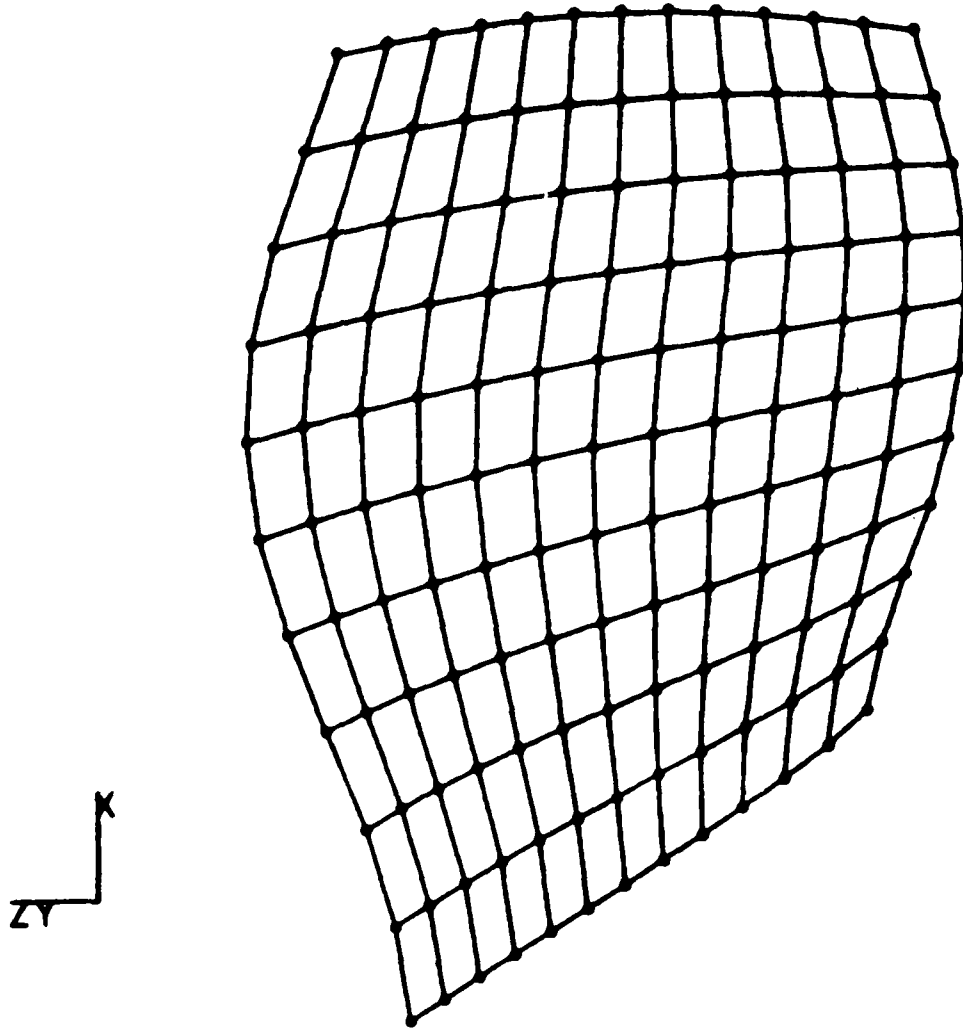
Figure 8. Quadrilateral Finite Element Model of Compressor Blade.

elements accurately simulated the dynamic properties of the blade. Actual blade geometry data was modified slightly by assuming that each blade element had a constant thickness equivalent to the average thickness of the local area.

For the purpose of understanding the effect of rotational restraints on the frequencies, a finite element model with the grid points having the degree of freedom per node (0-free or 1-fixed) was studied. Several cases were studied and the results from four cases are presented in Table 8. Relaxing the restraint in rotation about the Z axis for all grid points up to the mid-span and modeling a thick fillet at the base brought the analysis fundamental frequency much closer to that of the experiment. However, NASTRAN runs performed by Pratt & Whitney Aircraft Company (PWA) and by Puterbaugh (15) of AFWAL did not incorporate the base fillet and predicted a fundamental frequency which was lower than the experimental value. The analysis by UDRI considered the effect of a thick fillet at the trailing edge and our fundamental frequency prediction was very close to the experimental value. There was, however, a variation in the frequencies of higher modes.

Table 9 compares the results of the three analyses. The PWA analyses illustrated the effect of the centrifugal force field due to rotation on the modal frequencies. The flapwise, edgewise, and torsional modes were affected, with the flapwise fundamental frequency being drastically increased from 530-540 Hz at zero speed to 760 Hz at 21,500 rpm. Modal frequency changes due to speed and the comparison of frequencies and modes at zero speed can also be seen in the Campbell Diagram shown in Figure 9. Contour plots of modal displacements are provided in Figure 10. It was rather simple to identify flapwise, edgewise, and torsional modes from these plots. There was good correlation of the mode shapes furnished by the PWA with our analytical results. We should note that the laser holographic experiments did not record the edgewise bending mode. This mode was essentially in the plane of the disk, and the recording technique was not sensitive to small inplane displacements of the edgewise mode. The analytical effort

33

TABLE 8

SAP FINITE ELEMENT ANALYSIS OF
LOW ASPECT RATIO FAN (LARF) BLADE

Case No.	Node Numbers	X	Y	Z	X'	Y'	Z'	eigenfrequencies, (Hz)
1	1 through 130	0	0	0	0	0	1	523
	and							1308
	131 through 143	1	1	1	1	1	1	1500
								2433
								2628
								3276
								3632
2	1 through 130	0	0	0	0	0	1	662
	and							1348
	131 through 143	1	1	1	1	1	1	1769
								2480
								2814
								3358
								3767
3	1 through 77	0	0	0	0	0	1	589
								1320
	78 through 130	0	0	0	0	0	0	1557
	and							2460
	131 through 143	1	1	1	1	1	1	2681
								3319
								3687
4	1 through 77	0	0	0	0	0	0	598
								1325
	78 through 130	0	0	0	0	0	0	1594
	119	0	0	0	1	1	1	2482
	118							2701
	and	1	1	1	1	1	1	3333
	131 through 143	1	1	1	1	1	1	3712

Key to the Degree of Freedom: 0 - free

1 - fixed

TABLE 9
COMPARATIVE TABLE OF THE NATURAL FREQUENCIES (HZ)
OF A LOW ASPECT RATIO BLADE

Mode No.	UDRI N=0			ISRL* N=0	APL (15) N=21500	PWA-GPD (16) N=0	N=21500
	SAP IV Case 1	SAP IV Case 4	NASTRAN (CTRIA 2)			FROM GRAPH	
1	523	598	549	589	765	534	756
2	1308	1325	1363	–	1501	–	1744
3	1500	1594	1695	1728	1851	1700	1889
4	2433	2482	2487	2049	2533	1980	2649
5	2688	2701	–	2718/ 2763	–	2875	–

N - Speed in rpm

* Laser holographic interferometry experimental values
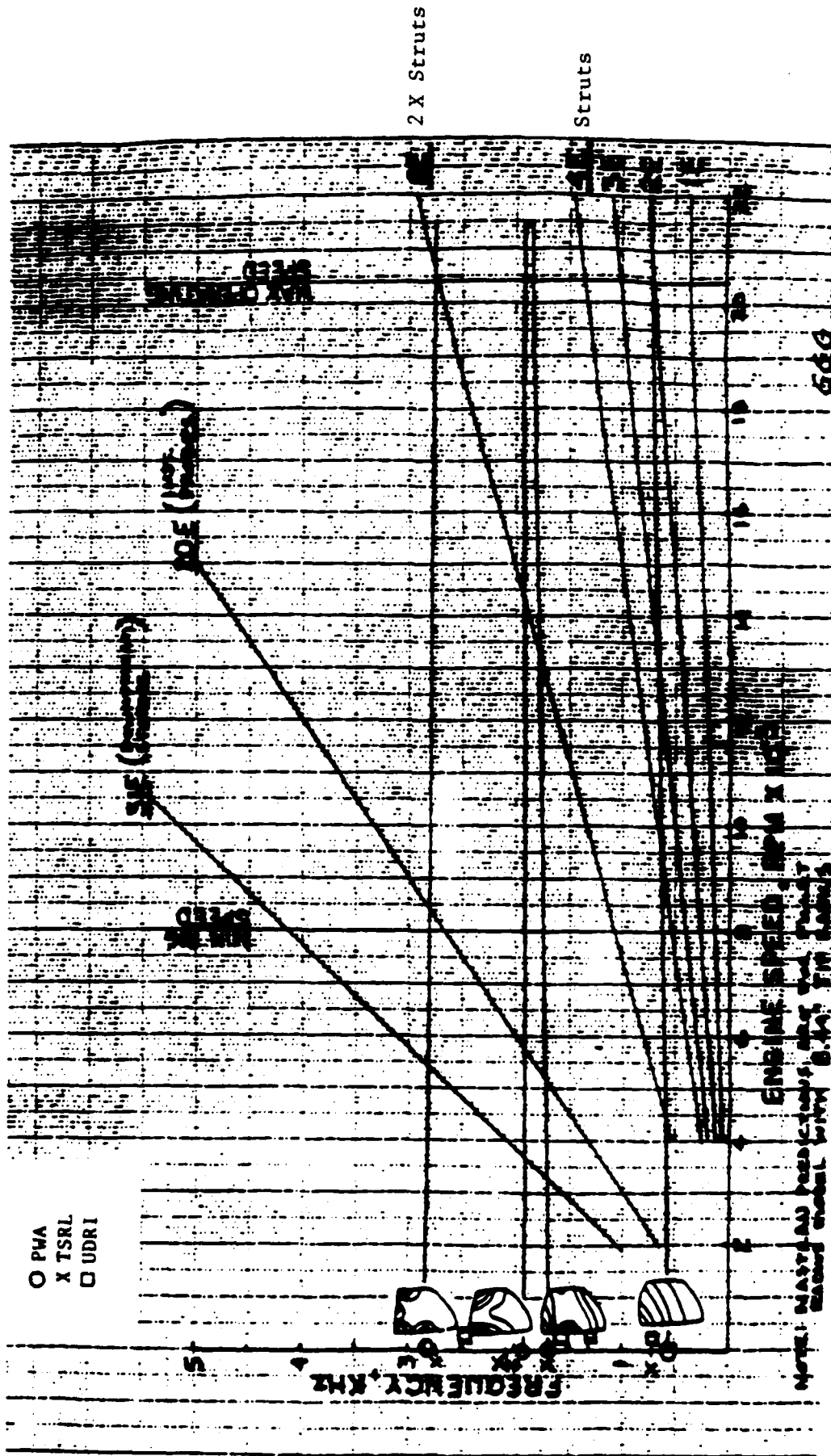
Figure 9. Campbell Diagram for the Compressor Blade.

36
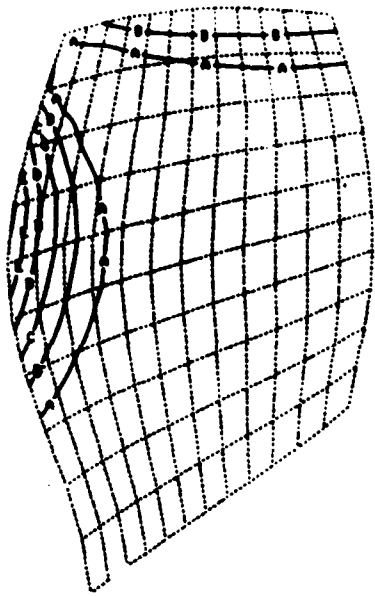
598 Hz
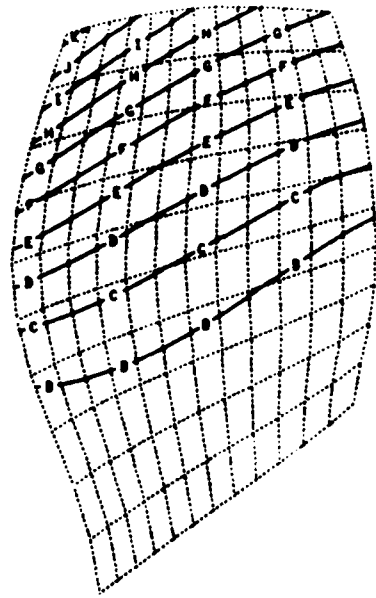
1,325 Hz
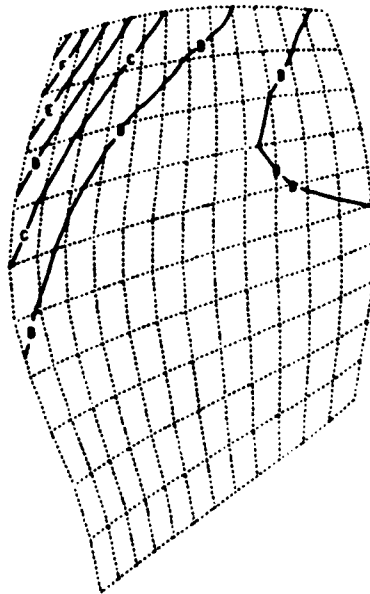
1,594 Hz

Figure 10. Contour Plots for Mode Shapes of Compressor Blades.
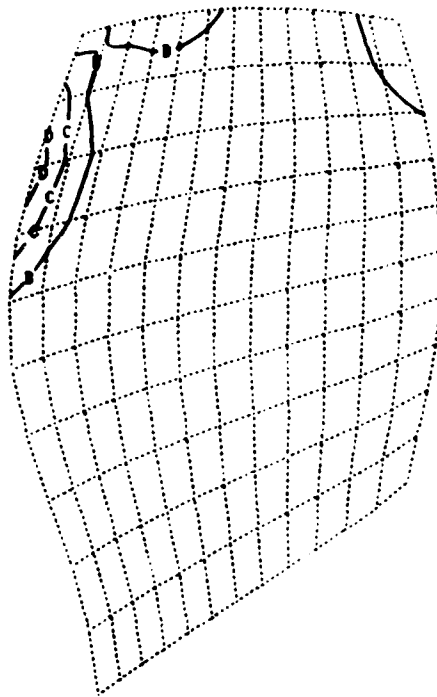
2,482 Hz
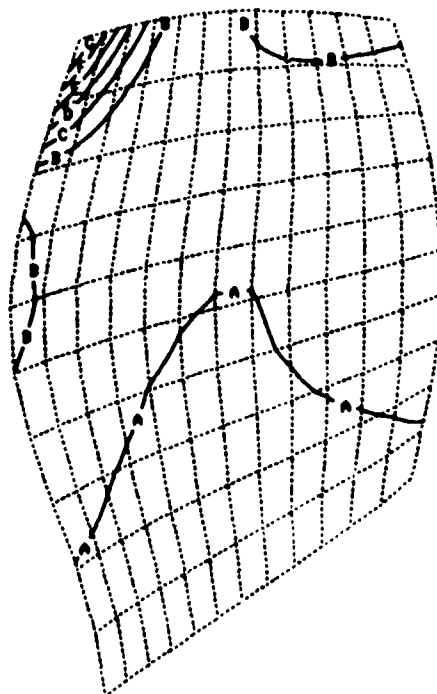
2,701 Hz

Figure 10(cont'd). Contour Plots for Mode Shapes of Compressor Blades.

conducted by UDRI is based on the information provided by other sources. A more ideal approach would be to generate geometrical data of the blades from a numerical control machine tape.

Three aspects of the analysis to define dynamics of fan blades were investigated. These were:

a. use of triangular elements to investigate the rotational effects,

b. development of a procedure to suppress the signularities in the finite-element analysis, and

c. use of quadrilateral elements available with NASTRAN.

2.4.2 TRIA2 Elements

Blade geometry was modeled with triangular plate elements. Blade geometry, mesh nature, and the axis of rotation are illustrated in Figure 11. The blade root fillet was modeled with several elements. Care was exercised to avoid biasing of stiffness properties of triangular elements by orienting the longer sides of elements to the left and right alternatively. Triangular elements have both membrane and bending properties. Membrane properties of the elements simulated well the in-plane centrifugal force field. The triangular and rectangular elements with their nodal degrees of freedom are shown in Figure 12.

Rigid format 13 of COSMIC NASTRAN was used to perform the normal mode analysis of a rotating compressor blade. Table 10 furnishes the natural frequencies for several modes of a blade at various rotational speeds.

A comparison with the results of PWA and General Electric Company (GE) was made for the fundamental mode only. GE used ANSYS and their fundamental frequency at operating speed was 776 Hz. PWA used MSC NASTRAN and their frequency was 673 Hz. Our use of COSMIC NASTRAN yielded a frequency 770 Hz. Differences between PWA and our results were primarily due to small variations
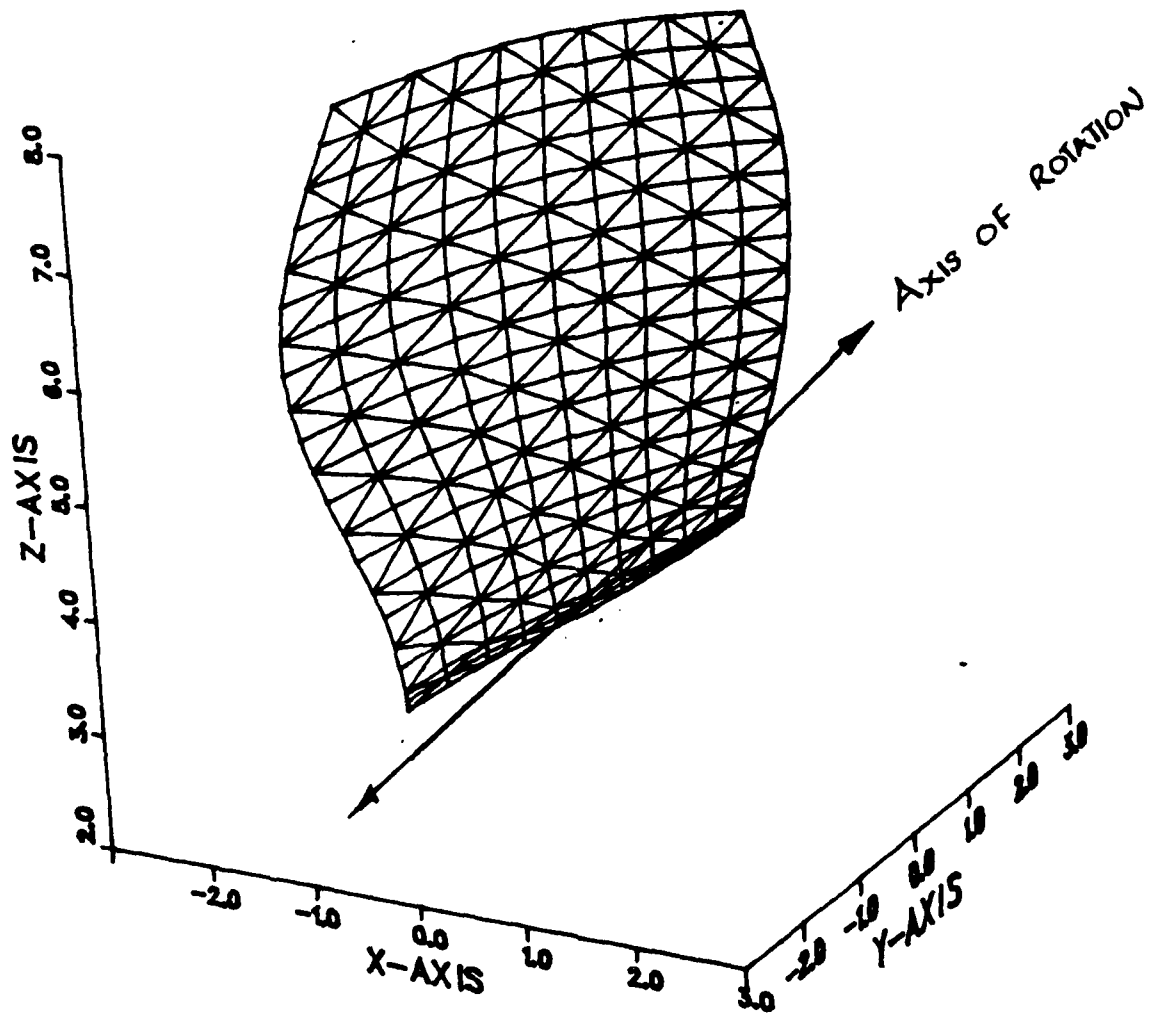
Figure 11.   NASTRAN Finite Element Model of Compressor Blade.
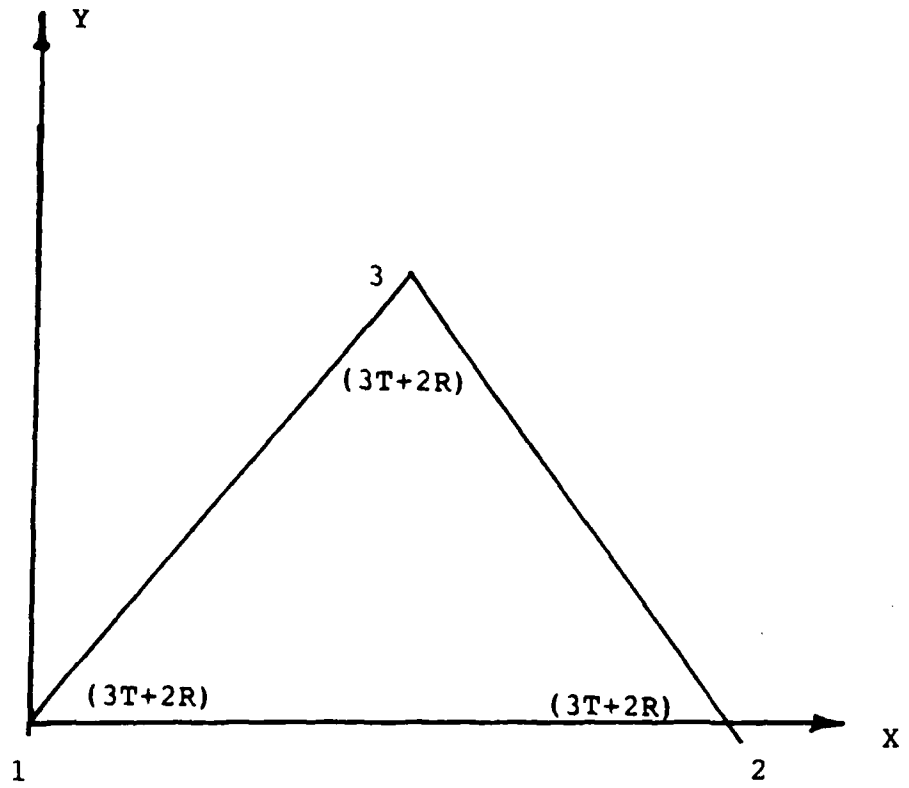
TRIA2 Element with 15 d.o.f. (T = Translation
R = Rotation)
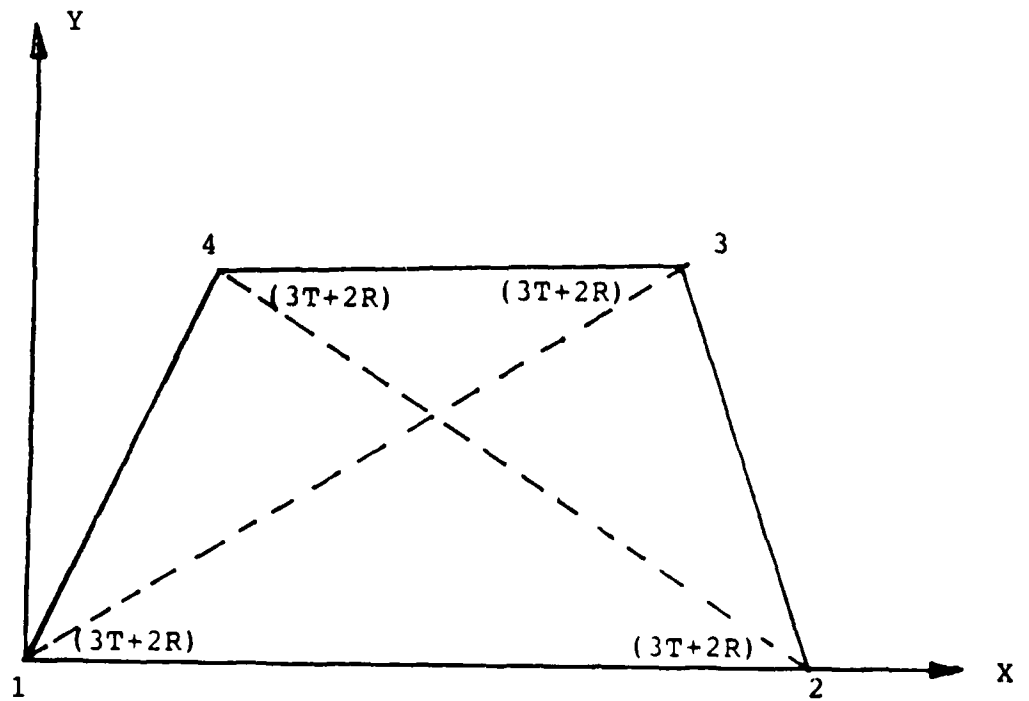
Figure 12. Triangular and Rectangular Plate Element Degrees
of Freedom.

41

TABLE 10

ROTATIONAL EFFECTS ON NATURAL FREQUENCIES OF
LARF BLADE WITH TRIA2 ELEMENT

		Frequency, Hz				
No.	(rpm)	f_1	f_2	f_3	f_4	f_5
1	0	550.3	1,363.9	1,696.1	2.492.5	2,667.7
2	6,000	573.0	1,379.4	1,709.2	2,497.8	2,671.9
3	12,000	635.9	1,420.6	1,749.3	2,511.9	----
4	18,000	726.9	1,478.3	1,818.5	2,530.4	----
5	20,500	770.8	1,504.7	1,856.3	2,537.8	2,703.3

in blade geometry. Comparison of results at higher modes or at other speeds could not be made as their results were not provided.

2.4.3 Singularities

Triangular plate elements, as mentioned before, have five degrees of freedom per node with the out-of-plane rotational constraint at the node point of the structural model confined to a single plane. This out-of-plane rotational constraint was easily incorporated in the input as single point constraints for all of the elements. But the compressor blade was severly twisted and curved, and the assumption of out-of-plane rotational restraint with respect to global coordinate systems was not justified. Either the releasing or the constraining in full of this degree of freedom causes under or over estimation of the frequency. Puterbaugh (15) in his analysis earlier had underestimated frequency and also had several singularity points. The grid points that had singularities were marked with an asterisk, as shown in Figure 13. When singularities appeared, results were not accurate. Therefore, our approach was to devise a scheme and apply a multipoint constraint method to suppress these singularity points.
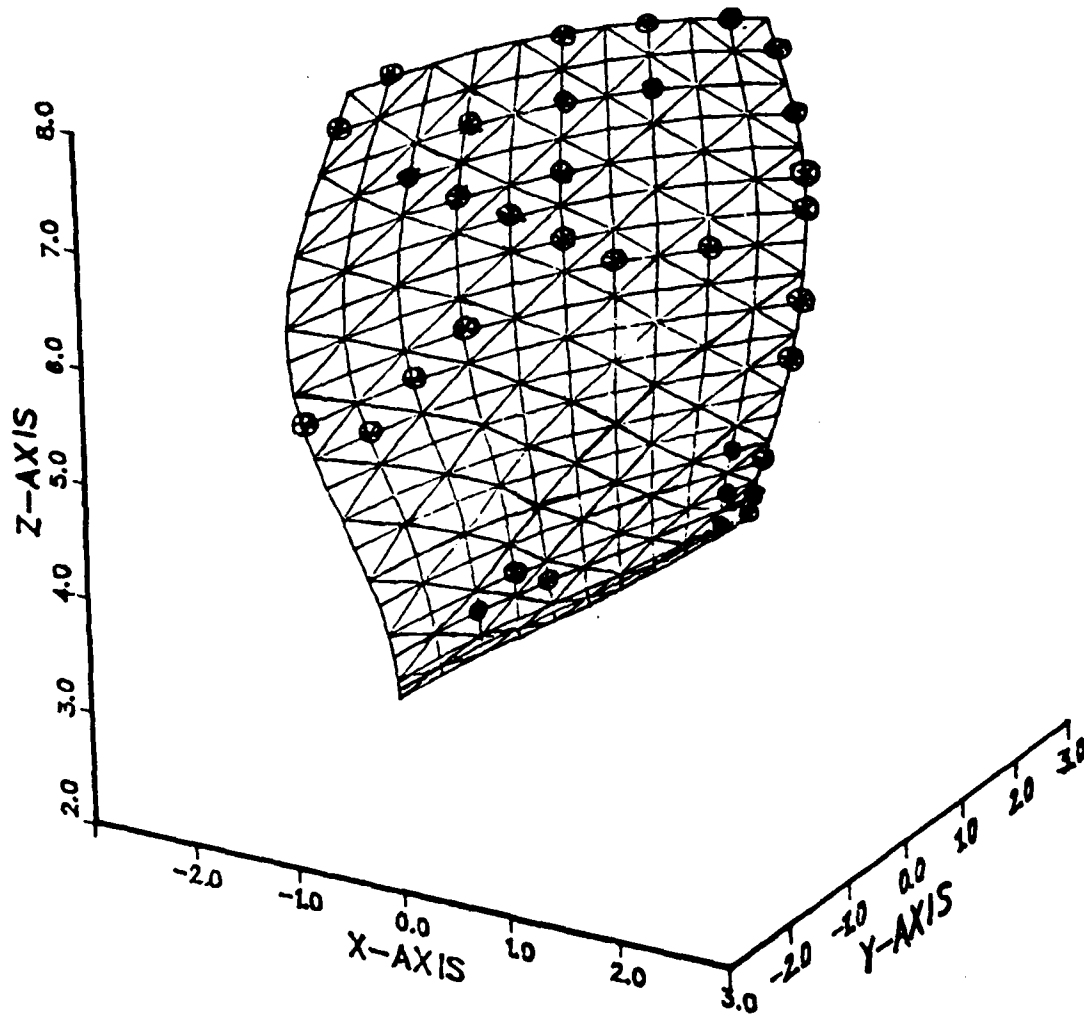
Figure 13. Grid Point Singularities of NASTRAN Compressor Blade
            Model.

The multipoint constraint method required the determination of normal vectors to each of the element grid points, and the direction cosine to the normal was given as a proportional and related constraint at the points where singularities appeared.

The procedure to determine normal vectors and direction cosines was as follows:

Let A, B, and C be the nodal points of the TRIA2 element. Their coordinates w.r.t global coordinate systems were $x_a, y_a, z_a : x_b, y_b, z_b$ and x_c, y_c, z_c. See Figure 14 for element and coordinate details.

Vectors A and B were given by

$$\bar{a} = (x_b - x_a)i + (y_b - y_a)j + (z_b - z_a)k \qquad (27)$$

and vector joining B and C was given by

$$\bar{b} = (x_c - x_b)i + (y_c - y_b)j + (z_c - z_b)k \qquad (28)$$

$$\bar{c} = \bar{a} \times \bar{b} \qquad (29)$$

or

$$
e = \begin{vmatrix}
i & j & k \\
x_b - x_a & y_b - y_z & z_b - z_a \\
x_c - x_b & y_c - y_b & z_c \ z_b
\end{vmatrix} \qquad (30)
$$

and the unit vector along $\bar{c}$ was given by

$$U_c = \frac{\bar{c}}{|c|} \qquad (31)$$

44

where $|\bar{c}|$ was the magnitude of vector $\bar{c}$. The direction cosines of the unit or normal vector were the coefficients α, β, γ of the unit vector u_c. α, β, γ were shown in Figure 15.

Multi-point constraints (MPC) require that the condition

$$\alpha_i U_i + \alpha_j U_j + \alpha_k U_k = 0 \tag{32}$$

be satisfied. In the equation the coefficients α_i, α_j, α_k were the direction cosines and u_i, u_j, u_k were the d.o.f. at each nodal point.

A computer program (VECTOR) was written to directly read the geometric coordinates of all the grid points from a NASTRAN file for TRIA2 elements and to estimate direction cosines of unit vectors for all grid points. Relevant direction cosine components for the singular points were input through MPC cards as described in the NASTRAN User's Manual. With the suppression of singularities, the analysis was rerun and the confidence in the results was restored. The method and its application to curved blade vibrations was presented in reference (17).

2.4.4 Quadrilateral (QUAD2) Elements

Superposition of four TRIA2 elements with bending and stretching properties would generate QUAD2 elements in NASTRAN. A QUAD2 element was illustrated in Figure 12b. It has 20 d.o.f. in all with the out-of-plane rotational restraint at nodal corners. The model compressor blade was divided into 120 QUAD2 elements and the input file was the same as the one used for SAP IV. The model was evaluated during disk rotation by releasing all d.o.f. for all grid points up to the midspan of the blade where curvature was appreciable. Rotational restraint normal to the surface was retained for the top half of the blade. The results obtained from this analysis were similar to those of SAP IV and were closer to the experimental values. Table 11 provides a comparison of results of COSMIC NASTRAN analysis, with TRIA2 and QUAD2 elements, at zero and at operating speeds of the compressor. Experimental and

45
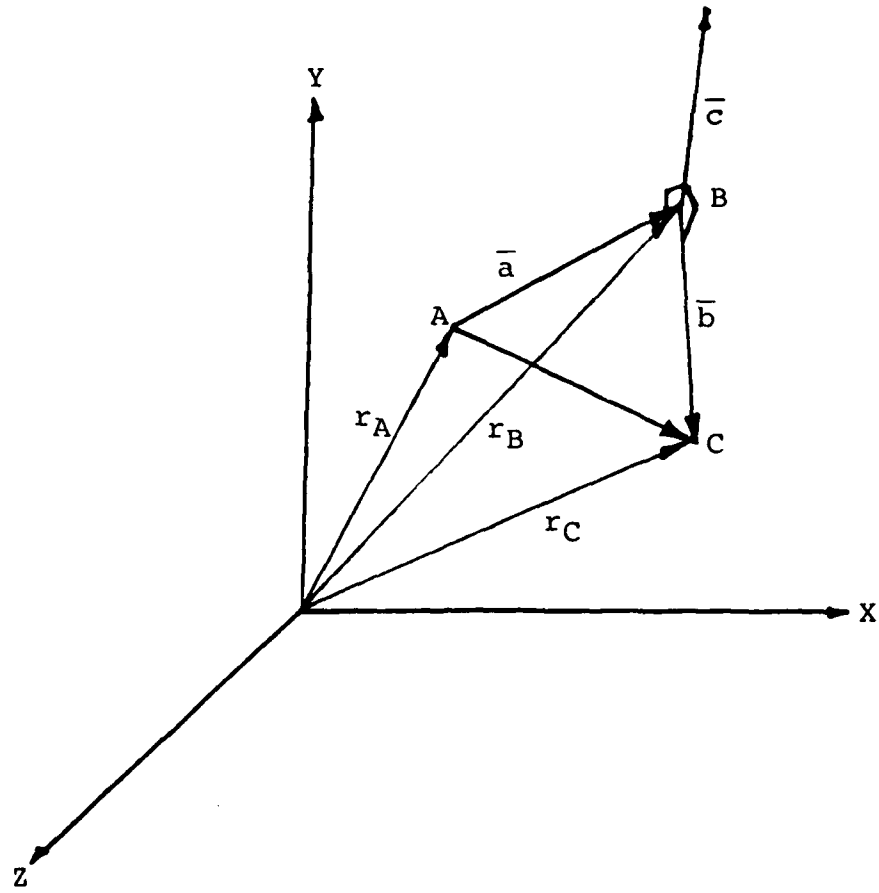
Figure 14.   Element Coordinate Axes.
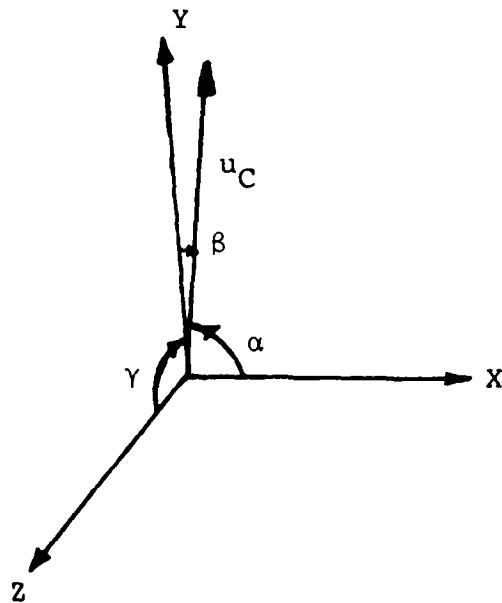
Figure 15.   Direction Cosines at Grid Points.

46

analytical results comparison from the available sources is also provided in this table.

TABLE 11

COMPARISON OF THE MODAL FREQUENCIES (HZ) OF A LARF BLADE AS
DETERMINED BY VARIOUS METHODS

Mode No.	Speed (rpm)	UDRI SAP IV Model 1	UDRI SAP IV Model 2	UDRI COSMIC NASTRAN TRIA2	UDRI COSMIC NASTRAN Model 1	UDRI COSMIC NASTRAN Model 2	ISRL Experiments	PWA MSC NASTRAN	GE ANSYS
1	0	523	598	550	500	571	589	534	580
2	0	1,308	1,315	1,364	1,178	1,415	-	-	-
3	0	1,500	1,594	1,696	1,611	1,657	1,718	1,700	-
4	0	2,433	2,482	2,492	2,321	2,617	2,049	1,980	-
5	0	2,688	2,701	2,668	2,771	2,920	2,718/ 2,763	2,875	-
1	20,500	-	-	770	-	788	-	756	776
2	20,500	-	-	1,508	-	1,511	-	1,744	-
3	20,500	-	-	1,856	-	1,860	-	1,889	-
4	20,500	-	-	2,538	-	2,639	-	2,649	-
5	20,500	-	-	2,703	-	3,035	-	-	-

NOTES: NASTRAN Model 2 has out-of-plane rotational restraint for grid points 1-77 and all d.o.f. for grid points 78-120.

Models 1 and 2 of SAP IV were compatible with Models 1 and 2 of COSMIC NASTRAN.

Model 1 has 6 d.o.f. for all grids except the fixed boundary.

2.5. INTEGRAL BLADED DISK MODELING AND ANALYSIS

The analysis, thus far, has considered the blades to be mounted on an infinitely rigid disk. This assumption does not accurately

represent the blade and disk interface compliance. Therefore, our analysis considered flexibility of the disk in analyzing the blade dynamics.

When the combined flexibility of the disk and blades was considered as a whole, the magnitude of such an analytical problem was large in terms of computer core memory and computational time. Modeling effort and analysis time can be drastically reduced if the cyclic symmetry of the structure was used in the analysis. Only one blade and its associated section of the disk need be considered for analysis. The photo in Figure 16 shows details of the axisymmetric integral bladed disk assembly. The disk has 20 blades in all, and the analysis was performed on an 18-degree segment of the disk. The rotational cyclic symmetry feature available with the COSMIC NASTRAN finite element program was used.

The scheme to analyze the problem consisted of two tasks: first, use of a preprocessor program (PATRAN) which automated the generation of the finite element model; and second, operation of the NASTRAN finite element program on the PATRAN model to define resonant characteristics of the bladed disk. Some details about the generation of the geometric and finite element model and the subsequent analysis of the disk sector are provided in the following paragraphs.

2.5.1 PATRAN-G Modeling of Bladed-Disk System

PATRAN was an interactive computer software program (18) for analytical solid modeling and finite element pre- and post-processing. The procedure for bladed-disk modeling using PATRAN was as follows: A set of grid points called the control points was selected that define the outlines of the structure to be modeled. These grid points were input to the PATRAN program in terms of their identifying numbers and their three spatial coordinates. The object contour was generated from these point coordinates. The material properties associated with these geometrical entities were also defined at this stage. This completed analytical solid modeling phase of the disk. The solid and thin lines in Figure 17 show the analytical geometry modeled

48

Figure 16.   Photo of Integral Bladed Disk Assembly.

76.2

38.1

23.9

38.10

19.05

5.0

3.13

5.1

25.4

12.7

12.7R

133.0   111.3   52.32

431.8   117.6   60.45

4.57

38.1   134.6   430.0

46.76   203.1

Size on Diameter

Size on Diameter

All Dimensions in mm

—— DESIGN OUTLINE

—— ANALYTICAL MODEL
      OUTLINE
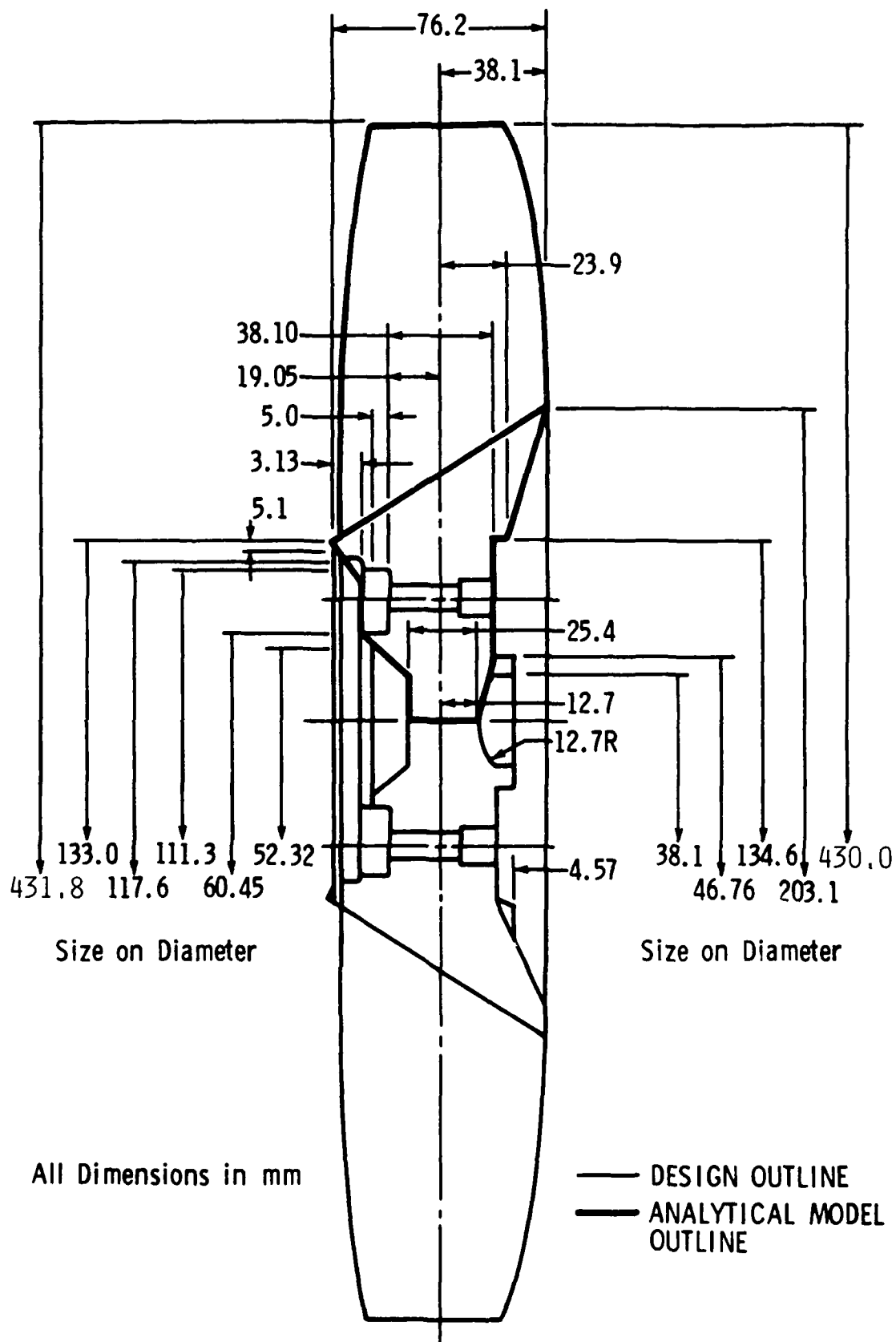
Figure 17.   Analytical Model of Bladed Disk Assembly.

and the finite element mesh pattern to follow. Starting with the control grid points and connecting lines and surfaces in the meridional plane of the blade and disk sections, PATRAN generated the three-dimensional solid body shown in Figure 18. Figure 19 shows a hidden line plot of the body as seen from the inlet side. Since only a curved surface representation was needed for finite element modeling of the blade, no solid volume was generated. Although only an 18-degree sector of the disk was used in the analysis, PATRAN can be used to develop the model for the complete 20 bladed-disk system with equal ease.

The next step in PATRAN modeling was the finite element discretization of the analytical solid body created earlier. This was done simply by specifying the nodal subdivision and connecting element types for the disk geometrical entity. The surface representing the blade was discretized using the four-node plate element QUAD. The three-dimensional regions representing the disk were discretized using eight-node HEX elements. Six-node wedge elements were also used where needed by the geometry. The varying blade thickness was specified using the data patch utility of PATRAN. A data patch was defined by specifying the thickness at 16 Gauss points of the surface representing the blade. Blade thickness at element centroids was interpolated from this data patch. Finally, the model was completed by equivalencing the nodes lying on common boundaries of adjacent connecting regions and then resequencing the node numbers so as to give an optimum bandwidth. These operations were also performed with PATRAN. Figure 20 shows the completed finite element model of the 18-degree sector of the bladed-disk system.

The above procedure created an output data file which was not specific to any particular finite element analysis program. The data translator program PATCOS was then used to convert the model-data file to the required COSMIC NASTRAN format. Further modifications, such as the specification of multipoint constraints to enforce compatibility between the QUAD and HEX elements, were performed separately. The rotational displacements of the blade at

51
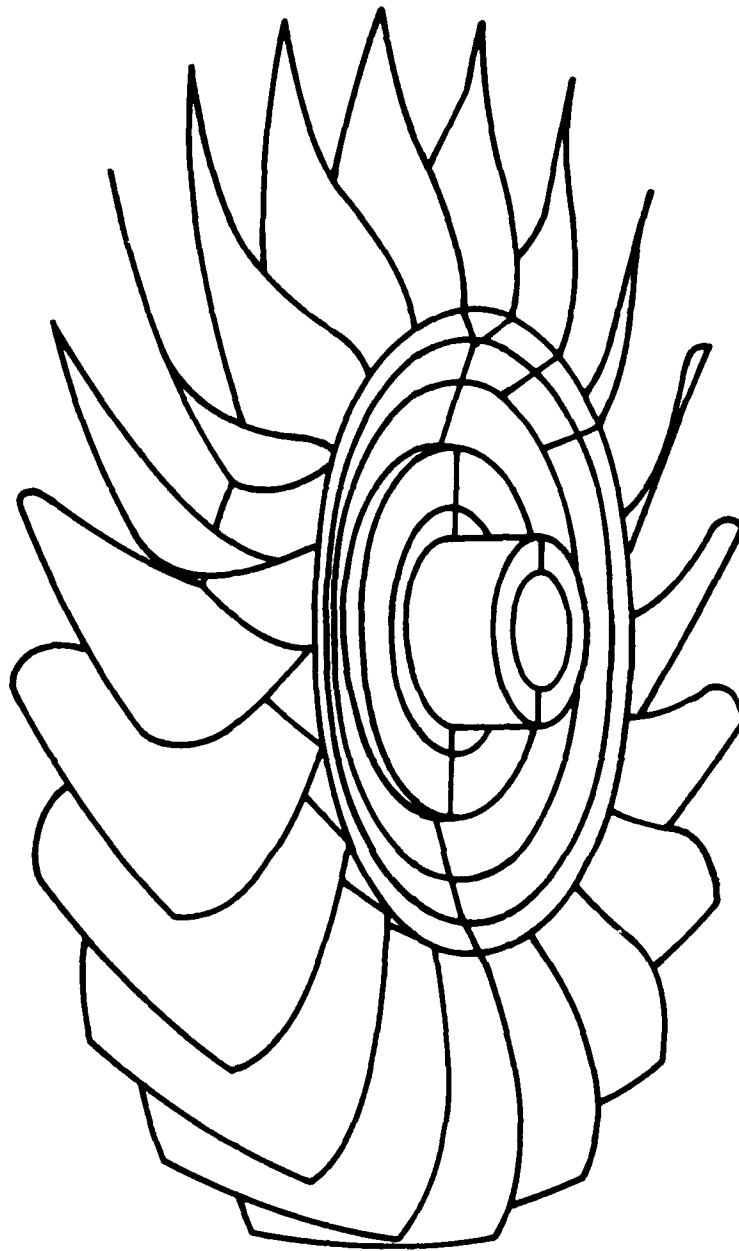
Figure 18. PATRAN Geometry Model of Bladed Disk.
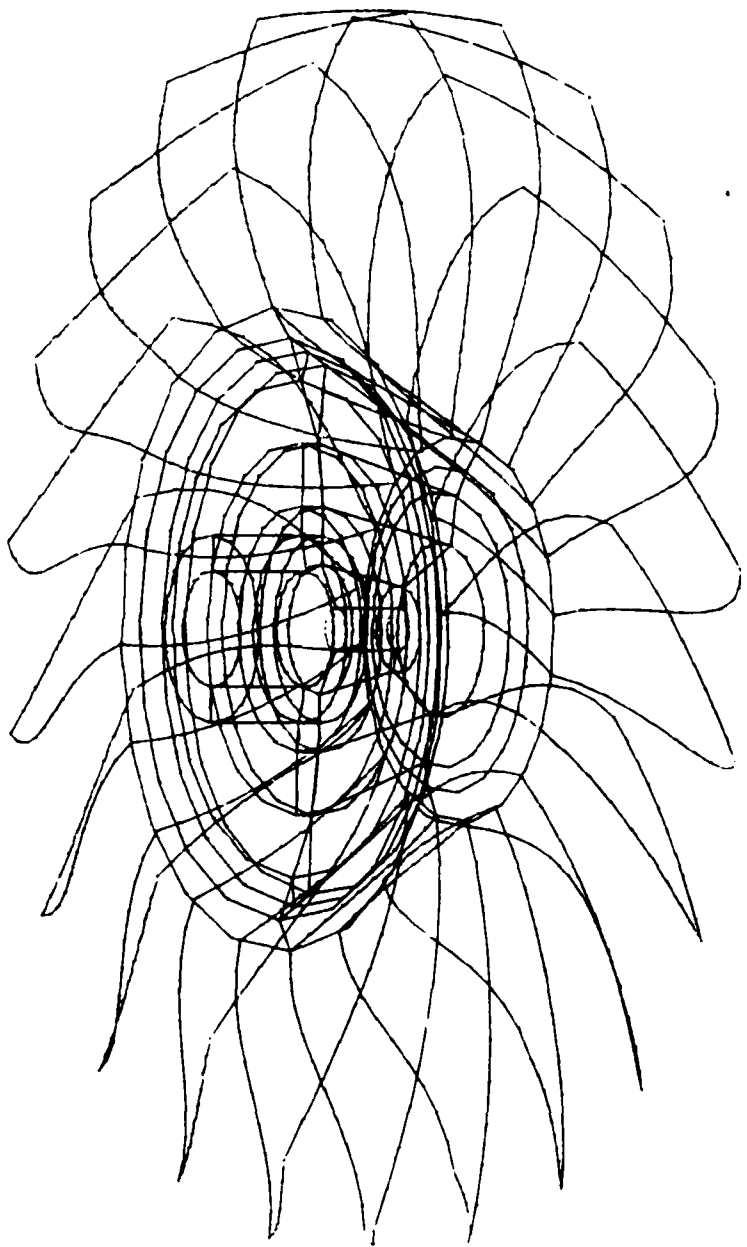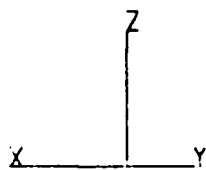
Figure 19. Hidden Line Plot of Bladed Disk.
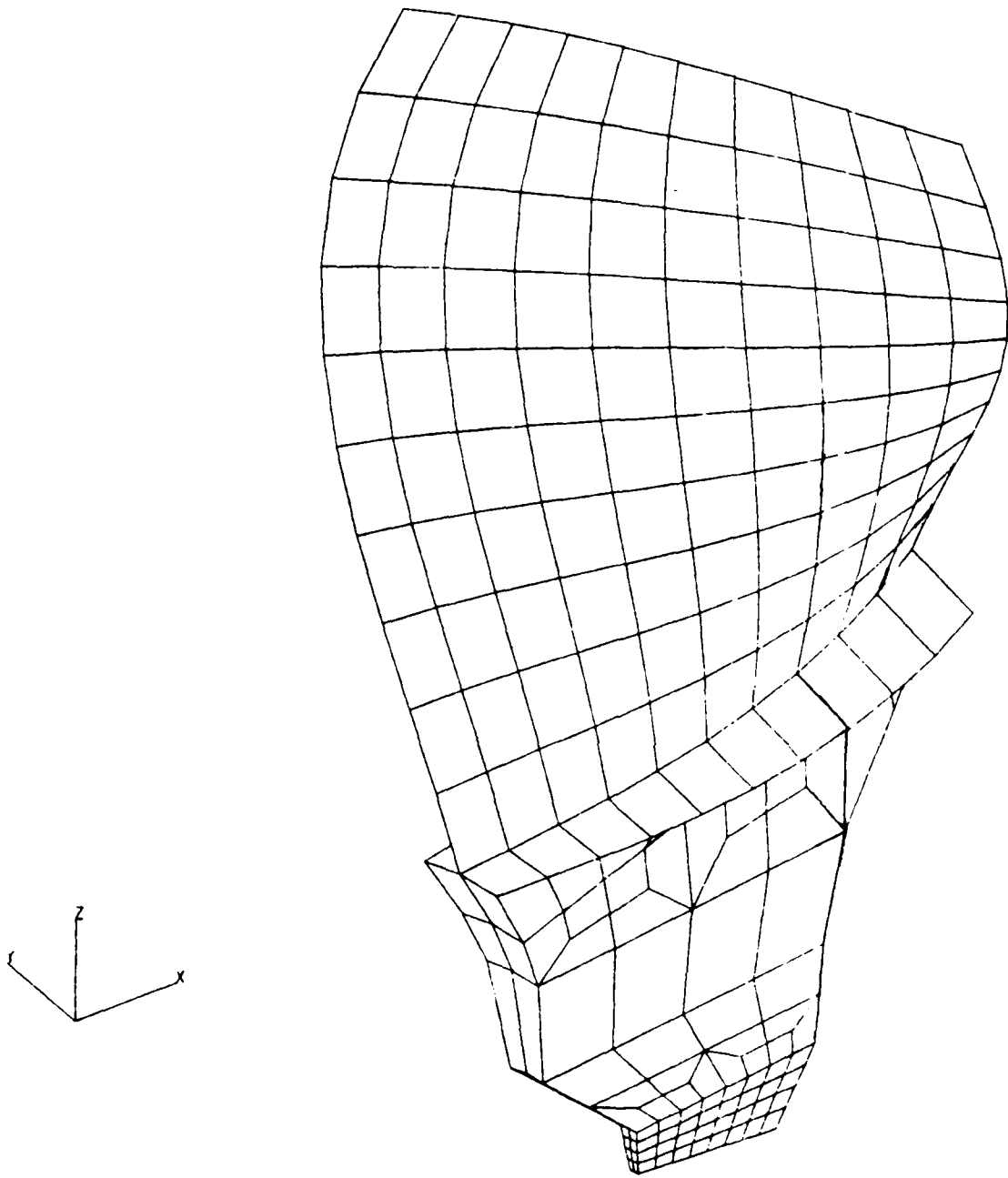
Figure 20. Finite Element Model of an 18° Sector of Bladed Disk Assembly.

the blade-disk interface were represented in terms of the translational displacements of the disk elements as:

$$\theta_x + (V_p - V_q) / \Delta Z - (W_p - W_q) / \Delta Y = 0 \qquad (33)$$

$$\theta_y + (W_p - W_q) / \Delta Z - (U_p - U_q) / \Delta Z = 0 \qquad (34)$$

$$\theta_z + (U_p - U_q) / \Delta Y - (V_p - V_q) / \Delta X = 0 \qquad (35)$$

where θ_x, θ_y, and θ_z were the rotational displacements of the nodes at the interface; U, V, and W were the translational displacements of the nodes p and q on the disk in the immediate vicinity of the interface; and ΔX, ΔY, and ΔZ were the distances between the nodes p and q in three coordinate directions. Figures 21a and 21b show the rotational and translational degrees of freedom relationship at the interfacial grid points on the blade and disk sections. The assumptions made and various steps involved in deriving the above equations and their application for bladed disk vibration analysis were presented in reference (19).

2.5.2   NASTRAN Finite Element Analysis of Axisymmetric Disks

Consider a circular disk of radius, a, and variable thickness, h(r), and subjected to transverse shearforce and bending moment around the radius, a. The governing differential equation of motion of a distributed model of the disk system was

$$\nabla^4 w(r,\xi) + \frac{\rho h(r)}{D(r)} \ddot{w}(r,\xi) = 0 \qquad (36)$$

where   w(r,f) was the transverse deflection,

ρ was the density of disk material,

D(r)   was the flexural rigidity,

and ξ was the angular coordinate.

Finite element method discretizes a structural system and the equation of motion of a discretized bladed disk sector was

$$[K] - \lambda^2 [M] \, \{X\} = 0 \qquad (37)$$

55
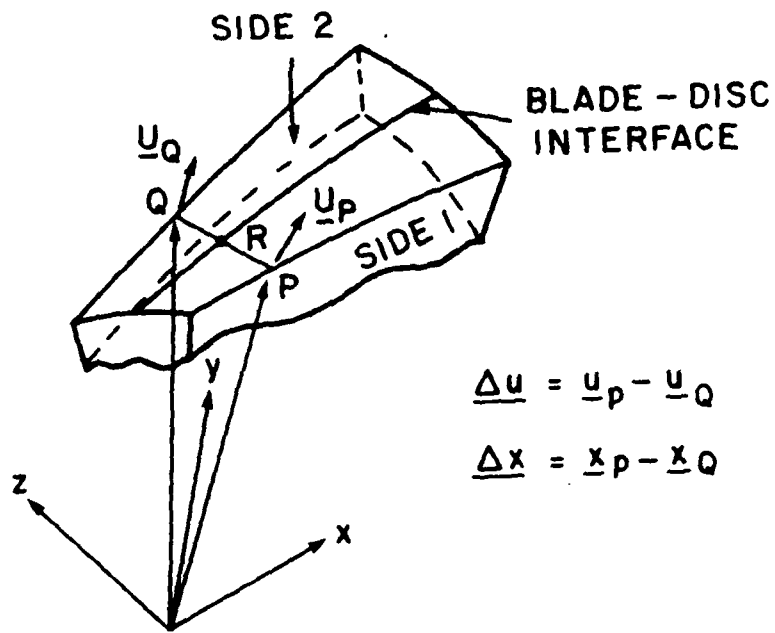
Figure 21a.   Relationship Between Translation and
Rotation Degrees of Freedom of a
Grid Point in 3D.
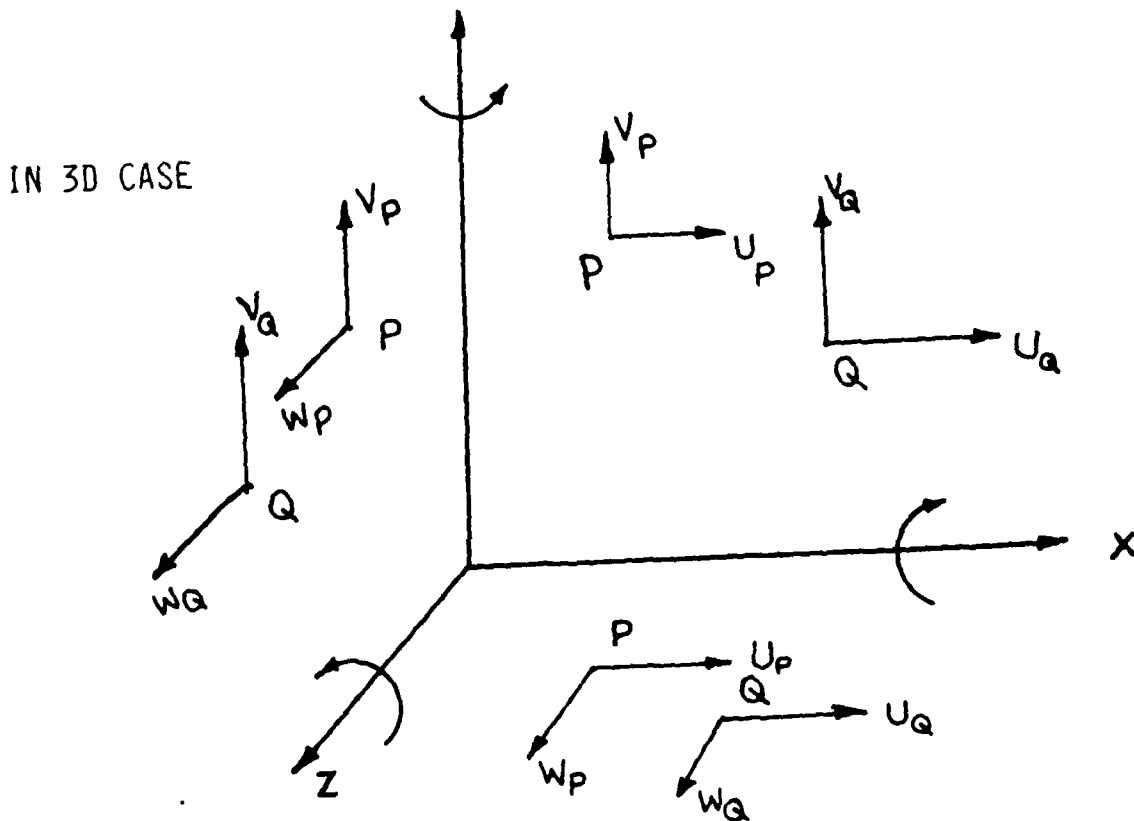
Figure 21b.   Degrees of Freedom Connections at the Blade and
Disk Interface.

where [K] was an assembled stiffened matrix of disk and blades,

[M] was mass matrix,

λ^2 was frequency parameter and equals to

$$\omega^2 = \frac{\rho h a^4}{D} , \tag{38}$$

and $\{\chi\}$ was a matrix of generalized coordinates. From the given geometry information of grid points and elements and the material properties, the computer program generated stiffness and mass matrices, imposes multi-point constraints as specified before and solved for eigenvalues (λ^2) of the system. Associated eigenvectors $\{\chi\}$ were evaluated and the deformed mode shapes were plotted using PATRAN post-processing capabilities.

The bladed part of the segment was modeled with QUAD2 elements with four nodal points, each with six degrees of freedom. The disk part of the segment was modeled with eight-node HEX solid elements with three d.o.f. per node. At the interface of the blade and disk, rotational degrees of freedom of QUAD elements were retained through multipoint constraints as specified in equations (33), (34), and (35).

The basics of the cyclic symmetry principle (20) for dynamic analysis of an 18-degree segment of a bladed disk were as follows: rotational transformation between a symmetrical structural segment was governed by the equation,

$$u^n = \bar{u}^0 + \sum_{K=1}^{KL} \bar{u}^{Kc} \cos(n-1)\ Ka$$

$$+ \bar{u}^{Ks} \sin(n-1)Ka + (-1)^{n-1} u^{-N/2} \tag{39}$$

where   n = 1, 2, ...N = Number of segments.

K = cyclic index

$K_L \leq \frac{N}{2}$ was the limit of K

u^n - a variable like displacement, stress, etc. in the nth segment.

$\bar{u}^0$, $\bar{u}^{Kc}$, $\bar{u}^{Ks}$ = symmetrical components (cyclic coefficients) used in the solution which defines the entire structure, and

$$a = \frac{2\pi}{N} = \text{circumferential angle for each segment.}$$

In the rotational symmetry analysis, the dependent displacements (side 2 of the model, the node points as specified through CYJOIN2 card in the Bulk Data) were related to the independent displacements (Side 1, as specified in CYJOIN1 Card) by the following equations of constraint for the boundaries.

$$\bar{u}^0_2 = \bar{u}_1 \tag{40}$$

$$\bar{u}^{Kc}_2 = \bar{u}^{Kc}_1 \cos Ka + \bar{U}^{Ks}_1 \sin Ka \tag{41}$$

$$\bar{u}^{Ks}_2 = \bar{u}^{Kc}_1 \sin Ka + \bar{u}^{Ks}_1 \cos Ka \tag{42}$$

$$\bar{U}^{N/2}_2 = \bar{u}^{N/2}_1 \tag{43}$$

where $K = 1, 2, \ldots K_L$.

The only symmetrical components coupled by the compatibility constraints were 1C and 1S, 2C and 2S, etc. From the compatibility constraint relations, we know that the selection of each K index predetermines the vibration modes which may occur in the entire disk model. In our case, K = 10 was identical to K = 0, since Ka = 2π and maximum K that could be used was 10.

Table 12 presents the results obtained from NASTRAN analysis using various constraint conditions. The list of frequencies shows that the fundamental frequency of the coupled system for K=0 was 712 Hz while the experimental value was 832 Hz. Several blade-alone frequencies were also evaluated by this analysis. Analytical mode shapes of the system corresponding to the

displacements in the axial direction (parallel to rotational axis) are illustrated in Figure 22. Similar contour plots corresponding to the displacements in the tangential direction were also generated. Holographic experiments have recorded the mode shapes of the bladed disk and experimental blade mode shapes are shown in Figure 23.

TABLE 12
NATURAL FREQUENCIES OF COMPRESSOR BLADED DISK
BY CYCLIC SYMMETRY ANALYSIS

Mode Type	Boundary Conditions in Analytical Model	Analytical Frequency (Hz)	Experimental Frequency (Hz)
Umbrella mode, OC	6 nodes on Flange-bottom and 3 nodes on disk-face fixed. 7.3% over estimate in frequency of OC	392 883 1279 1781	
Umbrella mode, OC	6 nodes on flange-bottom fixed. 6.3% under estimate in frequency of OC	391 771 1275 1778	588 823 – 1728
Blade-alone modes	Disk-blade Interface fixed	549 1364 1696 2493 2667	

Mode 1, 549 Hz
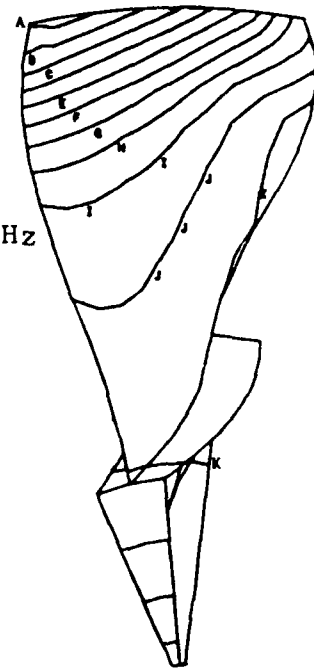
Mode 2, 1,364 Hz
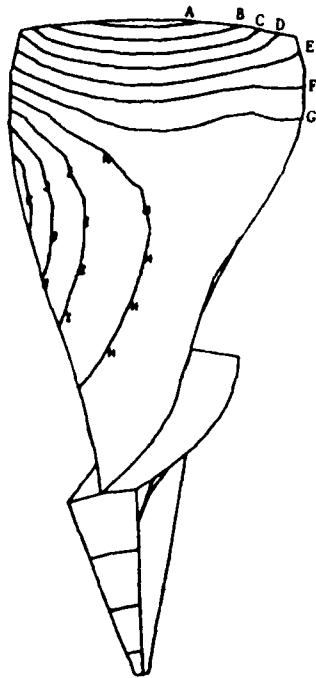
Mode 3, 1,696 Hz

Figure 22. Analytical Mode Shapes of Bladed Disk-
Cyclic Symmetry Analysis.
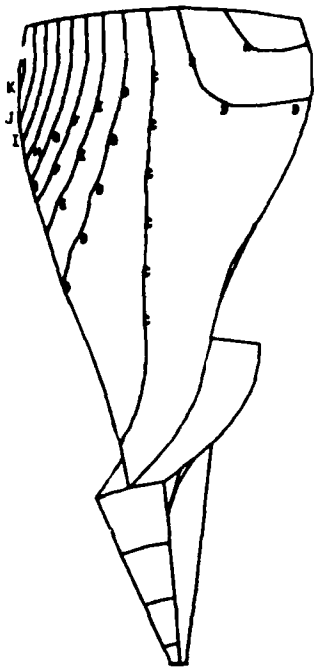
Mode 4
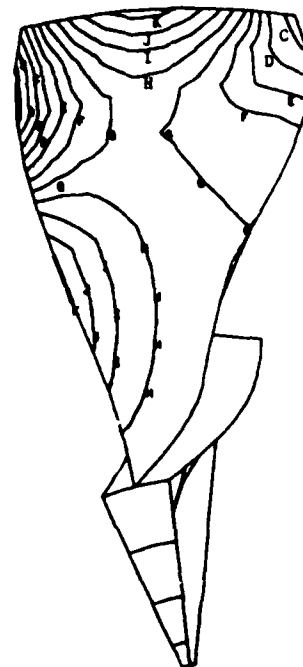
Mode 5
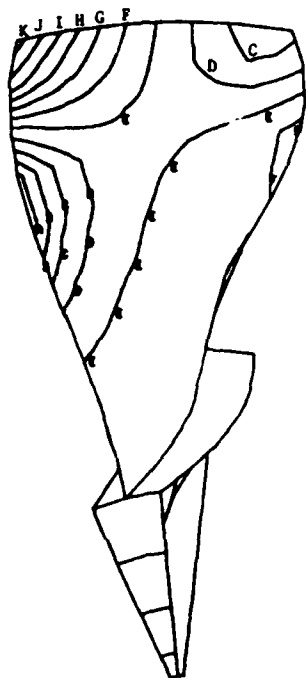
Mode 6

Figure 22(cont'd). Analytical Mode Shapes of Bladed Disk-
Cyclic Symmetry Analysis.

61
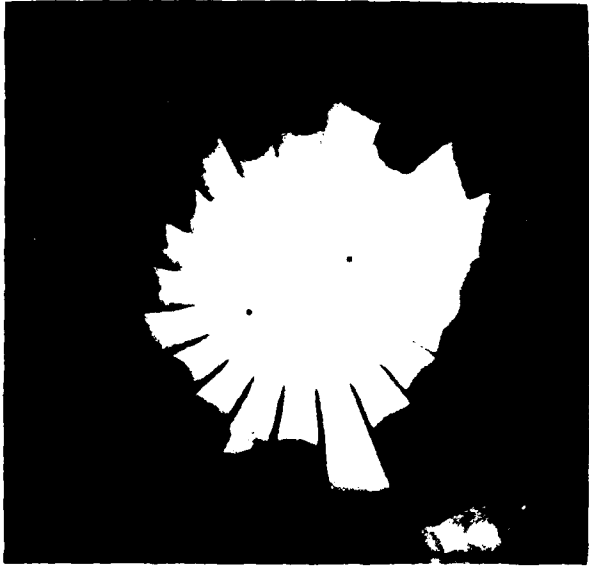
588 Hz
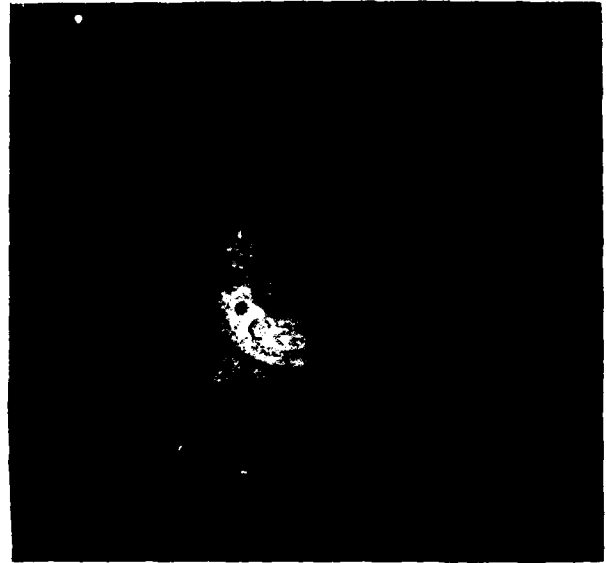
823 Hz
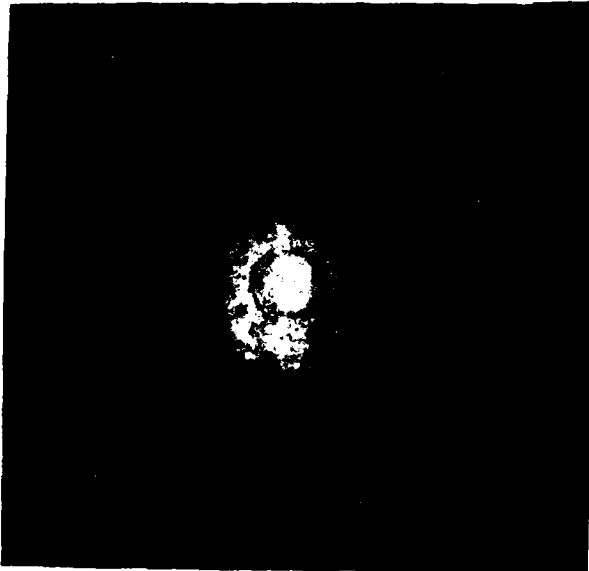
978 Hz
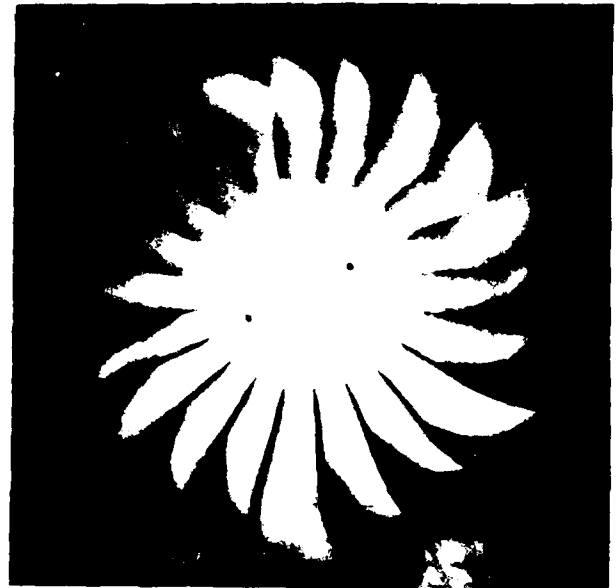
1,728 Hz

Figure 23.   Experimental Mode Shapes of Bladed Disk.
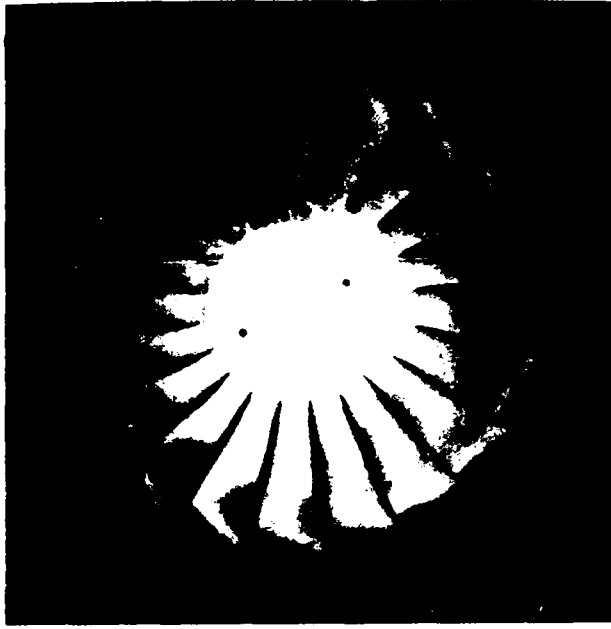
2,049 Hz
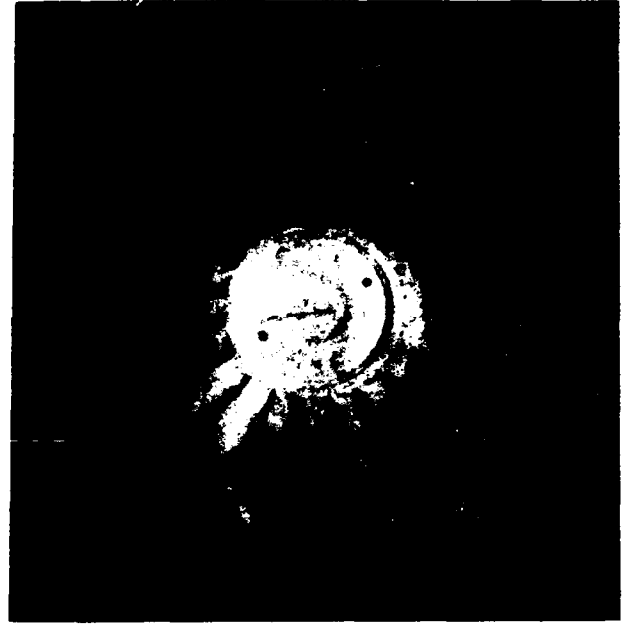
3,263 Hz
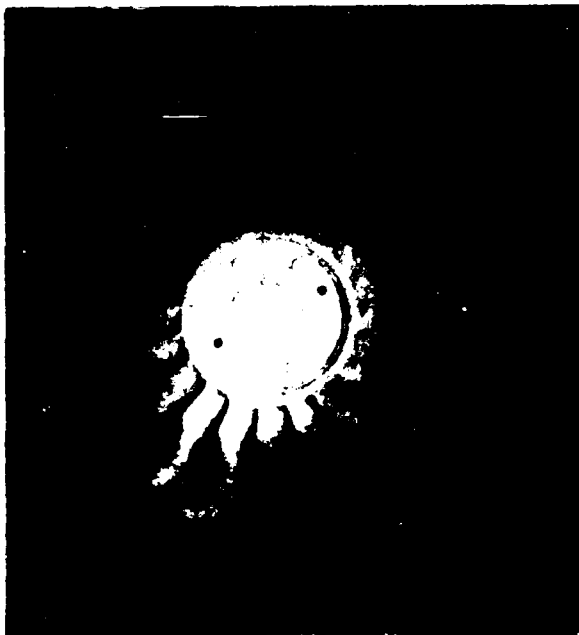
3,627 Hz
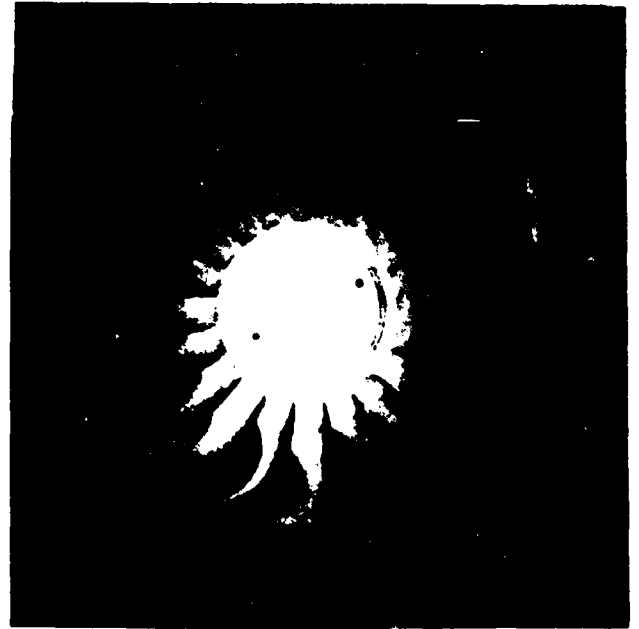
3,766 Hz

Figure 23(cont'd). Experimental Mode Shapes of Bladed Disk.

SECTION III
PROBABILISTIC ANALYSIS

This chapter outlines the general approach used to develop an analysis for estimating the variance of structural response variables, given the mean values and variances of system properties which are probabilistic in nature. The statistical analysis adopted was rudimentary, to be sure; however, the treatment is consistent with the level of information which is readily available to the engineer and lends itself to the analysis of relatively large and complex systems. The paragraphs below discuss the philosophy of the approach, the statistical parameters of interest, and the mathematical relationships needed for computing variances of response quantities such as displacement, stress, and natural frequency. The details of this development are contained in reference (5).

3.1 STRUCTURAL STATISTICAL ANALYSIS

The notion of a probabilistic analysis encompasses numerous possible analytical techniques. Given that certain properties or dimensions of a system are subject to uncertainty, the proper choice of analysis method depends strongly upon the difficulty and cost of a single simulation, and upon one's knowledge of the statistical parameters of interest. Some of the possible approaches are listed below.

Stochastic analysis involves stating the differential system of interest in terms of stochastic quantities, and solving directly for the response in statistical terms. This approach is an active research area in applied mathematics (21). Solutions of one-dimensional problems still represent a formidable challenge with this class of methods (22), and consideration of very complex systems was not feasible at this time.

Random field simulation is a relatively new approach developed by Liu and co-workers (23). In addition to discretizing the deterministic system of interest, new unknowns are introduced in a

finite element (or other numerical) model which describe higher statistical moments of the response. This augmented problem is solved in a single step for both the mean values (deterministic response) and the additional statistical variables. This method is capable of considering detailed autocorrelations for the statistical variables, but is best suited to moderately sized systems.

Monte Carlo simulation is appropriate if the statistical nature of the (few) independent variables is well-known, and the cost of a single simulation is small. Known information about the statistical parameters is used to generate a large number of samples with representative values, and a deterministic analysis is performed for each sample. The result is a sample of the response from which statistical information can be derived by standard methods (24).

In the present analysis, we viewed probabilistic properties of a system as discrete random variables. The elastic modulus of a turbine blade, for instance, might vary from point to point in a different fashion for every blade manufactured; we chose to characterize this modulus by a mean value and a single value of the variance. The information needed to perform a meaningful probabilistic analysis with this approach is usually available or can be estimated with a fair degree of accuracy. For example, if a modulus value is quoted as being "$E \pm \Delta E$," we normally interpret the quantity ΔE as representative three standard deviations; the range $E \pm \Delta E$ therefore includes approximately 99.7 percent of all samples.

The discrete random variable approach required a similar level of information about all statistical variables. Therefore, routine quality control data or manufacturer's tolerances are the only additional information needed beyond that used to construct a deterministic finite element model. Together with the relatively low cost associated with solving relatively large models, this simplicity makes the present method attractive for routine analysis work.

Note that the results of an analysis based on the discrete random variable approach are not related in a simple way to results from the alternative methods mentioned previously. However, the basic trends predicted by either method will agree; that is, if the dispersion in a particular variable is large, and if the structural response varies significantly with the variable in question, then we expect a large variance in the response. In some cases, it is possible to show that the variances predicted using the present method are conservative (overestimated). For example, the variance in natural frequencies predicted when a physical property is assumed to vary with position is generally less than that computed when the property is constant throughout the model, but subject to the same variation in magnitude.

3.2 STOCHASTIC ANALYSIS OF BLADED DISK SYSTEMS

The efforts on the probabilistic finite element analysis development were concentrated in three areas:

- □ steady-state forced response sensitivity;
- □ graphical output of probabilistic results; and
- □ example problem data pɪeparation.

Activity in each of these areas is summarized briefly below.

We completed a solution procedure for the probabilistic analysis. This path deals with steady-state forced vibration and the associated sensitivity analysis. The steady-state analysis still works with the dynamic equations of motion:

$$M\ddot{U} + KU = F(t) \tag{44}$$

However, the nodal forces (which result from both concentrated and distributed forces) are assumed to vary harmonically, that is:

$$F(t) = f \sin(\omega t) \tag{45}$$

If the damping forces are small, the response U(t) at large 't' is sinusoidal as well, and oscillates at the forcing frequency, ω. Therefore we assume

$$U(t) = u \sin(\omega t) \tag{46}$$

in which u represents the steady-state amplitude of the nodal displacements. The resulting system to be solved is

$$(K-\omega^2 M)u = f \tag{47}$$

Given the amplitudes of nodal forces and distributed loads which define f, and the forcing frequency, ω, the basic steady-state vibration solution determines the corresponding nodal displacement amplitudes, u, and the stress amplitudes

$$\sigma = DBu \tag{48}$$

We were interested in a range of frequencies, either in the neighborhood of a resonance or a specified number of excitations per revolution. The steady-state harmonic solution accepts a list of forcing frequencies, and generates a separate solution for each one in a single computer run.

Notice that for some systems the response near resonance is of primary interest, and damping forces must be included in the vibration analysis. This is common in noise control problems, in which broad-band excitation is the rule. For bladed disk systems the effect of structural damping is less pronounced, since the system cannot tolerate prolonged excitation close to a resonant frequency.

The steady-state forced response sensitivity solution does an additional analysis at each forcing frequency, for each statistical parameter in the system (modulus, density, thickness, or geometric

variable). For the parameters now being considered, it is reasonable to expect that the forcing frequency is independent of the statistical parameters; therefore, the sensitivities of the displacement amplitudes with respect to any parameter 'p' can be obtained from

$$(K-\omega^2 M)\frac{\partial u}{\partial p} = \frac{\partial f}{\partial p} - (\frac{\partial K}{\partial p} - \omega^2 \frac{\partial M}{\partial p}) u \qquad (49)$$

The corresponding stress amplitude sensitivities are simply

$$\frac{\partial \sigma}{\partial p} = \frac{\partial D}{\partial p}Bu + D\frac{\partial B}{\partial p}u + DB\frac{\partial u}{\partial p} \qquad (50)$$

in which both u and $\partial u/\partial p$ are dependent upon forcing frequency.

The steady-state forced vibration sensitivity branch has been coded, run successfully, and validated using examples for which analytical results could be obtained. As with the static and natural frequency sensitivity calculations, this branch obtains a solution quite economically because of the ability to reuse the already-factored coefficient matrix in the sensitivity solution.

The actual probabilistic calculations were performed as post-processing operations because of the wide variety of operations which are possible. Recall that, for a response quantity which depends upon a number of parameters,

$$\tau = \tau(p_1, p_2, \ldots, p_N) \qquad (51)$$

the variance of τ is related to the variances of the statistical parameters by

$$Var(\tau) = \sum_{k=1}^{N} [\frac{\partial \tau}{\partial p_k}]^2 Var(p_k) \qquad (52)$$

68

One interpretation of the probabilistic results which was both simple and informative was in terms of "percentile" values. The mean value, as computed from the basic finite element solution, was by definition a 50th percentile value; that is, we might expect the actual value (stress, for example) to be greater about half the time, and less about half the time. A Qth percentile value τ_Q was such that the true value of the variable was less than or equal to τ_Q in Q percent of all cases. Let τ_μ represent the mean value of our variable τ, and τ_σ the standard deviation (the square root of the variance). If τ has a normal (or Gaussian) probability distribution, the interval of values $(\tau_\mu - \tau_\sigma, \tau_\mu + \tau_\sigma)$ represents about 68 percent of all possible values of τ. The interval $(\tau_\mu, \tau_\mu + \tau_\sigma)$ therefore includes approximately 34 percent of all possible values of τ; this means that the value of τ will be less than $\tau_\mu + \tau_\sigma$ 84 percent of the time. That is, the value $\tau_\mu + \tau_\sigma$ was the $\underline{84}^{th}$ $\underline{\text{percentile value}}$ of τ. The percentile value also can be viewed as a figure of reliability or confidence level. The changes between percentile values provide a direct indication of the relative uncertainty in a particular response quantity.

3.3 SENSITIVITY ANALYSIS OF BLADED DISK SYSTEMS

The calculations necessary for computing both a fundamental solution and sensitivity data for the natural frequency problem were implemented and verified for a number of examples. In the following, we summarize the primary computational procedures and present a couple of typical examples.

3.3.1 Element Stiffness Derivatives

Consider a problem in which the stiffness and mass properties of a structure depend on a collection of independent

statistical parameters. For the purpose of computing response derivatives, we denote a typical one of these parameters by p, and adopt the following notation for parametric derivatives:

$$(\cdot)' = \partial(\cdot)/\partial p \qquad (53)$$

While it was possible to compute K' directly for an element and then obtain the product $K'U$, this approach was unnecessarily time consuming. We prefer to form the product $K'U$ directly in vector form, on an element-by-element basis.

Let the stiffness matrix for an element be given by

$$K = \int_{\Omega_e} A^T B^T DBA \ |J| \ d\Omega_e \qquad (54)$$

in which A was a transformation from local to global coordinates, $u=AU$, B was a strain-displacement matrix, and D was the elasticity matrix. The region Ω_e was the domain of the element in parametric coordinates. The transformation matrix A may vary from point to point for curvilinear elements, but was constant over an element in many simpler elements.

3.3.1.1 Intrinsic Parameters

The product $K'U$ was simplest when parameter p corresponds to an intrinsic property, such as the modulus or thickness, since only the elasticity matrix was affected. Noting that $AU=u$, the local displacement vector, we can compute

$$\bar{\sigma} = D'Bu \qquad (55)$$

and

$$K'U = \int_{\Omega_e} A^T B^T \bar{\sigma} \ d\Omega_e \qquad (56)$$

70

The product in equation (55) was analogous to the usual process of stress recovery, so that the calculation of **K'U** for an element resembles an evaluation of the internal nodal forces.

3.3.1.2 Geometric Parameters

When the parameter of interest affects the nodal positions, nonzero derivatives may occur for the element of area $|J|$, the strain-displacement matrix **B**, and possibly for the coordinate transformation matrix **A**. We assumed that the derivatives of the nodal coordinates were known, and represented these by $X'_{iK}=\partial X_{iK}/\partial p$, in which i ranges from one to three, and K from one to the number of nodes in the element. The calculation of **B'** and $|J|'$ depends primarily upon the computation of sensitivities for the shape function derivatives, $\partial(N_{K,i})/\partial p$. We can show that

$$\frac{\partial(N_{K,i})}{\partial p} \approx \frac{\partial(N_{K,i})}{\partial x_{mJ}} \frac{\partial x_{mJ}}{\partial p} \qquad (57)$$

Notice that x_{mJ} denote the coordinates in the local (element) system. Summation was implied over the appropriate range of all repeated indices. Since the derivatives of the coordinate transformation will be considered explicitly later, we can hold **A** constant to give

$$x'_{mJ} = A_{mn}X'_{nJ} \qquad (58)$$

It was straightforward to show that the product in equation (57) simplifies to

$$N'_{K,i} = -N_{K,m}N_{J,i}x'_{mJ} \qquad (59)$$

The derivative **B'** may be formed directly from $N'_{K,i}$, in the same way the original **B** matrix was obtained from the shape function derivatives $N_{K,i}$.

71

Similarly, since:

$$\frac{\partial |J|}{\partial x_{iK}} = |J| \, N_{K,i} \tag{60}$$

we obtain for the parameter derivative of the Jacobian

$$|J|' = |J| \, N_{K,i} x'_{iK} \tag{61}$$

The derivative of the transformation **A** can be obtained as a by-product of computing **A** itself, with a minimal amount of additional computation.

For geometric control parameters, then, the product **K'U** is, in general

$$\mathbf{K'U} = \int_{\Omega_e} \{ [(\mathbf{A'})^T \mathbf{B}^T + \mathbf{A}^T (\mathbf{B'})^T] \sigma |J| \tag{62}$$

$$+ \mathbf{A}^T \mathbf{B}^T [(\bar{\bar{\sigma}} + \bar{\sigma}) |J| + \sigma |J|'] \} \, d\Omega_e$$

in which

$$\sigma = \mathbf{DBu} \tag{63a}$$

$$\bar{\sigma} = \mathbf{DB\bar{u}} \tag{63b}$$

$$\bar{\bar{\sigma}} = \mathbf{DB'u} \tag{63c}$$

$$\mathbf{u} = \mathbf{AU} \tag{63d}$$

$$\bar{\mathbf{u}} = \mathbf{A'U} \tag{63e}$$

We have verified the computational algorithms used to implement (62) and (63) with a number of examples for which the results can be evaluated in closed form and for additional cases using finite difference approximations for the derivatives. Isoparametric finite element geometric sensitivity analysis is described in reference (25).

3.3.2 Mass Matrix and Natural Frequency Derivatives

Suppose that a solution has been performed for several of the dominant modes of a system

$$KU - \omega^2 MU = 0 \qquad (64)$$

Differentiating (64) with respect to the parameter of interest leads to the frequency sensitivity expression

$$\omega_i' = \frac{U_i^T(K' - \omega_i^2 M')U_i}{2\omega_i U_i^T MU_i} \qquad \text{(i not summed)} \qquad (65)$$

for the ith mode of vibration. Equation (65) remains valid when repeated roots were present, and for any method of normalizing the eigenvectors U_i. The denominator was a scalar multiple of the generalized mass for mode i, which we choose to evaluate at the system level. The product $U_i^T K' U_i$ may be computed element by element, using the procedure outlined previously. We discuss the evaluation of the vector $M'U_i$ below.

Letting v, V denote a particular component of the element displacement vector in local and global axes, respectively, we may write the contribution to the mass matrix for component V as

$$M_{VV} = \int_{\Omega_e} \beta A^T N N^T A \; |J| \; d\Omega_e \qquad (66)$$

in which β was a function of the element density and thickness. The best procedure for the sensitivity calculation in this case was element dependent. However, the fact that $N^T AV = v(x)$, the pointwise value of v, can always be exploited. Similarly, the

product $\mathbf{N}^T\mathbf{A'U}$ resembles a point displacement value, but without the same physical interpretation. Again, the basic sensitivity calculations were limited to $\mathbf{A'}$ and $|\mathbf{J}|$.

3.3.3 Solution Procedure

This section outlines computational procedures used in evaluating response sensitivities, which were needed for later use in the probabilistic calculations. We assume that element-level routines were available for evaluating the vectors $\mathbf{K'U}$ and $\mathbf{M'U}$, and the scalar products $\mathbf{U}^T\mathbf{K'U}$ and $\mathbf{U}^T\mathbf{M'U}$ as required. To implement these methods, we perform element calculations for a number of load cases or modes and a number of sensitivity parameters, all in parallel. Sensitivity parameters may include the material modulus or density, element thickness, and any geometric control parameter defined in terms of derivatives of the global Cartesian coordinates at selected nodes with respect to the parameter. We first review briefly a solution procedure for static problems to help fix ideas.

3.3.3.1 Static Response Sensitivity

In static analysis, we first factor the original stiffness and solve for the nodal displacements:

$$\mathbf{K} = \mathbf{LDL}^T \tag{67a}$$

$$\mathbf{LDL}^T\mathbf{U} = \mathbf{F} \tag{67b}$$

For the first pass of sensitivity calculation, form the right-hand side and solve for displacement sensitivities:

$$\mathbf{R} = \mathbf{F'} - \sum_{e=1}^{N_{el}} (\mathbf{K'U})_e \tag{68a}$$

$$\mathbf{LDL}^T\mathbf{U'} = \mathbf{R} \tag{68b}$$

74

The second pass of element sensitivity calculations yields the element stress sensitivities:

$$\sigma' = (DBA)'U + DBAU' \tag{69}$$

Which of the matrices D, B, A possesses nonzero derivatives was a function of parameter type.

Notice that if a particular sensitivity parameter does not affect a given element directly, the calculation of $K'U$ may be skipped, and the stress sensitivity reduces to $\sigma' = DBAU'$. In practice it was convenient to maintain a list of switches for each element, indicating the status (active or inactive) of all parameters. The selection of parameters such as modulus, density, and thickness may be tied to material or property set numbers, making it easy to determine whether a specific element was affected. If geometric parameters were defined in terms of nodal coordinate derivatives, the parameter was inactive for a given element only if all derivatives for each node connected to the element were zero.

3.3.3.2 Frequency and Mode Shape Sensitivity

For eigenvalue problems, we first solve the eigensystem and compute a generalized mass for each mode:

$$KU_i - \omega_i^2 MU_i = 0 \tag{70a}$$

(i not summed)

$$m_i = U_i^T MU_i \tag{70b}$$

For each parameter and mode, the frequency sensitivity equation (65) may be summed element by element:

$$\omega_i' = \frac{1}{2\omega_i m_i} \sum_{e=1}^{N_{el}} [U_i^T K'U - \omega_i^2 U_i^T M'U_i] \qquad \text{(i not summed)} \tag{71}$$

75

In computing sensitivities of the eigenvectors, we adopt a modal representation. For the ith mode, let the eigenvector derivative be

$$U_i' = \Psi \beta_i \qquad (72)$$

in which

$$\Psi = [\ U_1,\ U_2,\ \ldots,\ U_n\ ] \qquad (73)$$

is the modal matrix, and β_i was a vector of modal participation factors. Introducing (72) into the derivative of the original eigenvalue equation, and premultiplying by Ψ^T gives, for the ith mode

$$(k-\omega_i^2 m)\beta_i = -\Psi^T(K'-\omega_i^2 M')U_i + 2\omega_i\omega_i'\Psi^T M U_i \quad \text{(i not summed)} \quad (74)$$

Here $k = \Psi^T K \Psi$ and $m = \Psi^T M \Psi$ were the diagonal generalized stiffness and mass matrices. Note that only the ith component of the product $\Psi^T M U_i$, which was a column of m, was nonzero. The element of β_i corresponding to mode 'n' was therefore

$$(\beta_i)_n = \frac{-U_n^T(K'-\omega_i^2 M')U_i}{(k_{nn}-\omega_i^2 m_{nn})} \quad (i \neq n;\ \omega_i \neq \omega_n;\ i,n \text{ not summed}) \quad (75)$$

Let J be the degree of freedom which attains the largest value for mode i; that is

$$(U_i)_J = \sup_n (U_i)_n \qquad (76)$$

We force the normalizing basis for mode i to remain constant by requiring $(U_i')_J = 0$. This condition was sufficient to determine the remaining element of β_i:

$$(\beta_i)_i = -\frac{1}{(U_i)_J} \sum_{\substack{n=1 \\ n \neq i}}^{N} (\beta_i)_n (U_n)_J \tag{77}$$

in which N was the number of modes retained for the sensitivity solution. The necessary products besides the system generalized stiffness and mass consist of $U_n^T K' U_i$ and $U_n^T M' U_i$, which may be evaluated on an element basis.

3.3.4 Numerical Examples

Some typical validation problems used in verifying both the static and natural frequency sensitivity solutions were summarized briefly below. The validation problems solved to date include simple problems with analytical solutions, as well as complex cases in which computed sensitivities were compared with approximate parameter derivatives obtained with finite differences (26).

Example 1. Bending of a Cantilever Beam

Figure 24 shows a cantilever beam subjected to a transverse force at the tip. Again, an analytical solution was possible both for the displacement and rotation, and for the sensitivities with respect to modulus, E, thickness, t, and width, b. Five bilinear Mindlin plate elements (27,28) were used to model the beam; this number was sufficient for good accuracy but, since the elements have only linear displacement and rotation fields, does not reproduce the exact solution. Table 13 summarizes the computed results for the displacements and rotations. Note that the displacement sensitivities were no less accurate than the displacements themselves (all were approximately 1 percent in error), and that the rotational results were exact. Table 14 shows moment and shear results, and the force sensitivities which were nonzero. In all cases, the moment and shear sensitivities were exact, despite small errors in the displacement solution.
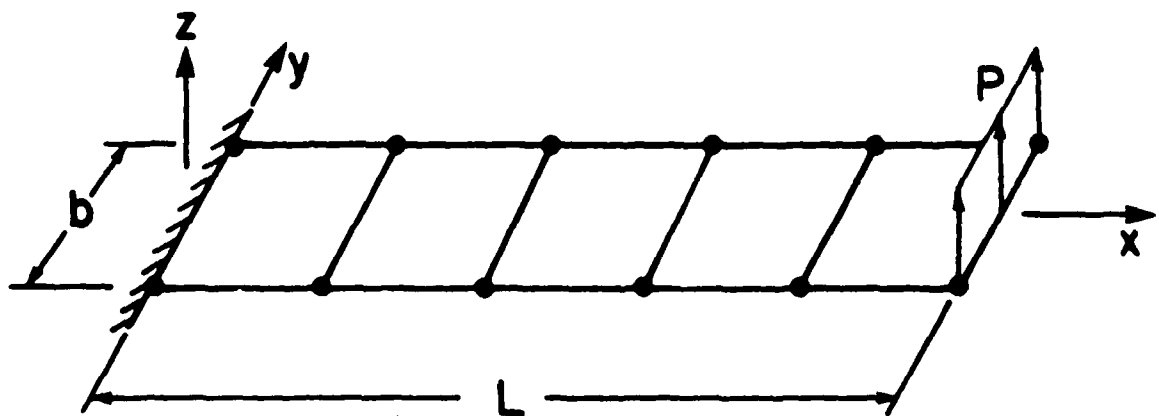
Figure 24.   Cantilever Beam with a Tip Load.

TABLE 13

DISPLACEMENT SENSITIVITY DATA FOR CANTILEVER BEAM[†]

Quantity	Exact	Exact (x=L)	Computed
w	$2P(3Lx^2-x^3)/Ebt^3$	-0.4	-0.39602
$\partial w/\partial E$	$-2P(3Lx^2-x^3)/E^2bt^3$	-4.0×10^{-8}	-3.96×10^{-8}
$\partial w/\partial t$	$-6P(3Lx^2-x^3)/Ebt^4$	-12.0	-11.88
$\partial w/\partial b$	$-2P(3Lx^2-x^3)/Eb^2t^3$	-0.4	-0.39602
θ	$6P(2Lx-x^2)/Ebt^3$	0.06	0.06
$\partial\theta/\partial E$	$-6P(2Lx-x^2)/E^2bt^3$	-6.0×10^{-9}	-6.0×10^{-9}
$\partial\theta/\partial t$	$-18P(2Lx-x^2)/Ebt^4$	-1.8	-1.8
$\partial\theta/\partial b$	$-6P(2Lx-x^2)/Eb^2t^3$	-0.06	-0.06

[†] $E=1\times10^7$; $\nu=0$; $t=0.1$; $b=1$; $L=10$; $P=1$

TABLE 14

FORCE SENSITIVITY DATA FOR CANTILEVER BEAM[†]

Quantity		Element Centers				
		x=1	x=3	x=5	x=7	x=9
M	Exact	-9.0	-7.0	-5.0	-3.0	-1.0
	Comp.	-9.0	-7.0	-5.0	-3.0	-1.0
$\partial M/\partial b$	Exact	9.0	7.0	5.0	3.0	1.0
	Comp.	9.0	7.0	5.0	3.0	1.0
Q	Exact	1.0	1.0	1.0	1.0	1.0
	Comp.	1.0	1.0	1.0	1.0	1.0
$\partial Q/\partial b$	Exact	-1.0	-1.0	-1.0	-1.0	-1.0
	Comp.	-1.0	-1.0	-1.0	-1.0	-1.0

[†] $E=1\times10^7$; $\nu=0$; $t=0.1$; $b=1$; $L=10$; $P=1$

Only nonzero values shown; $\dfrac{\partial M}{\partial E} = \dfrac{\partial M}{\partial t} = \dfrac{\partial Q}{\partial E} = \dfrac{\partial Q}{\partial t} = 0$ identically.

Example 2. Cantilever Beam Vibration

For the cantilever beam (Figure 24), an analytical solution for parameter sensitivities of the natural frequencies was quite simple. Defining

$$\beta = \sqrt{\frac{EI}{\rho A L^4}} = \sqrt{\frac{Et^2}{12\rho L^4}} \tag{78}$$

The bending frequencies were $\omega_i = \alpha_i \beta$, where α_i was independent of the geometry and properties of the beam. In particular, the first three frequencies have $\alpha = 3.52$, 22.0, and 61.7, respectively.

Table 15 summarizes the results obtained for a particular case, using three different meshes. The sensitivity parameters were modulus, E, density, ρ, thickness, t, width, b, and length, L. It was instructive to study the results from a relatively coarse model (five bilinear elements) first; this model was labeled Mesh 1 in the table. All computed results for the first mode were quite good for Mesh 1, with the error in frequency sensitivities being similar in magnitude to the frequency error itself. For the next two modes, the sensitivities for intrinsic parameters E, ρ, and t were at least equal in accuracy to the frequencies, for reasons explained in the last example. The length sensitivity in Mesh 1 has been defined by attributing coordinate sensitivities only to the end nodes, however, and was rather poor: this "local" geometry parameter does not enter the finite element frequency equation in the same manner as in the analytical solution.

Meshes 2 and 3 represent the two obvious solutions to the poor accuracy of Mesh 1 for the length parameter in higher modes. Mesh 2 was a refined model, in which ten elements were used, and the coordinate sensitivities were defined for the end nodes only, as in Mesh 1. All results were much improved, as expected; but the $\partial\omega/\partial L$ sensitivity was still less accurate (15.9

80

percent error for the third mode) than the frequency (7.2 percent error).

Mesh 3 was different from Mesh 2 only in the specification of the nodal coordinate sensitivities, which now were specified so that all nodes move proportionally when the length changes. Mesh 3 produces results which were essentially exact for Mode 1 and reduces the error in $\partial\omega/\partial L$ by half for the higher modes. For Mesh 3, the error in all of the sensitivity results was generally no larger than the frequency error for each case considered.

Example 3. Twisted Plate Vibration

Figure 25 shows a twisted cantilever plate which has been used extensively for the comparison of natural frequency predictions by MacBain, Kielb, and Leissa (29). We wish to compare natural frequency sensitivities obtained with the present analysis to those derived from finite differencing. For the case considered, we take $E=10^7$, $\nu=0.30$, $\rho=0.00026$; the dimensions were length a=3, width b=1, and thickness h=0.050, all constants being in inch units.

For the present analysis, we employ a 6×6 mesh of bilinear elements, which was adequate for the first few modes. As evidence of this, Table 16 summarizes the first several modes predicted for a twist angle of $\theta=30°$. Nondimensional frequencies obtained from NASTRAN using a mesh of 128 TRIA2 elements were tabulated as well, and the two solutions were in reasonable agreement.

Table 17 shows the computed frequency sensitivities for modes 1-4, for a twist angle of 32°. Finite difference estimates for the sensitivities were obtained from separate eigenvalue solutions performed for twist angles of 31.9° and 32.1°. The agreement of the predictions was reasonably good and was quite accurate where the sensitivity was large in magnitude.

81
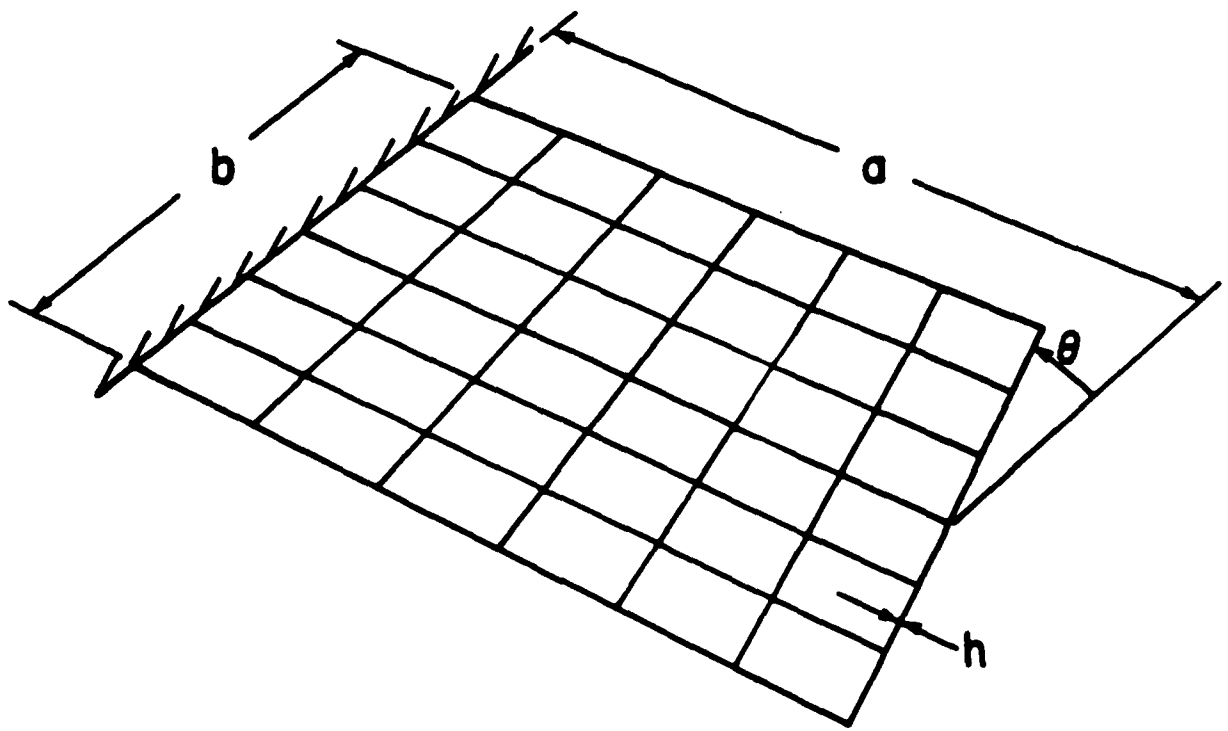
Figure 25.   Twisted Cantilever Plate.

TABLE 15

FREQUENCY SENSITIVITIES FOR CANTILEVER BEAM[†]

Mode	ω	$\partial\omega/\partial E$	$\partial\omega/\partial\rho$	$\partial\omega/\partial t$	$\partial\omega/\partial b$	$\partial\omega/\partial L$
1 Exact	201.6	1.01×10^{-5}	-3.97×10^{5}	2016.	0.	-40.32
Mesh-1	202.3	1.01×10^{-5}	-3.98×10^{5}	2023.	3.9×10^{-10}	-40.67
Mesh-2	201.6	1.01×10^{-5}	-3.97×10^{5}	2016.	4.9×10^{-10}	-40.37
Mesh-3	201.6	1.01×10^{-5}	-3.97×10^{5}	2016.	4.9×10^{-10}	-40.32
2 Exact	1260.1	6.30×10^{-5}	-2.48×10^{6}	12601.	0.	-252.03
Mesh-1	1391.9	6.96×10^{-5}	-2.74×10^{6}	13904.	3.8×10^{-10}	-310.24
Mesh-2	1292.9	6.46×10^{-5}	-2.55×10^{6}	12917.	4.6×10^{-11}	-265.25
Mesh-3	1292.9	6.46×10^{-5}	-2.55×10^{6}	12917.	4.6×10^{-11}	-258.46
3 Exact	3534.1	1.77×10^{-4}	-6.96×10^{6}	35341.	0.	-706.82
Mesh-1	4727.9	2.36×10^{-4}	-9.31×10^{6}	47120.	1.5×10^{-10}	-1260.49
Mesh-2	3790.1	1.90×10^{-4}	-7.46×10^{6}	37809.	5.8×10^{-11}	-818.98
Mesh-3	3790.1	1.90×10^{-4}	-7.46×10^{6}	37809.	5.8×10^{-11}	-757.10

[†] $E=1\times10^{7}$; $\nu=0$; $t=0.1$; $\rho=0.000254$; $L=10$; $b=1$

TABLE 16

FREQUENCY PARAMETER COMPARISON FOR 30° TWISTED PLATE[†]

Mode	Type	NASTRAN	Present
1	1-B	3.42	3.20
2	2-B	19.10	19.08
3	1-T	26.04	26.52
4	3-B	60.15	61.62
5	1-EB	73.00	74.19
6	2-T	78.50	82.93

[†] Normalized frequencies were $\lambda = \omega a^2\sqrt{\rho h/D}$

TABLE 17
FREQUENCY SENSITIVITIES FOR 32° TWISTED PLATE

Mode	Type	$\omega(31.9°)$	$\omega(32°)$	$\omega(32.1°)$	$\partial\omega/\partial\theta$[†]	$\Delta\omega/\Delta\theta$
1	1-B	921.16	920.23	919.29	-467.3	-535.1
2	2-B	5354.91	5346.21	5337.53	-4668.9	-4979.0
3	1-T	9006.48	9017.26	9028.02	4927.2	6170.8
4	3-B	17141.7	17119.2	17096.8	-12791.5	-12862.9

[†]Note that the sensitivity variable θ was defined in radians.

3.4 PROBABILISTIC FINITE ELEMENT CODE AND ITS APPLICATION TO BLADED DISK SENSITIVITY AND FREQUENCY RESPONSE ANALYSIS

The finite element sensitivity and probabilistic analysis techniques were implemented in a computer program called PROTEC (Probabilistic Response of Turbine Engine Components). PROTEC was written in ANSI FORTRAN 77 and has been executed on CDC Cyber, CRAY/XMP, and DEC VAX machines. The input to PROTEC was arranged in a series of input blocks such as boundary conditions, nodal coordiantes, coordinate derivative data, element connections, nodal force-moments, material properties, element geometry properties, etc. Data translation to and from PATRAN was performed by two intereface programs - PATPRO (PATRAN-TO-PROTEC) and PROPAT (PROTEC-TO-PATRAN). PATPRO converted a finite element neutral file from the geometric modeling program PATRAN into a standard input file for finite element analysis by PROTEC. PROPAT transformed a PROTEC results file into a PATRAN results file for post-processing.

The modeling-analysis-post processing cycle began in PATRAN where the finite element geometric model was generated. PROTEC performed vibration and sensitivity analysis from the information generated and received from PATPRO code. The results file POSFIL was then processed by PROPAT to make compatible plotting data for PATRAN. PRODIS (PRTEC-TO-DISPLA) was an output processor for

PRTOEC that performed probabilistic computations and presented graphics using the DISSPLA library. Two modes of presentation were included in PRODIS for display of probabilistic data. Nodal or elemental variance data from static or natural vibration solution could be displayed in histogram form to compare different parametric effects from different analysis cases. Also, the results from steady-state harmonic analysis with forcing frequency as an independent variable were typically presented as x-y plots or 3-D surfaces.

A concise general procedure flowchart for the stochastic analysis was shown in Figure 26. A 38-bladed disk designed for the United Technology Research Center NSMS demonstration test was chosen for an analysis model. The finite element model of the tuned system was created with PATRAN and was shown in Figure 27. Through PATPRO, the model data were input to PROTEC wherein the stress, deformation, and sensitivity information at the natural frequencies of the model were calculated.

Since the conventional stress and deformation results were not the focal point in this effort, the emphasis was placed on the sensitivity analysis. The natural frequencies of the tuned disk and the frequency variations caused by mistuning characteristics were tabulated in Tables 18 and 19, respectively. The variations were plotted in Figure 28.

The values in Table 19 were obtained from a probabilistic equation that has the following form:

$$\text{Var. } [\omega] = (\frac{\delta \omega}{\delta P})^2 \ \text{Var.(P)}. \tag{79}$$

where P was the sensitivity parameter (i.e., modulus, thickness, length) and ω was the natural frequency. Moreover, the variance of the sensitivity parameter can be obtained by a statistical computation (e.g., Monte Carlo simulation) or an analytical approach (e.g., micromechanics).

```
        ┌─────────────────────────────┐
        │      Apply ASD-PATRAN        │
        │  for finite element model    │
        └─────────────────────────────┘
                      │
                      ▼
    ┌───────────────────────────────────────┐
    │            Apply PAT_PRO               │
    │ for appropriate formatted input data   │
    └───────────────────────────────────────┘
                      │
                      ▼
              ╭───────────────╮
              │  Input Data   │
              ╰───────────────╯
                      │
                      ▼
    ┌───────────────────────────────────────┐
    │            Apply PROTEC                │
    │  for FEA and Sensitivity Results       │
    └───────────────────────────────────────┘
              │                    │
              ▼                    ▼
    ╭───────────────────╮    ╭───────────────────╮
    │  Deterministic    │    │    Sensitivity    │
    │  Results Data     │    │   Results Data    │
    ╰───────────────────╯    ╰───────────────────╯
              │                    │
              ▼                    ▼
  ┌───────────────────────┐  ┌───────────────────────┐
  │ Apply PRO_PAT         │  │ Apply PRO_DIS         │
  │ for deformation and   │  │ for sensitivity       │
  │ stress analysis data  │  │ analysis data         │
  │ display               │  │ display               │
  └───────────────────────┘  └───────────────────────┘
```
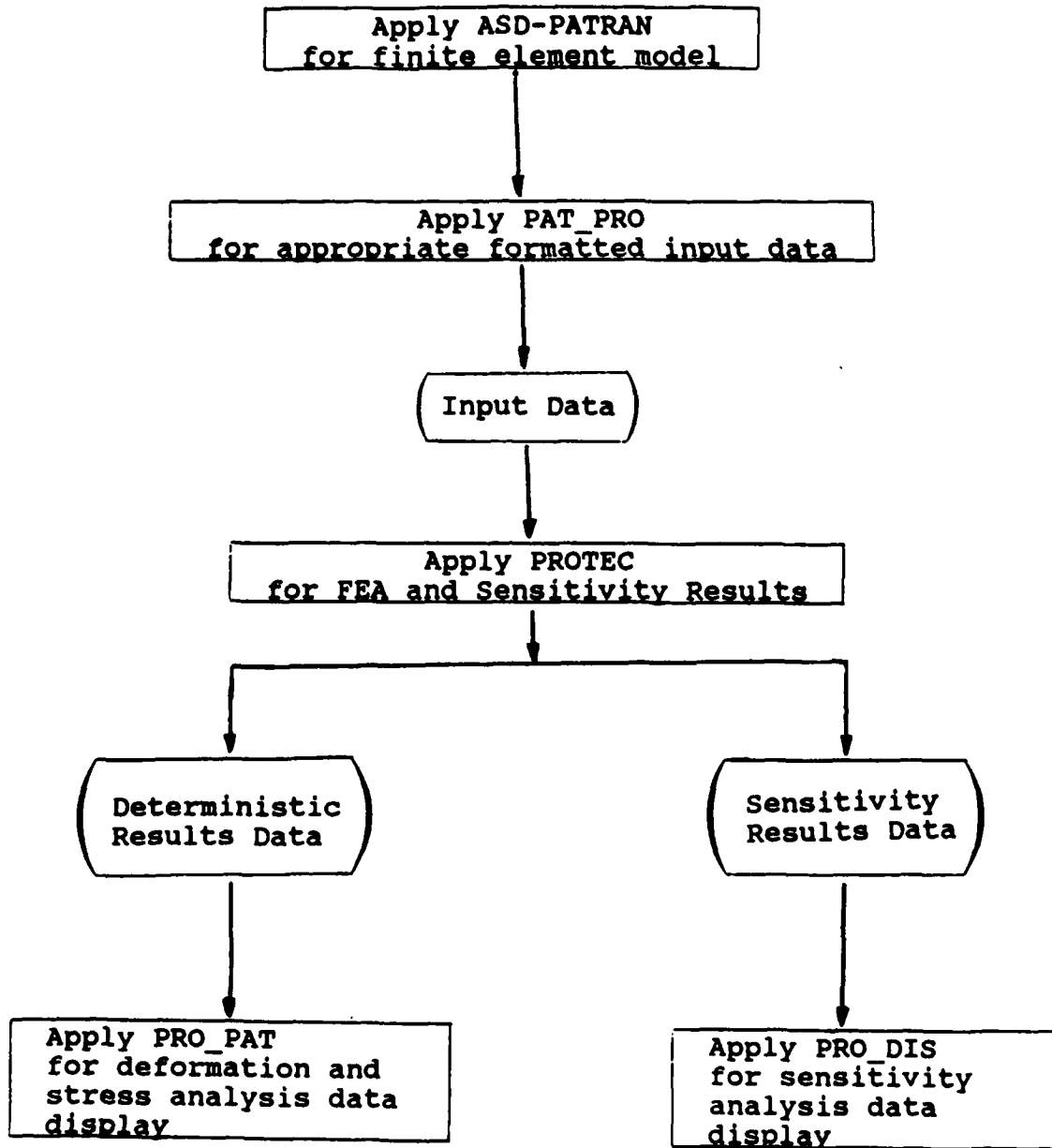
Figure 26.   PROTEC Solution Flow Chart.

mistuned blade
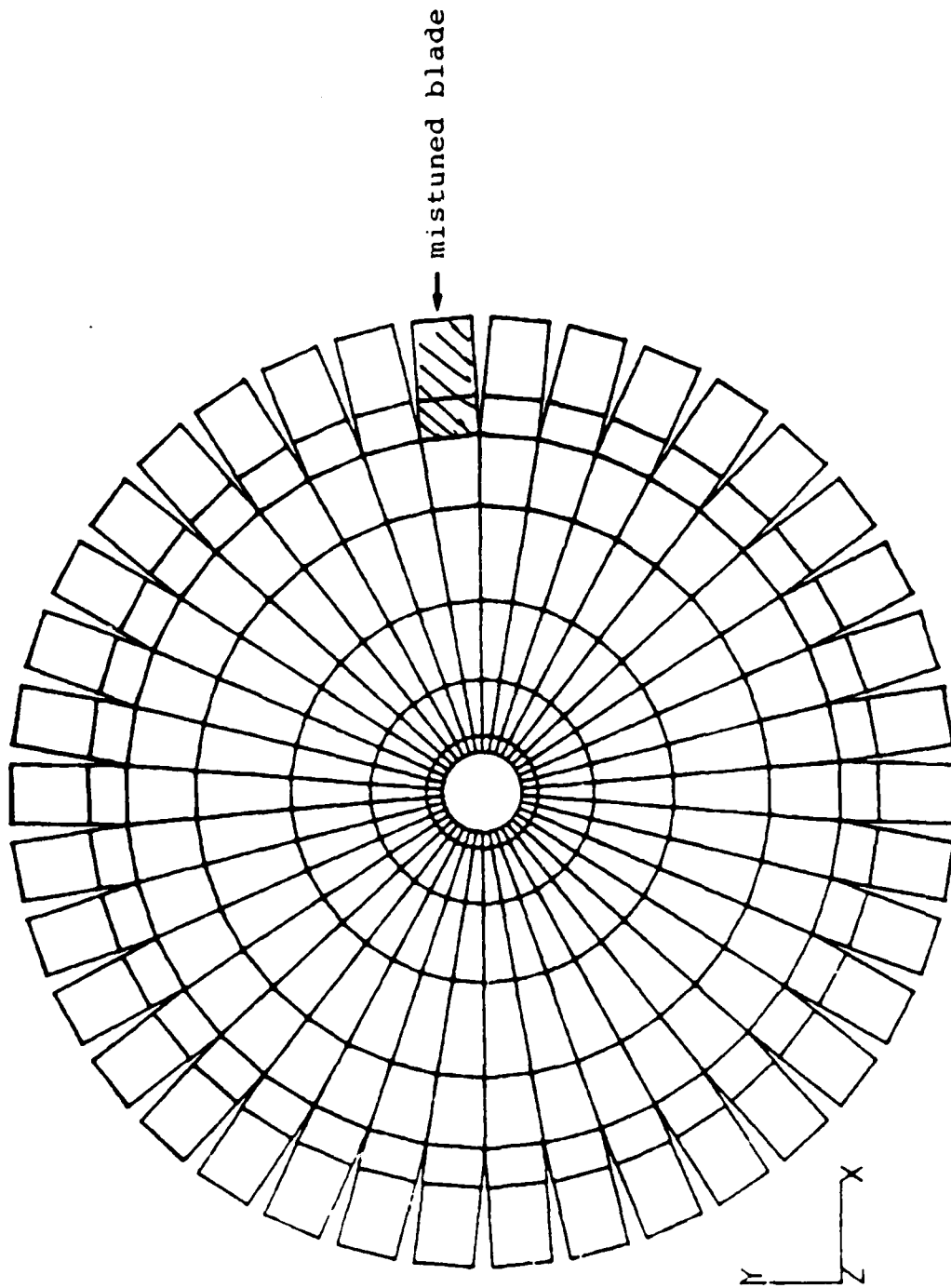
Figure 27.   PATRAN Generated 38 Bladed Disk FE Model.

87

To compare the sensitivity parameters with each other, they can be represented by:

$$S.V. = (\frac{\delta\omega}{\delta P})\ P \tag{80}$$

where P was the sensitivity parameter and S.V. was the sensitivity value, an index for comparison.

TABLE 18
NATURAL FREQUENCIES OF 38-BLADED DISK - PROTEC ANALYSIS

Disk Geometry
Overall Diameter: 11 inch
Clamped Inner Diameter: 2 inch
Blade Length: 1 1/2 inch
Disk Thickness: 1/16 inch
Material: Steel

MODE	NASTRAN	PROTEC	HOLOGRAPHIC EXPERIMENT
1D	72.2/72.2	77.8/77.8	75
OC	85.8	82.8	86
2D	103.3/103.3	102.8/102.8	106
3D	195.0/195.0	184.1/184.1	186
4D	294.1/294.1	--	287

TABLE 19

SENSITIVITY VALUES FOR BLADE MODULUS (E),

BLADE THICKNESS (T), AND BLADE LENGTH (L) VARIATIONS

Mode	SV(E)	SV(T)	SV(L)
1	0.030	5.48	9.0
2	0.062	3.30	6.0
3	0.242	8.19	10.5
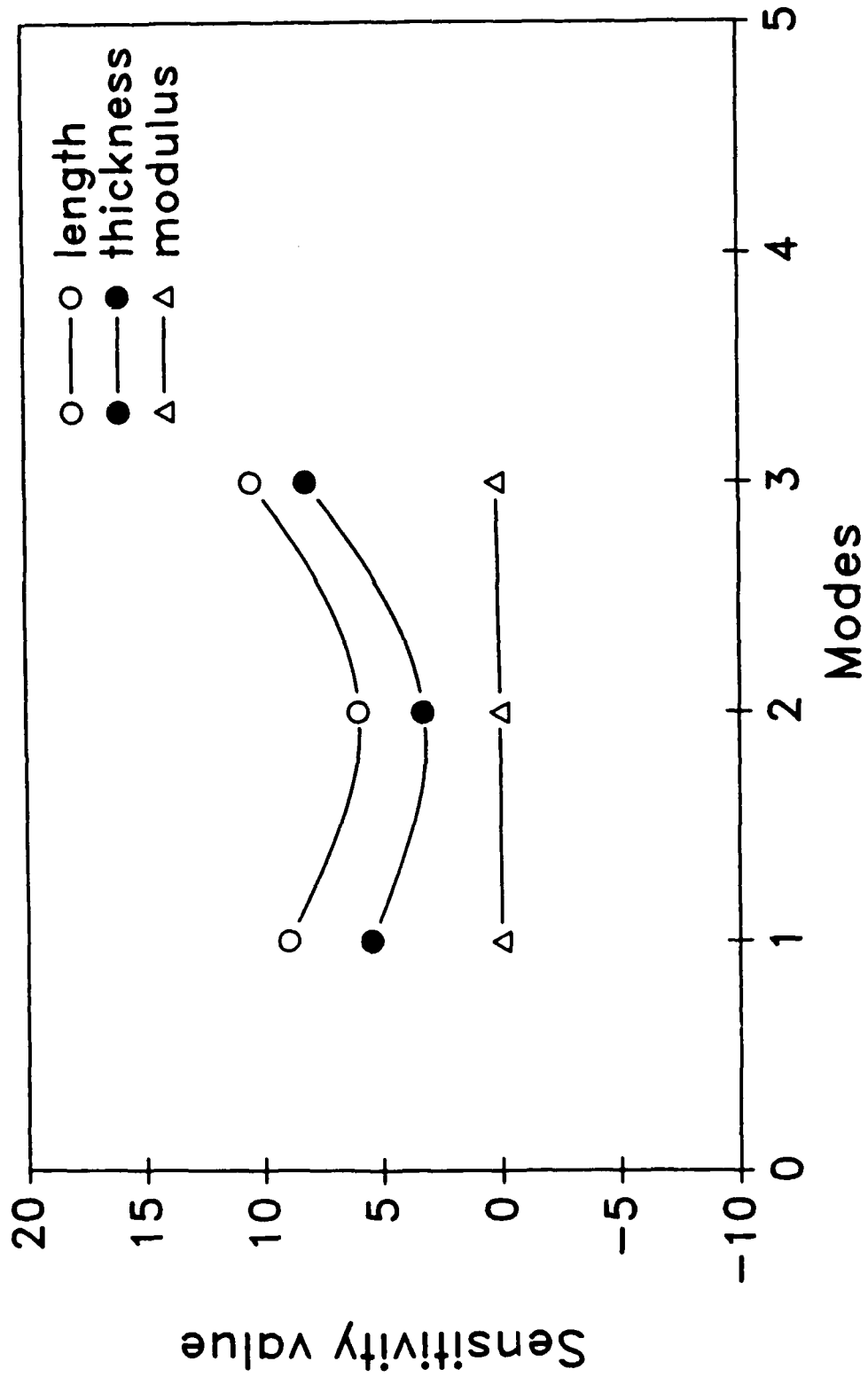
Figure 28. Frequency Sensitivities of Bladed Disk.

Based upon the results shown in Table 19 and Figure 28, the variation of the blade's length had the largest "influence" in the natural frequency sensitivity. Blade thickness had the next largest effect while modulus variations had only minor effect. In other words, the research focus should be placed more upon the shape imperfections than on the modulus variations of a mistuned bladed disk.

To understand the harmonic response characteristics of a 38-bladed disk system (UTRC model), three harmonic loading cases were analyzed. As shown in Figure 29, case A was a single point load, case B was a double point load with equal magnitude but opposite sign, and case C was a four point load with equal pairs of magnitude and opposite sign. The objective of the harmonic analysis was to determine the response behavior of the disk as it transited through resonance.

The first six natural frequencies of the bladed disk system, presented in Table 18 and shown in Figure 30, were calculated with PROTEC. The chosen frequency range of these six resonances was from zero to 300 Hz. The harmonic response calculations were performed within this frequency range. Finer frequency increments were used in the neighborhood of the resonances. Case A with the single point applied load had the response characteristics of the free vibration resonances, as we might expect. Case B had three resonance responses within the frequency range stated before, while case C had only two resonance responses. Cases B and C could not excite the OC (Umbrella Mode) response because of their bipolar loading conditions and could excite only the odd or even modes because of their geometries.

Figures 31 and 32 show the odd and even node stress distributions respectively on the bladed disk system due to the three different harmonic loads. The stress comparison between the single point load system and the double point load system was depicted in Figure 32. Since the double point load system only had three resonance responses within the frequency range analyzed, the stress comparison with the single point load system was limited to

90
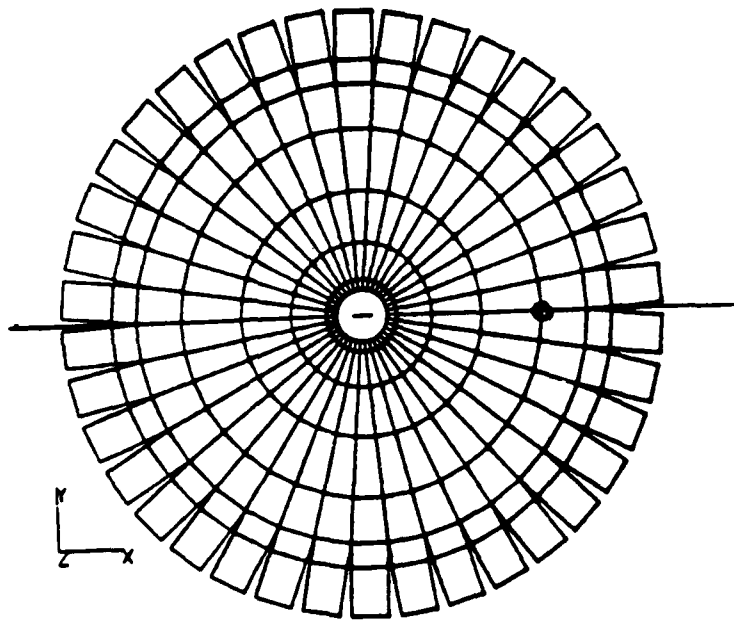
Case A = Single Point Harmonic Loading
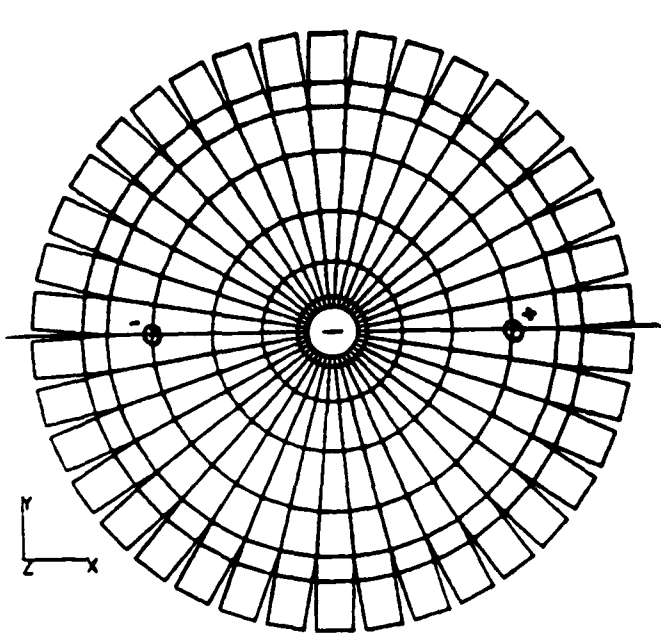
Case B = Double Point Harmonic
Loading
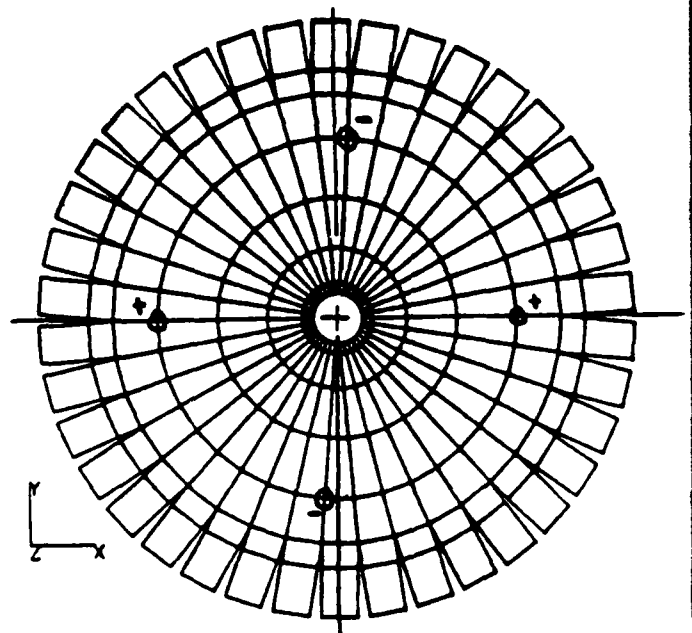
Case C = Four Point Harmonic
Loading

Figure 29.   Harmonic Loading on Bladed Disk.

91
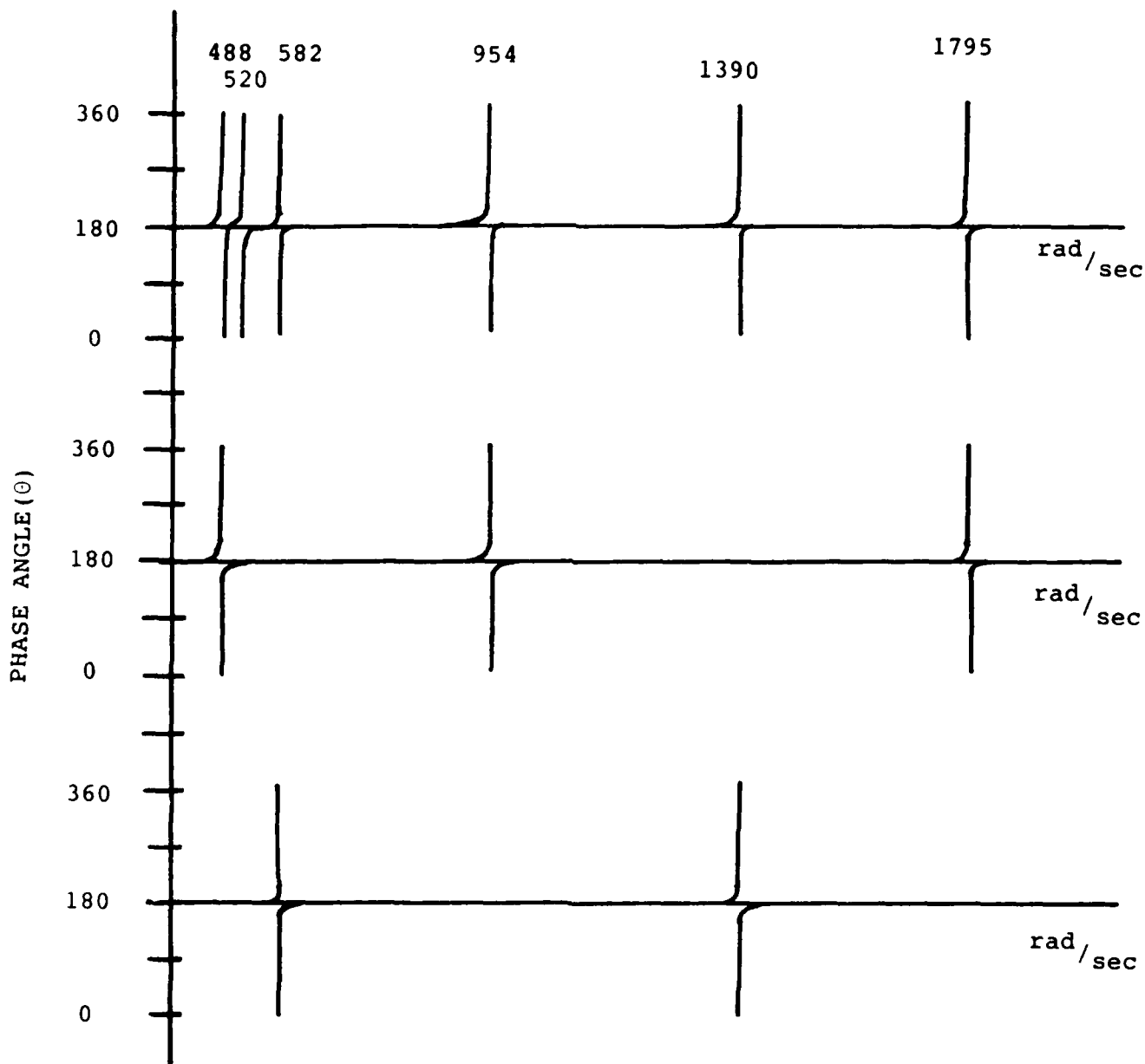
Figure 30.   Natural Frequency and Phase Changes under
Point Harmonic Loads.
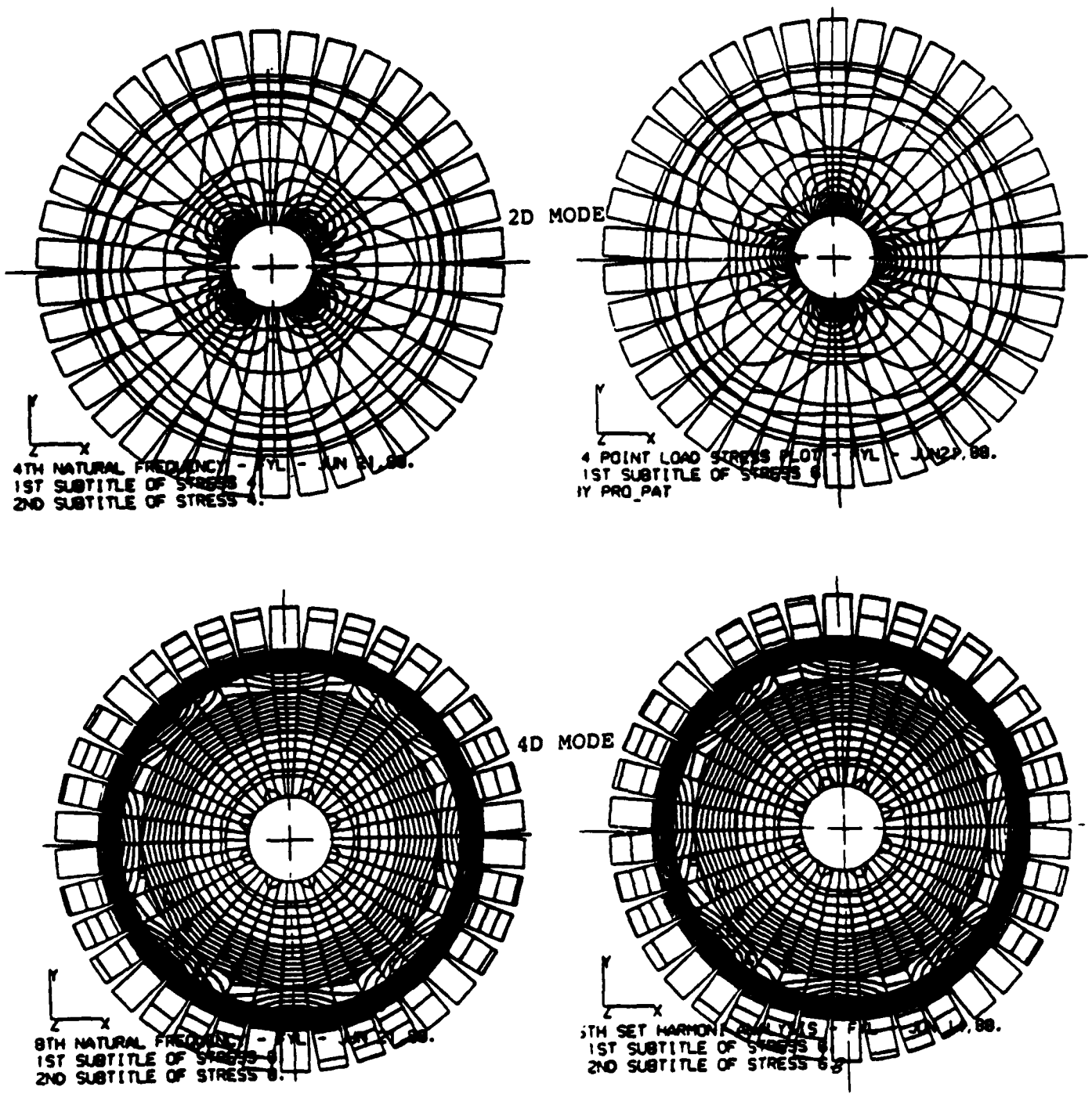
Figure 32.   Even Mode Stress Distribution of Bladed Disk.
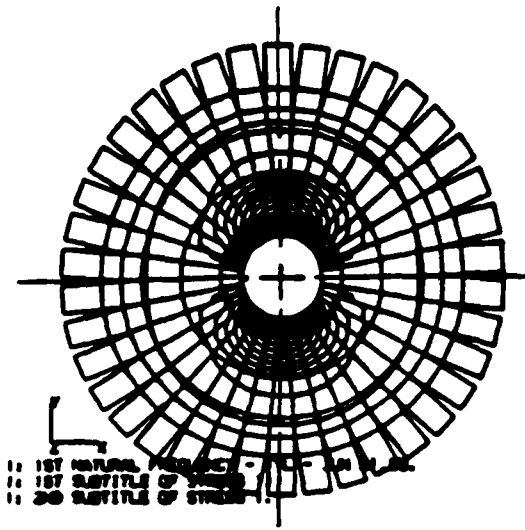
1D MODE
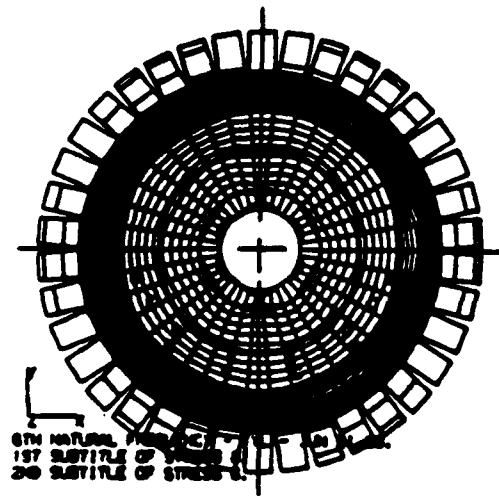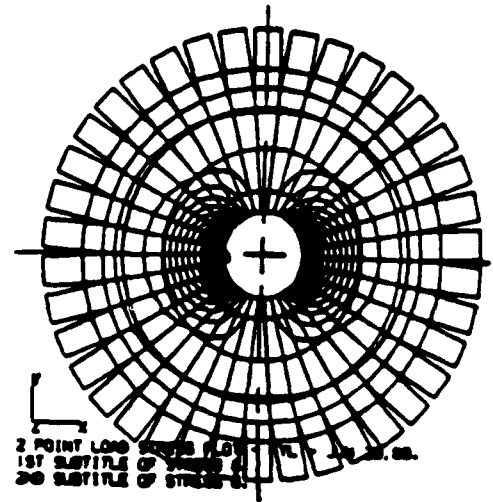
3D MODE
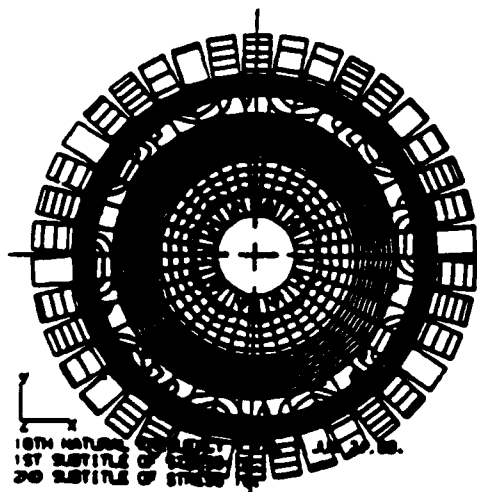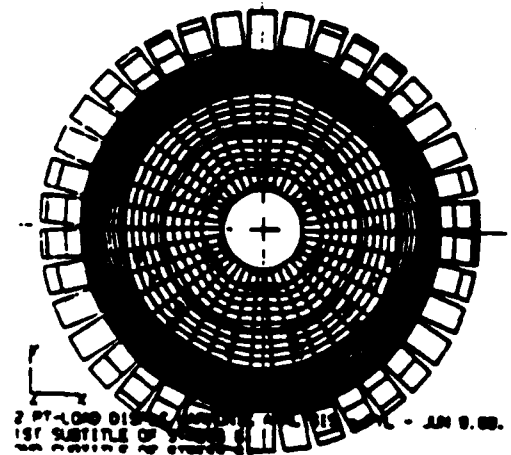
5D MODE
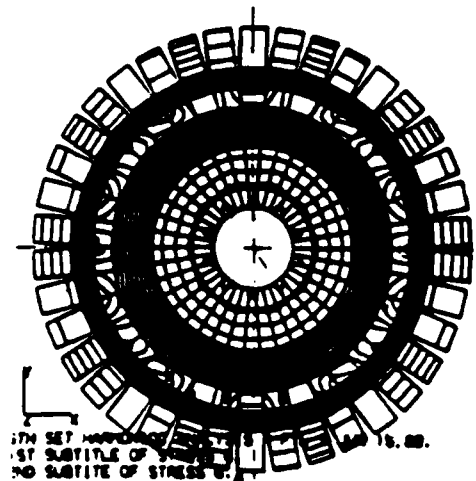
Single Point Load   Double Point Load

Figure 31.   Odd Mode Stress Distribution of Bladed Disk.

93

three corresponding natural frequencies. A similar stress comparison between the single point load case and the four point load case was shown in Figure 32.

SECTION IV
PLANE-OF-LIGHT PROBE SYSTEM DEVELOPMENT

In the past, measurement methods involving strain gage-slip ring, strain gage-telemetry, and laser interferometry systems have been used to monitor blade vibrations. These methods have disadvantages like (a) limited survivability in high temperature and high speed environments, (b) required disassembly of parts for sensor installation and repair, (c) location of sensors and transmitting elements on the rotor, and (d) nonaccessibility to viewing optics except for the front stage of the compressor. The drawbacks associated with the strain gage and interferometry methods have led to the development of noncontacting deflection measurement systems for rotating turbine/compressor blades. This section describes the concept and the optical and electronic development of a four-channel fiber optic plane-of-light sensor method, also referred as the noninterference stress measurement system (NSMS) in this report, to monitor blade tip vibrations of rotating turbine disks.

4.1 NONINTRUSIVE VIBRATION MEASUREMENT METHODS - RELEVANCE AND PAST DEVELOPMENT

The idea of measuring compressor blade vibrations by a remote optical sensor was proposed and implemented by Hohenberg (30) and Zablotskiy, et al., (31,32). Nieberding and Pollack (33) of NASA Lewis and McCarty and Thompson of AEDC developed (34) and measured (35) the compressor blade tip vibrations by a single spot sensor. Roth (36) and Endoh (37) developed multiprobe spot sensor methods to measure rotating blade vibrations. Spot sensors lack the ability to always measure the same location on the blade tip cross section. This leads to gross measurement errors. The use of multiple plane-of-light sensors to look at blade tip corners was proposed by Camarata et.al., (38). Chi et.al., (39) developed software programs to process the digital data from the plane-of-light sensors. Jones adapted (40) the multichannel NSMS system to measure the integral order vibrations (41) of compressor blades.

United Technologies Research Center (UTRC) assembled a test model of this system and demonstrated it for integral order vibration measurements for AEDC (42). Concurrently, UDRI designed and assembled, for ISRL, a NSMS using the same technological basis but implemented in innovatively different hardware and software systems.

4.2 PRINCIPLE OF OPERATION OF PLANE-OF-LIGHT PROBES

The method measures the time of arrival of the rotating blade tips and the differential arrival time for a vibrating blade as compared to an unexcited blade is a direct indication of the blade tip deflection.

To express the idea in basic mathematics, let a blade tip travel with constant velocity, $v(=\omega R)$, where ω is the angular velocity and R is the radius of blade tip. The distance, y, traveled by blade tip in time, t, is

$$y = Vt \tag{81}$$

Introducing variations in variables y and t, we obtain

$$\Delta y = V(\Delta t). \tag{82}$$

Obviously from this equation, the differential time measurements (Δt) will yield changes in positions or deflections (Δy) of the blade tip.

The schematic diagram in Figure 33 explains the concept application to a rotating bladed disk. Let a plane-of-light sensor be mounted in a stationary case, surrounding a constant speed, four bladed rotor. The sensor receives evenly spaced reflected light pulses off the blade tips when blades are in the undeformed state. Time interval (T_0) is digitally measured. If the blades are deflected to the left, the light pulses occur at a later time (T_1) and $T_1 > T_0$. Similarly, for the blades deflected right, $T_2 < T_0$. The time differential in either case, $T_1 - T_0$ or $T_2 - T_0$ is the

97
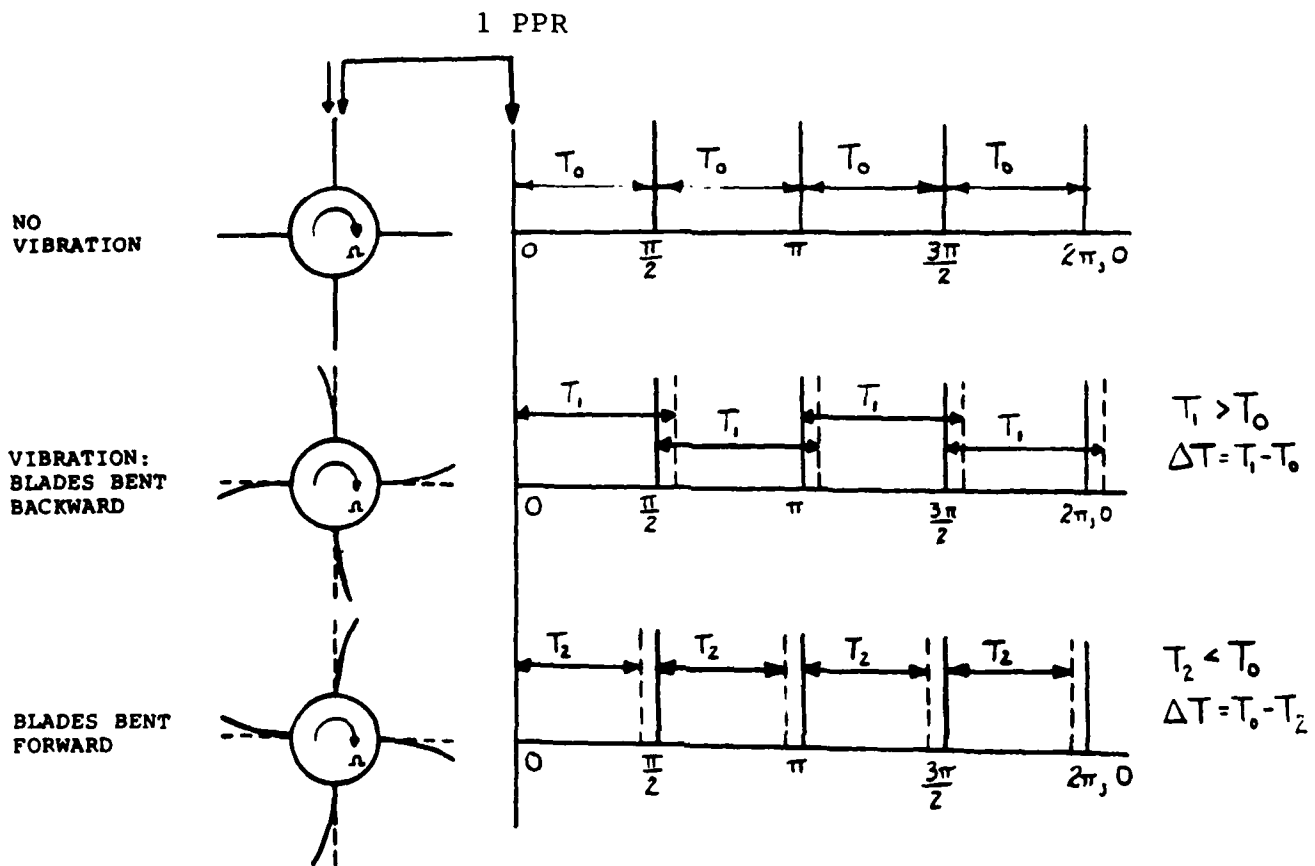
REFERENCE PULSES--SOLID LINES
VIBRATION PULSES--DOTTED LINES
T IS A MEASURE OF THE BLADE TIP DEFLECTION

Figure 33.   NSMS Principle of Operation.

direct measurement of the deflection of blade tips of a rotating bladed disk.

The above simple explanation can easily be extended to determine the average blade tip deflection (δ) over several rotations of the disk.

Differentiation of equation (81) gives

$$\Delta y = \Delta vt + v\Delta t \tag{83}$$

Neglecting small speed changes and averaging the differential deflections and time measurements over several rotations at a non-vibrating reference speed gives

$$\sum_{i=1}^{N} \frac{\Delta y_i}{N} = v \sum_{i=1}^{N} \frac{|\Delta t|}{N} = \delta_1 \tag{84}$$

Similarly the average deflections at a resonating speed are

$$\sum_{j=1}^{N} \frac{\Delta y_j}{N} = v \sum_{j=1}^{N} \frac{|\Delta t|}{N} = \delta_2 \tag{85}$$

The net blade tip displacement over N disk rotations is

$$\delta = \delta_2 - \delta_1 \tag{86}$$

Our analysis software considers and corrects for shaft speed variations (Δv) in equation (83) for each of the recorded rotations.

4.3 PLANE-OF-LIGHT INSTRUMENTATION OPTICS AND ELECTRONICS

4.3.1 One Pulse-Per-Revolution Electronics Probe

The Applied Physics Division of UDRI designed, constructed, and implemented an electro-optic system to provide accurate position information about the angular orientation of a turbine disk. The system provided a fast-rise time, one pulse-per-revolution (1 PPR) signal to provide synchronous clocking pulses.

The 1 PPR encoder provided pulse rise time of 0.5 microsecond results in an angular disk rotation of 0.003 degree for the rotational speed of 1,000 RPM and 0.018 degree for a rotational speed of 6,000 RPM. These angles represent 0.0003 inch and 0.0018 inch of blade tip motion for a 12-inch-diameter fan. The signal was processed to provide up to 1 part in 100 resolution during the pulse rise and the device, therefore, provided up to 0.00003 degree of angular resolution at 1,000 RPM and 0.00018 degree of resolution at 6,000 RPM.

The UDRI 1 PPR encoder relied on a long lever arm to sweep the retro-reflected laser beam across a detector surface at a high velocity. This was accomplished by a 20x microscope and a 3-meter lever arm. The optical arrangement, including the top and side views of the 1 PPR encoder mounted to the chamber with the test disk is shown in Figure 34.

The single pulse per revolution encoder contained three modules: (1) a Helium-Neon laser light source, (2) microscope assembly, and (3) a PIN photodiode detector. The associated optics consisted of one beam splitter, an access window to the chamber, four aluminum flat mirrors, and mounting hardware. The mirrors and beam splitter directed the laser beam to the microscope module and back to the detector module.

The Helium-Neon laser was a CJ Laser, Series 1,000, with a 2-milliwatt linearly polarized output. The laser operated in the TEM_{00} mode with a beam divergence of 1.1 milliradians and 632.8-nanometer wavelength. The laser was self-contained with power supply, laser tube, and shutter housed in a 3- x 12- x 2-inch housing. The laser was mounted on a 1/2-inch-thick aluminum plate bolted to the chamber, and provided a very stable, rugged, light source.

The microscope assembly constructed by UDRI, consisted of a 20x microscope objective mounted on a linear translation stage, and an aluminum turning mirror mounted on a three-degree-of-motion mount. This provided motion in the vertical direction as well as pitch and roll motion to allow the He-Ne beam to travel through the optical axis of the microscope objective. The linear

LASER LIGHT MODULE

beam dump

laser

DETECTOR MODULE

mirror

beam splitter

access window

mirror

LOWER LEVEL

retro-mirror

motor

fan

MICROSCOPE MODULE
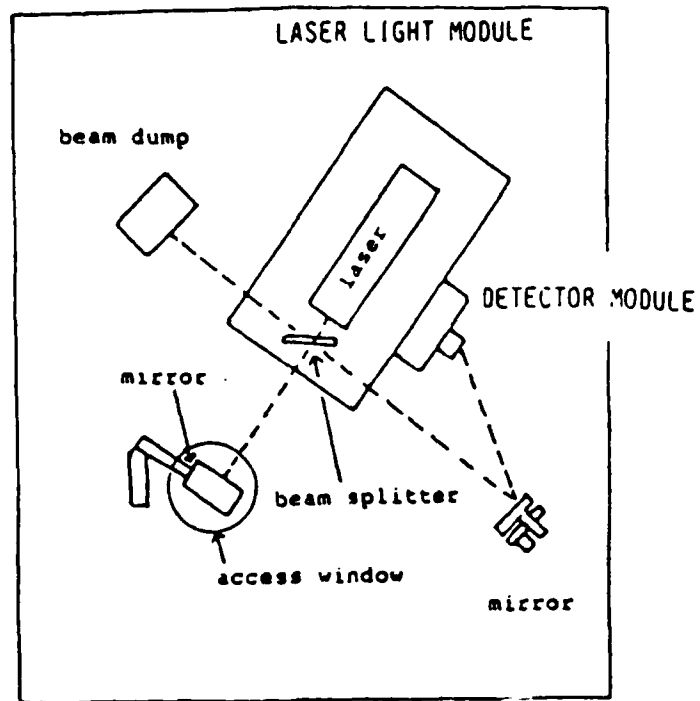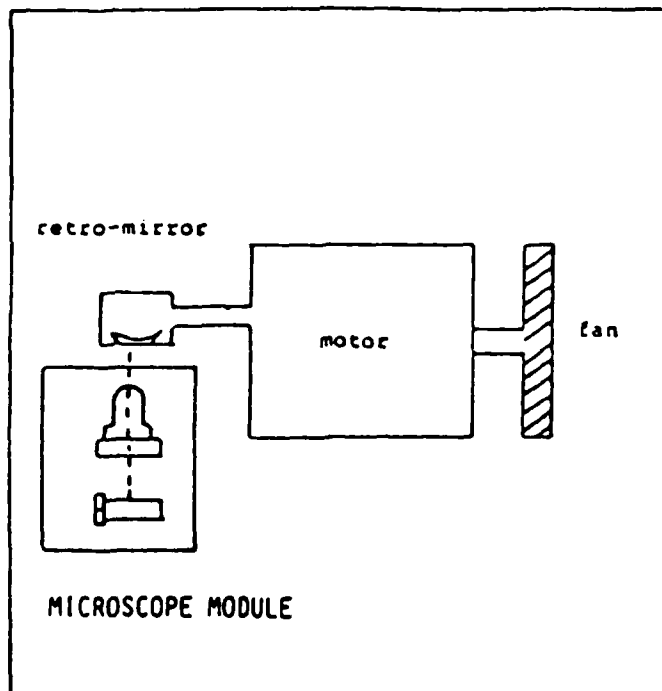
Figure 34. 1 PPR Optical Arrangement.

translation of the objective allowed fine focusing of the microscope. The assembly was mounted on a 1.5-inch-thick aluminum block which was clamped to the aluminum table on which the test fan drive motor was mounted.

The detector was a Hewlett-Packard PIN photodiode detector. The signal was conditioned by UDRI-designed electronics. The electronic circuit, shown in Figure 35, provided a TTL (transistor-transistor logic) signal compatible with the data acquisition system.

The He-Ne beam path, shown in Figure 36, was as follows: The He-Ne laser beam was transmitted through a beam splitter. The reflection portion was collected by a beam dump and the transmitted portion was directed into the chamber, by an aluminum mirror, through a 1-inch-diameter glass window in the chamber cover. As the beam reached the microscope module, a turning mirror directed the beam through the microscope objective. This focused the light onto a mirror on the drive motor shaft which reflected the beam back through the same optics. The reflected beam returned to the beam splitter which directed a portion of it to the detector. The horizontal turning mirror on top of the chamber lengthens the optical path causing the beam to sweep through a longer arc, and this long optical path shortened signal rise time for the detector.

Pulse shape with the optical 1 PPR system was shown in Figure 37. A 2 microsecond actual rise-time for the signal shown was achieved which proved sufficient to ensure accuracy of half-a-mil in blade tip deflection measurements.

4.3.2 Plane of Light Sensor Development

The UDRI Optics Group designed a fiber-optic plane of light sensor that provided fast rise-time and easy operation for the turbine blade deflection measurements. The sensor geometry and the emitting and sensing end details are shown in Figures 38 and 39 respectively. The linearly arrayed, bifurcated sensor provided light input and collection within a single assembly. Input and output bundles were separate and the fibers had minimal cross-talk.

102
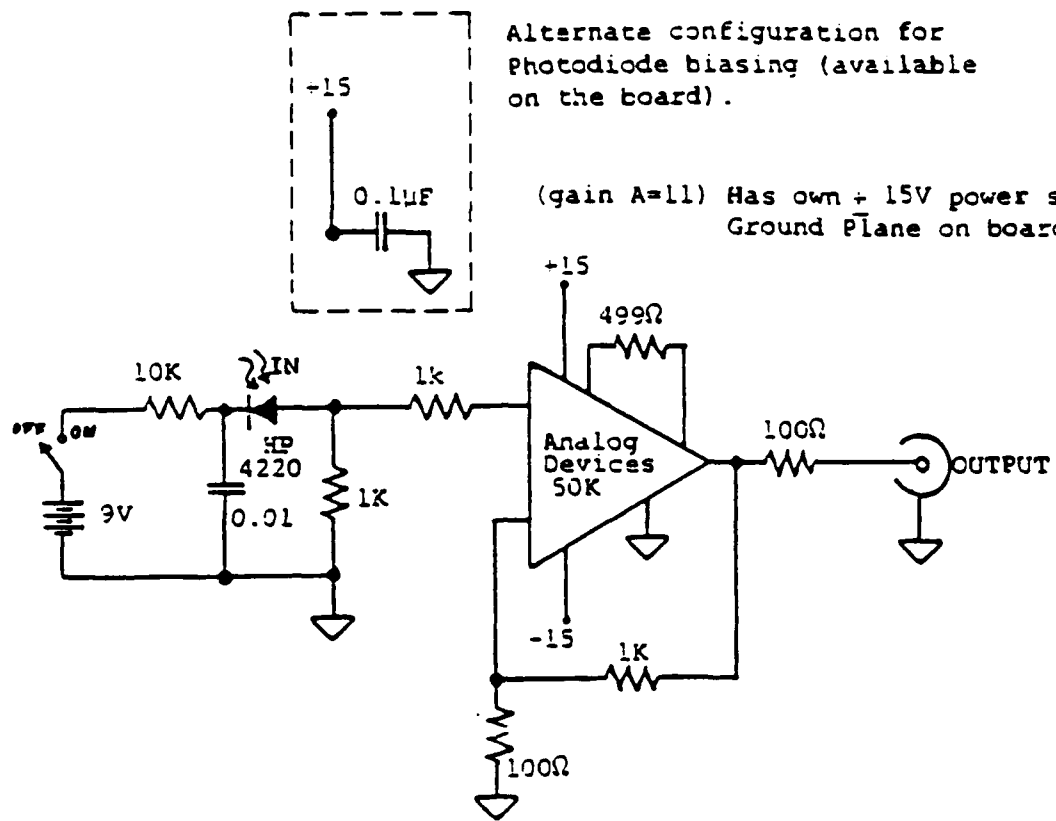
Figure 35.   Electronic Circuit for TTL Signal.
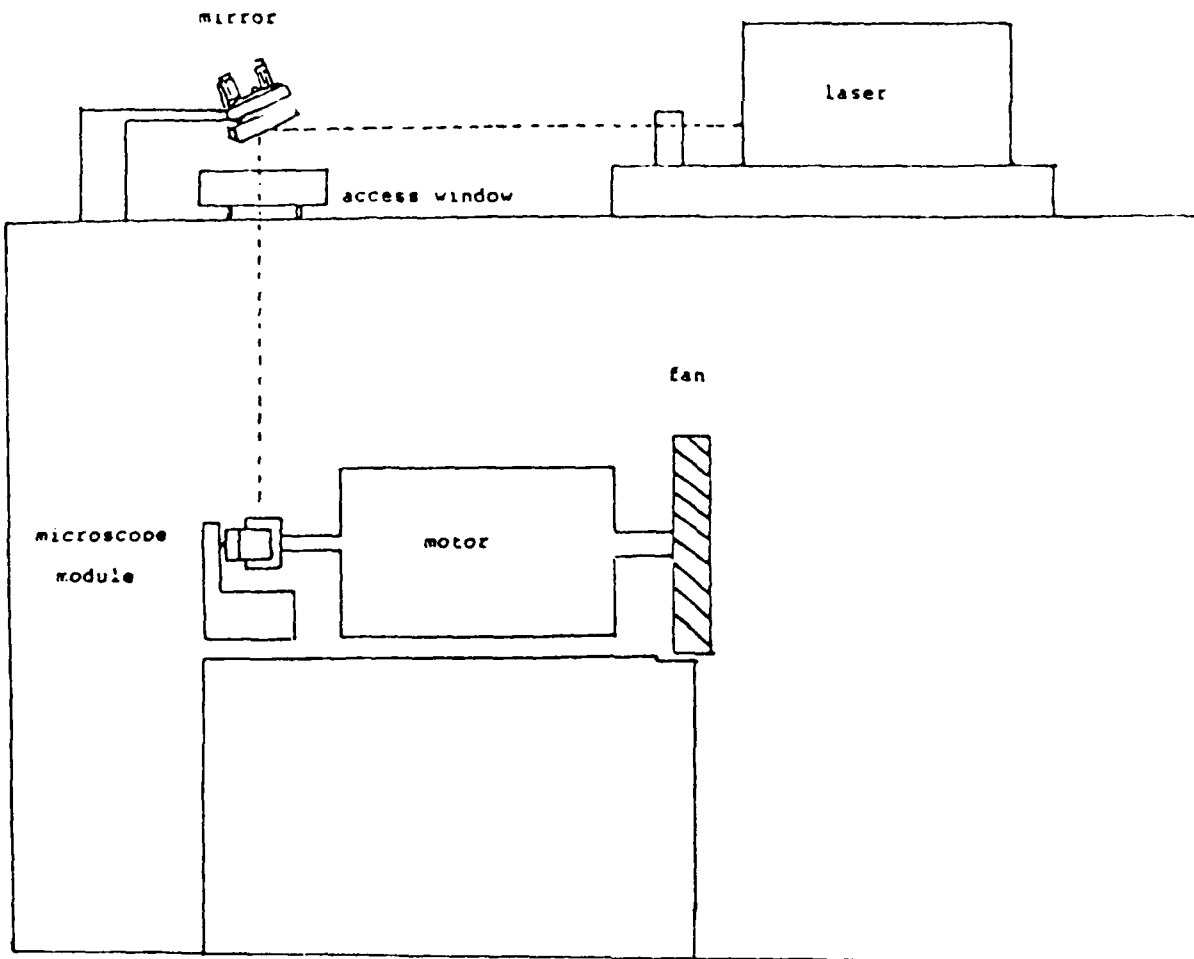
Figure 36. Optical Path for the 1 PPR Signal.
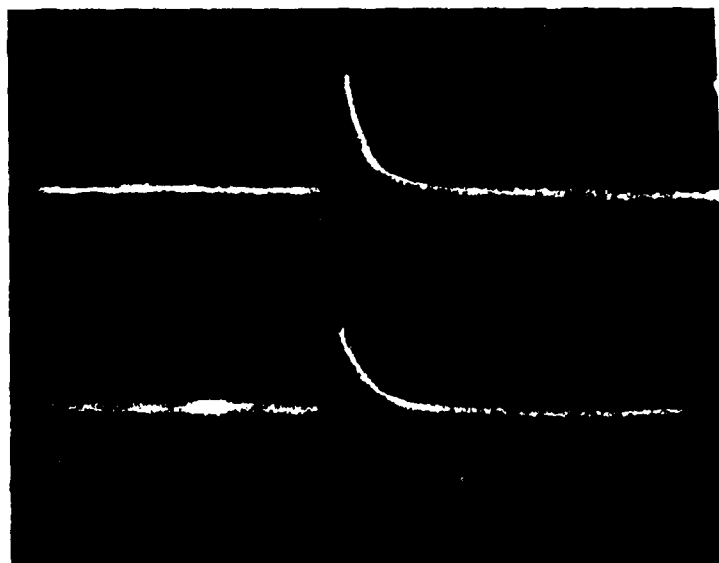
Figure 37. Pulse Shape of the 1 PPR Trigger Signal.
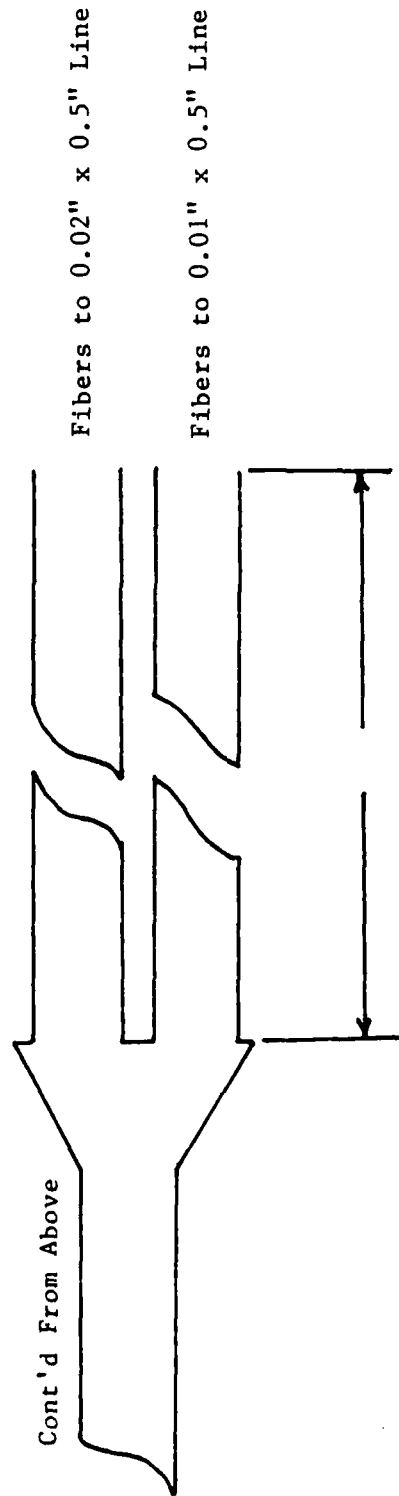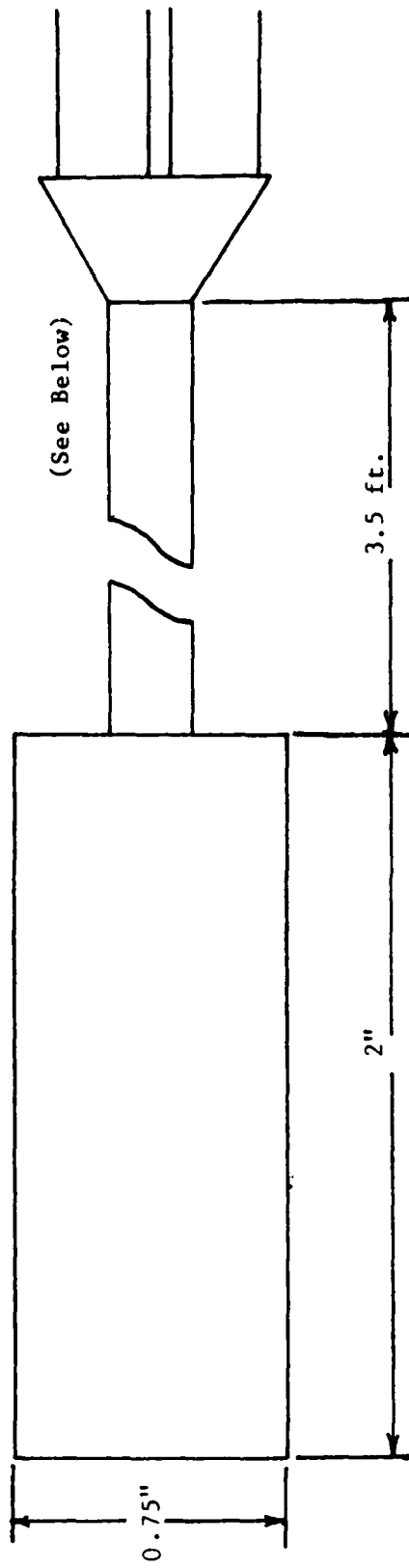
Each Bundle is
to be terminated
into 0.5" long x
0.19" diameter
Metal Fittings.

Figure 38. Plane-of-Light Sensor Geometry.

106
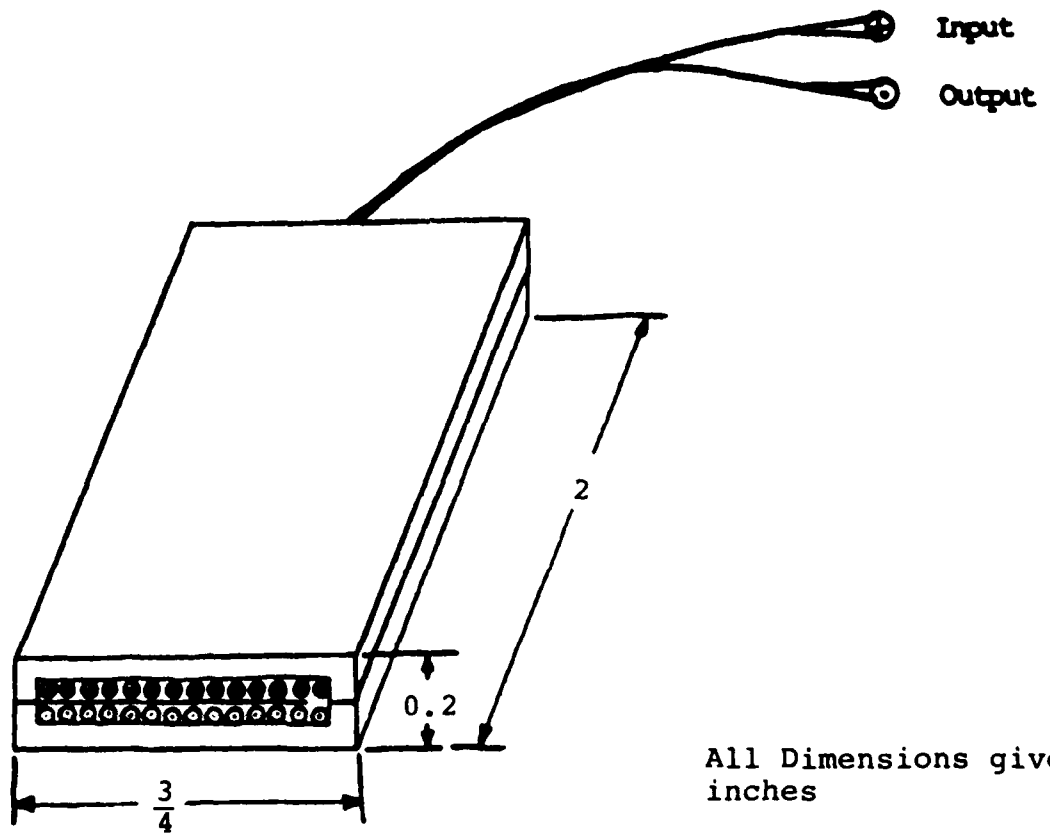
Figure 39.   Emitting and Sensing End of the Plane-of-Light
             Sensor.

About 75 individual fibers were in both the input and output portions of the sensor. The active areas of illumination and collection were each 0.5 x 0.002 inch with a separation of 0.002 inch between arrays. This configuration provided a compact source of illumination and plane of visual acceptance.

Some details of the fibers and the probe assembly were provided below.

Fiber: 200 microns core diameter

230 microns ± 5 microns clad diameter

Line dimensions: 0.5" x 0.01" nominal (both)

Note #1: The thickness of the line will be dependent on the diameter of the fiber.

Note #2:   Lines to be separated by a shim (0.002" to 0.005")

Aluminum Housing Dimensions: 2" x 0.75" x 0.2"

Sheathing: PVC/Monocoil

Overall Cable Length: 3 1/2'

The sensor made to the specifications was supplied by the Applied Fiber Optics, Southridge MA. All probes had well polished ends and good acceptance angles.

We used the sensors to detect the passing of the tips of simulated turbine fan blades. When the blade passed the fiber optic linear array, each individual fiber collected the reflected light and signified the actual position of the blade. The line sensor output was coupled to a linear detector array conveniently.

The light from each of the output fibers was integrated to result in a single output pulse signifying the passage of each blade. The two approaches used to accomplish this integration were (1) collecting the output light with a diffusing plate after the fiber optic, and (2) collecting the output light with an integrating sphere. The overall pulse width was increased, and the pulse shape was other than a pure square wave, but the front edge rise time was very short. The electronic thresholding was adjusted

108

to the sharp transition that corresponded to the first individual optic fiber sensing in the bundle.

4.3.3 NSMS Instrumentation Electronics

A software program was developed and implemented to interface a nine track tape drive with the microprocessor unit (MPU). The MPU and parallel interface were tested successfully to verify reading and writing of the various ports.

Three input/output (I/O) cards and three MPU were acquired, assembled and tested in parallel with the three fiber optic plane-of-light probes. An additional I/O card and MPU were designed and integrated with probe data acquisition system to work as system controller. The menu for the entire data acquisition, display and write was driven from this controller.

The prototype counter and latch cards were fabricated and tested for arbitrary short cable run lengths, but later redesigned to allow the maximum counter reading to be latched. The latch card was redesigned using differential line drivers to drive the longer cables. Because the drivers were differential, a differential line receiver card was designed to interface to the I/O card. These cards were fabricated and tested for satisfactory functioning. Because of the additional circuitry, a larger power supply for the extra load was required.

4.3.4 Plane-of-Light Sensor System Operation

A brief description of the interaction between four optical probes and the process electronics was provided here. In the systems data acquisition mode, each processor was designed to take a time reading as each blade passed the sensor. The source illumination through the fiber optic bundle reached the turbine blade tip and the reflected light reached the photomultipler tube (PMT). The PMT output signal proportional to the light level was amplified and compared with the threshold. If the light level was above the threshold, then the time of arrival was recorded by the processor. The electronic block diagram shown in Figure 40 explains the system operation.
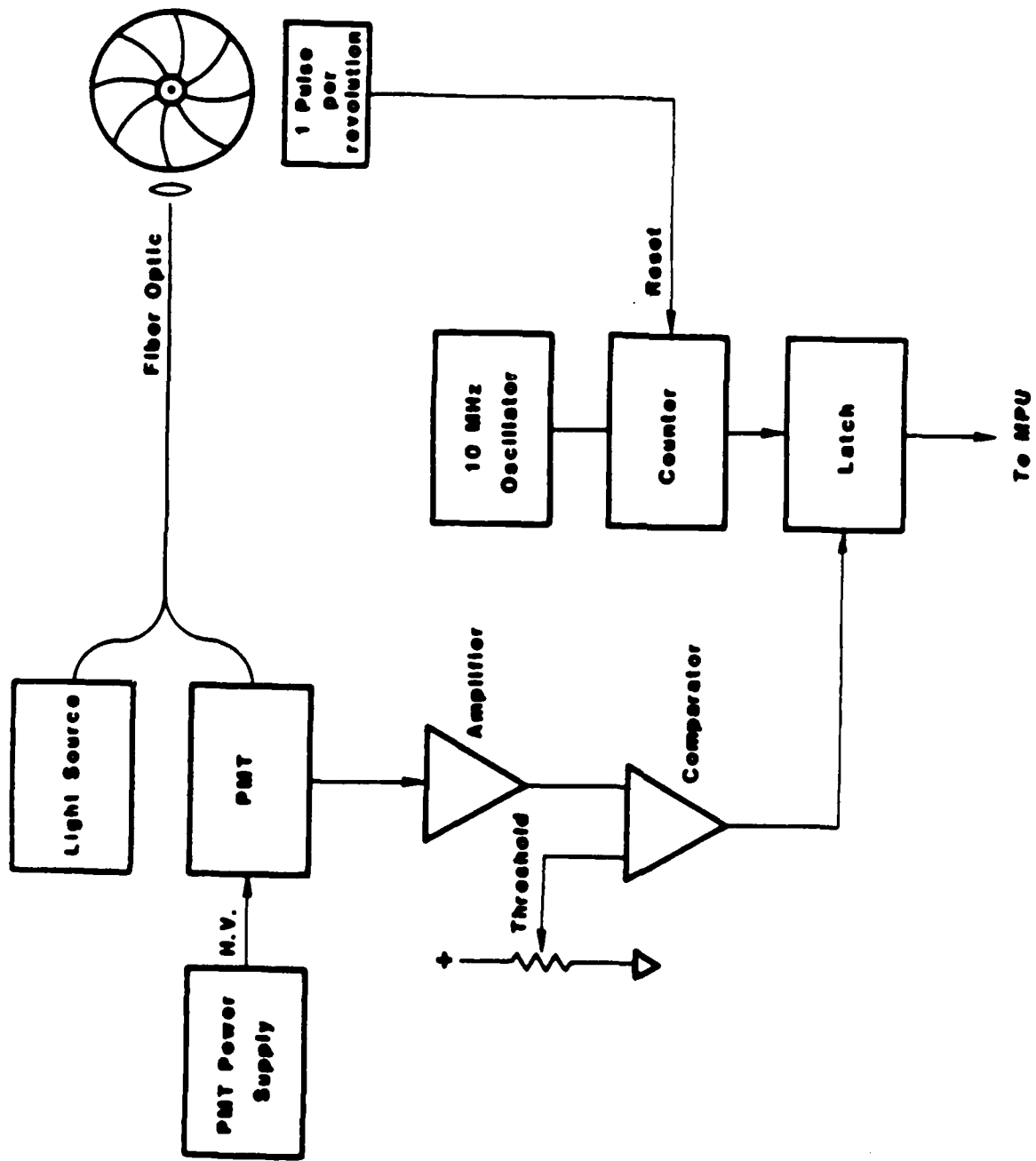
Figure 40. Data Acquisition Operation by the Optical Probe System.

110

The time for the four sensors was derived from a 20-MHz crystal oscillator. This clock time was divided by a 2 to generate a buffered complementary 10 MHz, 50-percent duty cycle square wave. The clock output was used to clock a 20-bit synchronous counter from five 4-bit counters with external look ahead carry to speed up their operation. The outputs from each counter card were buffered to drive a latch card. The counter was reset by the one pulse per revolution encoder on the turbine blade shaft. The encoder was asynchronous with the master clock but the counter reset must by synchronized with the clock which was accomplished by using three D flip-flops (bistable toggle switches). In these, preset and clear were overriding controls. The first was set high by the rising edge of the reset pulse from the encoder. This enables the second D flip-flop which was set by the next leading edge of the 10-MHz clock. The counter was reset by this signal which also enables the third D flip-flop which was set by the following clock pulse leading edge. The output of the third D flip-flop cleared the first and second D flip-flops. When the D flip-flop was cleared, the next leading edge of the clock clears the third D flip-flop.

When the light level on a PMT exceeds the threshold value, the current counter value was set in the latch card for that channel. The PMT output was asynchronous with the 10-MHz clock and was synchronized with the clock by the same type of circuit as that used to synchronize the reset for the counter. The latch signal was also used to trigger the computer to read the latched values. The latches had a high current output stage to drive the cables connecting the front end electronics to the computers.

Each data channel computer recorded the arrival time of each blade as it reached the sensor of that channel. The four data channel computers record the four stations. After the data had acquired, the data channel computers transferred the data to the system computer for recording on a nine-track magnetic tape. There were separate records from the four data channel computers. Each record might start with a different blade number occurring as the first blade in that record, depending on the blade and sensor

spacing. The system computer also controlled the setup and collection of data for the four channels.

The design of the four-channel system including counter cards and latch cards was described in full in References (1,2).

4.4 TURBINE BLADE DATA ACQUISITION SYSTEM

The UDRI designed turbine blade data acquisition system consisted of five major components - the 1 PPR detector, 1 PPR amplifier, the detector/electronic chassis, the computer system rack and the video graphics terminal. A printer was attached to the system for obtaining hard copy outputs of the terminal screen. These components were shown in the block diagram, Figure 41.

The 1 PPR detector together with its amplifier provided a TTL compatible signal to synchronize the system operation. The detector/electronics chassis received the signals from the 1 PPR and four probes and converted them to time data which were transferred to the computer for storage. A 10-MHz counter in the detector/electronics chassis drove five latch cards, one for the 1 PPR and four for four probes. When the system received a 1 PPR pulse, the value of the counter was latched in to the 1 PPR latch card, and then the counter was reset. When a blade passed a probe, a pulse was generated and the counter value was latched into the card corresponding to that station. The card then sent a valid data signal to the computer which read the data and reset the card. Thus all data were referenced in time to the 1 PPR and the blade arrival time data extracted.

A nine-track tape unit was provided to allow the data to be stored. This was a write-only tape system, and the data was to be read and analyzed on another computer.

The menu driven operating checklist provided for item entries such as test date and time, test specimen details, data acquisition, data display and data write and data discard. The system presents two modes of display - one, histogram for each of the four probe data versus number of blades, and two, a real-time display of blade arrival times for up to five blades at a
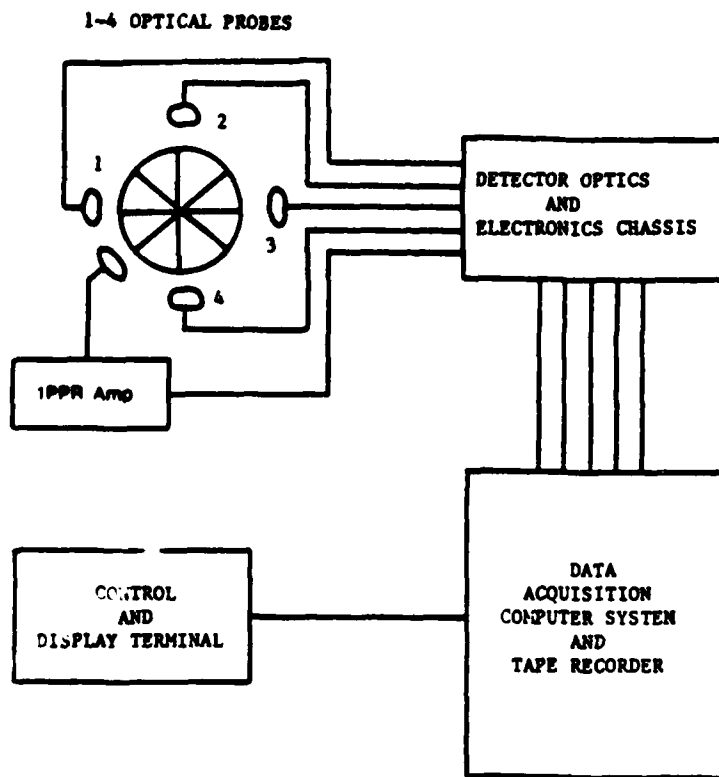
Figure 41.   Four-Channel Plane-of-Light Sensor
             System-Block Diagram.

113

particular station. The user can sequentially obtain and display data for all the probes.

A screen display of control monitor menu scheme was shown in Figure 42. Data values (number of counts) versus the number of blades of the rotating test disk were displayed in a typical histogram in Figure 43. This data display could be updated for a pair of revolutions of user's choice. The gradual step increase in data values was due to speed change of the test disk in each revolution. Figure 44 shows a typical real-time display of the data for five blades from a particular probe. The data values were normalized with reference to the 1 PPR count values. Similar data displays were provided by each of the three plane-of-light probes.

NSMS Data Acquisition System

Revolution   204 of 1000

              Current   Minimum   Maximum
              -------   -------   -------
Speed: 625   625   625   RPM

C = Change Date / Time / Specimen Data

D = Discard Data

H = Histogram

R = Real Time Display

S = Start Taking Data

W = Write Data To Tape

Figure 42.   Menu Display of the NSMS System
             Operation.

Test run   Station-4   98 Hz   984 RPM

Counts = 1488

BLADES NOS.
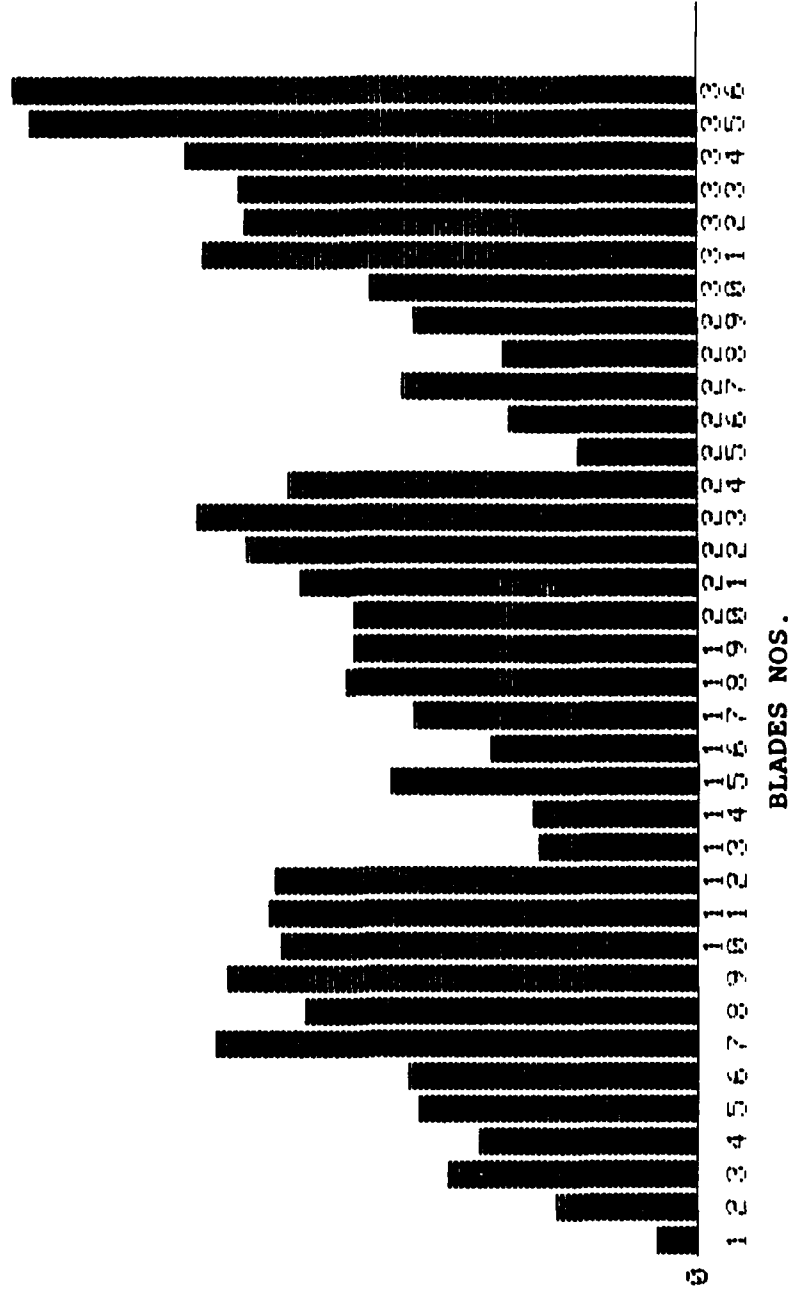
Figure 43.   Count Values Vs. NUmber of Blades Display of the UDRI NSMS.

116

Station-2   98 Hz   764 RPM
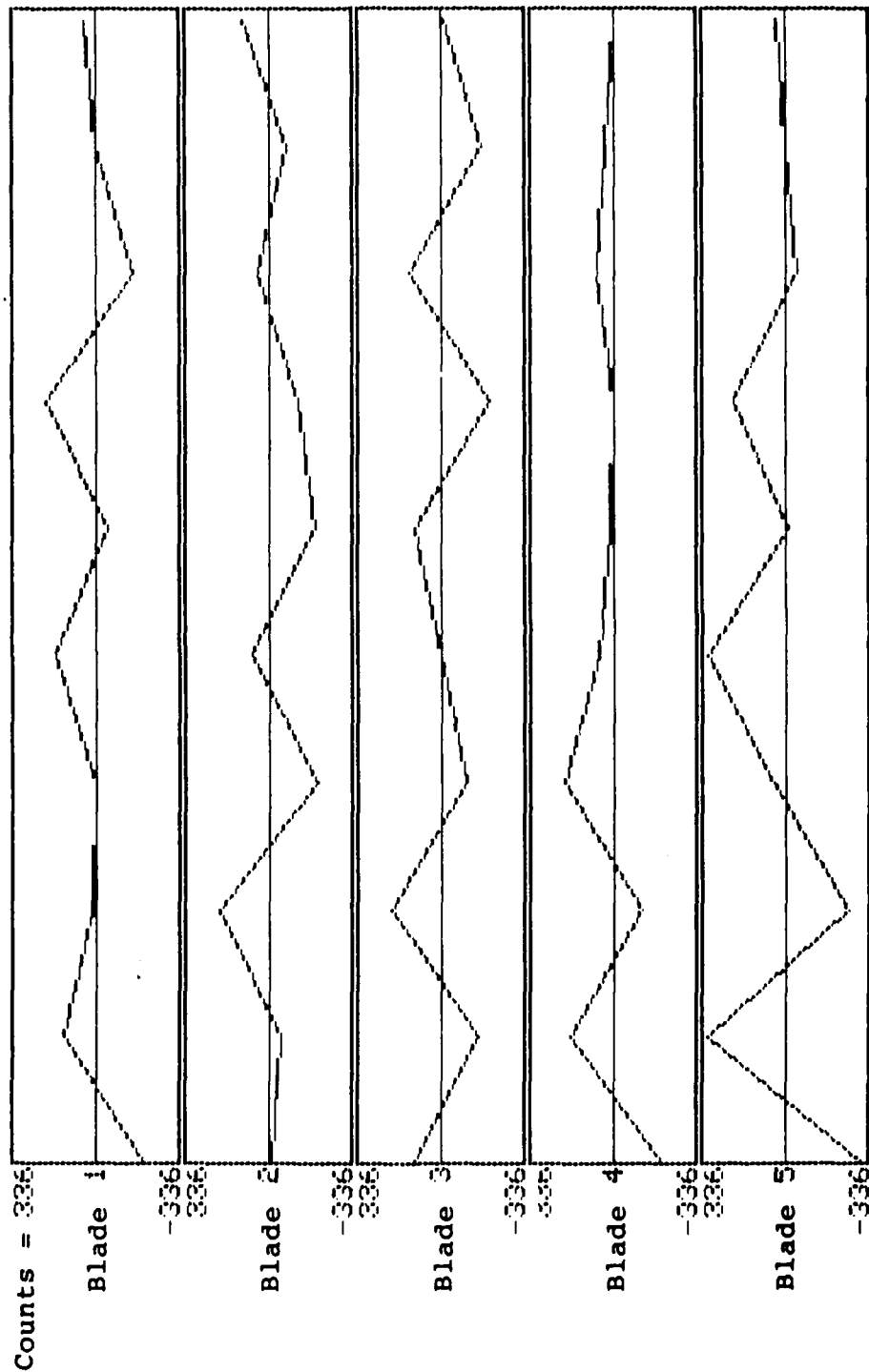
Figure 44. Real Time Display of Blade Deflection from NSMS.

117

SECTION V
Z-GRID INSTRUMENTATION DEVELOPMENT

In view of the objective of this technical program, we also developed a nonintrusive, frequency modulated (FM) vibration measurement system and evaluated its performance at ISRL. The basic concept involved in this technique was that a miniature permanent magnet mounted at the tip of a rotating and vibrating turbine or compressor blade would modulate a carrier frequency of a case mounted stationary grid, and the subsequent demodulation and integration provided a signal which was proportional to the vibratory motion of the blade. The proposed technique had a good potential for application in real engine systems in operating conditions. Therefore, UDRI pursued this technique and designed an FM technique to demonstrate the process under laboratory conditions. The following paragraphs describe various phases of grid wire development and its application for measuring blade vibrations.

The first phase involved the tasks of selection of a suitable permanent magnet, the design, fabrication and evaluation of a single channel FM-grid to generate acceptable signal level. The next phase involved the design and testing of a two-channel FM system for measuring two components of vibratory motion of an instrumented blade and comparing the results with those of an array of fiber optic plane-of-light sensors.

5.1 PRINCIPLE OF OPERATION OF THE GRIDWIRE SYSTEM

The basic principle of operation of the proposed frequency modulated system and its implementation to measure the vibratory motion of a blade in the laboratory conditions are explained here. A conductive wire grid was firmly embedded in the casing wall, and the grid was laid out in the form of an evenly pitched square wave. A permanent magnet such as Samarium Cobalt buried in the tip of a rotating blade generated an electromagnetic force (emf) in the stationary grid circuit each time it crossed a bar of the grid.

GRID 1

GRID 2

$R_i=3.5$"

$R=3.75$"

$R_o=4.0$"

$R=4.75$"

$R_o=5.0$"

$R_i=4.5$"

T_1

T_2

———·———·——— Path of Magnet
T_1 Terminals for Grid 1
T_2 Terminals for Grid 2
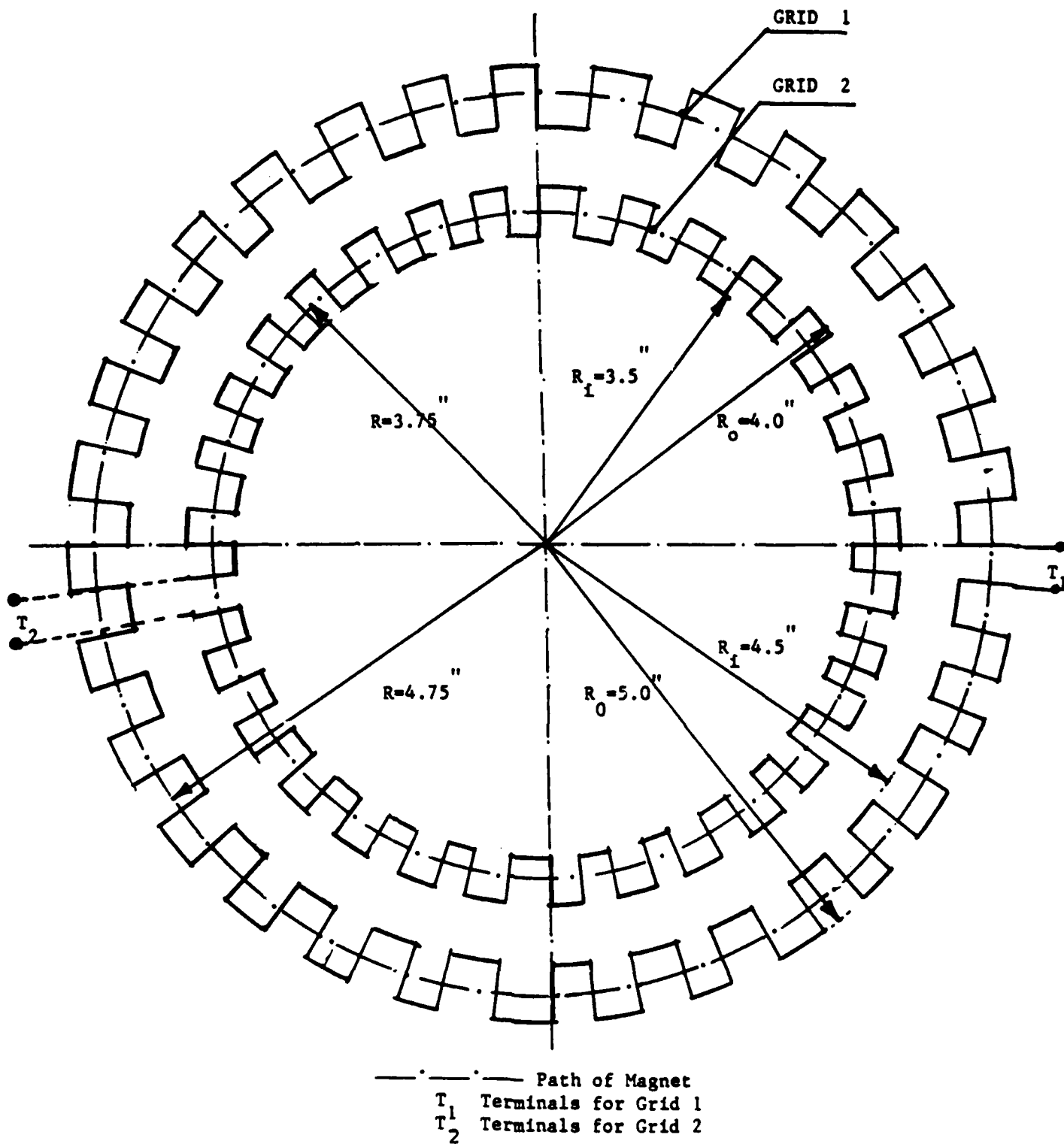
Figure 46. Two Square-Grid Wire Layout.

121

Several runs were made for each grid, with different air gap separations between the grid and the magnet. In all these experiments, the aluminum disk carrying the magnet was positioned parallel to the stationary wooden disk with grids. The magnet swept past the grid wires with constant velocity. The disk was run at several speeds and the output terminals were directly connected to an oscilloscope. Amplitude and frequency of the resulting signals were read off the oscilloscope screen. Results are presented in Tables 20 through 23 and also in graphical form in Figures 47 and 48. These graphs show the dependence of the output signals on the variables of speed of rotation (velocity) and gap between the magnet and grid.

The observed output signals were clean at all speeds. Flats between pulses were more obvious for the Grid 1 whose circumferential spacing was large (0.51 inch) compared to the magnet size (0.25 inch). Figure 49 shows a gradual increase in quality output signal level with the increase in rotational speed. Output signal levels of 2.5 mV when the magnet was separated by a distance of 10 mm from the grid wires was considered adequate for further signal processing.

We have also studied the grid emf signals from a partial grid loop installed in a 12.4-inch-inner-diameter instrumentation ring. Two 1/4 x 1/8-inch-square super magnets were installed on opposite blades of the 0.065-inch-thick, 38-bladed, 11-inch-diameter test disk which was installed in the spin test setup. We mounted the 12.4-inch ID grid support ring eccentrically to the magnet spin circle with various clearances to the 12 grid wires as shown in Figure 50. The test disk then was spun at speeds up to 4,200 rpm. The voltage signals generated in the test grid at speeds of 3,600 and 4,200 rpm for the passage of the strongest of the two magnets past the grid are shown in Figure 51. The minimum pulse amplitudes of 35 to 45 millivolts and the pulse shapes certainly were amenable to recording of the pulse peak occurrence times on the NSMS instrumentation system.

TABLE 20
GRID WIRE SIGNAL OUTPUT FROM GRID 1 WITH GAP 1

Grid Details: Inner Radius = 4.5"; Outer Radius = 5.0"
                     Number of Grid Wires = 58; Gage No. 26

Magnet Details: Dia. = 1/4"; Length - 1/8"; Path Radius = 4.75"

Gap between magnet tip and grid

4mm

3mm

Left Window

5mm
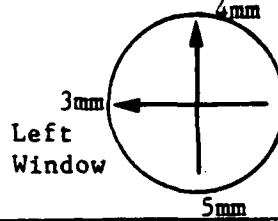
Speed (rpm)	Signal Output (mV)	Comments
200	10.0	Triangular pulses with flats in between
400	15.0	Triangular pulses with flats in between
600	17.5	Triangular pulses with flats in between
800	20.0	Triangular pulses with flats in between
1000	25.0	Triangular pulses with flats in between
1200	26.0	Triangular pulses with flats in between
1400	30.0	Beating of Signals
1600	35.0	-
2000	40.0	Noisy
2400	47.5	-
3000	50.0	Beating of Signals

TABLE 21
GRID WIRE SIGNAL OUTPUT FROM GRID 1 WITH GAP 2

Grid Details: Inner Radius = 4.5";   Outer Radius = 5.0"
                     Number of Grid Wires = 58;   Gage No. 26

Magnet Details: Dia. = 1/4"; Length - 1/8";   Path Radius = 4.75"

Gap between magnet tip
and grid

Left 5 mm
Window

5 mm (top)

8 mm
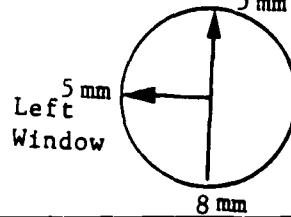
Speed (rpm)	Signal Output (mV)	Comments
200	7.5	Triangular pulses with flats in between
400	10.0	Triangular pulses with flats in between
800	12.0	Triangular pulses with flats in between
1200	15.0	Beating of Signals
1600	17.0	-
2000	20.0	-

124

TABLE 22
SIGNAL OUTPUT FROM GRID 1 WITH GAP 3

Grid Details: Inner Radius = 4.5";   Outer Radius = 5.0"
                  Number of Grid Wires = 58;   Gage No. 26

Magnet Details: Dia. = 1/4";   Length - 1/8";   Path Radius = 4.75"

Gap between magnet tip
and grid
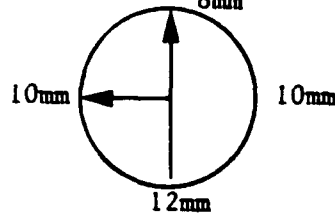
Speed (rpm)	Signal Output (mV)	Comments
200	2.5	Less Triangularity in pulses and with less flats between them.
400	7.5	Less Triangularity in pulses and with less flats between them.
800	10.0	Less Triangularity in pulses and with less flats between them.
1200	12.0	Less Triangularity in pulses and with less flats between them.
1600	15.0	Less Triangularity in pulses and with less flats between them.
2000	16.0	Less Triangularity in pulses and with less flats between them.

TABLE 23
SIGNAL OUTPUT FROM GRID 2

Grid Details: Inner Radius = 3.5";   Outer Radius = 4.0"
                      Number of Grid Wires = 58;   Gage No. 26

Magnet Details: Dia. = 1/8";   Length - 1/8";   Path Radius = 3.75"

Gap between magnet tip
and grid

4 mm

3mm

Left
Window

5 mm
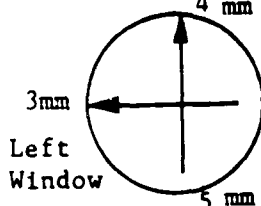
Speed (rpm)	Signal Output (mV)	Comments
200	7.5	Triangular pulses with less flats in between
400	8.0	Triangular pulses with less flats in between
800	10.0	Triangular pulses with less flats in between
1200	15.0	Triangular pulses with less flats in between
1600	17.0	Triangular pulses with less flats in between
2000	20.0	Triangular pulses with less flats in between
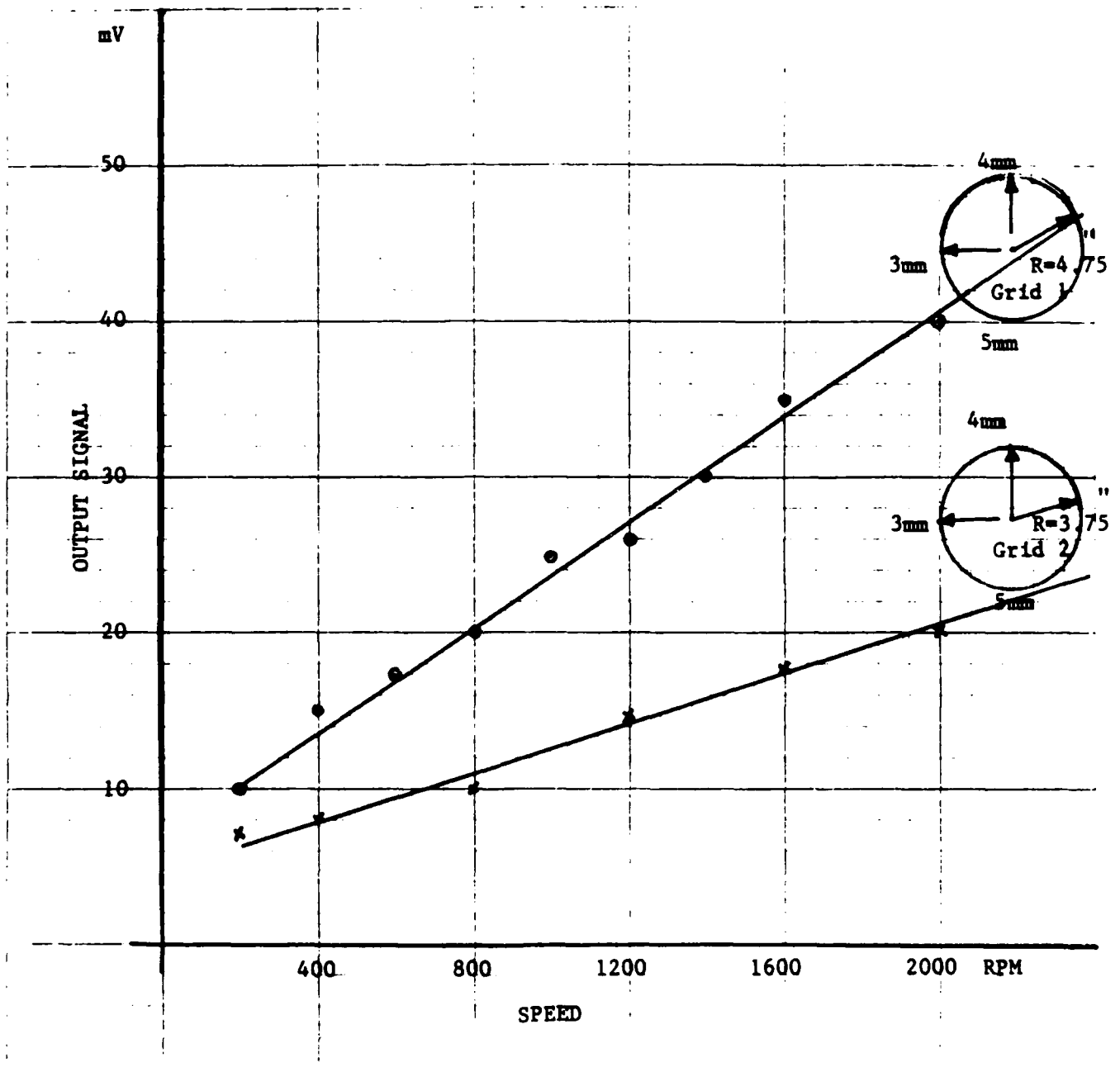
Figure 47. Grid Wire Signal Growth with Speed
and Radial Position.

127
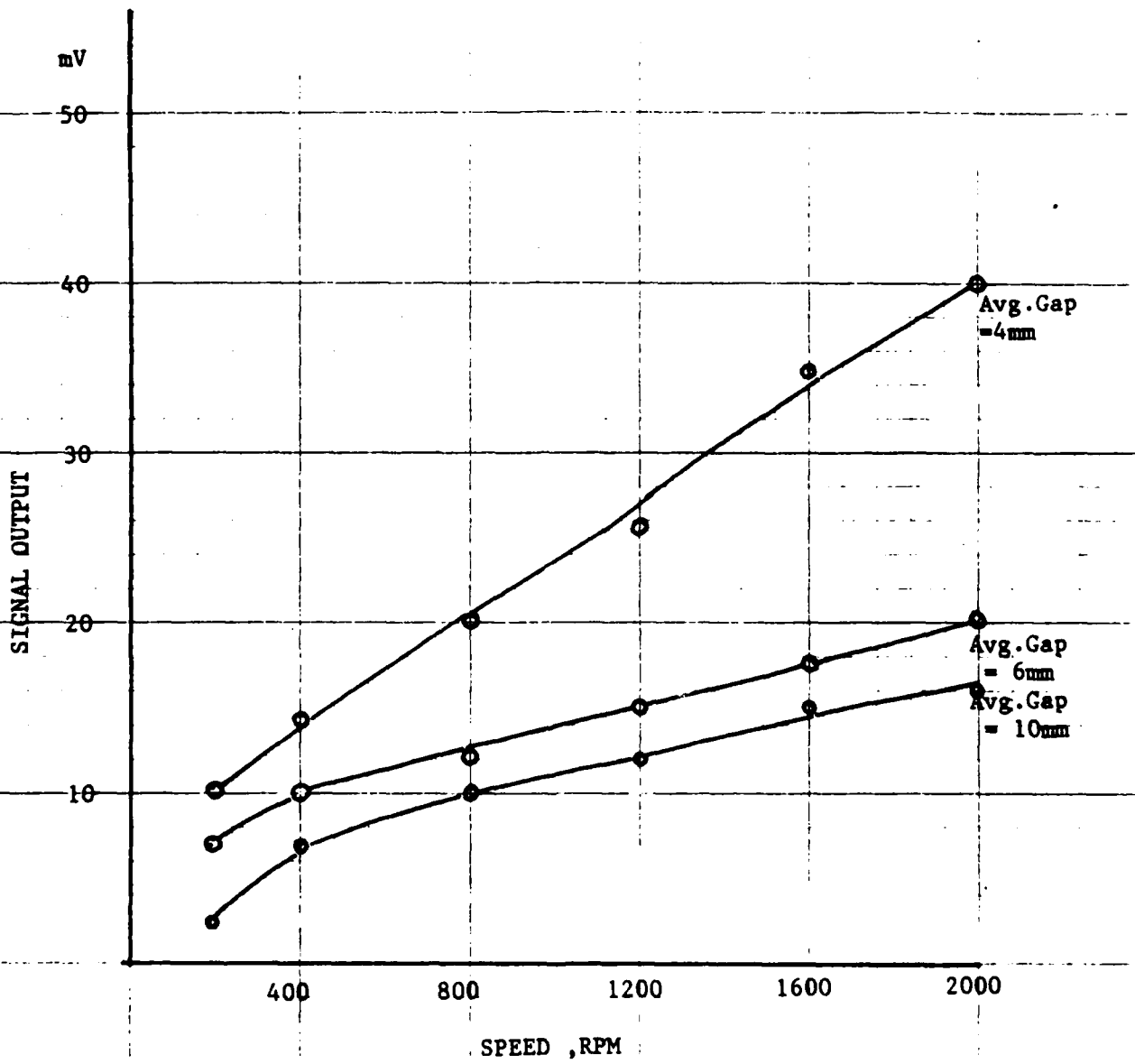
Figure 48. Grid Wire Signal Growth with Speed and Gap.
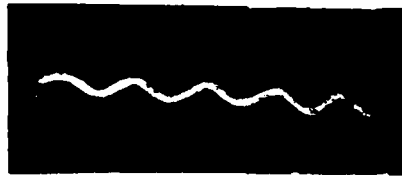
200 RPM
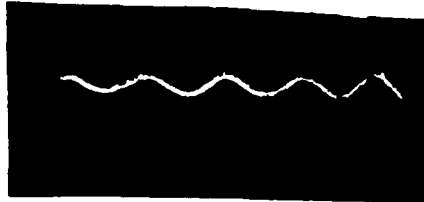
400 RPM
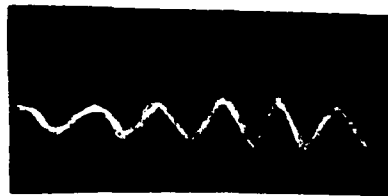
800 RPM

Figure 49. Growth of Output Signal with Speed.

Figure 50.   Grid Wire with Varying Magnet Gaps.

12.4" ID Grid Support
Ring Mounted Eccentrically
To Axis of Rotation of
11.0" OD Bladed Disk

Two Rare Earth Supermagnets
1/8" Squqre x 1/4" Long
Bonded to Blades 10 and 29
To Extend 1/10" from Blade
Tips
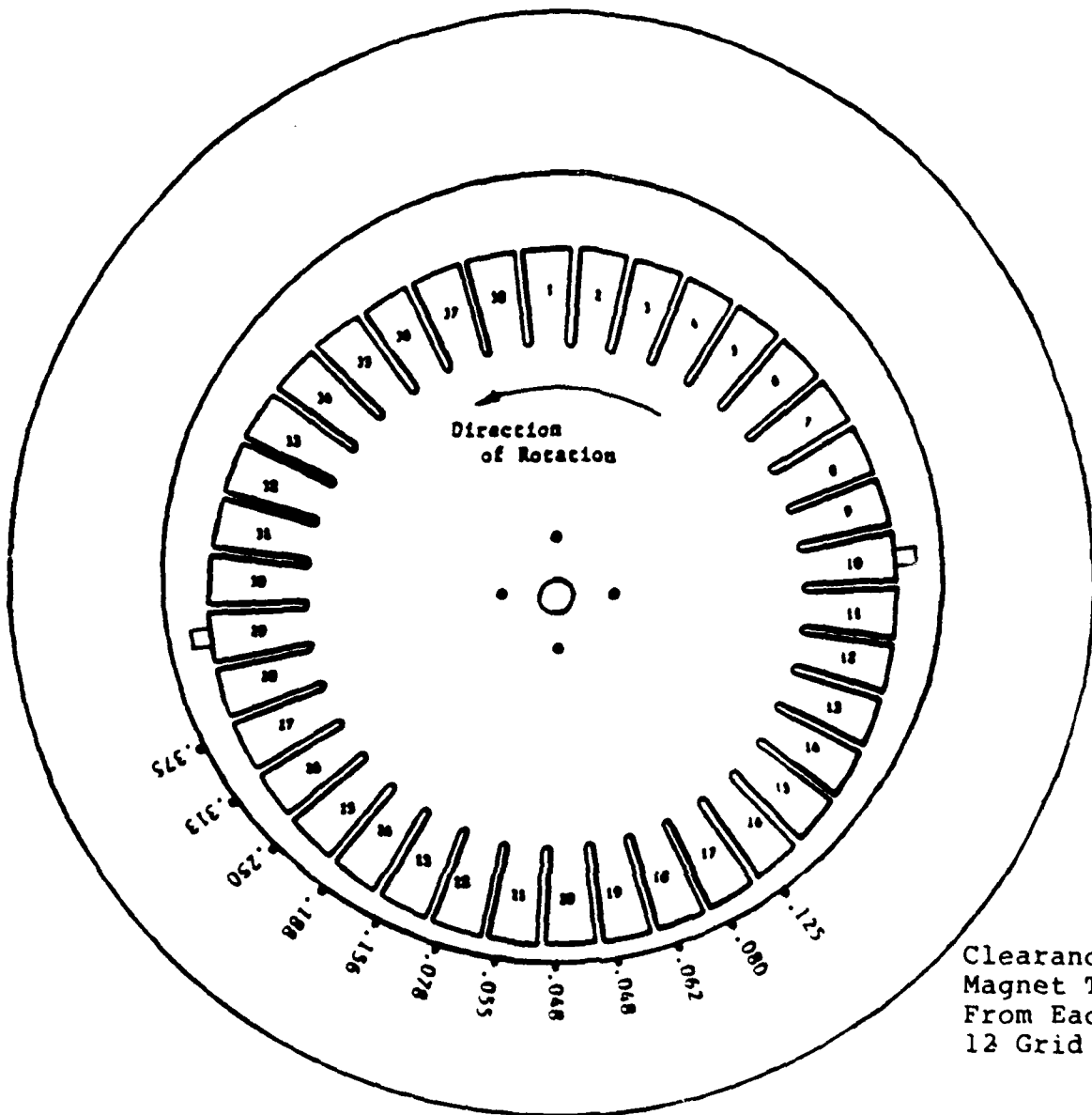
Clearances of
Magnet Tips
From Each of
12 Grid Wires
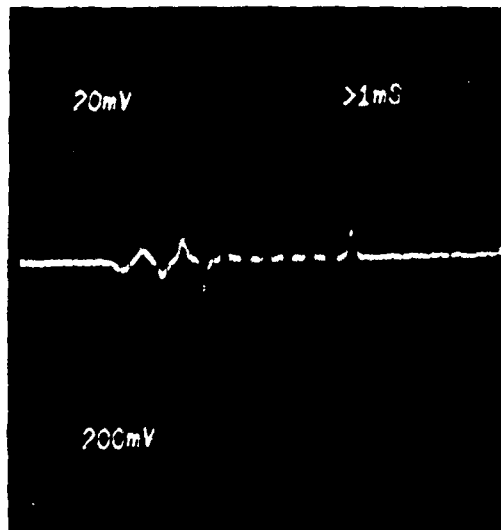
3,600 rpm
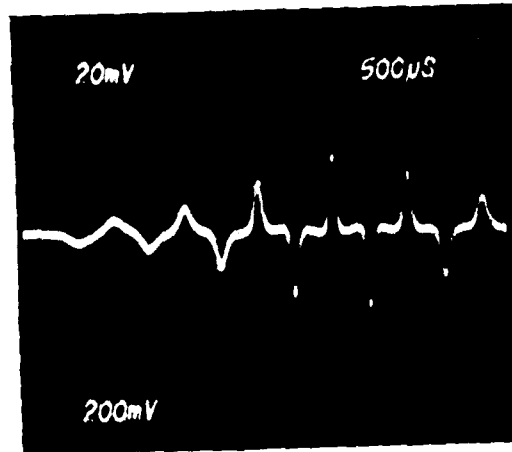
4,200 rpm

Figure 51. Oscilloscope Display of Eccentric Grid Wire Signals.

A ring with 36 grid wires described in the next section was supported symmetrically around the ISRL test shaft spin axis by bolting it to the optical probe supporting. A source magnet and counter weight were mounted to the tips of two diametically opposite blades on an 11-inch-diameter disk as shown in Figure 52. The test disk was installed on the drive shaft in axial alignment with the center of the grid system ring. The two grid system signal leads then wired to a dual channel oscilloscope.

The resulting pulse trains from the two grids as displayed on the oscilloscope screen were shown in Figure 53. The regularity of the pulse amplitude and pulse intervals for a spin speed of 4,000 rpm with a magnet-grid gap of 0.060 inch was extremely good. Signal amplitude was adequate, and there was no mutual interference contamination of the two grid signals. The pulse arrival times were resolved by the ISRL NSMS since the signal trace widths were due to trace blooming in the screen phosphors, as expected, and not due to high frequency noise.

5.3 DESIGN OF THE DUAL Z-GRID SYSTEM

5.3.1 Z-Grid Support Ring

As a result of preliminary investigation on grid signals, a grid support ring was designed for use with an 11-inch-diameter disk. Two orthogonally crossed grid wires (30 AWG) at 45° to the rotational axis of the disk were used to resolve both horizontal and axial components of an instrumented blade vibration. These dual grid wires overlaid in the letter form Z (hence, Z-Grid system) were insulated and wound around the inner diametral surface of a support ring. The geometry and the layout of the dual grid wire system and its support ring are shown in Figure 54. The grid support ring with thirty-six 30-mil-deep grooves to accommodate the conducting grid wires fabricated from polypropylene material was coaxially installed with the test disk. Thirty-six grids for each of the two grid loops were used to resolve at least nine modes of a rotating disk with sufficient accuracy.

132
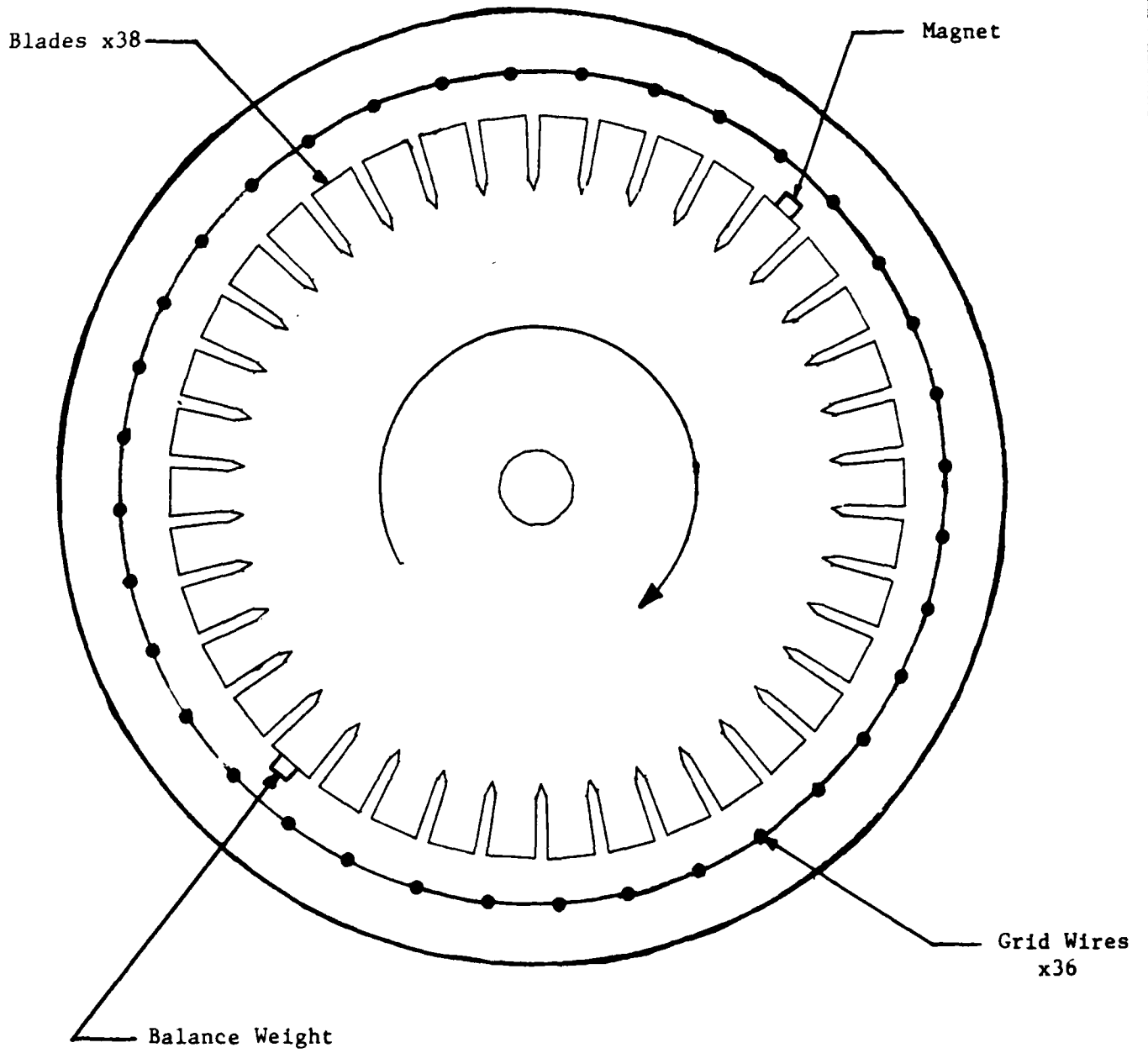
Figure 52. Source Magnet on One of 38 Blades on Concentric
Disk with Wire Grid.
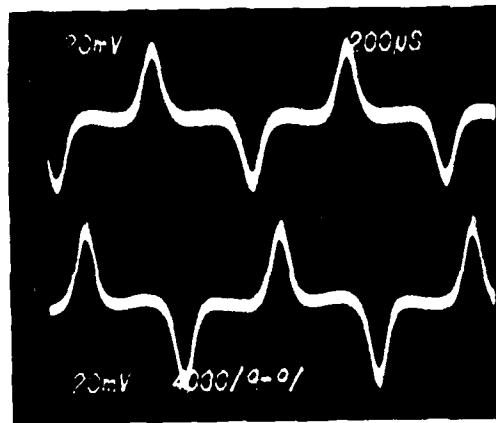
Figure 53. EMF Pulse Train for Concentric Wire Grids.

$\frac{13}{64}$ Clnc. for $\frac{3}{16}$ Bolt-4 places @ 90°on 15.0" D.

B

B

16.0 D

11.300 D
$\pm$.005

A

15.0 D

A

A

1.000$\pm$.003

16.0 D

11.300 D

GROOVE ID CORNERS
45°X 0.050$\pm$0.010 DEEP

VIEW   A-A

36 Eq Spcs @ 10 around ID

10°   10°   0.986
REF.

6 Thru Slots
at 2, 5, 6,
8, 10, & 14
Grid Centers

at
45°
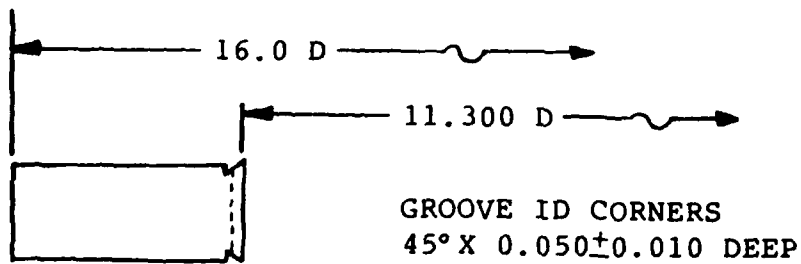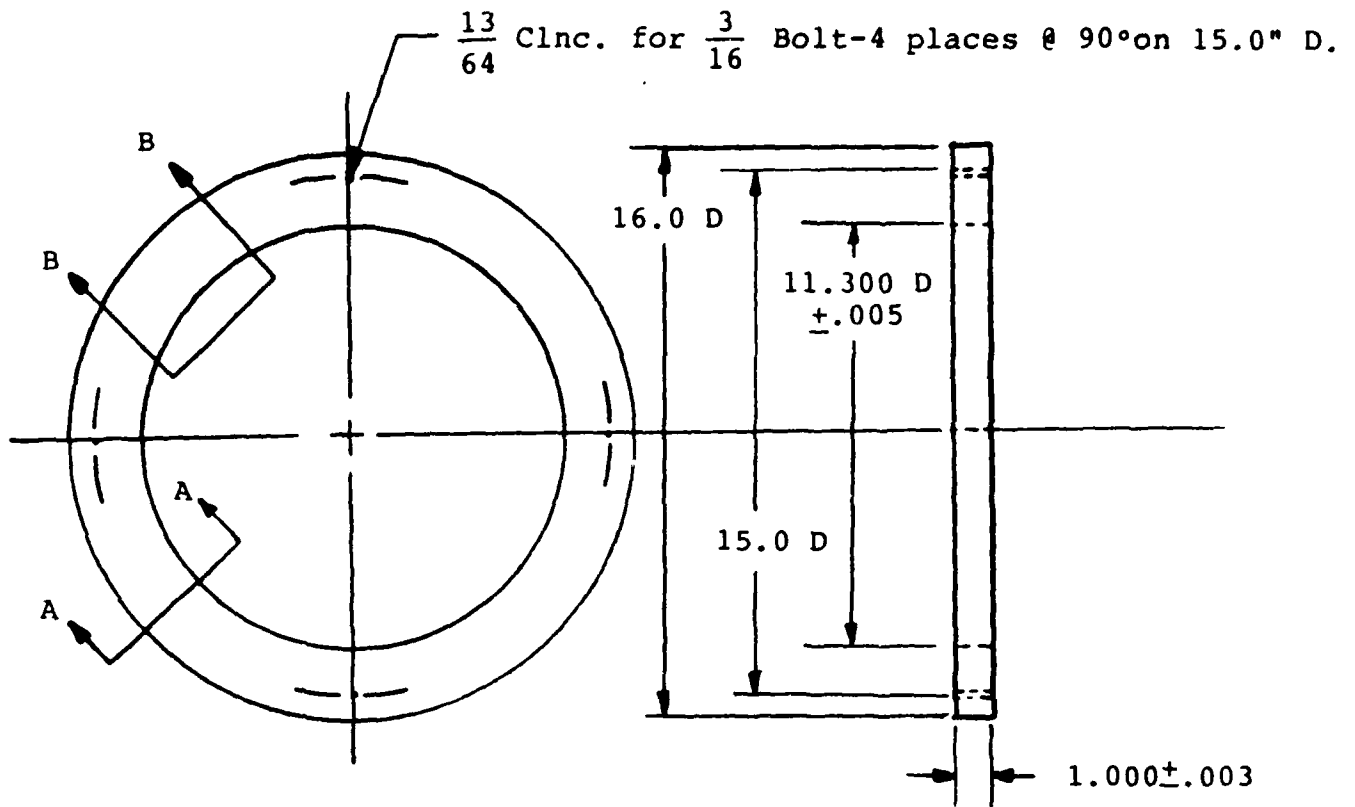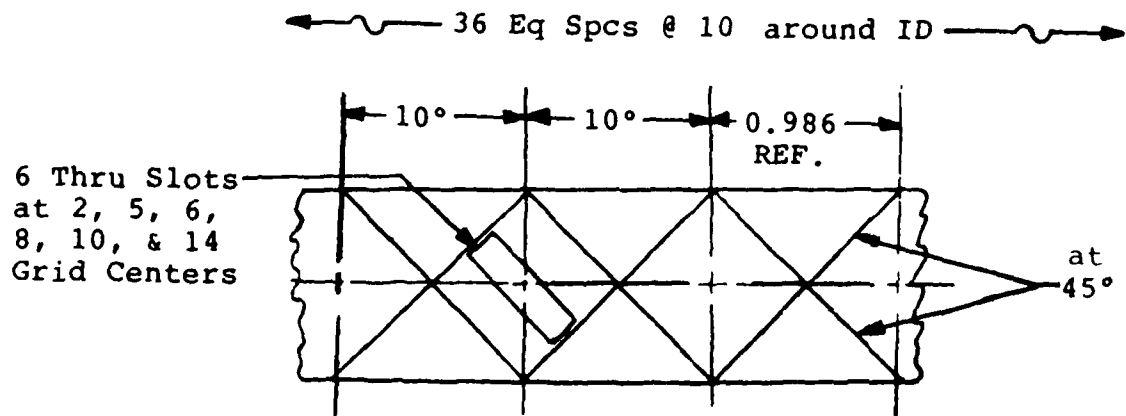
VIEW   B-B

All Dimensions are given in inches

Figure 54.   Z-Grid Support Ring and the Grid Layout.

135

5.3.2 Digital Design of the Grid Wire System

The optical pulse train due to the reflections off the blade tips in the optical system and the emf bipolar pulse train due to a source magnet in the Z-grid system had similar digital characteristics. Both signals after referring to the 1 PPR signal will yield differential time measurements for a specific blade. This differential time measurement was a direct measure of blade tip deflection in the optical and Z-Grid systems. This measurement-similarity in both systems prompted us to design a digital Z-Grid system for measuring blade tip deflections of a rotating disk. Instead of analog demodulation of the grid signals as was done by the Rolls Royce Company, UDRI designed a digital system for the grid signal demodulation. This step allowed us to use the existing optical (NSMS) data acquisition and data storage hardware. UDRI developed speed compensation algorithm, digital time-series, and Fast Fourier Transform analysis also were used effectively with minimum cost and time.

However, the following modifications had to be incorporated into the Z-Grid system electronics to make it compatible to the optical system. First, bipolar grid signals had been converted to monopolar pulse train. These signals were then amplified and filtered by a bank of filters, by an electronic signal conditioning arrangement as shown in Figure 55.

5.4 Z-GRID SYSTEM ELECTRONICS

The Z-Grid signal processing system was designed to process two frequency modulated waveforms. These waveforms were generated by the motion of a magnet mounted on one rotating turbine blade, past two wire grid rings. The individual conductors of the two grids were insulated from each other and crossed orthogonally. The rotation of the blade produced variable phase differences between the two FM signals, dependent on the location of the magnet as it passes under the series of paired conductors of the grid. The signal processing system processed these waveforms and generated pulses corresponding to the peaks of the input waveforms. These

136
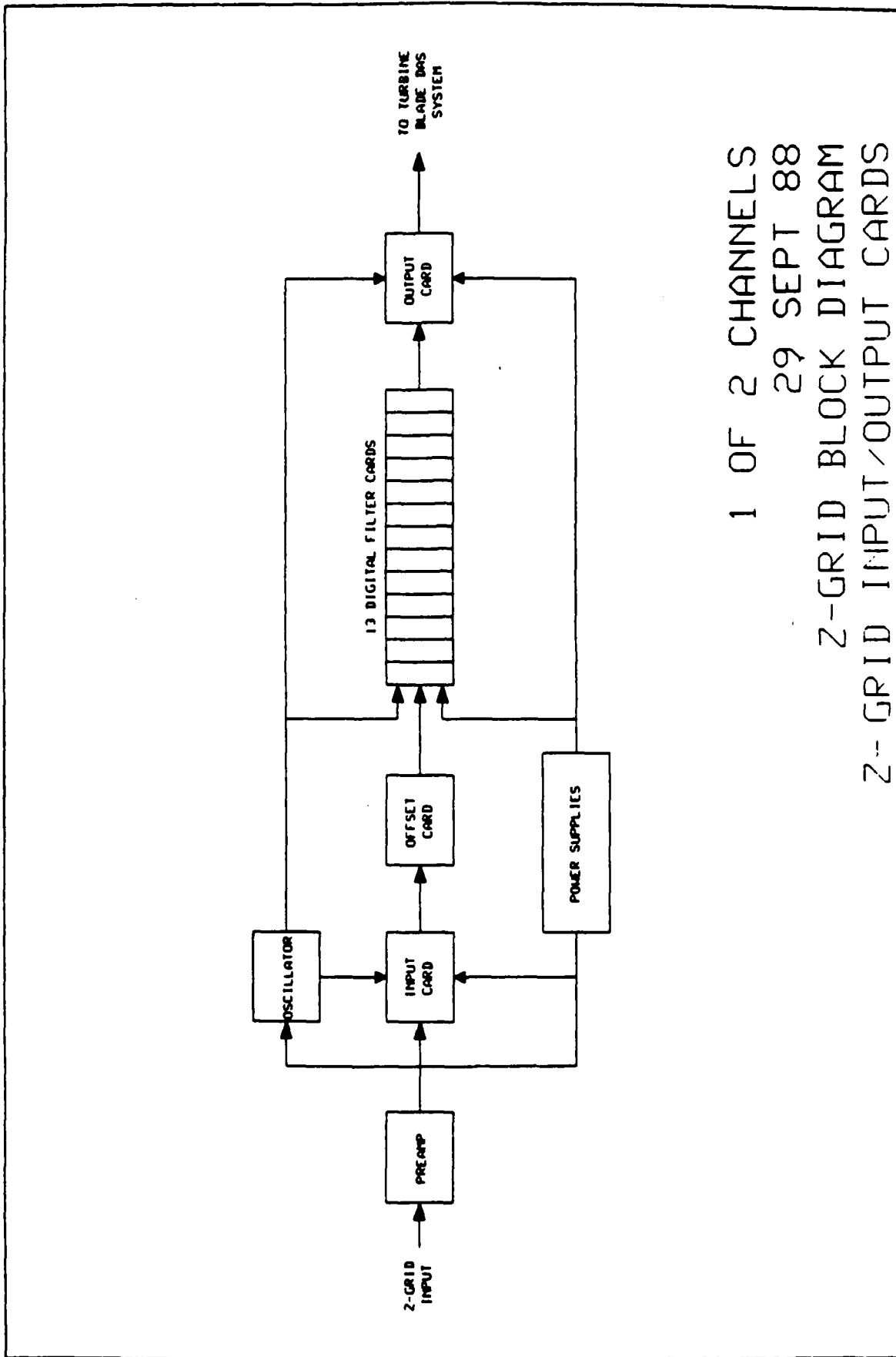
1 OF 2 CHANNELS
29 SEPT 88
Z-GRID BLOCK DIAGRAM
Z-GRID INPUT/OUTPUT CARDS

Figure 55. Z-Grid Signal Conditioning Arrangement.

pulses drive a light emitting diode (LED) for each of the two channels. The LEDs replace two of the fiber-optic bundles on the NSMS Data Acquisition System. The data were then acquired similar to that of plane-of-light sensor method.

5.4.1 System Connections

The Z-Grid signal processing system hardware consisted of two combination power supply - signal conditioning units, one for each of the two grid wire circuits. After mounting these units in the vibration-instrumentation rack of the ISRL rotating test rig, two grid wire circuits and the digital hardware were connected, because this system was designed to be used in conjunction with the NSMS data acquisition system. A BNC cable from the grids to the preamplifiers for the signal conditioning system was connected. The data acquisition block diagram for the digital Z-Grid system is illustrated in Figure 56.

5.4.2 System Operation

The operation of the Z-Grid signal processing system was designed to be transparent to the user of the NSMS System. All procedures for operating the system were identical to those of NSMS except setting the number of blades equal to 36, where the number 36 was equal to the number of grid wires in the dual grid rings. The output display for both channels can be accessed in the same way as in NSMS. A typical histogram for one of the Z-Grid channels is shown in Figure 57. This histogram resembled the optical system histogram except for the number of blades on the abscissa.

Two adjustments on the Z-Grid signal processing system were the preamp level and the time delay adjustment. These were adjusted when a new speed was used or the configuration of the system was changed.

The preamp level was adjusted while the system was running for an output level between one-half and one volt, and this was achieved by using a specific potentiometer on the preamp board. At present the Z-Grid signal conditioning system was set to process

138
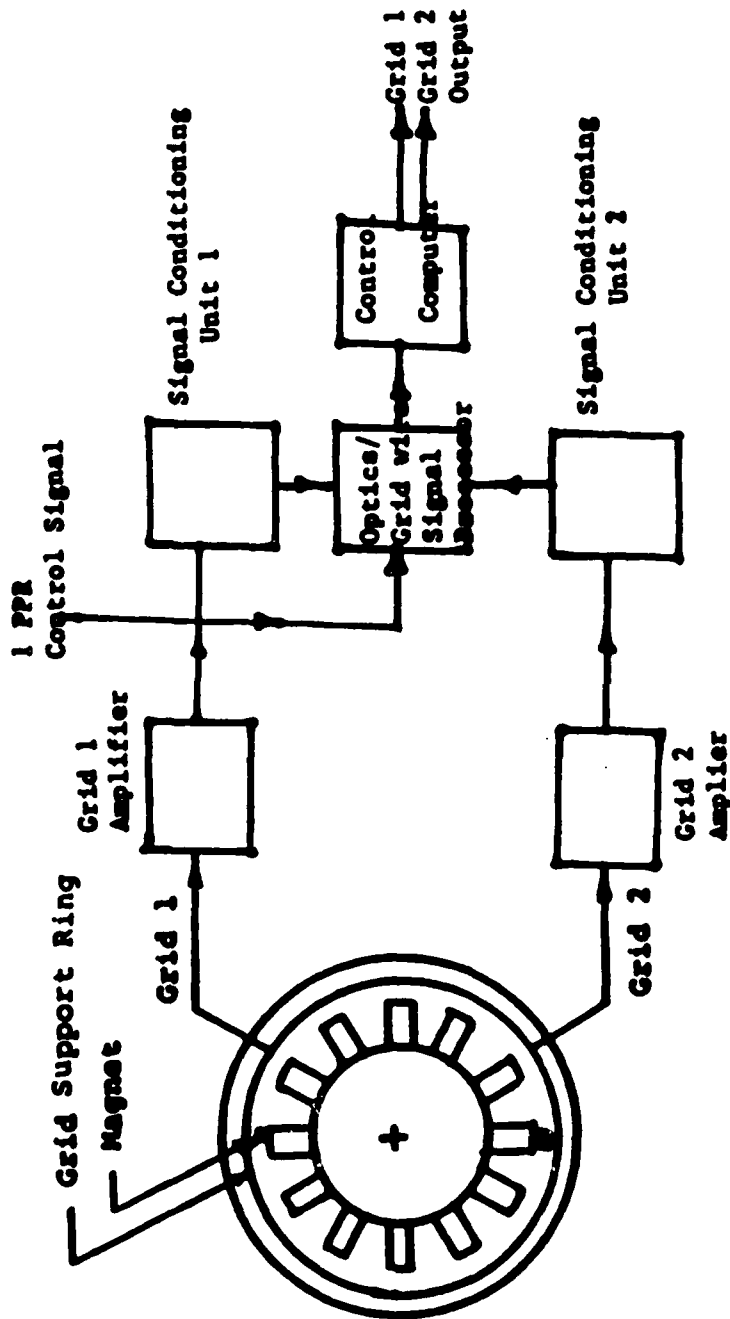
Figure 56.   Data Acquisition Block Diagram for the
Digital Z-Grid System.

139

Station-3   Hz   3671 RPM   8-Nov-88   09:08:16

117
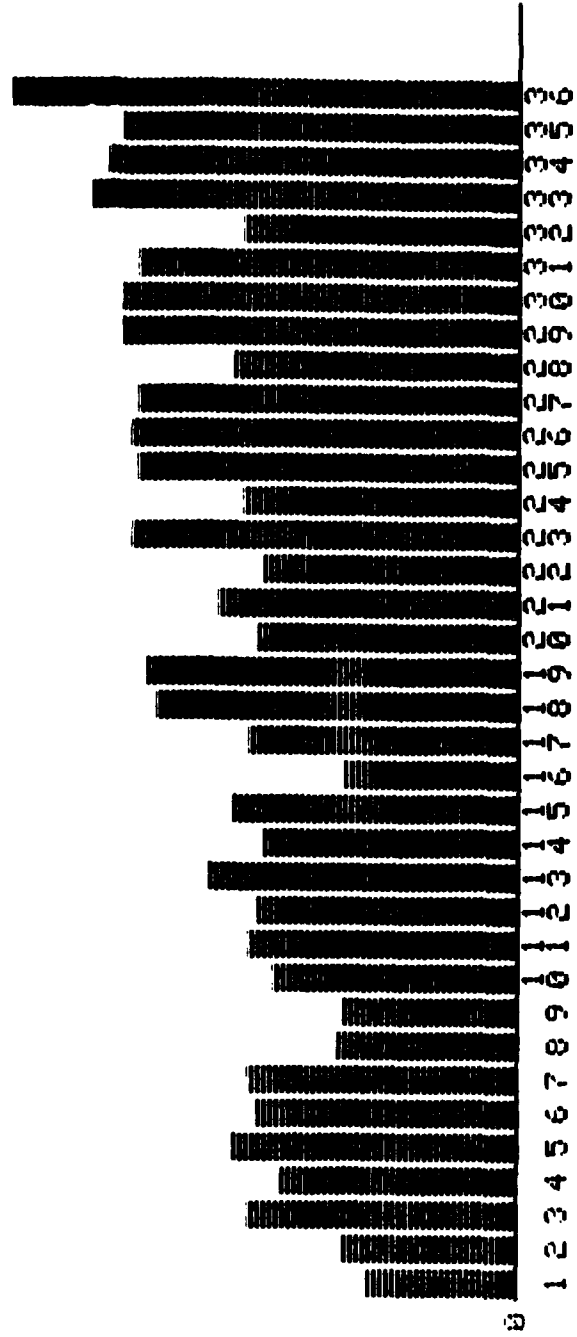
Figure 57.   Z-Grid Histogram Display for One of the Two Channels.

data for the speed range of 1,000-6,000 rpm. It was possible, however, to change these settings for other test speeds.

The first method of setting the delay was to set the switches based on a given speed. Using this method, we located the speed to run the turbine in the RPM column and set the dip switches on the output card using the binary switch column of the chart. The second method was to set the switches for a given delay time. The relationship between the grid input and LED output signals is shown in Figure 58. The delay time that triggers the generation of LED input pulses of the grid wire emf signal peak had to be set so that the output pulse fell within the period labeled ΔT. We needed to ensure that the delay time was not so short that the output pulse occurred within the same input waveform, nor so long that the output pulse occurred during the next input waveform.

The Z-Grid system design, electronics, operation, and diagnostic checks were fully described in Reference (4).
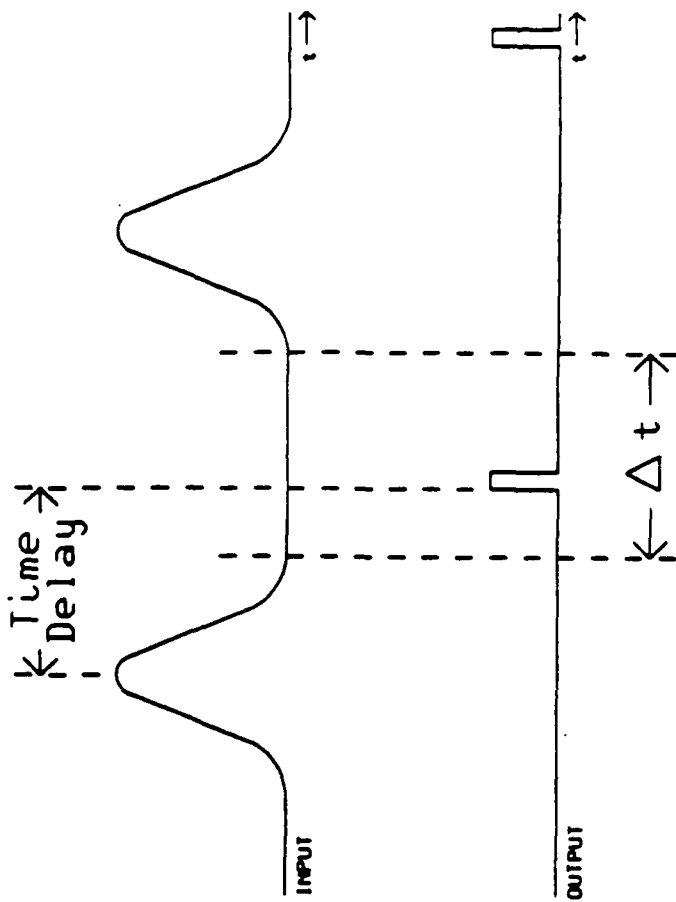
Figure 58. Grid Wire EMF and LED Output Signal Relationship.

142

SECTION VI
NSMS BLADE DEFLECTION DATA REDUCTION AND ANALYSIS

UDRI developed a set of data analysis programs to extract the deflection and frequency information from the data generated by the two noncontacting blade deflection measurement systems discussed earlier. The four-channel plane-of-light system provided vibratory data for all blades of a rotating bladed disk at a specific sensor location while the dual Z-Grid system provided similar dynamic data for one blade over the entire revolution. Both data sets are processed by the UDRI algorithms. Both systems acquire the vibration data through a common data acquisition system and stores it on a nine-track magnetic tape. The NSMS data acquisition system is not capable of analyzing the data in real-time; therefore, the data analysis had to be performed in a separate computer system. A set of UDRI developed analysis programs performed the data reduction and analysis tasks on a DEC VAX computer at the ASD Computer Center. The following subsections describe raw data acquisition, data correction for speed variation, dynamic analysis by optical and Z-Grid methods, and the FFT spectra determination of blade tip deflection.

6.1 DATA REDUCTION AND ANALYSIS STEPS

The rotating blade deflection and frequency derivation cycle consists of four major steps (Figure 59):

1) Make data acquisition runs in the laboratory and store the data on a magnetic tape.

2) Store the data tape in the ASD Computer Center tape library and transfer these data on command to ASD VAX disk.

3) Run the appropriate software programs using the test tape data as input and plot blade deflections in time and frequency domains.

4) Archive the data onto the ASD central file system.

1. Make NBDMS data tape

2. Transfer tape data to ASD AWC VAX

3. Run analysis software

6. Archive NBDMS data onto CFS

4. Plot analysis data

5. Print analysis reports
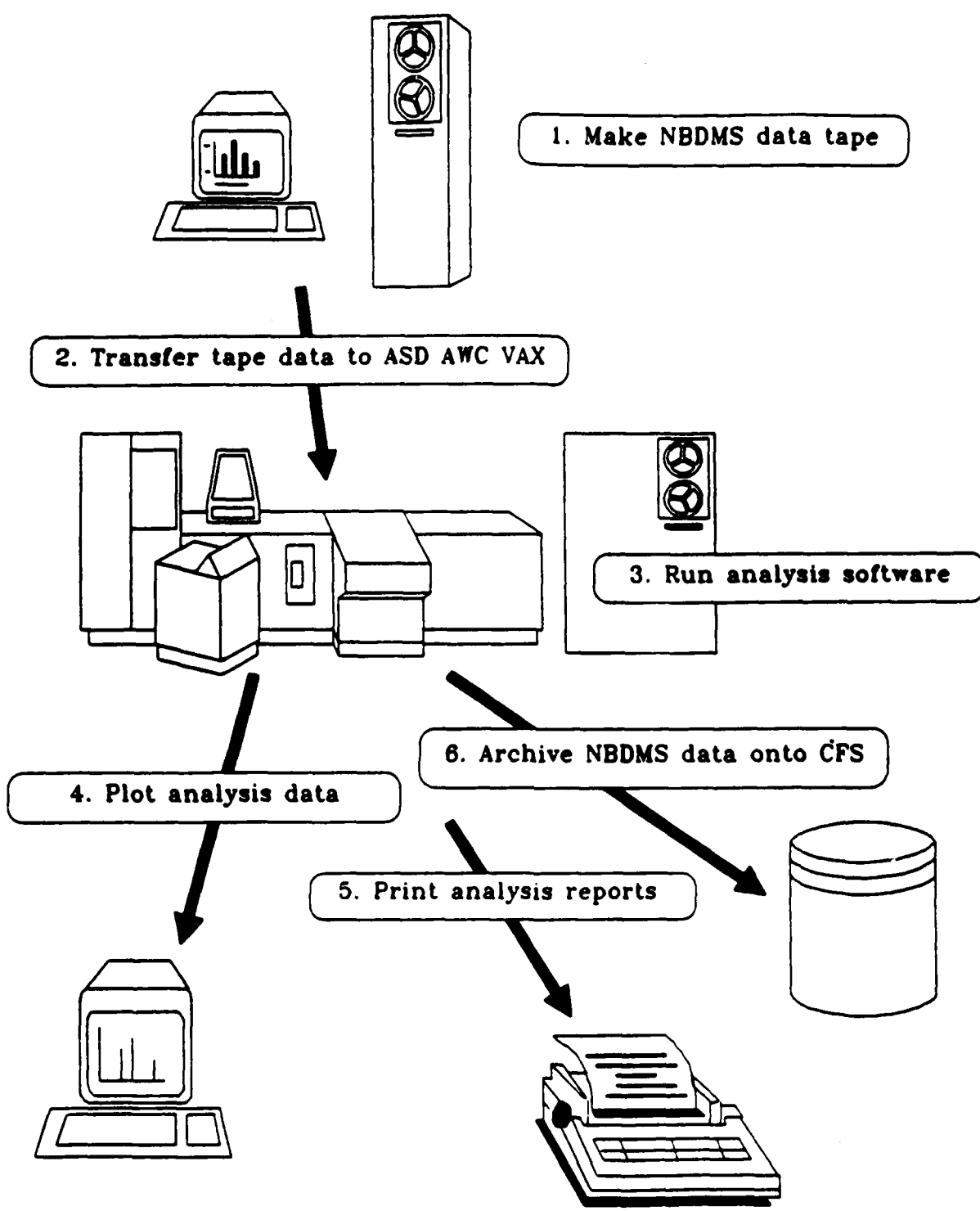
Figure 59.   NSMS/Z-Grid Data Analysis Cycle--Hardware
              Setup.

144

6.2. TEST SHAFT SPEED CORRECTION EFFORTS

Early data runs showed instability in the speed of the test shaft drive motor as well as intermittent inconsistencies. To provide information on the uniformity of the motor speed within a single revolution, a 30 faceted polygon mirror was fastened to the motor shaft. Data were taken on this polygon with the fiber optic plane-of-light sensor. A He-Ne laser served as the light source and the fiber optic plane-of-light sensor was set at approximately one meter from the polygon to produce a 2-microsecond rise-time. Figure 60 shows the installation of the polygon on the test shaft, and Figure 61 shows the setup for making the measurements.

Sets of data were taken on the turbine fan with and without vibration excitation. All data were taken at low speed and with atmospheric pressure in the test chamber. The first sets of data exhibited features which were not well understood. Figure 62 shows two sets of data taken on the 12-bladed fan spinning at 1,150 rpm with no external excitation. These two sets of data show the repeatability of the plane-of-light sensor measurements. Figure 63 shows a data run with the fan spinning at 1,430 rpm. These data sets show a pseudo-displacement measurement which has a frequency of one-fourth of the fan speed at 1,150 rpm and one-fifth of the fan speed at 1,430 rpm. We believed these data showed variations in the test shaft speed, within each revolution, caused by the 16 PPR shaft speed feedback control system. Note that amplitudes were very low for blades 1 and 12. Speed-variation-caused data peaks were minimized on these blades because they were adjacent to the 1 PPR mirror, and all the data readings were normalized by the 1 PPR values. We expected that if these were, in fact, shaft speed changes, as they appeared to be, they would be greatly reduced when higher shaft speed testing was performed.

The optical simulator was set up to provide accurate information for the PMT, electronics, and software. Optical waveforms for both the 1 PPR and 8 blades per revolution were created with a drive circuit and LED light sources. The rise time

145
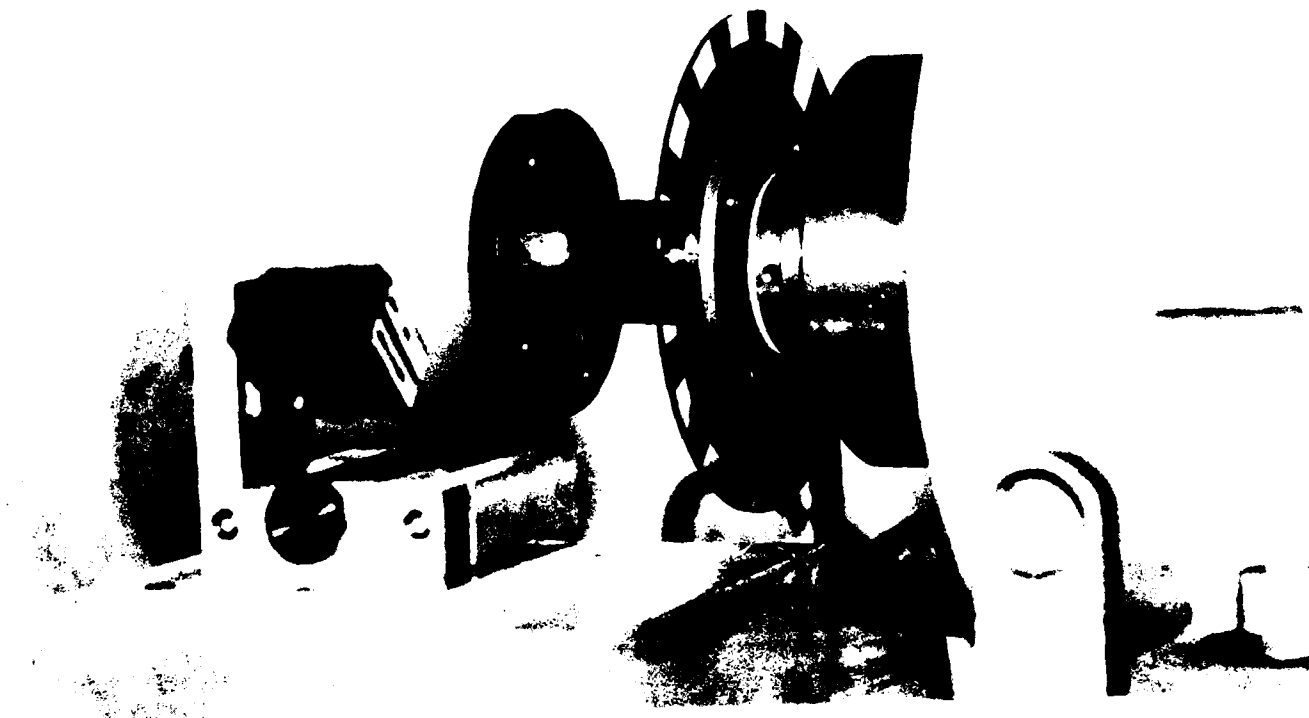
Figure 60. 30 Faceted Polygon for Speed Checkout.

Figure 61. Speed Accuracy Measurement Setup.

LD7:RUN035.DAT
revs plotted = 29
range = 0.914 degree
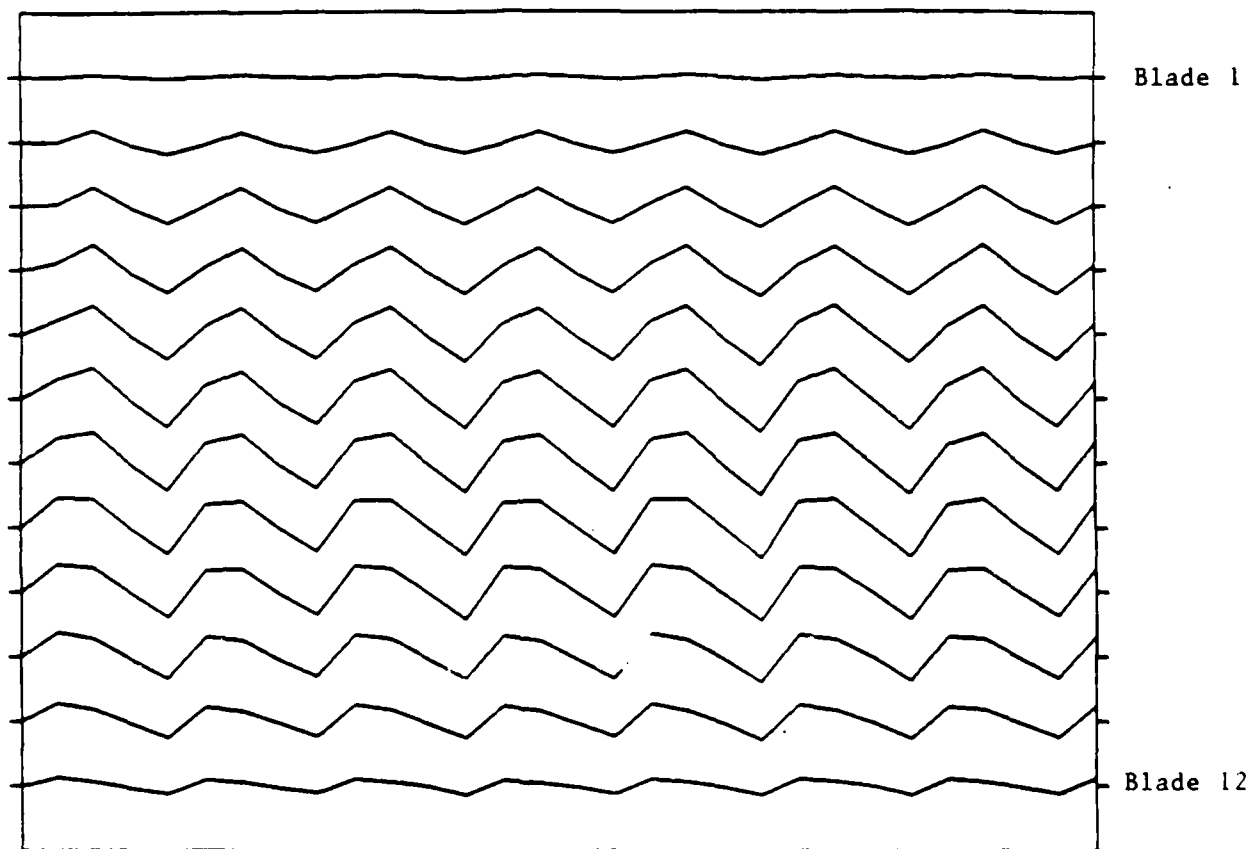
Figure 62.   No Excitation Polygon Data Set at 1,150 rpm.
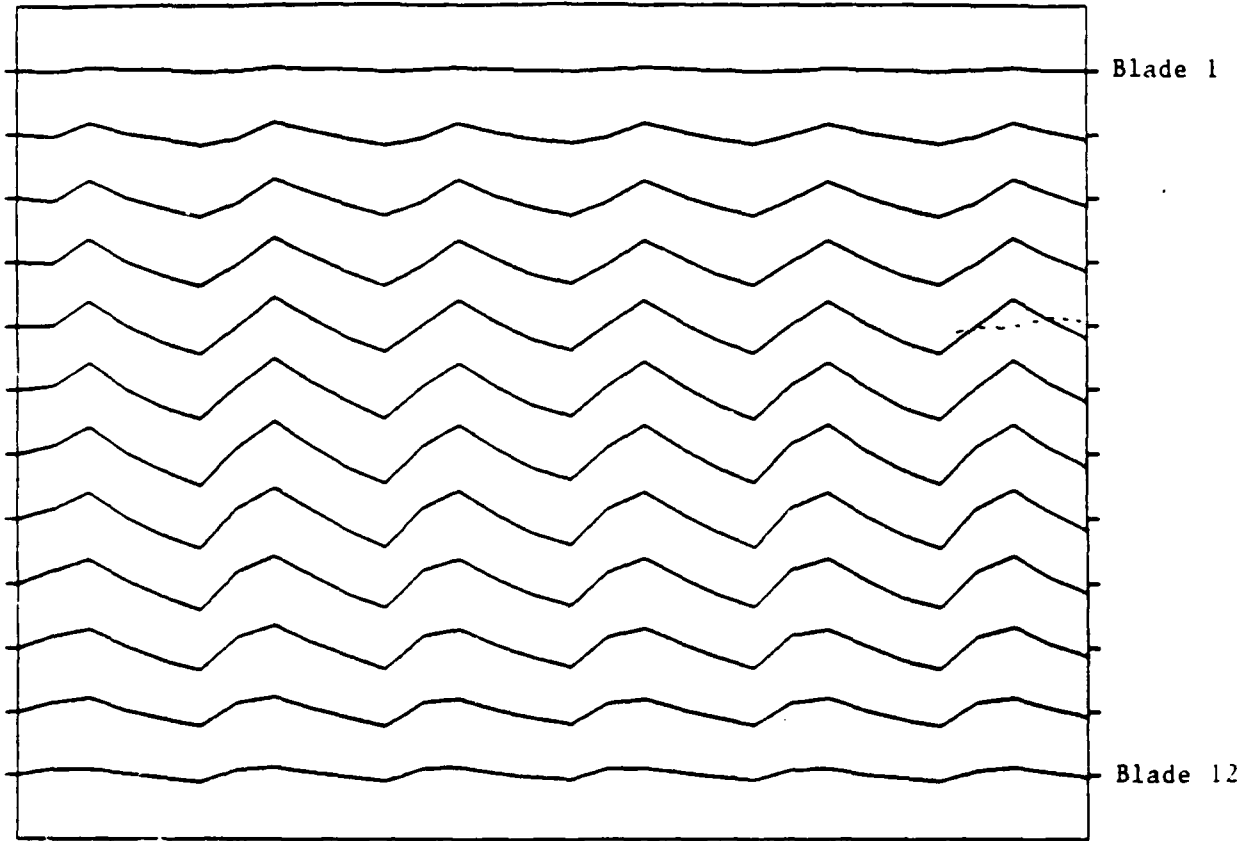
Figure 63. Polygon Data Set at 1,430 rpm with Excitation.

of each optical signal wave form recorded over 100 revolutions period was better than 1 microsecond. The scale has been adjusted to show ± one bit of sensitivity which showed that the PMT electronics and software were all operating at their peak performance.

From several sets of data for 30 revolutions of the polygon at 752, 1,129 and 1,694 rpm, we observed that the velocity uniformity appeared to improve at higher rpm, and the data from the polygon segments nearest the 1 PPR mirror were again minimized by the normalization of the data by the 1 PPR readings.

6.2.1 Test Shaft Speed Variation Improvement Efforts

After identifying speed changes in a single revolution, we diagnosed the controller system operation from the schematics. We made several unsuccessful attempts to replace the controller timer and motor torque control input with a programmed Apple Computer. The level of speed stability achieved was approximately equal to that achieved by the original control system. One thing we achieved was that we discovered that the 16 pulse per rev (16 PPR) shaft speed optical encoder was generating 17 pulses per rev due to a stray piece of tape across one of the 16 windows in the encoder disk. Removal of this tape strip resulted in the system returning to its former mode of operation of running within 1 or 2 rpm of the speed set point for long term average speed but did not solve the problem of short term speed changes.

Inability to solve this speed control problem with what we considered to be a much improved control signal generator led us to evaluate the speed variations of a synchronous motor. For this evaluation, we excited the field coils of a commutator-less dc motor having a four-pole permanent magnet armature with a controllable frequency and controllable voltage ac power supply. This motor showed about the same rev to rev speed variations as the ISRL induction motor system and showed larger speed variations within each rev, probably due to the four-pole armature and a fairly low inertia of the armature and shaft system. It then

149

seemed unlikely that we could improve the test shaft speed stability by replacing the motor-controller system.

6.2.2   Development of Speed Correction Algorithm

Instead of replacing the motor system, we decided to record the 16 PPR signals from the optical shaft position encoder on one channel of our data system. We then devised a method to correct the blade deflection readings through the use of this multipulse per rev shaft position information. Circuitry to accomplish the recording of that signal was designed, fabricated, and installed. The eight test runs completed are listed in Table 24. Figures 64 and 65 show the speed variations for seven consecutive shaft revolutions of Runs 1 and 2 of non-excited 12-bladed test disk at 1,200 and 1,800 rpm, respectively, as indicated by the deviations from their long term means of the shaft 16 PPR and 1 PPR data readings. Constant shaft speed would produce consecutive identical readings (no deviation from the mean) of the pulse series from each shaft position encoder within the accuracy of the encoder and recording system. These two plots show that shaft speed was always changing, that the speed changes were not large, and that the percentage speed changes were larger at 1,200 rpm ($\pm$600 counts out of 500,000 or $\pm$0.12 percent) than at 1,800 rpm ($\pm$300 counts out of 333,333 or $\pm$0.09 percent). The latter would be expected because rotary inertia effects increase as the square of rpm, tending to reduce accelerations of the shaft as revolution speed increases.

Two facts were readily discernible from Figures 64 and 65 when we realized that blade tip deflection data dispersions about their means were generally no greater than half of the 1 PPR readings dispersion. First, no measure of the 1 PPR data could be adequate for correcting the blade data readings. Evidently corrections of individual blade data readings must be made based on on the rotational speed of the particular revolution in question. Second, since revolution speed was constantly changing, as shown by curvature in all the plots of shaft position for individual revolutions, a linear slope correction for each revolution, based on the 1 PPR reading at the end of the revolution, would not

TABLE 24
SPEED CORRECTION TEST RUN OF DETAILS
16 PPR SHAFT ENCODER RECORDED IN CHANNEL 1
VIBRATION MODES STATIONARY ON THE 12-BLADED DISK
375 REVS RECORDED PER RUN

Run #1	1,200 RPM No Excitation
Run #2	1,800 RPM No Excitation
Run #3	1,800 RPM 2D @ 125 Hz Fex = 185 Hz
Run #4	1,800 1D @ 86 Hz Fex = 116 Hz
Run #5	1,800 3D @ 199 Hz Fex = 289 Hz
Run #6	1,200 3D @ 196 Hz Fex = 256 Hz
Run #7	1,200 1 D @ 83 Hz Fex = 103 Hz
Run #8	1,200 2D @ 121 Hz Fex = 161 Hz

Figure 64. Shaft Speed Variations at 1,200 rpm.

152

Figure 65. Shaft Speed Variations at 1,800 rpm.

153

adequately correct the blade deflection readings during most
revolutions. Instead, a correction was required based on the
instantaneous speed error (i.e., shaft position error) when the
data reading was made.

Considering the above, we formulated a correction to
individual blade data readings based on the location of the mean of
each blade data set along the constant speed line defined by the
mean of the 1 PPR data set and the deviation of the shaft speed
from that constant speed line as defined by the 16 shaft position
encoder and 1 PPR reading deviations from their means.

The correction was performed during computer
processing of the recorded data set and is described below:

$$V_{Bik}=(R_{Bik}-M_{Bi})-(R_{SLik}-M_{SLi})+F_i\ (R_{SLik}-M_{SLi})-(R_{SHik}-M_{SHi}) \quad (87)$$

where

> V   = corrected data value
>
> R   = data reading
>
> M   = mean of the data set readings
>
> Bi = Blade number i
>
> k   = rev number k
>
> SLi = shaft encoder position immediately below Bi
>
> SHi = shaft encoder position immediately above Bi
>
> F_i = $\dfrac{MB_i-MSL_i}{MSH_i-MSL_i}$ = interpolation factor for Bi

The factor Fi provided linear interpolation of the shaft speed
readings for the encoder (tachometer) positions last before and
first after each blade mean position (M_{Bi}) along the constant speed
line. All the mean values, the SLi, SHi, and Fi for each blade,
and the standard deviation of the data set for each blade, encoder
position, and the 1 PPR were determined in a preprocessing run.
Then we corrected the data readings and performed a frequency
analysis of the data set. Linear interpolation between the shaft
speed values at adjacent shaft encoder positions appeared valid if
the straight line segments between the positions were adequate to
closely define the curvature present in the speed line for each

revolution. That seemed true in our case, even at the low average speed of 1,200 rpms. Note that we had 17 line segments defined by 18 shaft encoder readings which were then zero reset after the 1 PPR, the 16 PPR readings, and the 1 PPR reading. Another valuable feature of the method was that neither the blades nor shaft encoder (tachometer) positions needed to be spaced nor needed to be assumed to be spaced symmetrically around the circle of rotation because the means of their data sets located them accurately in time of revolution and consequently in space.

We processed a number of test run data sets through the preprocessing and data correction programs. We processed the corrected and uncorrected data sets through a statistical routine that computed the standard deviation (σ) values of each data set. The σ values for Run 1 (1,200 rpm) and Run 2 (1,800 rpm) are presented in Tables 25 and 26, respectively. Channel 1 contained the 16 shaft encoder values and channels 2, 3, and 4 each included plane-of-light detector readings for each of the 12 blades on the test disk. The 1 PPR data readings were included as the last reading of each revolution for each channel. The corrected σ values include both random and systematic errors due to instrumentation errors and noise, unbalance of the test specimen, bearing noise, and buffeting of the blades due to changes in air circulation in the open test chamber, but errors due to speed changes of the test shaft were eliminated, or nearly so.

Data values for other test runs 3 through 8 were corrected for shaft speed variations. The subsequent frequency analysis made on the corrected data sets revealed the 1, 2, and 3 diametral mode shapes of the test disk.

6.3 STATIONARY AND TRAVELING WAVE DATA ANALYSIS

The data reduction and analysis system used for the ISRL NSMS data of this effort was documented fully in a report, "Data Analysis Guide for the Noncontacting Blade Deflection Measurement System,"(7). The data processing procedures are described briefly in the paragraphs that follow.

TABLE 25
RUN #1, *1,200 RPM, *NOT EXCITED, *Σ VALUES

Blade	Chan 1 Raw	Chan 2 Raw	Chan 2 Corrected	Chan 3 Raw	Chan 3 Corrected	Chan 4 Raw	Chan 4 Corrected
1	1 - 3	21	11	15	11	23	6
2	2 - 22	44	6	40	32	49	8
3	3 - 42	70	7	68	34	74	8
4	4 - 61	94	7	89	34	98	10
5	5 - 80	119	5	113	34	123	7
6	6 - 99	144	7	142	34	149	14
7	7 - 118	169	6	164	34	174	8
8	8 - 136	194	6	187	34	199	11
9	9 - 155	219	6	214	35	223	6
10	10 - 174	243	5	237	34	247	5
11	11 - 192	268	8	262	33	273	9
12	13 - 229						
13	14 - 247						
14	15 - 265 1 PPR						
15	16 - 283						
	1 PPR 298						

TABLE 26
RUN #2, *1,800 RPM, *NOT EXCITED, *Σ VALUES

Blade	Chan 1 Raw	Chan 2 Raw	Chan 2 Corrected	Chan 3 Raw	Chan 3 Corrected	Chan 4 Raw	Chan 4 Corrected
1	1 - 1	8	7	4	4	9	6
2	2 - 6	13	5	15	11	15	6
3	3 - 12	20	5	45	34	22	7
4	4 - 17	27	6	51	34	28	7
5	5 - 23	34	4	31	31	35	5
6	6 - 28	41	5	45	32	44	10
7	7 - 33	48	4	53	33	49	6
8	8 - 38	55	4	61	33	56	8
9	9 - 44	62	4	69	34	63	4
10	10 - 49	69	5	72	33	69	4
11	11 - 54	76	6	79	34	77	6
12	12 - 59	82	4	89	35	83	5
13	13 - 65						
	14 - 70						
	15 - 75						
	16 - 80						
	1 PPR 84						

* We think the noisy data on channel 3 was due to wide dispersion of
the light beam from the transducer, which has been replaced with
our spare transducer for the next test run series.

156

6.3.1 NSMS Data Reduction Procedures for Stationary Wave Analysis

UDRI NSMS data reduction software was designed to run on a VAX computer. To perform data reduction analysis, the user stores test NSMS data on magnetic tape. The tape was then read on the UDRI VAX, and the data from the recorded runs were sorted and cataloged onto disk.

The user then processed these data for analysis and results-plotting. Terminal access to the VAX for these purposes was made through dial-up connections from WPAFB or direct terminal connections at UDRI.

When a test disk was excited in a stationary wave mode on the disk, the NSMS system collected data for blade deflections at each of three plane-of-light detectors. These detectors were normally connected to NSMS system channels 2, 3, and 4. If each channel was working correctly, the user would get an independently complete set of data on each of the three channels, and he needed to process only one of these to analyze the specimen response.

For this type of test, the data reduction software first would read in the channel data and perform a statistical analysis of the data. The program then corrected the channel data for shaft speed variations and repeated the statistical analysis. The correction was based on the following linear speed correction equation, developed by UDRI:

$$V_{Bik} = (R_{Bik} - M_{Bi}) - (R_{SLik} - M_{SLi})$$

$$+ F_i * [(R_{SLik} - M_{SLi}) - (R_{SHik} - M_{SHi})] \qquad (88)$$

Where

V_{Bik} = Corrected data value for Blade i, at rev k.

R_{Bik} = Recorded reading for Blade i, at rev k.

M_{Bi} = Mean value for Blade i over all good recorded revs.

R_{SLik} = Recorded reading, at rev k, for the 16 PPR shaft encoder position immediately preceding Blade i.

M_{SLi} = Mean value over all good revs for the 16 PPR shaft encoder position immediately preceding Blade i.

R_{SHik} = Recorded reading, at rev k, for the 16 PPR shaft encoder position immediately following or coincident with Blade i.

M_{SHi} = Mean value over all good revs for the 16 PPR shaft encoder position immediately following or coincident with Blade i.

$$F_i = \frac{M_{Bi} - M_{SLi}}{M_{SHi} - M_{SLi}} = \text{interpolation factor for Blade i.}$$

The shaft encoder data was stored using the NSMS system channel 1.

6.3.2   Time and Frequency Analysis

After the preliminary reduction was completed, a printable report of the statistical analysis was generated. The program then created a time series for each of channels 2, 3, and 4 using the corrected data, and then performed a frequency analysis.

The frequency analysis consisted of a Fourier analysis of the time series generated previously for one of the data channels. The program used an FFT routine from the ISML library to perform the Fourier analysis. The ISML library was a commercial mathematics and statistics software package, and was available on both the UDRI VAX and the ASD SEWS ADA VAX.

As a final step, the data reduction software program writes to disk any requested time series data and results of the frequency analyses. These disk files can be used for plotting time series or frequency spectrum data.

An example of a typical flow chart for the stationary wave speed correction, time and spectrum analysis and plotting software program is shown in Figure 66.
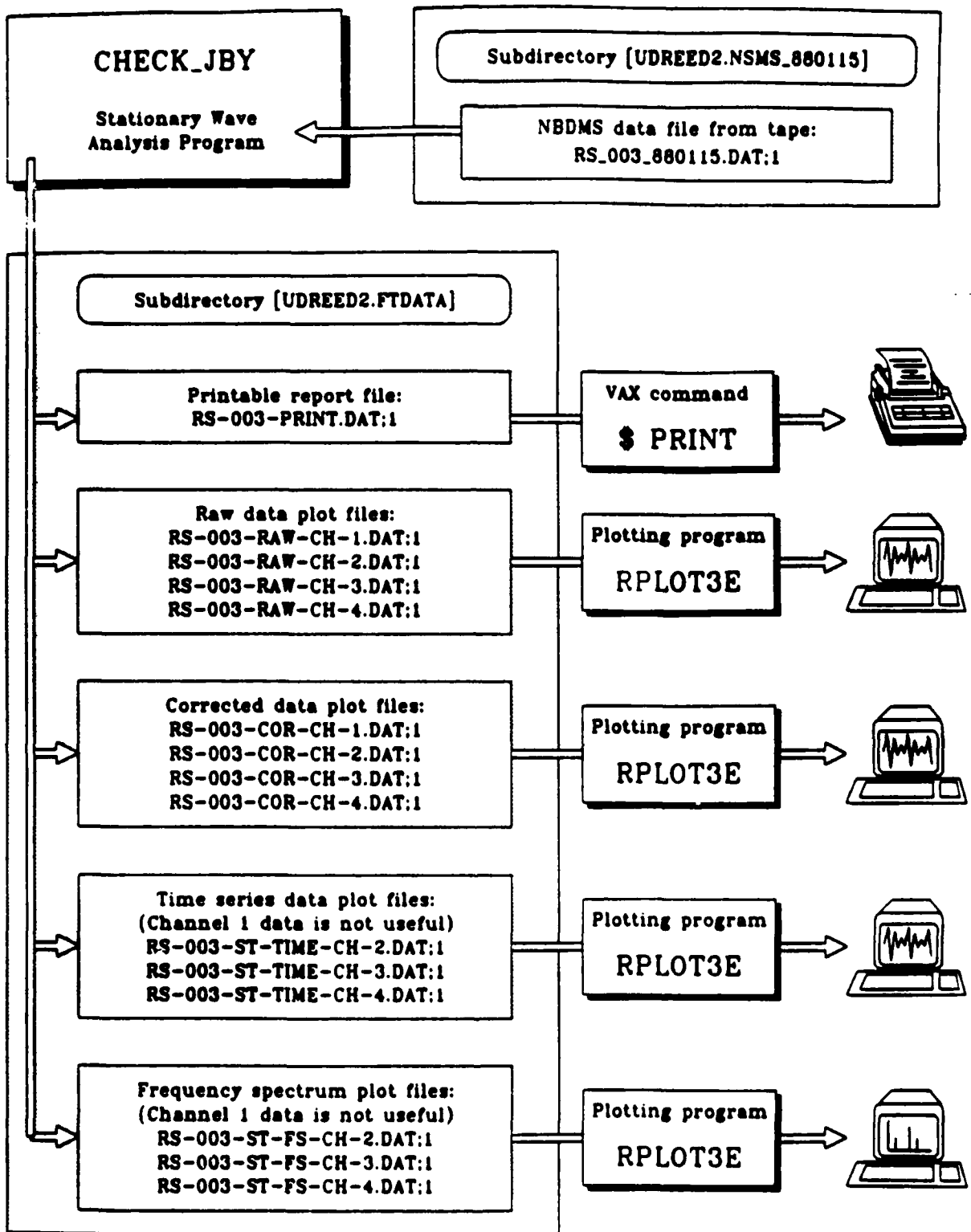
Figure 66.   Standing Wave Software Program Flow Chart.

6.3.3 NSMS Data Reduction Procedure for Traveling Wave Analysis

When a test disk was excited in a traveling wave mode on the disk, the NSMS system again collected data for blade deflections at each of the three plane-of-light detectors. For this test mode, however, the user needed results from each of the three NSMS data channels to generate an appropriate time series for the vibration analysis. Also, an additional low-response test run was required to generate a nonvibrating reference data set for the specimen's magnet-transducer configuration. The remaining system channel was used, as before, to collect the 16 PPR shaft speed variation correction data.

For the traveling wave test, the nonvib data set was first analyzed and processed as described previously. The data were corrected for shaft speed variations, and for channels 2, 3, and 4, the scaled mean of each blade's passage time count was stored. That is, the mean of a blade's passage time reading over all good recorded revolutions was divided by the mean 1 pulse per rev count value (1PPR) for the nonvib run. Since the nonvib run and its corresponding vibration run were made at different shaft speeds, the mean 1PPR values would be different between the two data sets and their ratio can be used to predict the nonvib reference value of each blade at the test condition rpm of each rev.

In the next step, the traveling wave data reduction software read in each channel's data from the vib data set. The program performed a statistical analysis of the raw data. The program then corrected channel data for shaft speed variations and repeated the statistical analysis. The corrected data for each of the three data channels then was referenced to the nonvib data mean for each blade as adjusted for the rev speed difference. These corrected differential time of arrival values were converted to deflection values and then were incorporated into time history data sequences for the FFT frequency analysis procedure, as in the stationary wave analysis.

160

These analysis steps were implemented in the traveling wave software program, and both nonvib and vib data sets are illustrated in the flow diagram, Figure 67. For traveling wave analysis with three probes, the system measured response at three evenly spaced points of a test mode wavelength. This arrangement used three sample points per each revolution, and the increased sample rates were achieved by storing data from symmetrically positioned blades. This analysis used lists of symmetrically located blades. The blade number arrangement for 2, 3, and 4 diametral modes is shown in Tables 27, 28, and 29 respectively.

6.3.4 Z-Grid Data Reduction Procedure

The optical system traveling wave analysis program can also process the Z-Grid data. The grid analysis program referred to the grid pulses as "blade" values, but these were data sets from a single blade as it passed across 36 grid wires in each of the dual grid rings. The user should respond to the software prompt questioning the number of blades as 36 while analyzing the Z-Grid data.

When the test disk was excited in traveling wave mode, the dual Z-Grid system acquired data for the magnet tipped blade at each of the 36 grid wires around the grid ring. These data were reordered on channels 3 and 4 of the optical data acquisition system. Also, an additional low-response data test run was made to generate the nonvibrating reference data set as in the optical system.

For the Z-Grid system, the nonvibrating data set was first analyzed and corrected for shaft speed variations. To correct for speed changes, the mean of a Z-Grid pulse response for 500 revolutions was divided by the mean of 1 PPR for the non-vibrating run. In the next step, the traveling wave data reduction software performed statistical analysis on the resonance data and corrected it for shaft speed changes. The corrected data for two Z-Grid channels takes the form of equation (87) in Section 6.3.2. The analysis program at this point treated each Z-Grid pulse as if it were a blade reading on a test disk with 36 blades. The
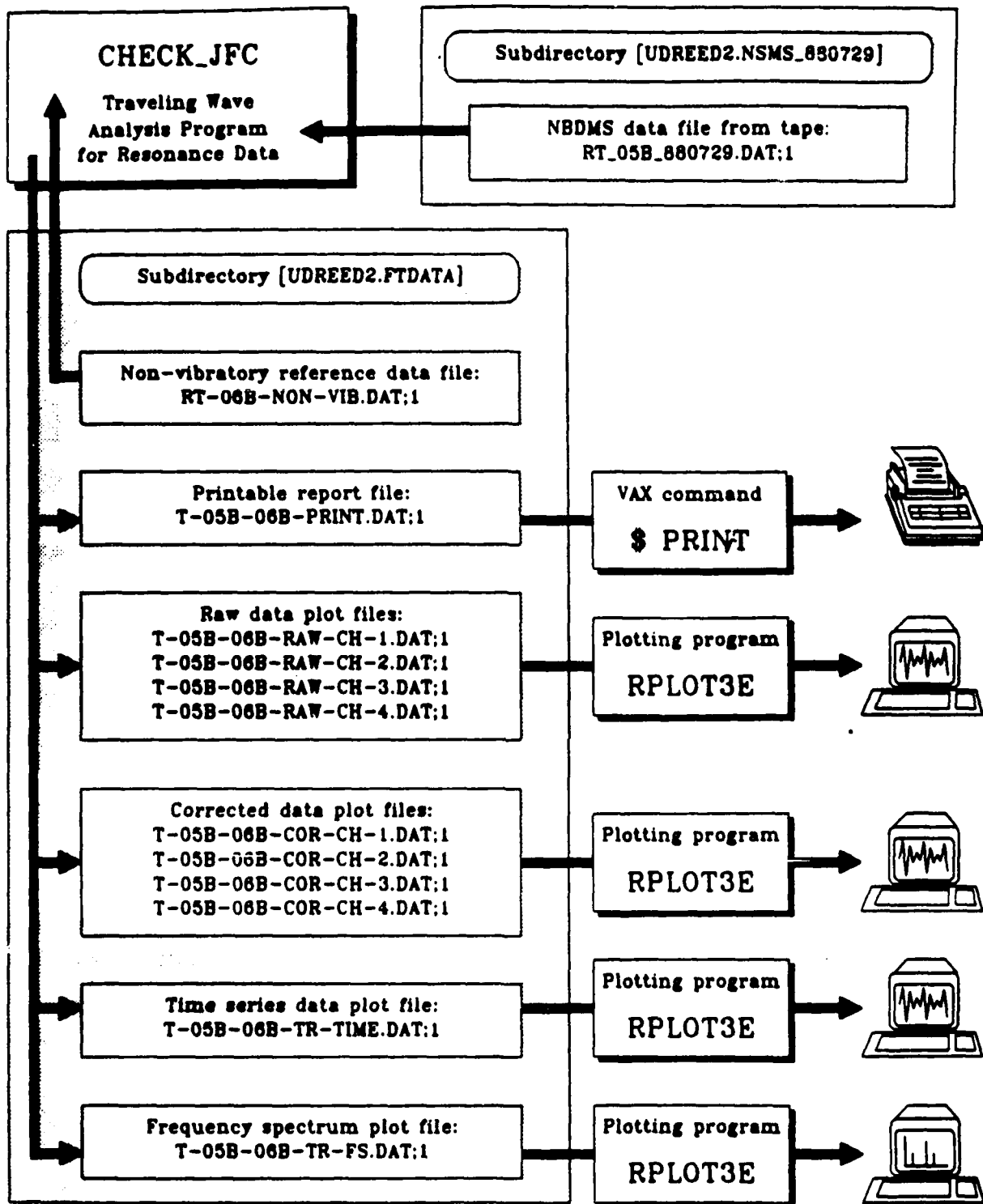
Figure 67. Traveling Wave Software Program Flow Chart.

162

TABLE 27

2D MODE OPTICAL PROBE ARRAY FOR TIME SERIES

Transducers placed at 60-Degree intervals around the specimen. Symmetric blade ordering uses the following blade arrays:

Array Set 1:

Channel	2	3	4
Blades	1	7	13
	20	26	32

Array Set 2:

Channel	2	3	4
Blades	2	8	14
	21	27	33

Array Set 3:

Channel	2	3	4
Blades	3	9	15
	22	28	34

Array set 4:

Channel	2	3	4
Blades	4	10	16
	23	29	35

A time series sequence for Set 4 (as an example) would be a repeated sequence of the data from the following:

Event Number:	1	2	3	4	5	6
Blade.......:	4	10	16	23	29	35
Channel.....:	2	3	4	2	3	4

163

TABLE 28

3D MODE OPTICAL PROBE ARRAY FOR TIME SERIES

Transducers placed at 40-degree intervals around the specimen.
Symmetric blade ordering uses the following blade arrays:

Array Set 1:	Channel	2	3	4
	Blades	1	5	9
		13	17	21
		26	30	34

Array Set 2:	Channel	2	3	4
	Blades	2	6	10
		14	18	22
		27	31	35

Array Set 3:	Channel	2	3	4
	Blades	3	7	11
		15	19	23
		28	32	36

Array set 4:	Channel	2	3	4
	Blades	4	8	12
		16	20	24
		29	33	37

A time series sequence for Set 4 (as an example) would be a
repeated sequence of the data from the following:

Event Number:	1	2	3	4	5	6	7	8	9
Blade........:	4	8	12	16	20	24	29	33	37
Channel.....:	2	3	4	2	3	4	2	3	4

TABLE 29

4D MODE OPTICAL PROBE ARRAY FOR TIME SERIES

Transducers placed at 30-degree intervals around the specimen. Symmetric blade ordering uses the following blade arrays:

Array Set 1:	Channel	2	3	4
	Blades	1	4	7
		10	13	16
		20	23	26
		29	32	35

Array Set 2:	Channel	2	3	4
	Blades	2	5	8
		11	14	17
		21	24	27
		30	33	36

Array Set 3:	Channel	2	3	4
	Blades	3	6	9
		12	15	18
		22	25	28
		31	34	37

Array set 4:	Channel	2	3	4
	Blades	4	7	10
		13	16	19
		23	26	29
		32	35	38

A time series sequence for Set 4 (as an example) would be a repeated sequence of the data from the following:

Event Number:	1	2	3	4	5	6	7	8	9	10	11	12
Blade.......:	4	7	10	13	16	19	23	26	29	32	35	38
Channel.....:	2	3	4	2	3	4	2	3	4	2	3	4

correction and the analysis formulae for the Z-Grid system have the same form as in the optical system.

The basis for configuring the dual grid wires in the letter form "Z" was to enable the grid wire system to measure axial and tangential components of the blade tip deflection. An enhanced analysis procedure was added to the grid wire software analysis to resolve blade tip axial and tangential deflection components from the dual grid system blade tip time of arrival data sets. The rationale for the deflection resolution in two directions is explained below.

If the blade had both axial and tangential displacements, their resolution into independent components required the application of two grid wires. In the ISRL grid system, two conducting grid wires were perpendicular to each other and at 45° to the blade tip magnet path. This arrangement measured both components of the blade tip vibration. If the blade with the source magnet experienced only axial vibration, then the time of arrival values for one grid would be equal to but opposite in sign to those of the second grid. If the blade experienced only the tangential vibration, the time of arrival values for both grid wires would be either greater or smaller by equal amount depending on the phase of vibration of the instrumented blade. If the vibration was skewed to the reference axis, the two orthogonal vibration components would be resolved.

We determined the axial and tangential displacement components of the instrumented blade using our digital Z-Grid system. To resolve these components, the time of arrival data from the two grid circuits were corrected for speed changes. The sum and difference of the time of arrival data sets were then calculated grid wire by grid wire. When these two data sets were added, the tangential motion of the blade was obtained. Their difference defined the axial displacement of the blade. These calculation procedures were incorporated in the system data analysis software.

This method of analysis was applied to a sample data run, and the results from this analysis matched well with the respective time series data and FFT spectra from the optical system and hence confirmed the validity of the analysis procedure.

The results from a comparative study of the optical and Z-Grid system performance for the integral order vibrations of UTRC test disk are summarized in reference (45).

6.4. DIFFERENTIAL DOUBLE PULSE INTERFEROMETRY FRINGE ANALYSIS

The double exposure method, involving two holographic exposures of the vibrating disk in rapid succession, was used to record disk modal patterns. The resulting interference fringe patterns could then be interpreted to provide net displacement of the disk between the two exposures. This amplitude was used to determine the peak to peak vibration of the disk. The method of calculation is explained below.

Consider the disk vibrating sinusoidally in its normal mode when two exposures were made by pulsing the ruby laser (λ = 694 nm) at time t_1 and t_2, as shown on the acceleration signal of Figure 68a. The displacement Z at time t_1 was

$$Z_1 = A \sin \omega t_1 \tag{89}$$

where ω was the circular frequency ($\omega = 2\pi f$) and A was the half amplitude vibration. The displacement Z_2 at time t_2 is

$$Z_2 = A \sin \omega t_2 \tag{90}$$

The net displacement is

$$Z_2 - Z_1 = A(\sin \omega t_2 - \sin \omega t_1) \tag{91}$$

but $t_1 = 0$, $\omega t_1 = 0$, $\sin \omega t_1 = 0$, and $z_1 = 0$ for integral order traveling wave modes, and t_2 was the pulse separation time (Δt). Then
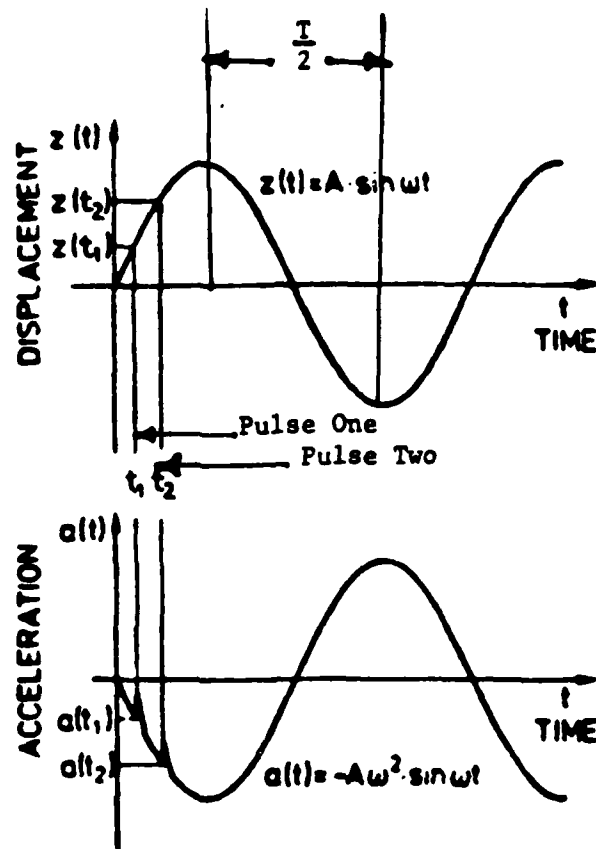
Figure 68a. Laser Pulses at t_1 and t_2 on the Triggered Accelerometer Signal.
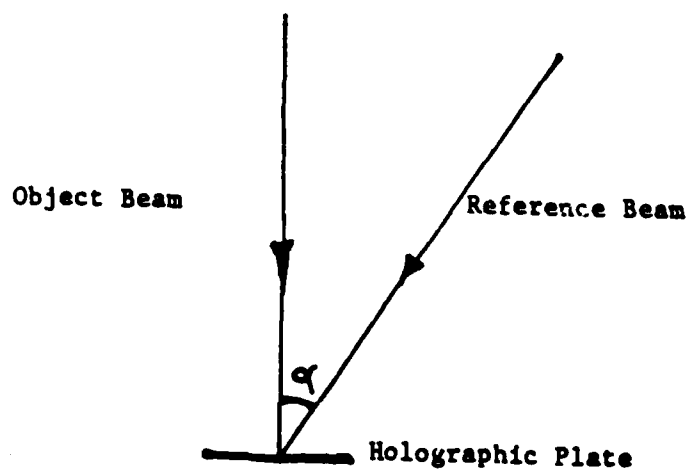
Figure 68b. Object and Reference Beam Angles with Reference to Hologram Plane in Double Exposure Method.

168

$$Z_2 - Z_1 = A \sin (\omega \Delta t) \tag{92}$$

In the double exposure method interference fringes occur when

$$Z_2 - Z_1 = \frac{(2n-1)\ \lambda}{4} \tag{93}$$

where n was the number of fringes and λ was the wave length

From (91) and (92)

$$A = \frac{(2n-1)\ \lambda}{4 \sin\ (2\pi f \Delta t)} \tag{94}$$

The out-of-plane displacement of the disk must be corrected for the beam separation angle (α of Figure 68b) by $\frac{1}{\cos \alpha}$. Then

$$A = \frac{(2n-1)\ \lambda}{4 \sin\ (2\pi f \Delta t)\ \cos \alpha} \tag{95}$$

and peak to peak vibration was

$$2A = \frac{(2n-1)\lambda}{2 \sin\ (2\pi f \Delta t)\ \cos \alpha} \tag{96}$$

For this data set

$$
\begin{aligned}
\lambda &= 694 \times 10^{-9}\ M = 0.02732\ \text{mil} \\
\Delta t &= 10^{-5}\ \text{seconds} \doteq 10\mu\text{sec} \\
\cos \alpha &= 0.82\ (\alpha = 34.92°) \\
F_{2D} &= 135.4\ \text{Hz} \\
F_{3D} &= 182.0\ \text{Hz} \\
F_{4D} &= 243.0\ \text{Hz}
\end{aligned}
$$

and

$$2A = (n-1/2)\ \frac{0.03332}{\sin\ (6.2832 \times 10^{-5} f)} \tag{97}$$

Then

$$2A_{2D} = (n-1/2)\ 3.9025\ \text{mils} \tag{98}$$

169

$$2A_{3D} = (n-1/2) \ 2.9138 \text{ mils} \tag{99}$$

$$2A_{4D} = (n-1/2) \ 2.1823 \text{ mils} \tag{100}$$

The equations (98, 99, and 100) present the scaling factors to be used for conversion of the interferograms to peak-to-peak deflection in mils for the usual cases when the hologram pulse interval time was 10 μsec. They were calculated assuming the sine equal to the angle in radians for these very small angles. They can be scaled to other pulse intervals by dividing the scaling constant by [0.1 x (pulse interval in μsec)] for any of the three modal vibration patterns used in the test series.

SECTION VII
BLADED DISK VIBRATION INSTRUMENTATION EVALUATION TESTS

Turbine ar.1 compressor disks vibrate at 1X, 2X, 3X, and at higher multiples of excitation frequencies. Synchronous and asynchronous excitation conditions of these disks were laboratory simulated to test flexible blades and bladed disks for vibrations in static and rotating conditions. Appropriate hardware and evaluation tests were designed to study the modal response of tuned and mistuned disks. Suitable instrumentation schemes for the bladed disk modal definition were implemented.

This section describes the instrumentation and measurement systems preparation for the rotating bladed disk vibration experiments. Slip-ring design and its installation, stationary and traveling wave excitation methods, positioning of plane-of-light vibration sensors and the setting up of the dual Z-grid ring were described. Application of double and triple pulse laser interferometry for the mode shape definition of the rotating bladed disk assemblies together with the AEDC NSMS evaluation test series is described.

7.1 DISK INSTRUMENTATION FOR VIBRATION MEASUREMENTS

7.1.1 Excitation and Response Instrumentation for the Test Disks

Several bladed disks were fully characterized during this contract period for vibrations. Static and rotating disks were excited by one or two stationary electromagnets. Input voltage and the frequencies of these excitation magnets were controlled by a combination function generator-power amplifier set. To enable higher power levels, the excitation magnets for the rotating disk were freon-cooled.

Two bladed disks - a 12-inch-diameter, 12-bladed disk and an 11-inch-diameter and 38-bladed disk were instrumented, tested and evaluated for vibration characteristics in static conditions. Resonances were identified through Lissajous figures

on the oscilloscope and FFT spectra displays on the spectrum
analyzer. Time average holography recorded several diametral and
circumferential mode shapes of static bladed disks.

7.1.2 New Slip-Ring Design and Installation for Rotating Disks

During the test runs on a 12-inch-diameter disk, the
lead wires on the test disk accelerometers and the leads to the
four channel slip-ring mounted on the drive shaft behind the test
disk failed when the spin speed exceeded 2,000 rpm. Considerable
time was lost for repair and reinstallation. As a remedy, we
designed and installed a ten channel slip-ring set directly on the
front face of the test disk. This unit has ten brass rings and can
accommodate three isolated strain gage circuits, two accelerometer
and two piezo crystal circuits. Lead wires of these sensors
were laid with care to avoid mistuning mass effects. The brush
assembly was fabricated, and a transfer of electrical signals from
disk sensors to the stationary signal conditioning and analysis
equipment through the slip-ring - brush assembly was ensured.

The drawing for the ten-channel slip-ring components
is shown in Figure 69, and a photograph of the unit installed for
use is shown in Figure 70. Figure 71 shows the transducers
installed on the disk to use the new slip-ring circuits.

7.2. TRAVELING WAVE (INTEGRAL ORDER) EXCITATION TESTS

A joint effort with the Unite Technology Research Center
(UTRC) and Arnold Engineering Development Center was undertaken to
excite and measure a flexible bladed disk traveling wave motion.
This excitation condition simulated the static pressure field
induced oscillations on a rotating turbine disk.

Discussions with AEDC and UTRC engineers on the evaluation of
their NSMS led to the design of a suitable test specimen and test
setup. The test specimen had to meet three requirements: first,
UTRC preferred a 38-bladed disk with modal frequencies in the
frequency range of 100-250 Hz for the lower order modes; second,

12 Holes @ 30° on 1.70-Dia. Circle

Slip
Rings
$2.00^{+0.000}_{-0.010}$

1.40 ± 0.002

Spacers
2.25
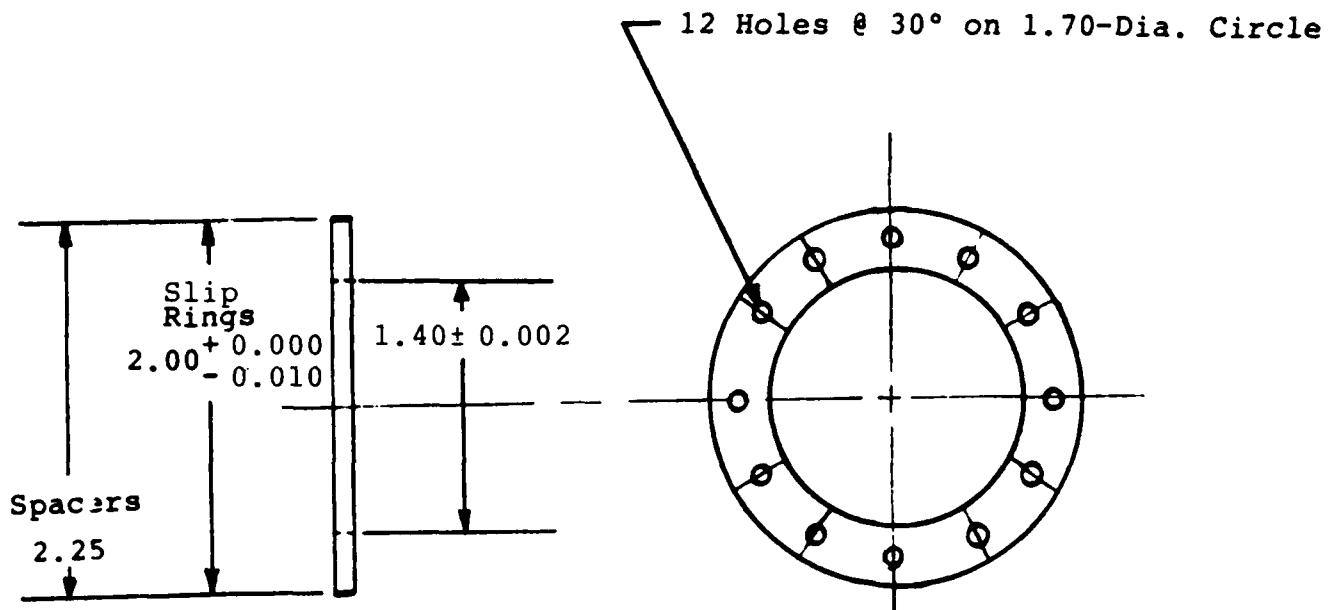
Slip Rings--0.080 Brass

12 Holes @ 30° on 1.70-Dia. Circle

2.25 D

1.40
D

0.25

1.75
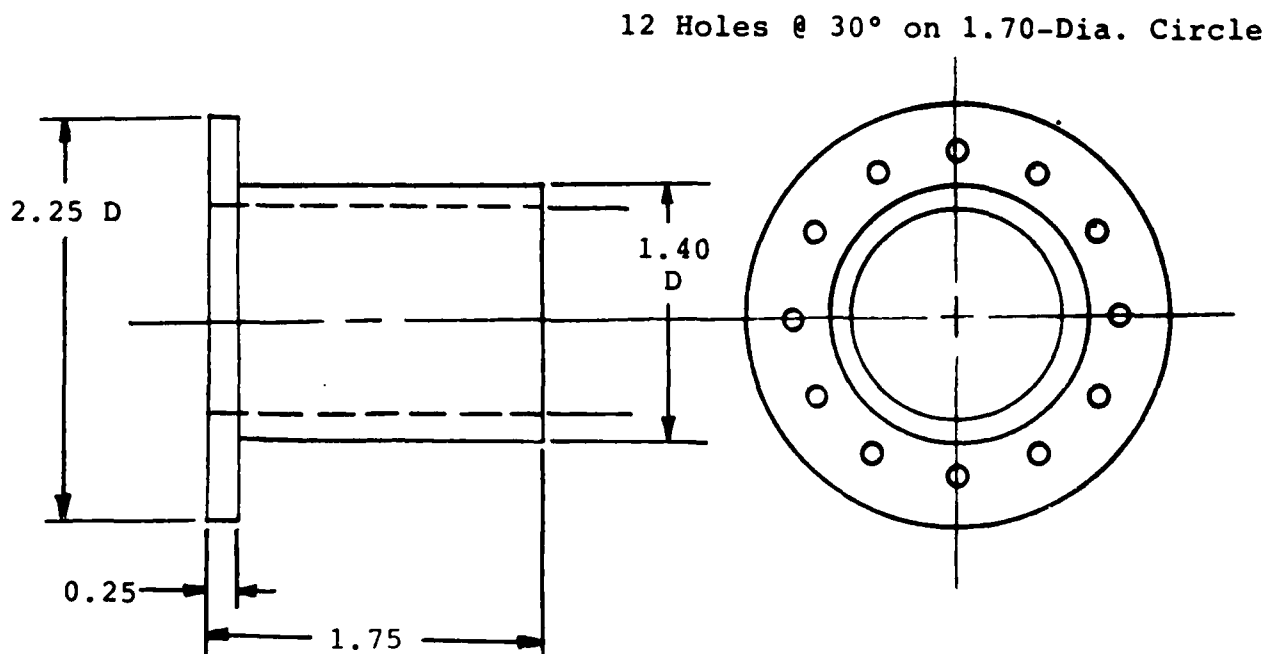
Slip-Ring Set Hub--Polypropylene

All Dimensions are given in inches

Figure 69.   Ten-channel Slip-Ring Components.
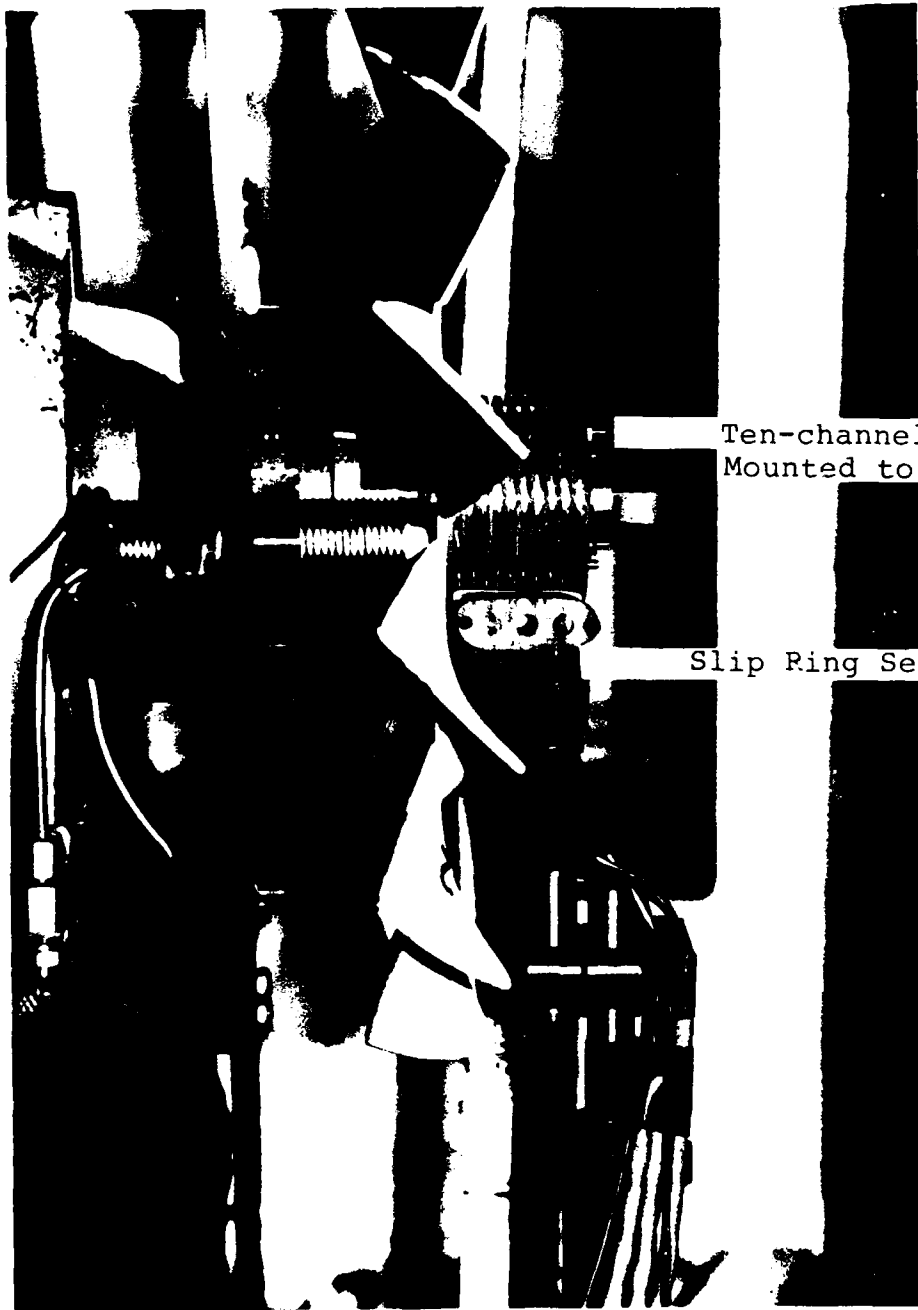
173

Figure 70. Slip-Ring Mounting to the Disk Hub.
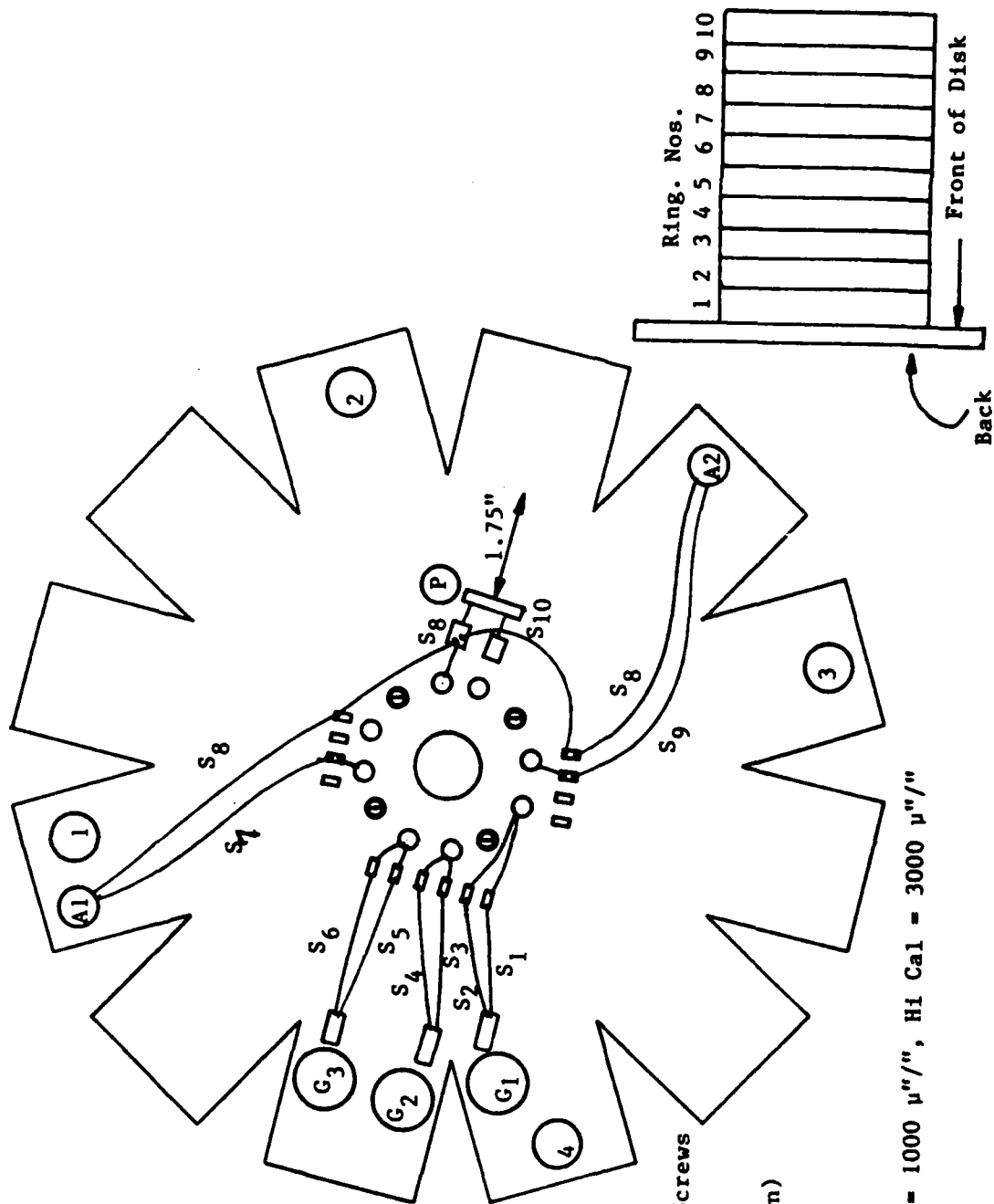
BACK OF DISK SHOWN

⊕ – Slip Ring Attachment Screws

$S_{\#}$ – Slip Ring Numbers

▭ – Terminals (Spares Shown)

(Ax) – Accelerometers

(G) – Strain Gage – Lo Cal = 1000 $\mu''/''$, Hi Cal = 3000 $\mu''/''$

(P) – Piezocrystal

(•) – Quadrant Nos. (on front)

Figure 71. Instrumentation on 12-in.-Dia. Disk.

175

the disk should show large deflection at blade tips so that UTRC optical probes could capture these deflections with ease; third, the size of the test specimen was not to exceed 12-inch diameter, a size that was acceptable for optical holography.

7.2.1 Test Disk Design

Prior experience with disk dynamics guided UDRI to select the approximate diameter and thickness for the proposed test disk. NASTRAN based finite element methods were used to design the test disk to satisfy frequency-amplitude-size requirements. Four possible test disk configurations were analyzed. Their natural frequencies were summarized in Table 30. The two 12-inch-diameter

TABLE 30
NATURAL FREQUENCIES OF FOUR 62.5-MIL-THICK TEST DISKS (HZ)
AT ZERO SPEED

Disk Dia(in)	12.0	12.0	10.0	11.0
Blade Length (in)	1.5	3.0	1.0	2.0
Mode				
1D	59.29	57.04	90.82	72.56
0C	71.45	63.83	107.89	83.99
2D	87.16	68.92	133.98	96.34
3D	168.98	101.86	269.17	166.16
4D	--	125.59	434.17	231.26

disks produced low frequencies, whereas a 10-inch disk yielded higher frequencies. The 11-inch-diameter disk with 2-inch blades was selected because it yielded frequencies close to UTRC specifications. Considering the size of excitation magnets, blade length was later changed to 1-1/2 inches. Disks of 62.5- and 50-mil thickness were analyzed, and their natural frequencies are presented in Table 31. The 62.5-mil-thick disk had a 4D frequency of 294 Hz at zero speed and would have required much larger excitation force to produce acceptable blade tip deflections. The disk of 50-mil thickness was selected for more detailed analysis.

176

TABLE 31
NATURAL FREQUENCIES (HZ) OF 62.5- AND 50-MIL THICK
DISKS, EACH 11-INCH DIA. WITH 38 BLADES OF
1.5-INCH LENGTH AT ZERO SPEED

Mode	62.5-Mil Thickness	50-Mil Thickness
1D	72.5	58.2
0C	85.8	69.6
2D	103.3	84.4
3D	195.0	161.8
4D	294.1	244.0

A reasonable number (38x8) membrane and bending, constant thickness plate elements were used to model a 38-bladed, 11-inch-diameter, 50-mil-thick disk. The normal mode method (Rigid Format 3) of analysis was used to determine the natural frequencies and modes of the centrally clamped, nonrotating bladed disk. The centrally clamped model was used because a 2-inch-diameter ten-channel slip-ring assembly was directly mounted to the disk center to connect disk response monitoring accelerometers and piezo crystals to a frequency analyzer. Two cases of hub-clamping, one without a slip ring but centrally clamped over a 1-inch-diameter and the other with a slip-ring assembly rigidly fixed at the 2-inch diameter, were analyzed; see results in Table 32.

To reduce computational effort, a simple assumption of infinite rigidity was assumed for the 1- or 2-inch diametral surface at the disk hub. Natural frequencies of the 11-inch diameter, 50-mil-thick disk with the slip ring were within acceptable limits. Out of plane normalized vibration contours of the disk diametral modes were determined analytically.

Static bench tests to establish modal characteristics were performed for fabricated 50-mil and 62.5-mil thick steel disks. Time-average holography was used to record mode shapes of

these disks. Verification of analytical frequencies and modes
helped us to continue the disk analysis for the rotational effects.

TABLE 32
HUB SLIP-RING EFFECT ON NATURAL FREQUENCIES
AT ZERO RPM OF 50-MIL-THICK DISK OF 11-INCH DIAMETER
WITH 1.5-INCH-LONG BLADES

Mode	Without Slip Ring	With Slip Ring
1D	58.2	80.5
0C	69.6	83.9
2D	84.4	100.4
3D	161.8	165.1
4D	244.0	244.6

7.2.1.1 Rotational Effects on the Test Disk
        Frequencies

NASTRAN's differential stiffness feature,
Rigid Format 13, was used to analyze the disk rotational effects.
Modal frequency increase due to centrifugal stiffening during
rotation were determined, and the resulting frequencies are shown
in Table 33. Information from this table was used to construct the
frequency-speed diagram to determine the critical speeds of the
test disk.

TABLE 33
ROTATIONAL EFFECT ON DISK NATURAL FREQUENCIES (HZ)
DISK GEOMETRY: 11-INCH-DIA., 50-MIL-THICK 38 EACH OF 1.5-INCH-
LONG BLADES
2-INCH-DIA. HUB SLIP RING UNIT

Mode	SPEED IN RPM					
	0	1000	2000	3000	4000	5000
2D	100	103	109	115	130	148
3D	155	158	163	170	185	201
4D	225	227	234	241	250	264

178

7.2.1.2 Excitation of a Rotating Disk Due to a Static Force Field

While analyzing the dynamics of rotating turbine disks, we need to discuss important contributions made to the turbine disk dynamics research by several researchers. Tobias and Arnold (46) in their first extensive study of the dynamics of imperfect disks, set up simple analytical models and excited a rotating disk by a single stationary magnet for measuring critical resonances. Ewins (47) extended Tobias and Arnold work and developed a generalized force model for the coupled bladed disk response and used it to perform a numerical study on a simple mistuned disk. Ewins (48) also analyzed the individual blade and disk participation in the total disk response of tuned bladed disk assemblies. Srinivasan conducted extensive analytical and experimental investigation of the blade-to-blade response of mistuned turbine disks and summarized the disk dynamics research in a survey article in reference (49).

To understand the disk vibrations due to a static force, consider a point force F_o acting on the disk at $\theta = \theta_r$. This point force can be represented by the Fourier series as

$$F(\theta) = \frac{F_o}{2\pi} + \frac{F_o}{\pi} \sum_{m=1}^{\infty} \cos m(\theta - \theta_r) \tag{101}$$

The generalized force in each mode can be determined from the relation

$$Q_i = \int F(\theta)\, \phi_i(\theta)\, d\theta, \quad i = 1, 2 \tag{102}$$

and

$$Q_i = \frac{F_o}{2\pi} \int_0^{2\pi} \begin{vmatrix} \cos \\ \sin \end{vmatrix} n\theta\, d\theta + \frac{F_o}{\pi} \int_0^{2\pi} \sum_{m=1}^{\infty} \cos m(\theta - \theta_r) \tag{103}$$

$$\begin{vmatrix} \cos \\ \sin \end{vmatrix} n\theta\, d\theta, \quad i = 1,2$$

Resonance condition occurs when $Q_i \neq 0$ and $m = n$ and

$$Q_i = F_o \begin{vmatrix} \cos \\ \sin \end{vmatrix} n\theta_r \tag{104}$$

179

θ_r, the position of static force was time variant due to the disk rotation at speed Ω. Therefore,

$$\theta_r = \theta - \Omega t \qquad (105)$$

and letting $\theta = 0$ and for any time t Eq. (104) becomes

$$Q_i = F_o \begin{vmatrix} \cos \\ \sin \end{vmatrix} n\Omega t \qquad (106)$$

From this equation, it was evident that a disk rotating past a static force was stimulated for a specific mode of vibration at speed Ω.

Considering only one mode of vibration, the generalized excitation force was $Q = F_o \cos n\Omega t$.

The vibration of an axisymmetric disk due to a stationary concentrated harmonic force $F_o \cos \omega t$ can be written as

$$\phi_i = A_i \begin{vmatrix} \cos \\ \sin \end{vmatrix} n\theta \cos \omega t \quad , \quad i = 1, 2 \qquad (107)$$

where ϕ_i was the solution of the equation of motion of disk in generalized coordinates; A_i was the amplitude of vibration and a function of radius, excitation force and magnification factor; θ was the angular coordinate of the disk relative to inertial frame; $\cos n\theta$ and $\sin n\theta$ were the shapes of vibrations of two dual modes; and t was the time.

Letting $\theta_r = 0$ in Eq. (105), we get the instantaneous position of excitation force as

$$\theta = \Omega t \qquad (108)$$

Substituting Eq. (108) into Eq. (107) and from the trigonometric identities $\cos \omega t \cos n\Omega t = \frac{1}{2}[\cos(\omega+n\Omega)t + \cos(\omega-n\Omega t)]$ and $\cos \omega t \sin n\Omega t = \frac{1}{2}[\sin(\omega+n\Omega)t - \sin(\omega-n\Omega t)]$ Eq. (107) becomes

$$\phi_i = \frac{A_i}{2} \begin{vmatrix} \cos \\ \sin \end{vmatrix} n\theta \begin{vmatrix} \cos (\omega\pm n\Omega)t \\ \sin (\omega\pm n\Omega)t \end{vmatrix} \qquad (109)$$

From Eq. (109), four conditions for resonance were possible for an imperfect disk. These are

$$\cos (\omega + n\Omega)t \text{ and } \sin (\omega + n\Omega)t \qquad (110a)$$
$$\text{and} \qquad \cos (\omega - n\Omega)t \text{ and } \sin (\omega - n\Omega)t \qquad (110b)$$

Eq. (110a) represents two forward traveling waves whereas Eq. (110b) represents two backward traveling waves. These were shown in the frequency-speed diagram (Figure 72), of the disk.

But in this analysis, the disk was treated as perfect and hence, only two resonance conditions were possible.

By extending backward traveling wave branches of Eq. (110) to intersect the speed (Ω) axis, we obtain critical speeds of the rotating disk.

Using the information in Table 33 and the conditions in Eq. (110), we determined the critical speeds for our test disk from Figure 73. These speeds were 3,950 rpm for 2D, 3,640 rpm for 3D, and 3,900 for 4D. At these speeds, an excitation force with zero excitation frequency would set the disk in resonance.

Assuming nonpreferential modes for the disk, its vibration can be written as

$$\phi = a_1 \cos n\Omega t \sin \omega t + a_2 \sin n\omega t \sin(\omega t + \epsilon) \qquad (111)$$

and letting $a_1 = a_2 = a$ and $\epsilon = \frac{\pi}{2}$ by the assumption of one mode being orthogonal to the other, Eq. (111) becomes

$$\phi = a \sin (\omega - n\Omega)t \qquad (112)$$

This was a backward traveling wave at speed $n\Omega$. This wave appears stationary to a stationary observer in space. The experiments were designed to excite the backward traveling wave on the disk due to a static force field in space.
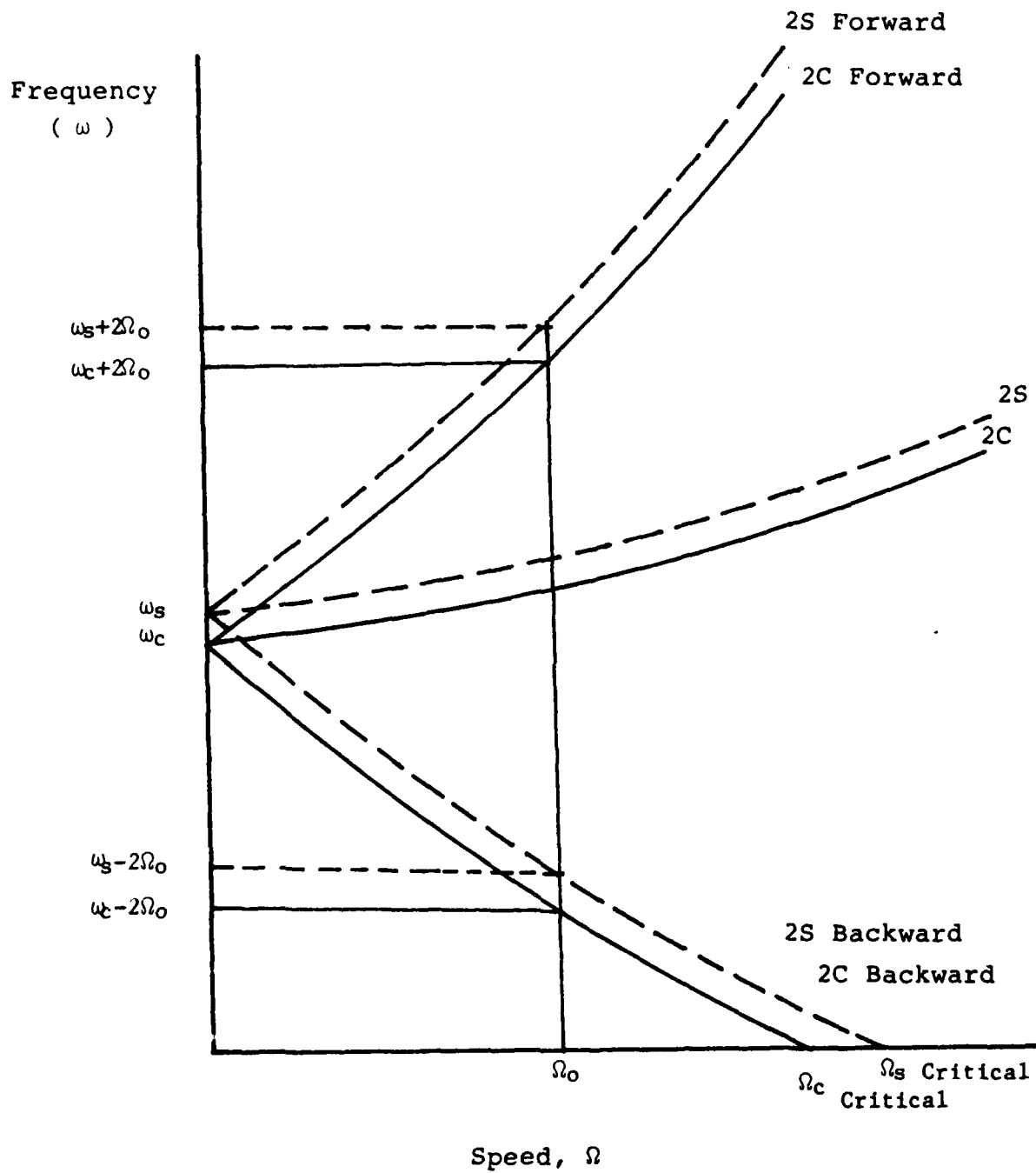
Figure 72. Frequency - Speed Diagram of an Imperfect Disk.

182

11" DIA., 0.05" THICK DISK WITH 38−1.5" LONG BLADES AND 2" DIA. HUB SLIPRING
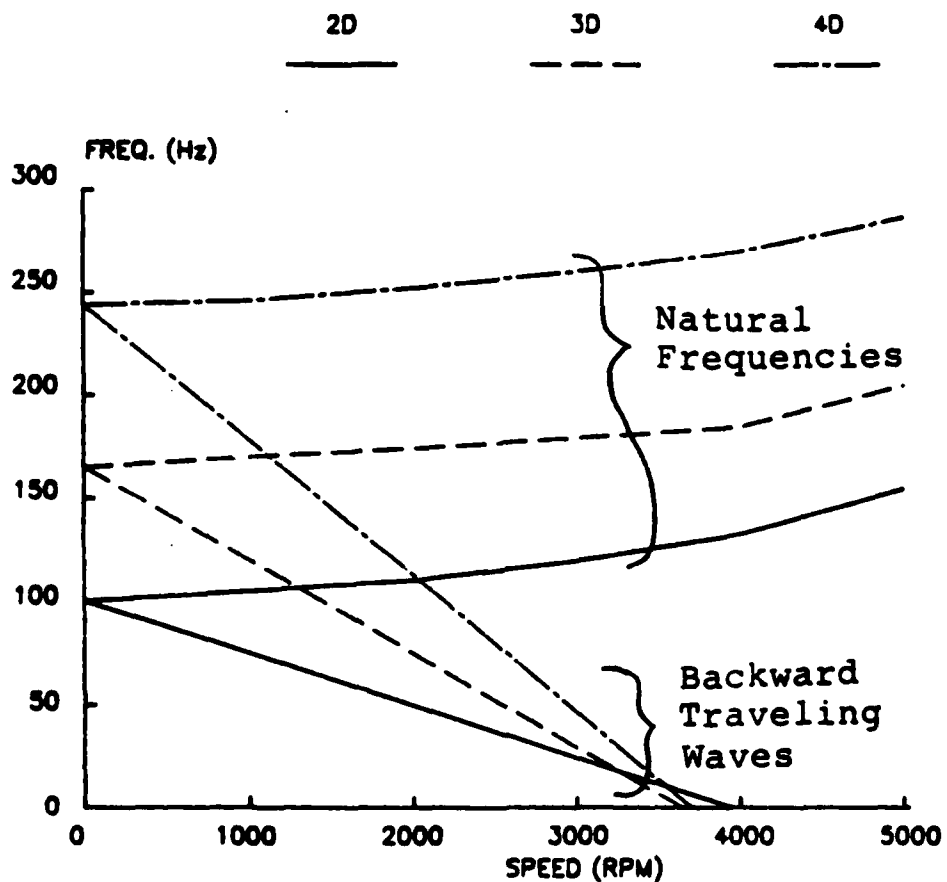
Figure 73.   Frequency-Speed Diagram of 11-in.-Dia., 50-mil-Thickness Tuned Disk.

7.2.2 Excitation Method

As agreed by APL-UDRI, AEDC-UTRC, UDRI designed an excitation system to excite the disk in its 2, 3, and 4 diametral modes and measure its response.

Stimulus to form a pure mode was provided by placing permanent magnets at desired sine wave response peaks. Magnets (4 for 2D, 6 for 3D, and 8 for 4D) were positioned on both sides of the disk at wavelength intervals of the desired mode-pattern but offset by half a wavelength on the front and back sides. Half the number of excitation magnets were positioned in the front while the other half were at the back side of the test disk. Aluminum bars, shown in Figure 74 were used to support the front magnets from a circular yoke. The back magnets were held by a plate fixed to the test chamber floor and motor support frame behind the disk. A general front magnet holder mounting configuration is shown in Figure 75 for the three test modes. A specific excitation scheme for the 2D mode is illustrated in Figure 76.

7.2.3 Probe Positions

In these tests, plae-of-light sensors were used to measure blade tip deflections of the rotating disk. Since the speed of the rotating disk and the speed of the response wave were the same, a stationary probe measured nearly constant amplitude as the disk-blades passed the probe. In effect, one probe, provided only a constant amplitude each time a blade passed the probe, so this arrangement masks the actual dynamic response of the disk. Therefore, more than one probe was necessary to define the blade and disk traveling wave vibrations in integral order modes.

Four AEDC and three UDRI plane-of-light sensors were used here to define modal deformation of the test disk. The following paragraphs describe some considerations for probe locations to monitor three diametral modes of the disk.

Positioning of three UDRI probes to measure 2D, 3D, and 4D mode shapes is shown in Figure 77. A photograph in Figure 78 shows UDRI optical probes in the test setup. For 2D mode excitation, probes were spaced 60 degrees apart in space around the

184
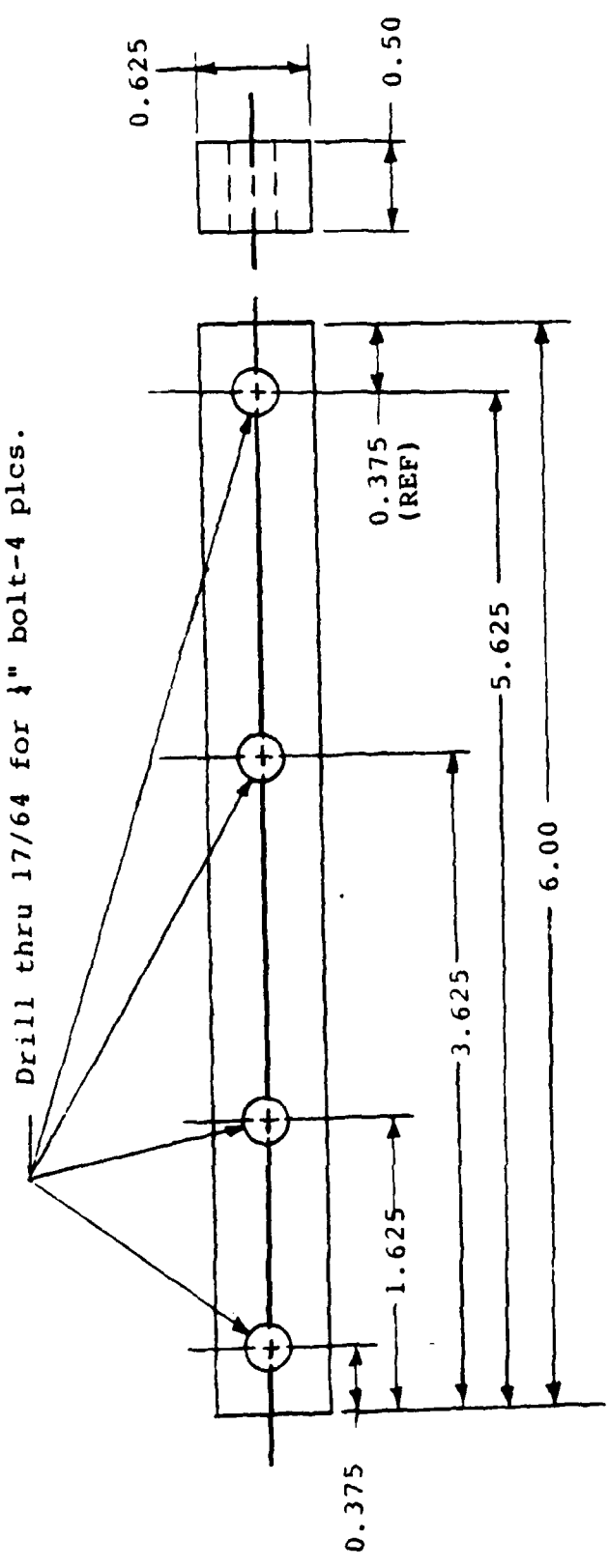
Figure 74. Support Bars for the Excitation Magnets.
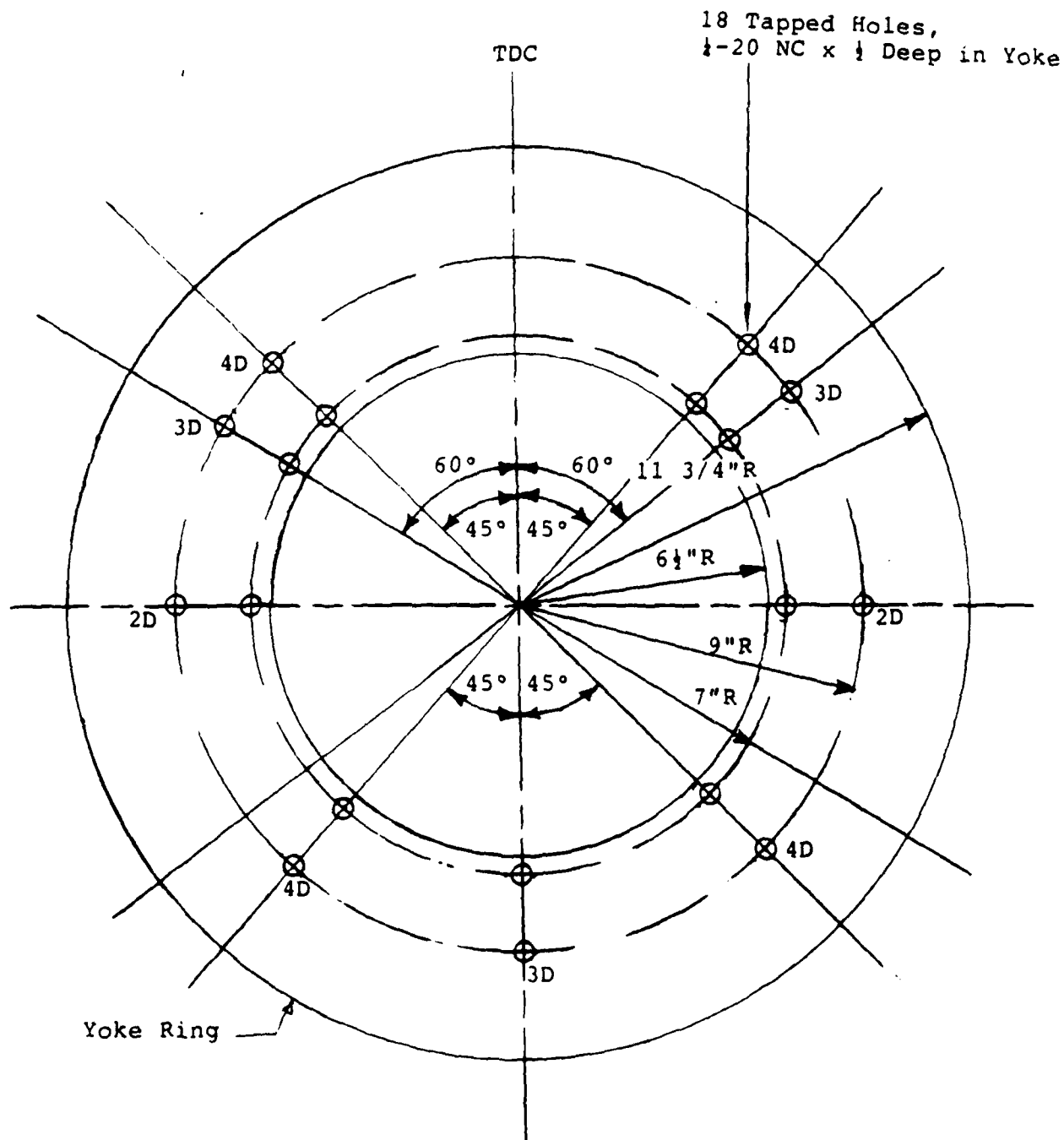
Figure 75. Excitation Magnet Positions.

186
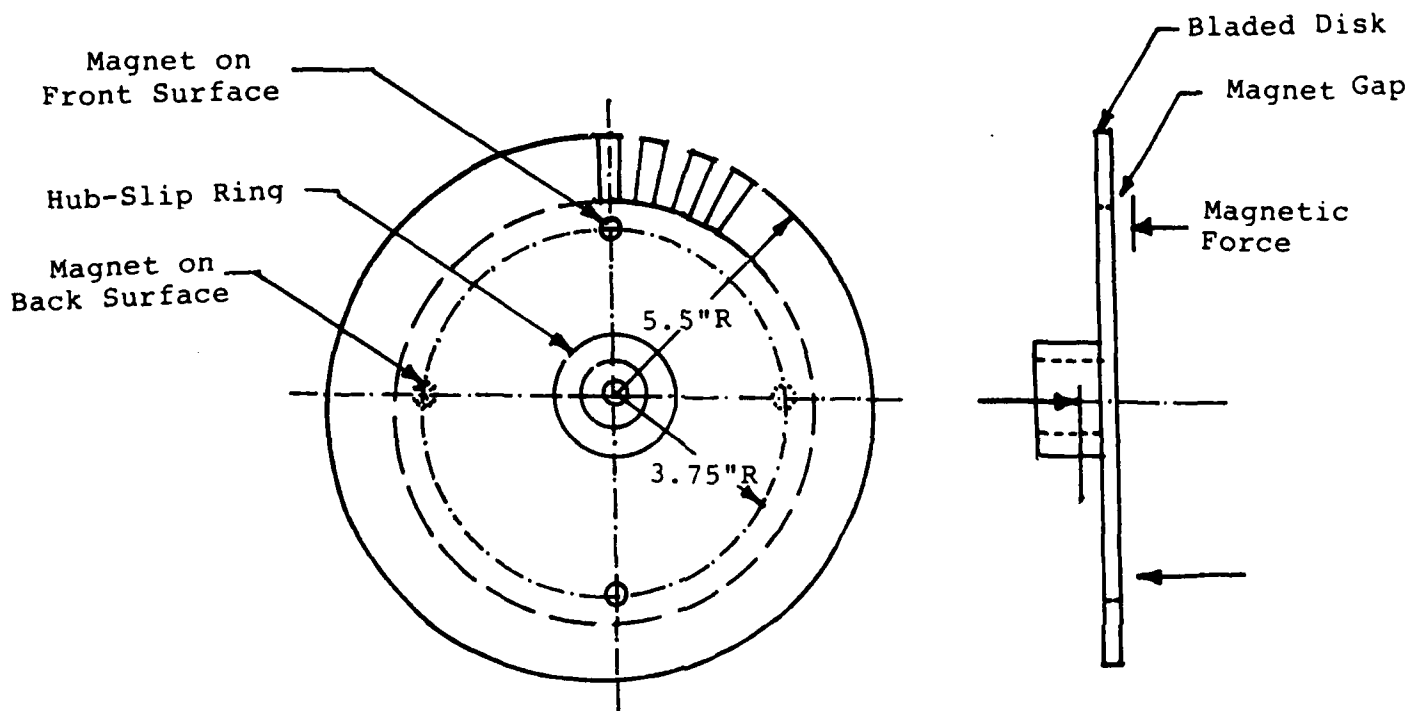
Figure 76. Excitation Magnet Position for 2D Mode.
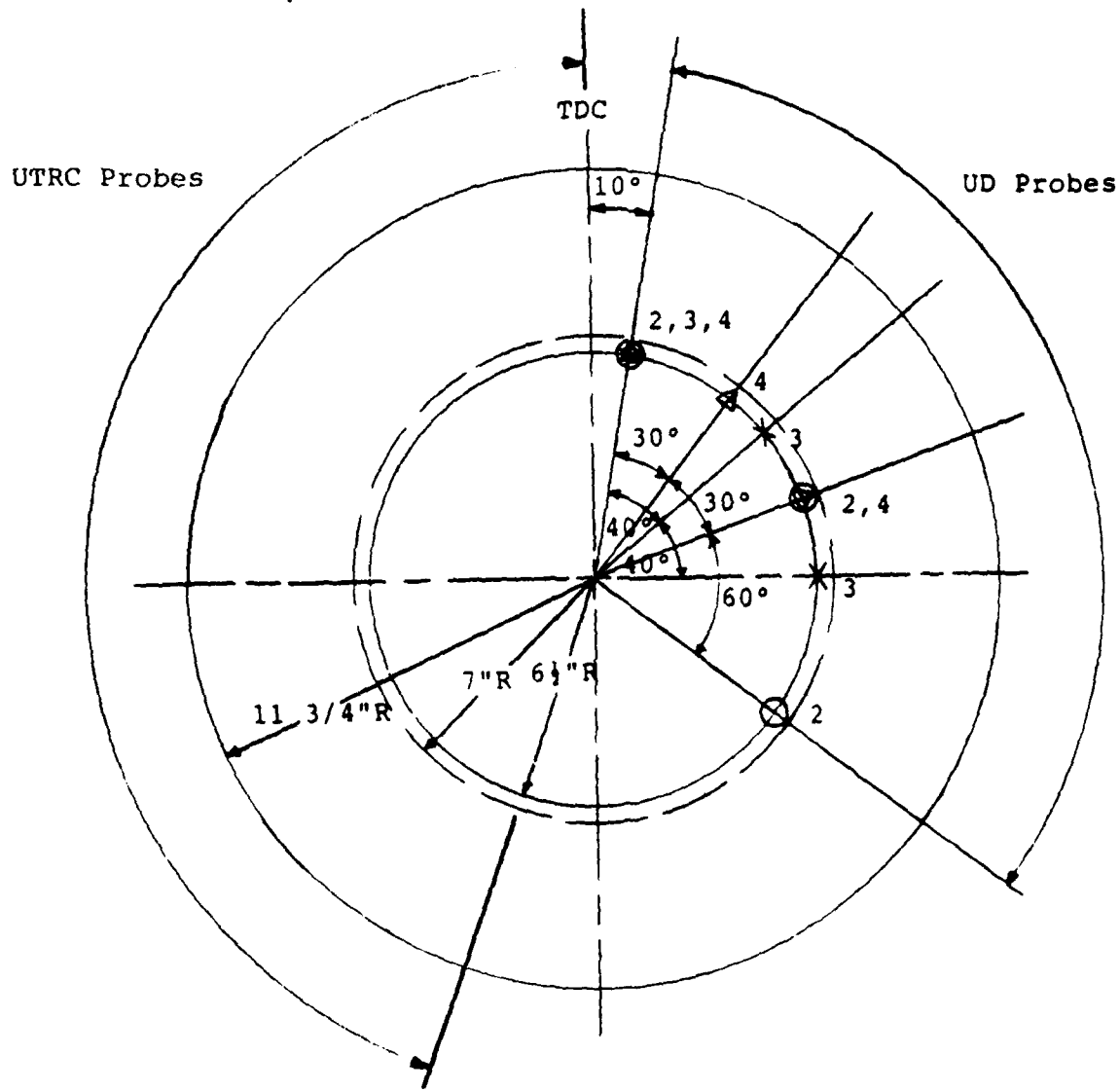
Figure 77. Plane-of-Light Probe Positions.

188
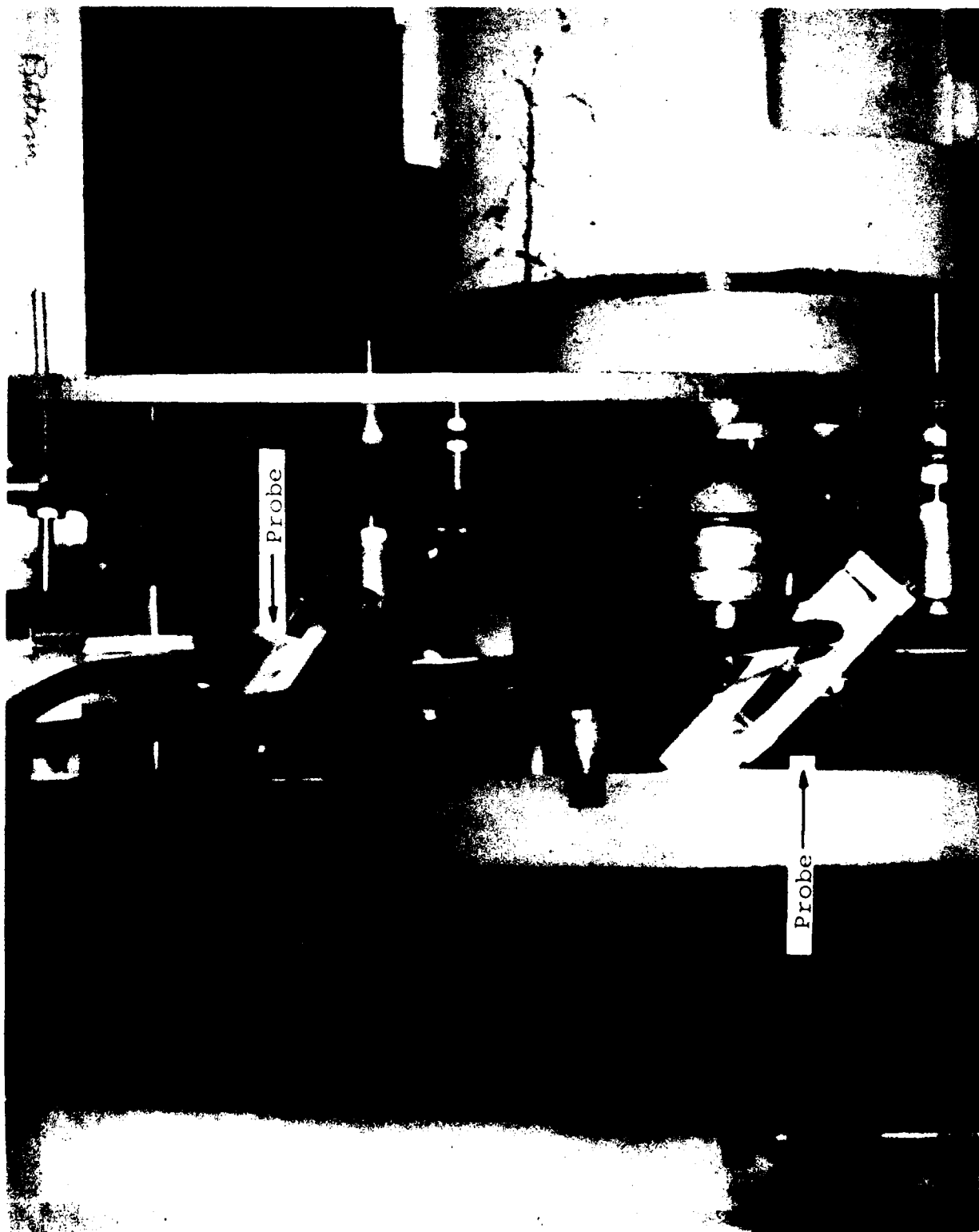
Figure 78. UDRI Optical Probes in the Test Setup.

perimeter of the test disk, while for the 3D and 4D modes, the probes were spaced at 40 and 30 degrees, respectively. The probe location requirement was to space the three probes 120° apart within the modal pattern of each response so a standard Fourier transform routine based on uniformly spaced time samples could be used to analyze the optical data.

The AEDC NSMS measuring system required four blade deflection measurements within a modal wavelength. The transducer locations need not be symmetrically spaced within the wavelength, but the locations must be known relative to each other. The four deflection amplitude readings were used to define the blade response equation of the known mode shape to yield the modal amplitude and frequency.

Figure 79 shows the UTRC plane-of-light probe mounting blocks. The four probes are mounted in the test setup (Figure 80).

7.2.4 Instrumentation Ring (Yoke) Design, Fabrication and Assembly

A yoke was used to mount the UD and UTRC optical probes and the front excitation magnets. The yoke, shown in Figure 81, was designed by UTRC to mount their sensors and modifications to the design for our requirements were added by UDRI. After the yoke was fabricated by the Air Force machine shop, it was mounted within the test chamber (Figure 82). Mounting brackets, shown in Figure 83, held the yoke in position. Tolerances provided in the holes of these mounting brackets allowed the yoke to be positioned concentrically with the test disk. Concentricity within 3 mils was established using a dial gage mounted directly on the test disk by slowly rotating the disk and adjusting the position of the yoke with respect to the disk.

7.2.5 Test Disk Vibration Monitoring Instrumentation, Excitation System and Preliminary Tests

The test disk was instrumented with three miniature accelerometers and two piezo crystals. The instrumented disk with its sensing elements and their slip-ring connections is shown in Figure 84. The specimen and test monitoring system consisted of
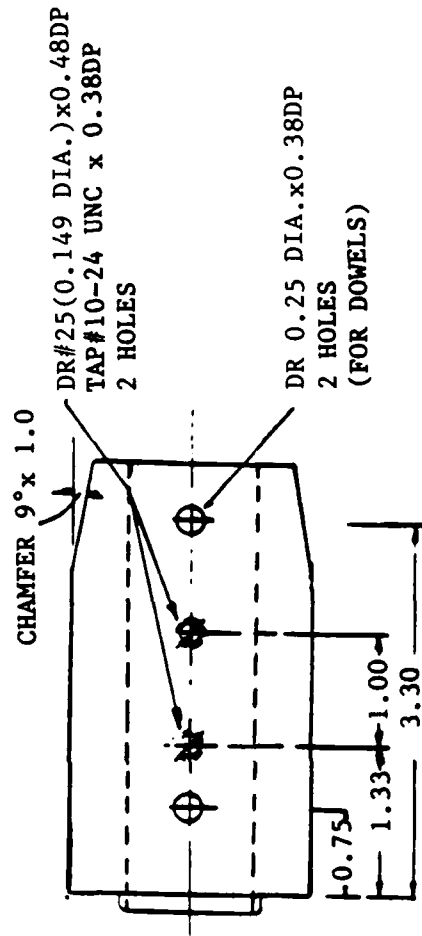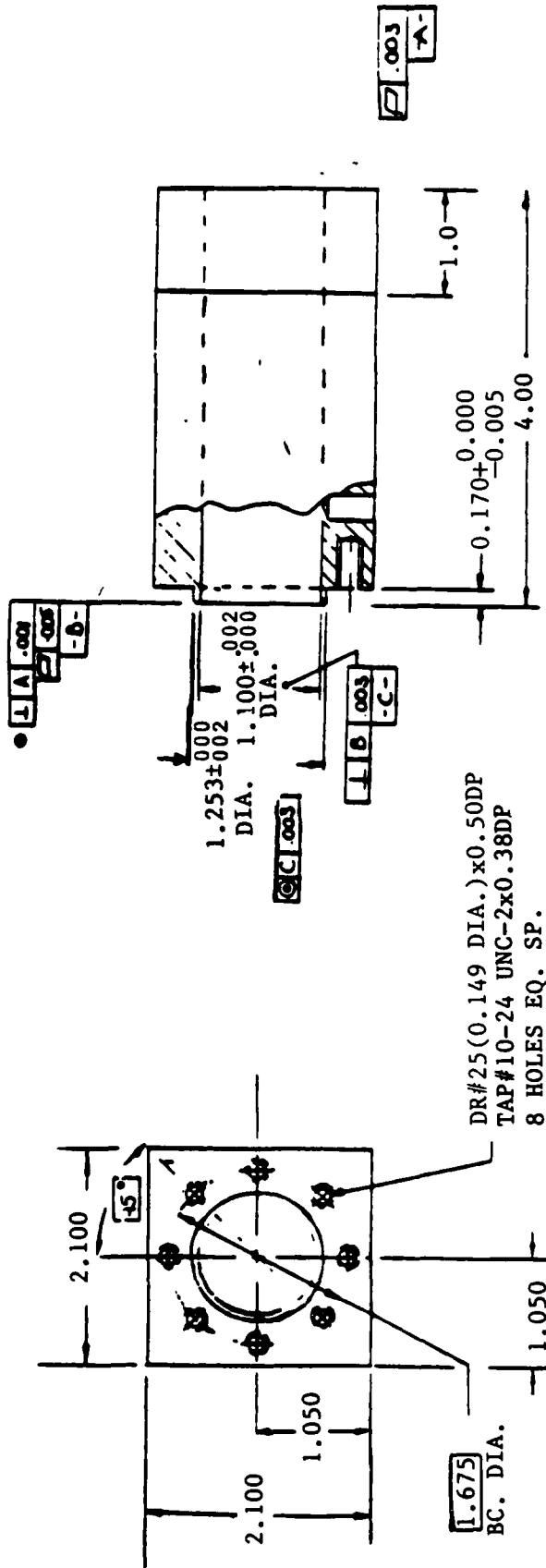
Figure 79. UTRC Probe Mounting Blocks.

191
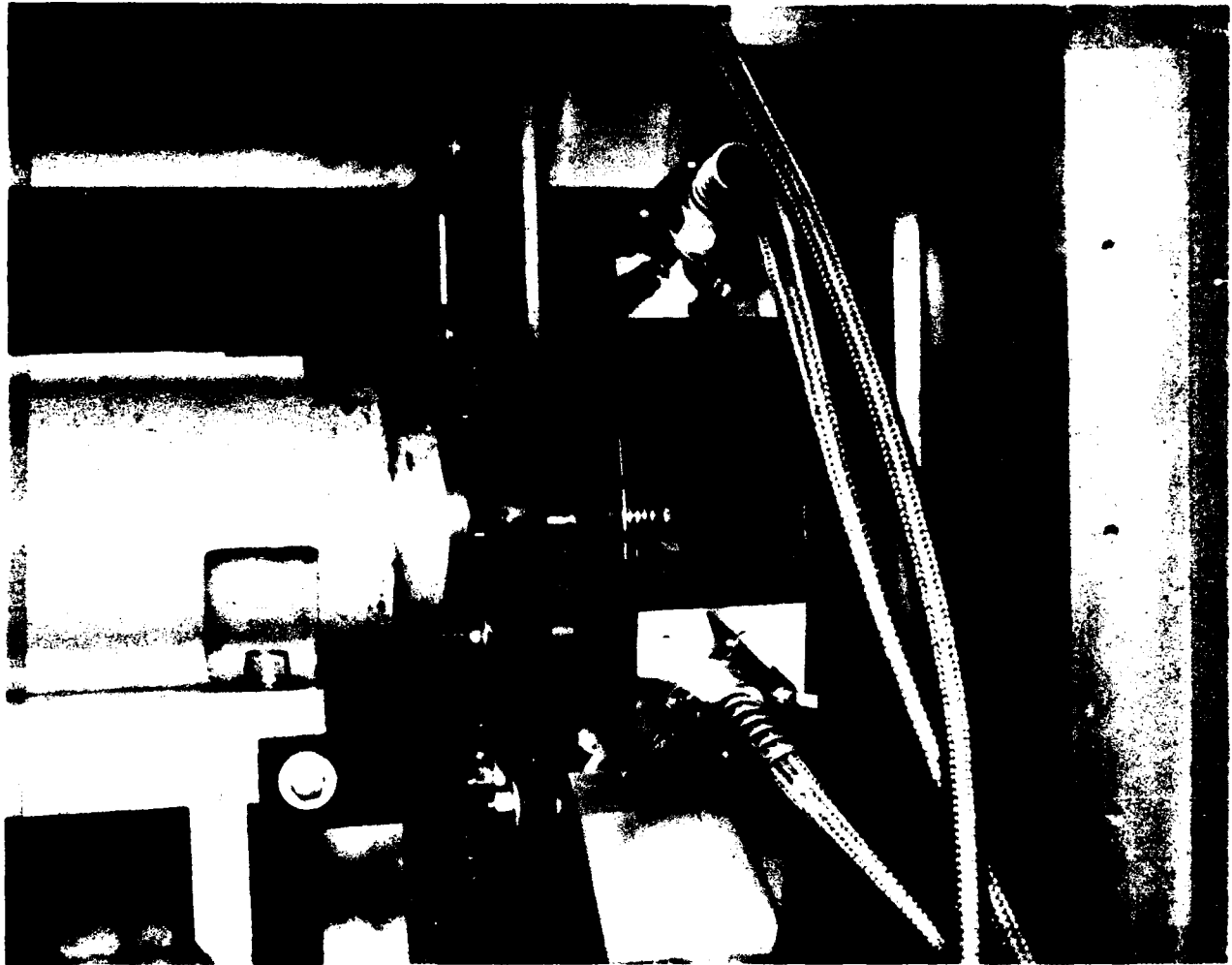
Figure 80. UTRC Plane-of-Light Sensor Probes.
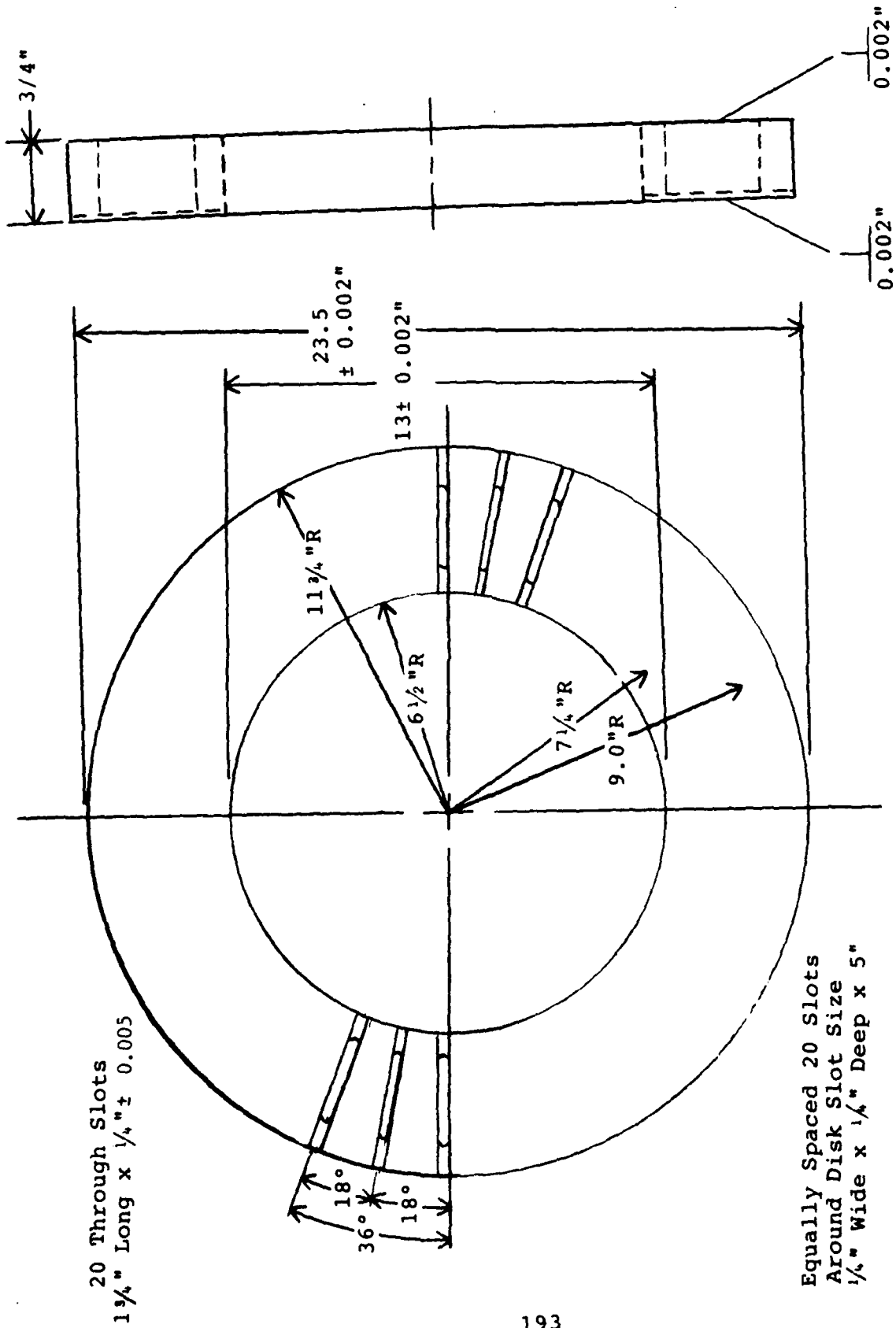
Figure 81. Instrumentation Support Ring (Yoke).

3/4"

0.002"

0.002"

0.002"

23.5 ± 0.002"

13 ± 0.002"

11¾"R

6½"R

7¼"R

9.0"R

18°

18°

36°

20 Through Slots
1¾" Long x ¼" ± 0.005

Equally Spaced 20 Slots
Around Disk Slot Size
¼" Wide x ¼" Deep x 5"
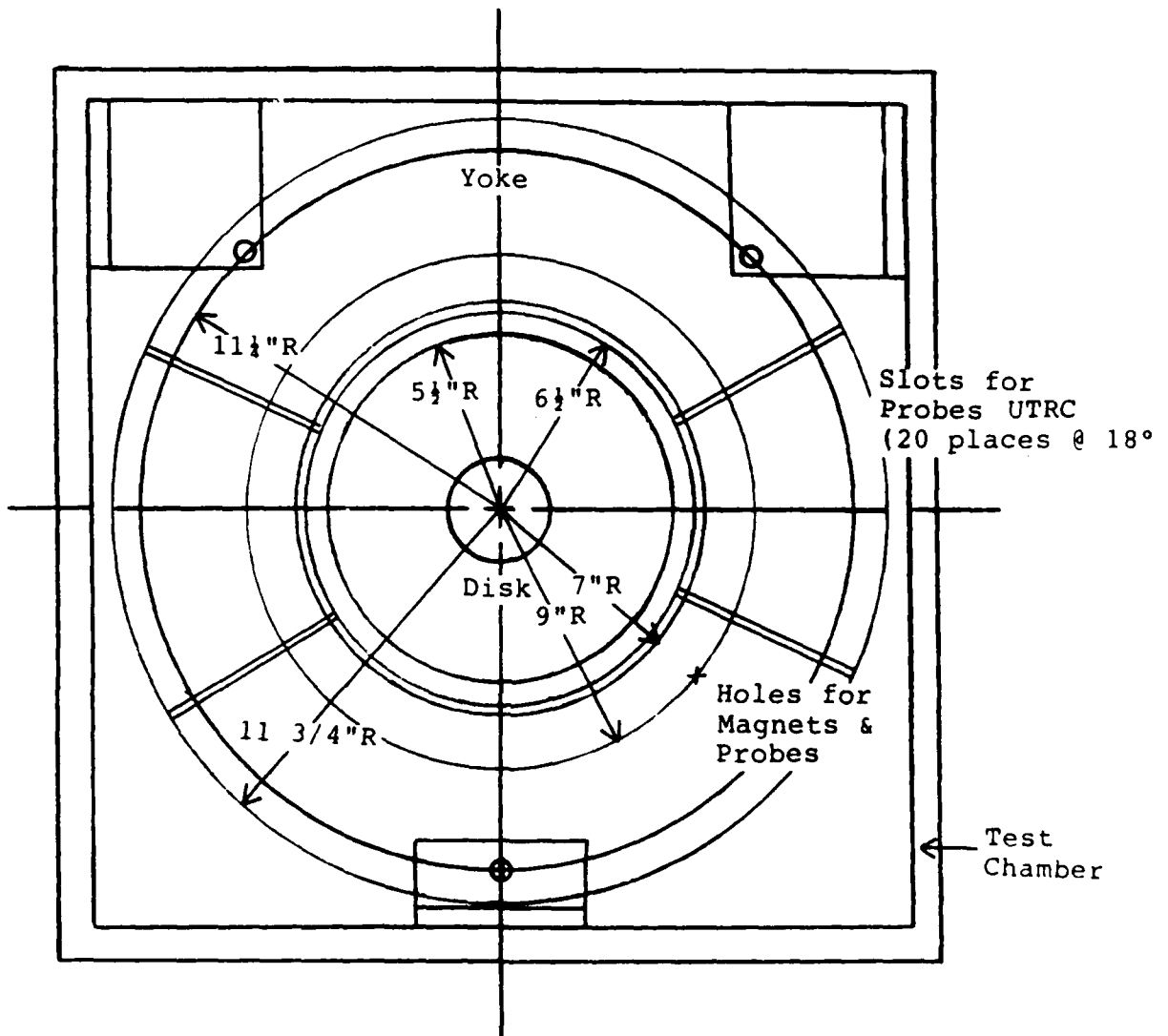
Figure 82.   Assembly of Instrumentation Ring in the Test Chamber.
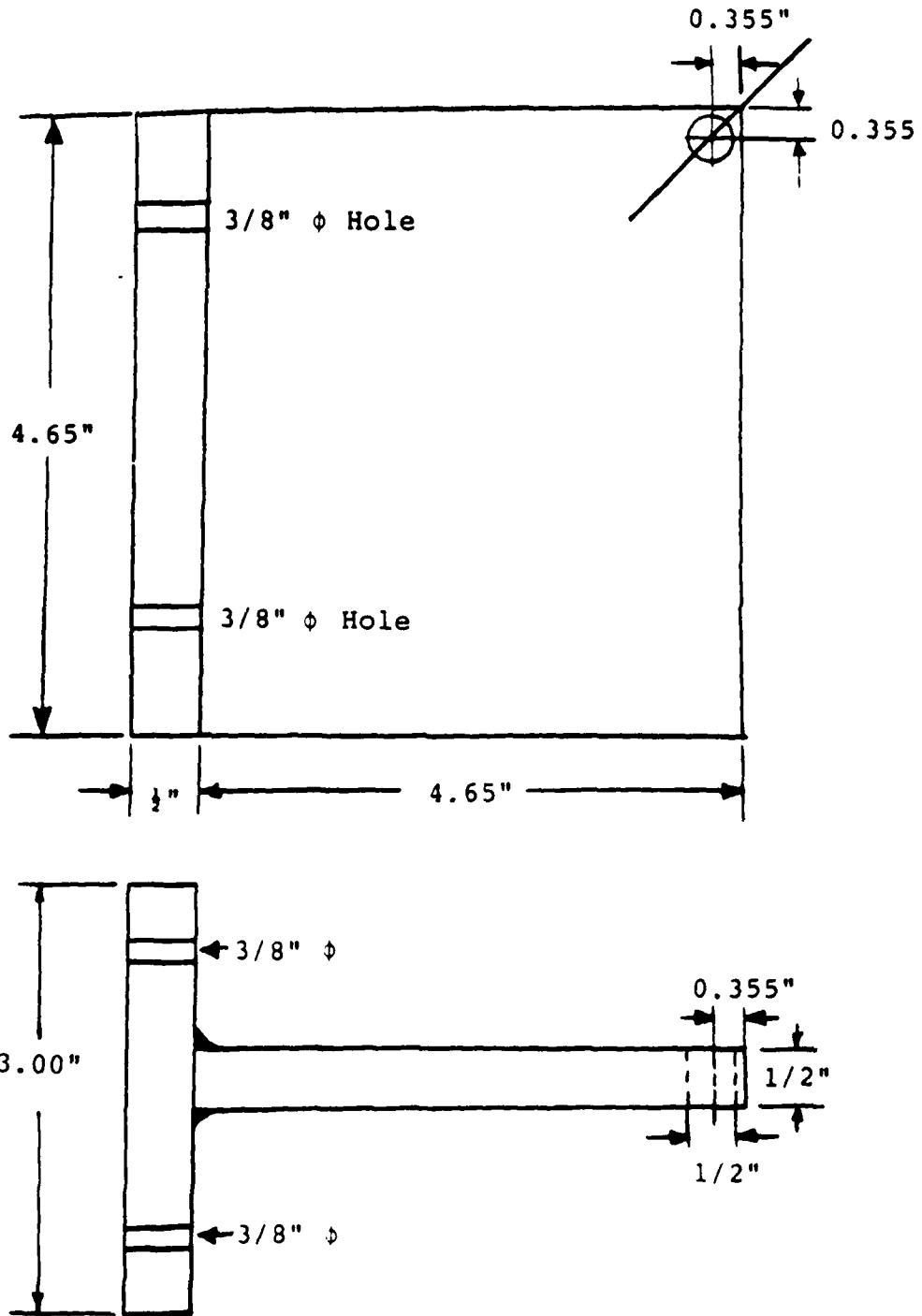
Figure 83.   Mounting Brackets for the Yoke.

the instrumented disk, the slip ring unit, preamplifiers, a spectrum analyzer, and several oscilloscopes.

Preliminary tests were conducted to excite the test disk by permanent magnets at the disk critical speeds. Half-inch-diameter Samarium-Cobalt permanent magnets were installed to an existing mounting plate and were positioned perpendicular to the aft disk surface at a 3.75-inch radius from the spin axis.

Spin tests were conducted with four magnets mounted at 90 degree spacing, two magnets mounted at 180-degree spacing, and with a single magnet installed. The accelerometer signal spectra for three typical runs are shown in Figure 85. The magnets were widely spaced in comparison to their diameter, and tended to excite all the lower order modes of the bladed disk test specimen. Figure 86 shows, from top to bottom, vibration spectra generated by four, two, and one magnets. The 4-D disk system mode was marked by the bright spot at the top of the spectral peak in the range of 260 to 293 Hz for the three spectra shown.

It can be seen in the spectra: that all magnet configurations excite the lower four modes of the system; that a single magnet excites all modes of the system, much like an impact, but the odd-order modes were excited relatively more strongly than the even-order modes; and that for excitation by two or four evenly spaced magnets, the even-order modes were excited more strongly then the odd-order modes, except for the 1-D mode. In addition to the characteristics shown in the spectral plots, holographic interferograms were produced which showed that a particular mode could be emphasized by rotating the specimen in the magnetic field configuration at a speed where that mode became dominant. This test series showed that we could excite backward traveling vibration waves on our test disk with the magnets on hand. From these tests we observed that a fine speed control was required to generate a pure stationary wave. To circumvent this difficulty and to excite a selected mode with ease, we decided to install excitation magnets on both sides of the disk.
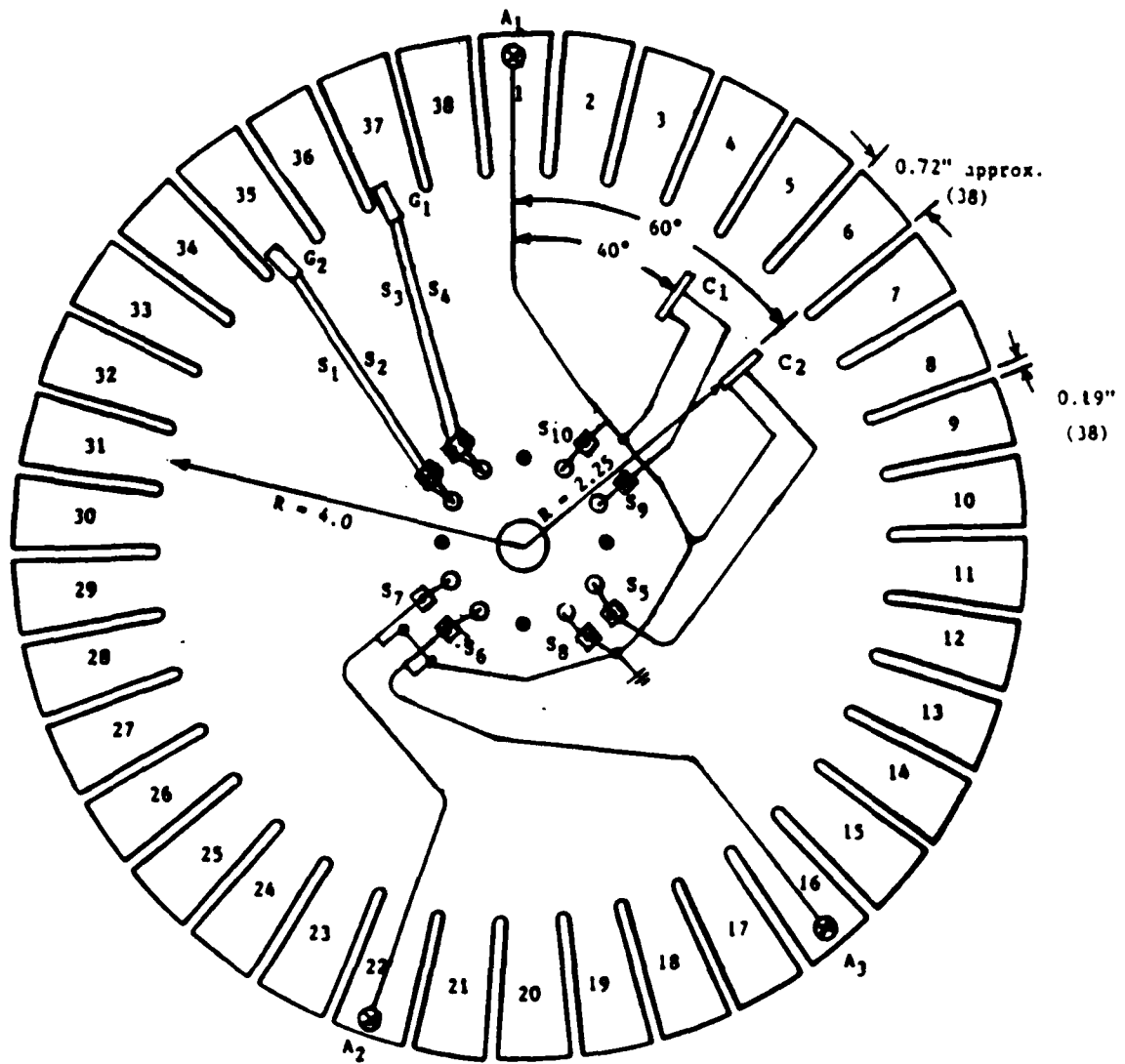
Figure 84.   Instrumentation of 11-In.-Dia. Disk.

197
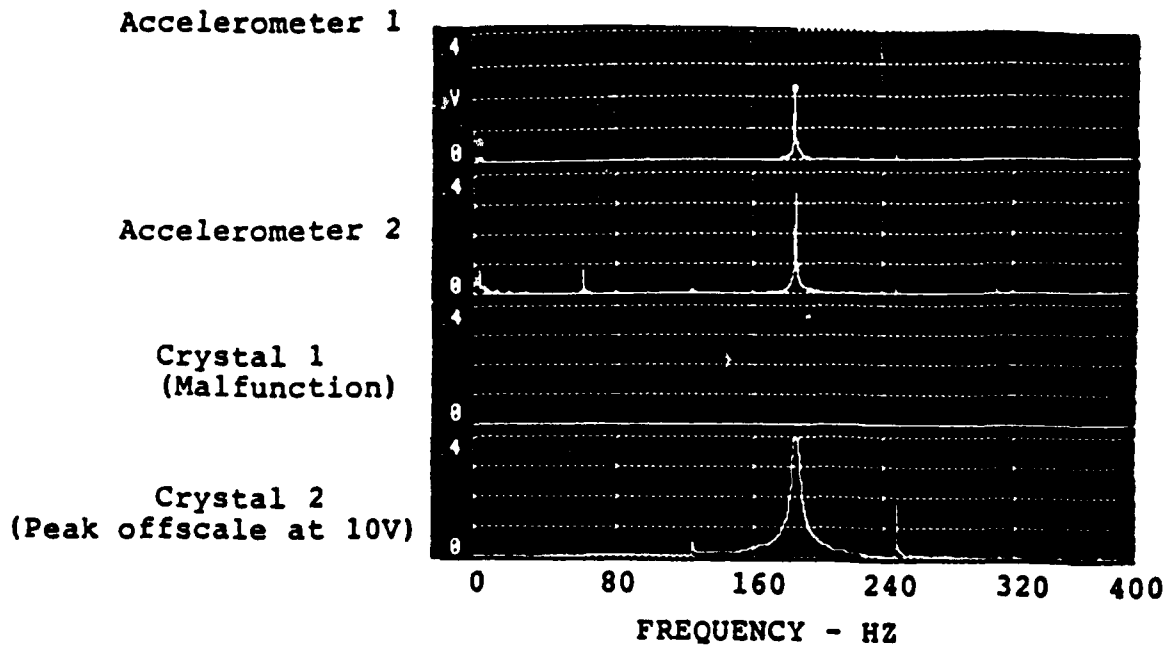
Figure 85. Accelerometer Output Signals.
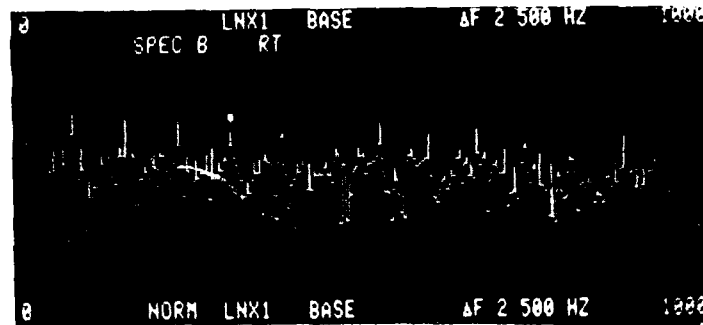
4 Magnets - 4400 RPM
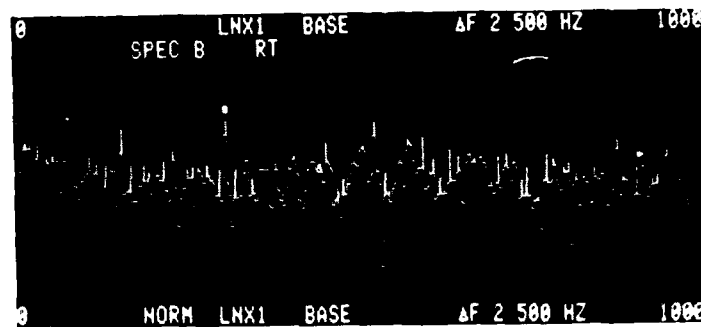
2 Magnets - 3900 RPM
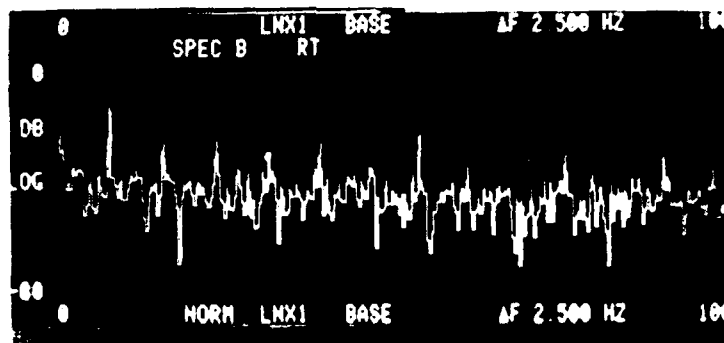
1 Magnet - 4405 RPM

Figure 86.   Response Spectra Due to Magnetic Excitation.

199

7.3. UDRI AND UTRC PLANE-OF-LIGHT SYSTEMS EVALUATION TESTS

An AEDC NSMS Evaluation test series was conducted during the week 11-15 April 1988. While the disk was running at constant speed with peak response of each modal pattern, indicated by peaking of the signals from the accelerometers and crystals mounted on the disk as displayed on the spectrum analyzer screen, UDRI recorded blade tip deflection data on the ISRL NSMS data system; while UTRC, as the AEDC NSMS contractor, recorded blade tip deflection data on the AEDC NSMS data system. Also, a triple-pulse holographic interferogram (50) was recorded on film from the ISRL optical instrumentation system. UDRI reduced the ISRL NSMS data and compared it to the AEDC NSMS data and the holographic data.

7.3.1 First Test Series

In the first test run, six permanent magnets spaced at 60 degree intervals on alternating sides of the disk at the 3.75-inch disk radius and spaced 5/16 inch from each surface produced a 3D mode fixed in space (a backward traveling 3D mode on the disk at the disk rotational speed) with peak disk response occurring at 3,732 rpm. The photograph in Figure 87 shows the rotating disk deflected in 3D standing wave. The test run was recorded by UDRI with zero response reference runs recorded first at 1,500 and 3,000 rpm for use in the data reduction programs. UTRC recorded a resonance data set and then asked to record spin-up and spin-down runs through resonance as additional data sets. When these runs were made, we found that a broad resonance peak occurred more or less continuously from 3,700 to 3,850 rpm with a normal onset at the lower speed but an abrupt dropoff at the higher speed. Resonance onset then could not be achieved until the rotational speed was reduced to about the midpoint of the resonance speed range.

With the magnet-disk gaps at 5/16 inch, a number of holograms were made of the 3D integral mode at 3,720 rpm. UTRC then recorded an AEDC NSMS data set at 3,720 rpm followed by a reference data set at 3,720 rpm with the excitation magnets removed.
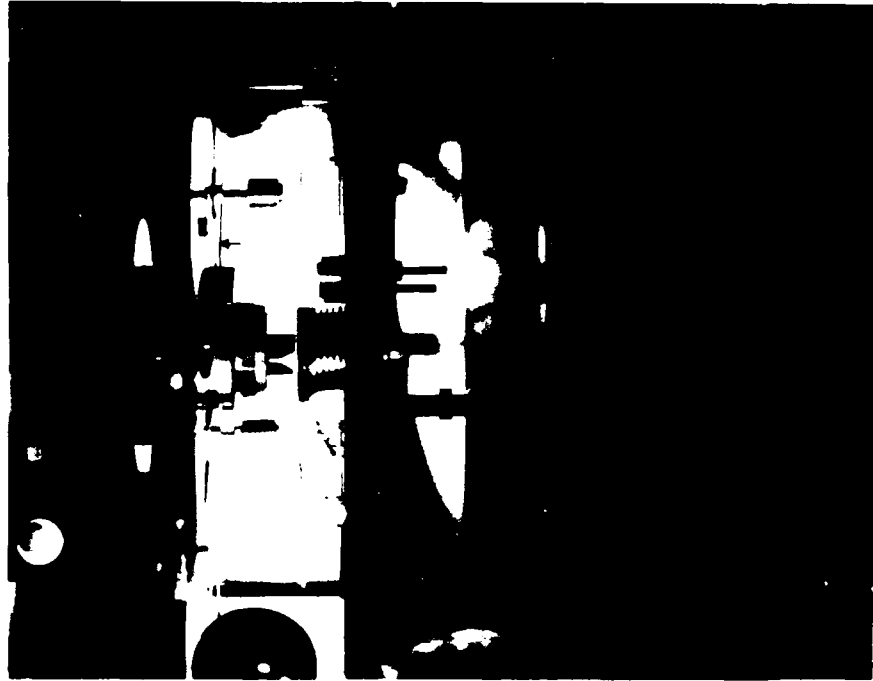
Figure 87.   Rotating Disk Deflected in 3D Mode.

For the next test, four magnets were installed at 90-degree intervals and 5/16-inch spacing from the test disk to excite the 2D integral mode. We found that if the disk was accelerated very slowly, the resonance could be extended from 3,600 to 4,300 rpm before it collapsed. UTRC then recorded the 2D blade deflections at ˆ,920 rpm on the AEDC NSMS and recorded a reference data set at speed with the magnets removed. Since the interferograms recorded earlier for 3D, have displayed unresolvable number of fringes, we decided to reduce the disk response amplitude by reducing the excitation force due to stationary magnets. The magnets then were set at 7/16 inch from the disk and the 2D mode was recorded on the AEDC NSMS, on the ISRL NSMS, and on a series of triple-pulse holograms at 3,780 rpm. The response amplitude was decreased nearly half by this lower excitation force, and the resonant frequency and response frequency range of the disk also were reduced, but the resonance response characteristic remained the same. Eight magnets then were installed at 7/16 inch from the disk to excite the 4D mode. Again, the same response characteristic of the disk occurred. The response peak seemed highest at 3,630 rpm, and data were taken there on the two NSMS systems and on holographic film.

Six magnets were installed at 7/16 inch from the disk to repeat the 3D mode test at the same excitation level used for the 2D and 4D modes the previous day, which had seemed to produce the desired number of fringes on the holograms. Then the hologram reference beams were also adjusted to remove the apparent fringe muddling. The 3D modal data then was recorded by the three instrumentation systems. Again, we found that the resonance frequency could be sustained over a range of about 300 rpm with a sharp collapse and instantaneous phase shift of the response at the upper speed (or frequency) limit of the resonance, suggesting a nonlinear disk response.

During the course of this testing program, UDRI recorded response data on the ISRL NSMS for the 3D mode with 5/16-inch magnet spacing and for the 2D, 4D, and 3D modes with 7/16-inch magnet spacing. For each of those records, reference data were

taken immediately before or immediately after the modal data at 1,500 and 3,000 rpm where no disk response was indicated by the monitoring instruments on the disk or in the recorded reference data. The ISRL NSMS data records are listed in Table 34.

Similarly, data were recorded on the AEDC NSMS for these conditions, but the reference data for these records were taken at the same rpm as the resonance data with the excitation magnets removed. No accel or decel data were taken on the AEDC NSMS because of the nonlinear response characteristic of the test disk. We were later informed by the project monitor that none of the holographic data was useful except that which was recorded for the 3D mode.

TABLE 34
AEDC NSMS EVALUATION TESTS - FIRST TEST SERIES
ISRL NSMS DATA SYSTEM TEST RECORDS
APRIL 12-15, 1988

Date	Run #	Mode	Magnet Gap (Inch)	RPM	Data Type	Remarks
4/12	1A	3D	5/16	1500	Reference Speed 1	No AEDC Data
	2A	3D		3000	Reference Speed 2	ISRL Data OK
	3A	3D		3732	Resonance Data	No Phase Records
4/14	4A	2D	7/16	3780	Resonance Data	ISRL & AEDC
	5A	2D		3000	Reference Speed 1	Data OK
	6A	2D		1500	Reference Speed 2	No Phase Records
4/14	7A	4D	7/16	1500	Reference Speed 1	ISRL & AEDC
	8A	4D		3000	Reference Speed 2	Data OK
	9A	4D		3630	Resonance Data	Small Phase Change
4/15	10A	3D	7/16	1500	Reference Speed 1	
	11A	3D		3000	Reference Speed 2	
	12A	3D		3560	Resonance Data	No Real Resonance

7.3.1.1 Nonlinear Response Studies of the Disk

As mentioned previously, one of the plans during the April test series was that UTRC wanted to accomplish two types of data collection and data reduction with the AEDC NSMS instrumentation system. The first of these was for steady-state

data collected at the peak modal response for the 2D, 3D, and 4D resonant modes of the test disk. The second was for data collected during spin-up and spin-down through each resonance response, the so-called accel and decel test runs. However, during testing we found that the test disk displayed nonlinear response in that a normal onset of resonance with a gradual phase shift was not displayed during spin-up to resonance, but that an abrupt collapse of response with an accompanying immediate phase shift occurred as speed was increased through the resonance response range. Then as speed was decreased back through the resonance range, an abrupt response onset with an immediate phase shift occurred at a considerably lower spin speed within the spin-up resonance response speed range. This resonance characteristic is shown in Figures 88 and 89 for 2D and 3D response modes for small magnet gap settings.

We thought that the nonlinear response of the test disk was a function of the strength of the force field of the excitation magnets. A number of test runs then were made with magnet spacing from the test disk varied from 5/16 inch to 9/16 inch, but the same nonlinear type of response was shown during all test runs. UDRI then was asked to try air-jet excitation of the test disk. This was accomplished in early May of 1988 with two small air jets supported at 3/8-inch spacing from each side of the disk to excite the 2D modal response. The results of this test, shown in Figure 90, indicated the same nonlinear response.

Subsequently, at a meeting between UDRI and APL/POTC personnel, it was decided to attach stiffener plates of 2.25-inch diameter and 0.115-inch thickness to each side of the hub area of the instrumented test disk in the expectation that this would improve the linearity of the modal responses. UDRI fabricated the plates, removed the slip ring hub, installed the plates with high-strength HySol EA934 epoxy adhesive, and re-installed and rewired the slip ring hub set. Then tests were conducted to determine if the reinforced-hub test disk possessed nonlinear behavior in nonrotating conditions. The test disk was hard mounted and was driven by an electromagnet exciter at a constant level of excitation voltage but with different gaps
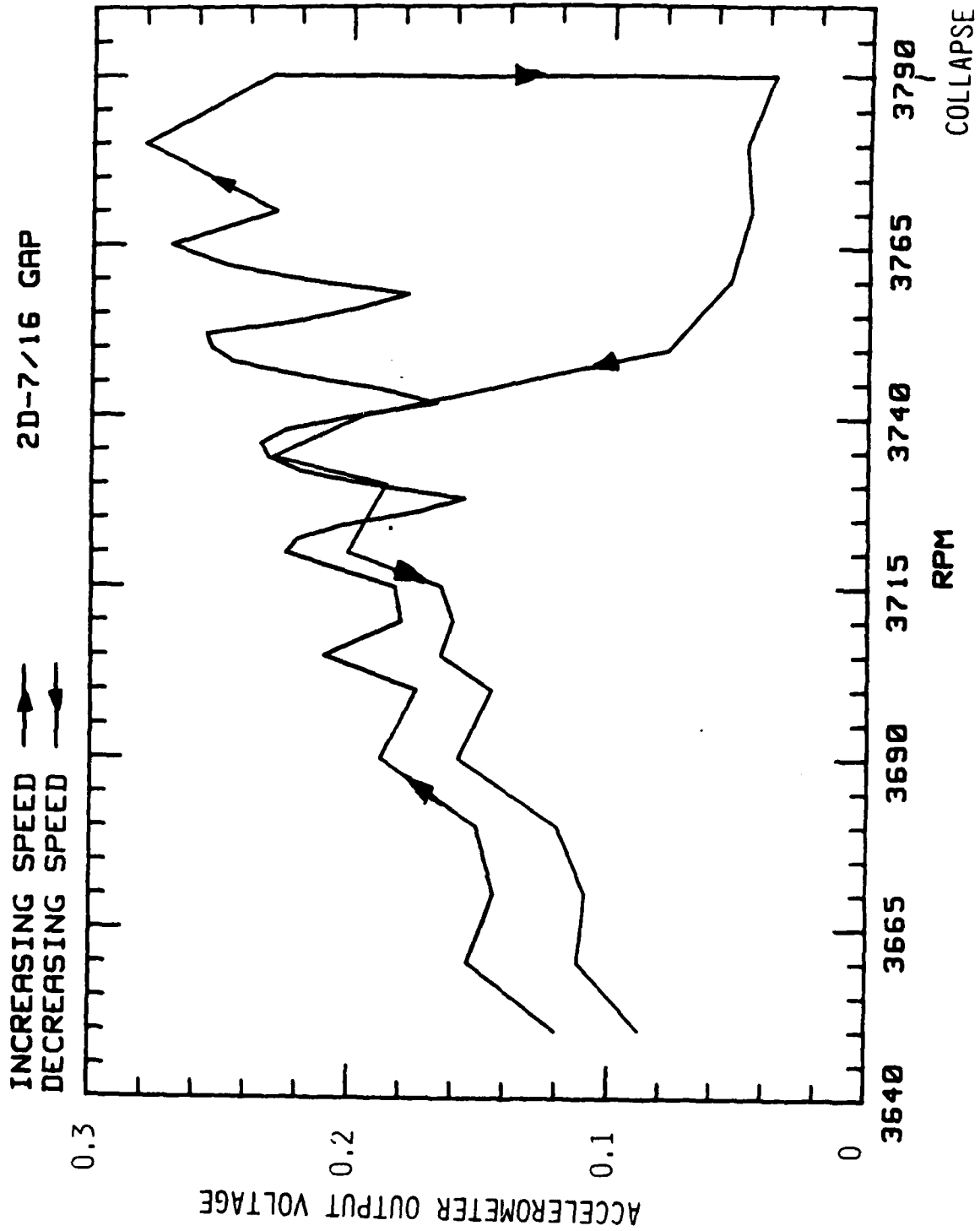
Figure 88.   2D Mode Amplitude Collapse Due to Disk Nonlinearty.

1/2" GAP - April 29, 1988 - 3E Excitation, 3D MODE
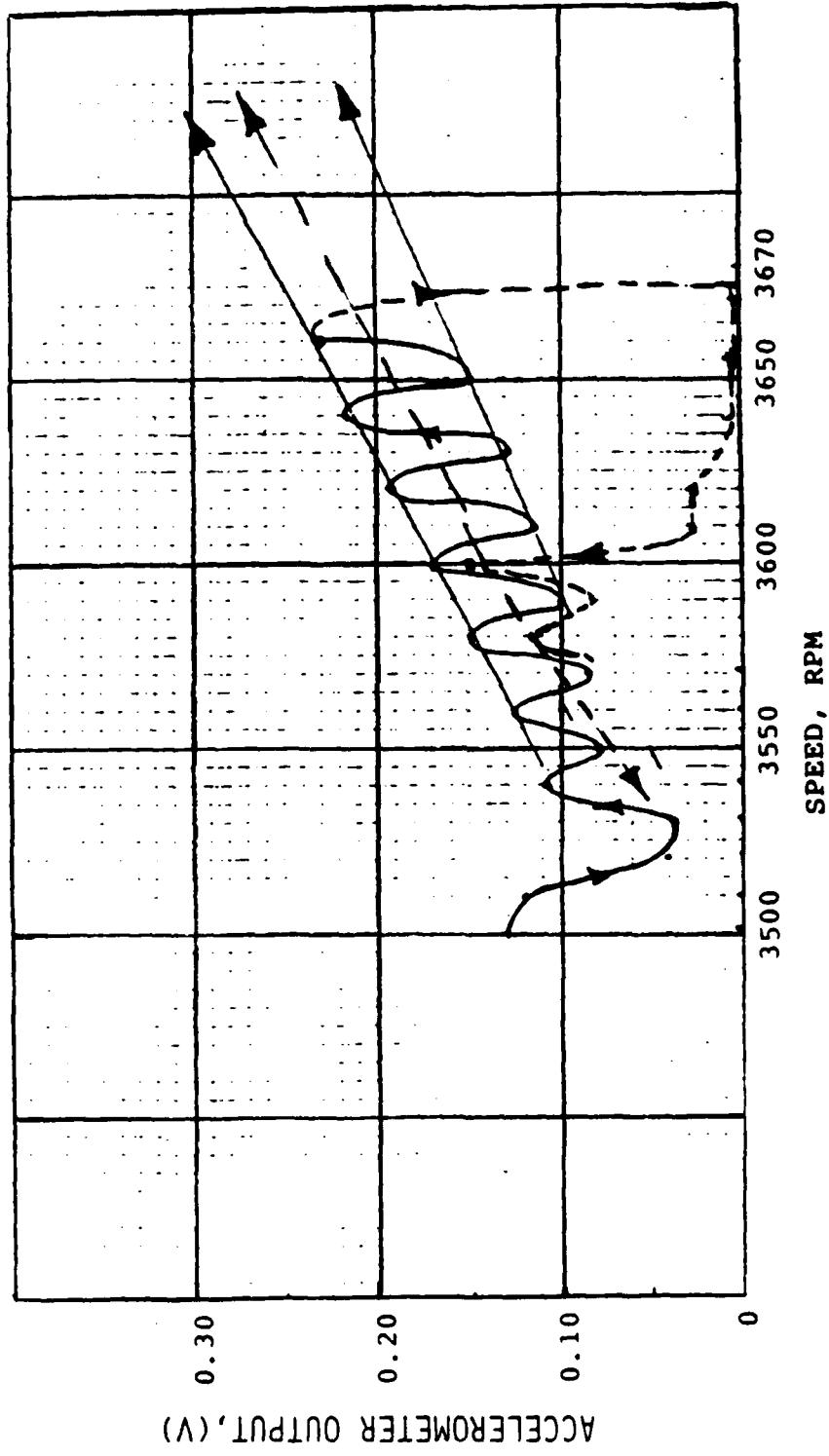
Figure 89. 3D Mode Amplitude Collapse Due to Disk Nonlinearty.

4 Airjets, 3/8" GAP, 70 PSI, 1/16" Dia Nozzles
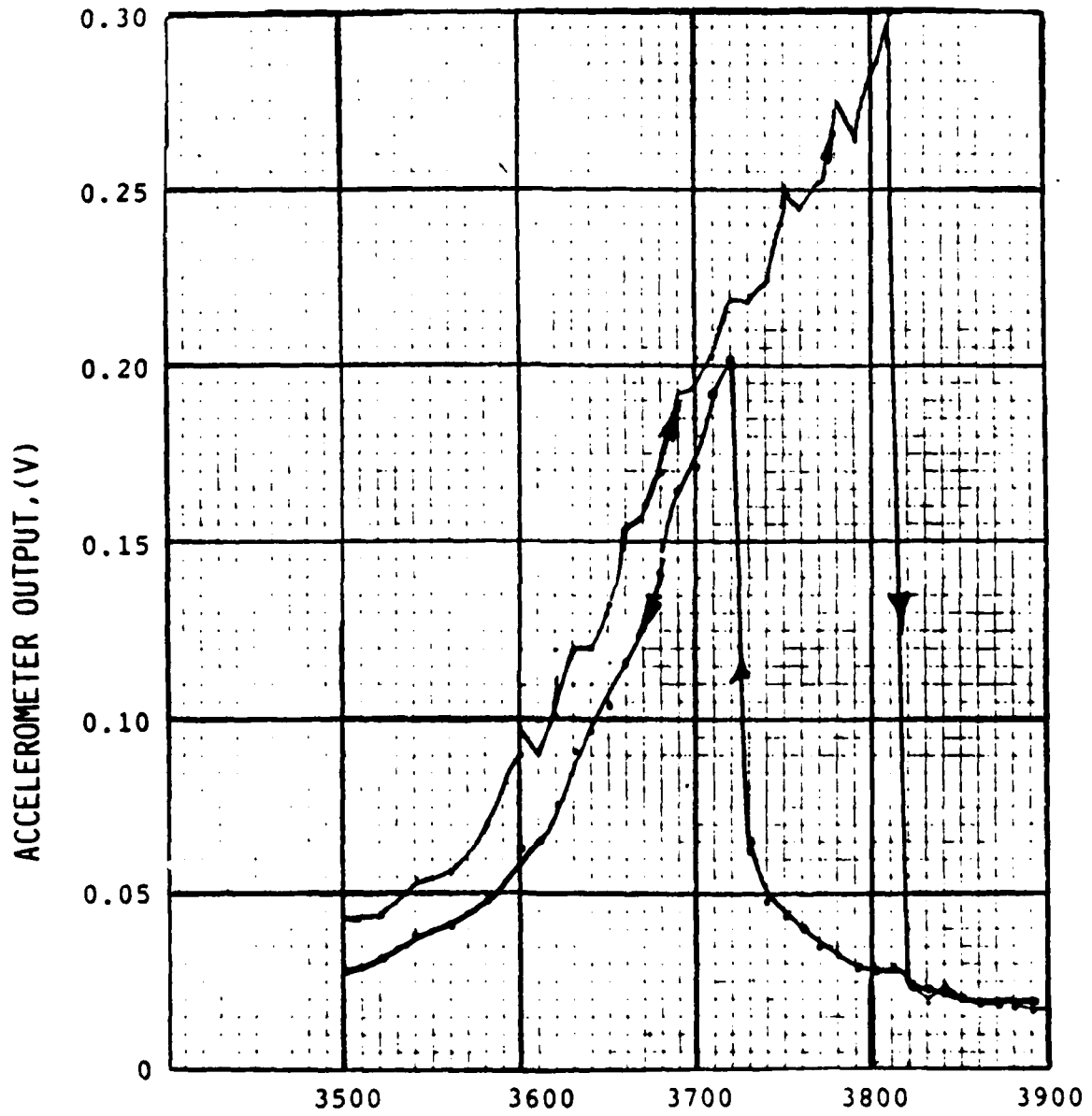
Figure 90. Disk Nonlinear Response Under Air
Jet Excitation.

between the electromagnet and the test disk. The static test results shown in Figures 91 and 92 indicated that the disk behaved like a soft spring. Variation of response frequency with amplitude of excitation force decreased with an increase in the mode number of vibration. For example, leftward shift of the response frequency peak with higher excitation force was more pronounced for 1D as compared to the 3D and 4D modes.

After the static vibration tests were completed, the disk was reinstalled in the spin test setup and was excited in the 2D mode at various magnet gap spacings from the disk. The results of five successive runs in which the magnet gaps were increased from 3/8 inch to 5/8 inch in 1/16-inch increments indicated that the disk now displays a linear response in the 2D mode if the magnet gaps were 9/16 inch or greater, as seen in Figure 93. The response amplitude, however, was reduced appreciably at the larger magnet gaps and the accelerometer output amplifier gain was doubled when the magnet gaps increased from 1/2 inch to 9/16 inch.

7.3.1.2 Triple Pulse Holographic Interferometry Problem and Its Diagnosis

One of the requirements introduced by UTRC for the triple-pulse, double-image holograms was exact measurement of the pulse spacing between the first and second pulses, which produce the first interferogram, and the second and third pulses, which produce the second interferogram. The exact times were needed to establish the frequency and phasing of the two images. The desired time intervals were 10 μsec between the successive pulses. UDRI monitored some triple-pulse events with a high frequency oscilloscope, but pulse intervals could be measured with confidence only to 1 μsec accuracy on the oscilloscope screen.

However, during the study of the pulse interval timing problem, we found that the Appollo ruby laser often produced spurious pulses. Sometimes as many as five or six pulses occurred, as shown in the oscillograph screen pictures of Figure 94. Careful study of the three storage circuits of the triple-pulse system showed a shorted silicon controlled rectifier (SCR), a missing

208
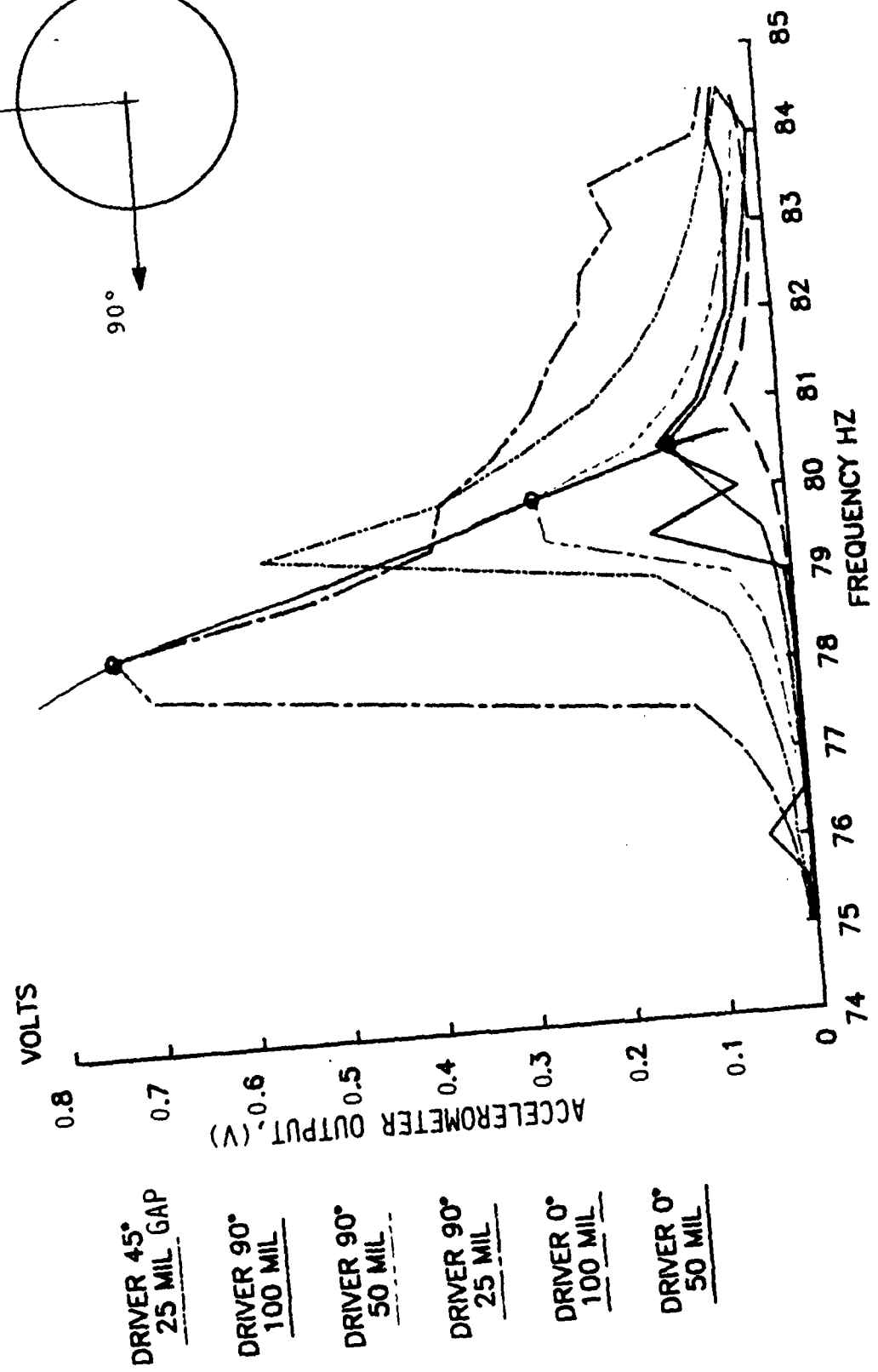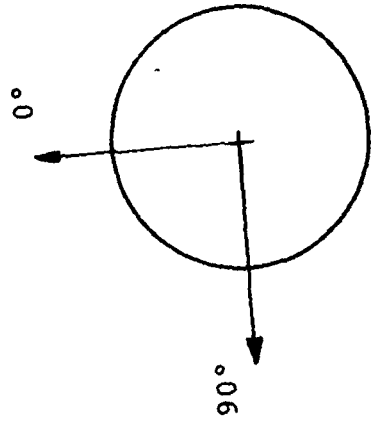
Figure 91. Hub Stiffened Static Disk Frequency Response – 1D.

209
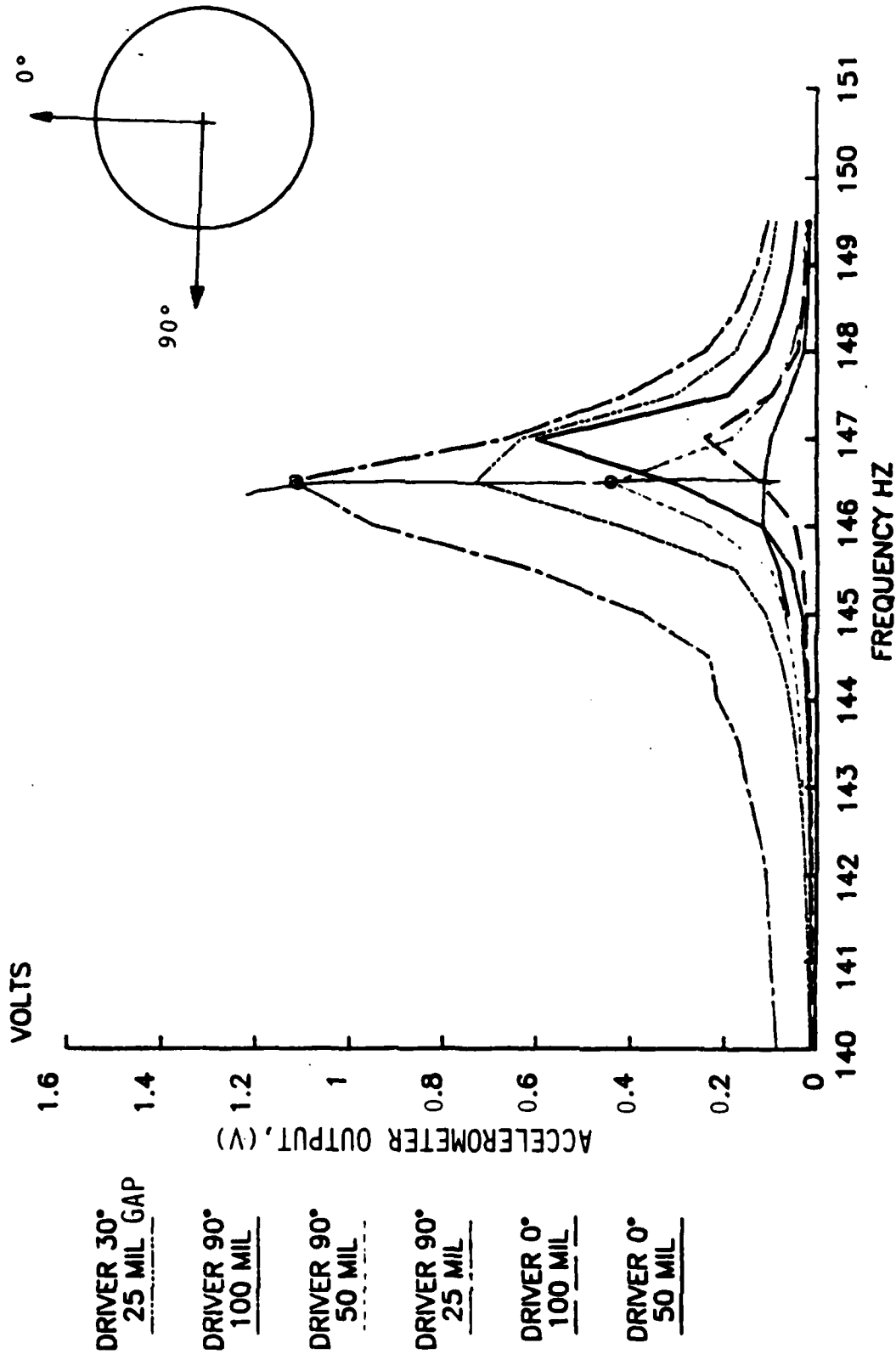
Figure 92. Hub Stiffened Static Disk Frequency Response - 3D.

210
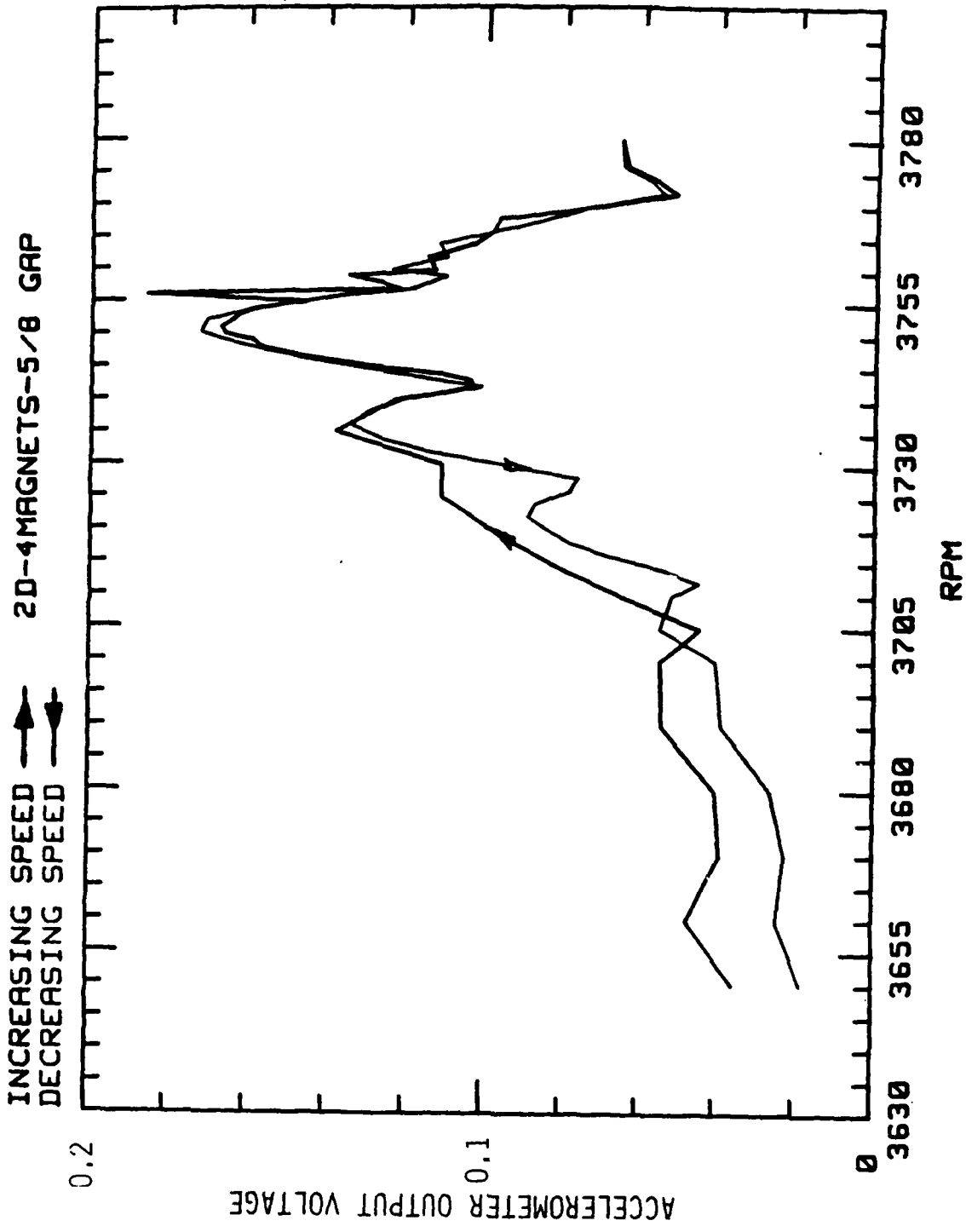
Figure 93. Linear Response of the Test Disk with Large Magnet
Spacing.
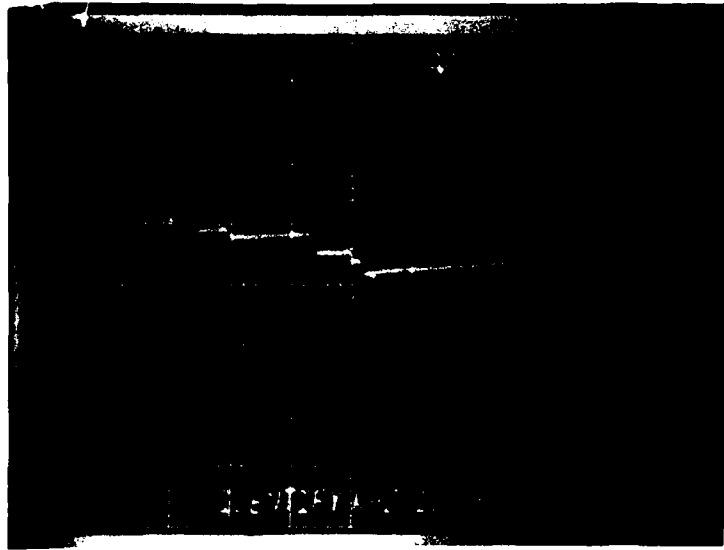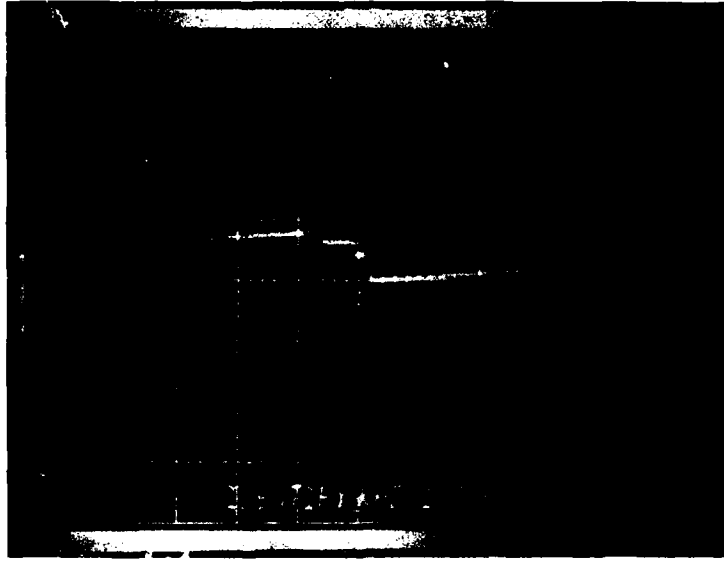
Figure 94. Multi-Pulse Operation of the Ruby Laser.

diode, and a thyratron that sometimes broke down spontaneously at normal operating voltage, all in the energy storage circuit for the third laser pulse. Obviously, the multipulses occurred because of the faults in that circuit. We (a) checked the power storage, the voltage sensing, and pulse-timing circuits of the laser power head; (b) identified and replaced a shorted silicon controlled rectifier and missing diode; and (c) reduced the high voltage level on the third Pockels cell to an acceptable level. These efforts had resulted in suppressing the spurious pulses of the laser, but the system seldom produced the desired triple-pulse train. Note that at every stage of modification, output of the sensing photo diode and the input to the internal Pockels cell were monitored and displayed on a digital storage oscilloscope. We were convinced from these oscilloscope records that the changes incorporated into the circuitry of the laser power supply unit had altered the thresholds of the three firing thyratrons, and a new set of optimum voltage settings needed to be established for the Pockels cells to produce a triple-pulse train with a specified time of separation between pulses.

Phone conferences were held with Mr. Ralph Page of the Appollo Co., and he suggested that, contrary to what was prescribed in the system operations manual, triple-pulsing was more easily achieved by first adjusting the third pulse circuit, then the second and the first, instead of the specified ascending order. He also said a success rate of greater than 30 percent was not to be expected for the triple-pulse system. By following his directions, UDRI was able to achieve a triple-pulse success rate of about 25 percent for either 10 or 25-μsec pulse intervals.

After restoring the system to its triple pulse operation with pulse separation accuracy of 1μs as displayed in Figure 95, several triple-pulse (sequential double pulse) holograms were tried while the test disk was in resonance. The three pulses were achieved by sequential switching of the laser head three internal and the two external Pockels cells. But it was discovered that even when no third pulse was displayed on the pulse monitoring scope, the reconstructed image contained spurious fringes. This
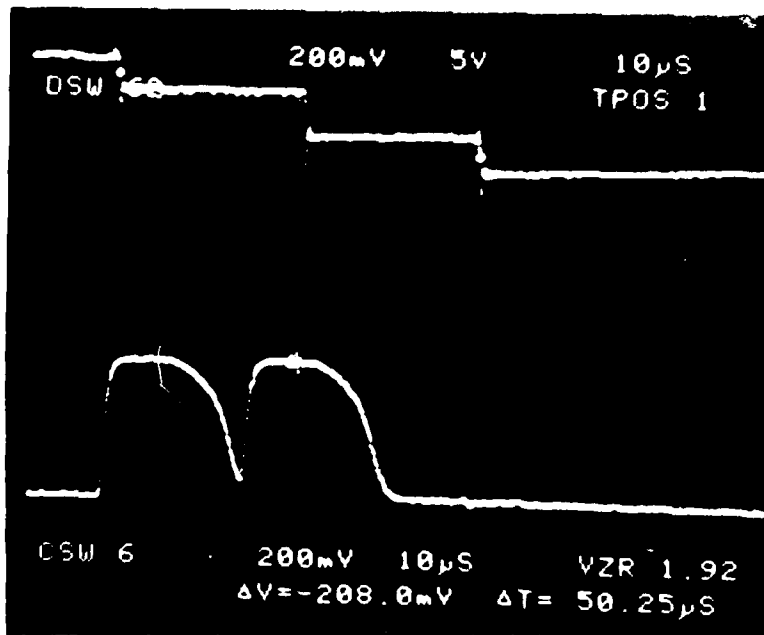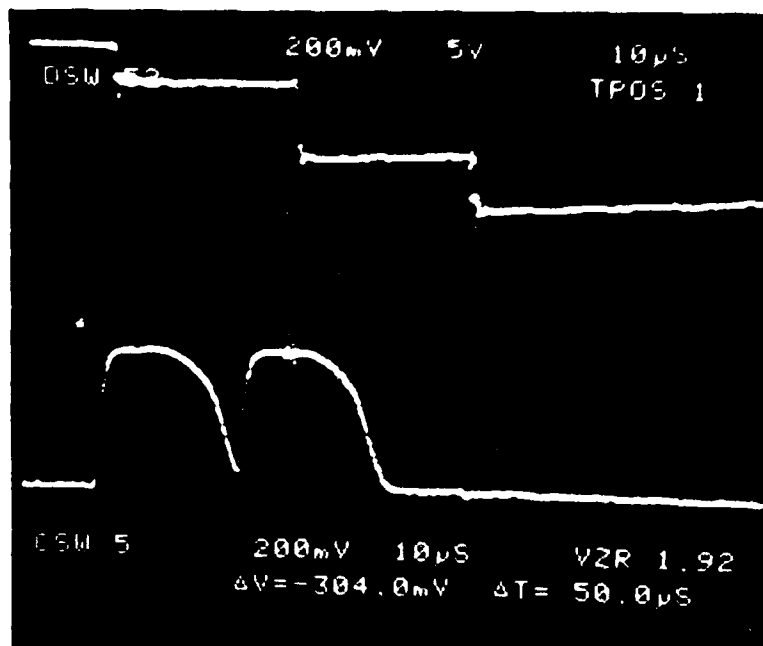
Figure 95.   Pulse-Separation Measurement.

fact led us to believe that the external Pockels cells in the reference path had a poor extinction ratio and allowed light passage when it was intended to completely block a laser pulse. This leakage of laser light through one of the external Pockels cells combined with the hologram due to the two intended pulses produced an effect similar to Moire. One such sample interferogram was enclosed in Figure 96 to show the difficulty in interpreting such holograms. An attempt to quench the leakage by placing a combination polarizer-filter in front of the Pockels cells proved to be a failure as the same effect was seen in the interferograms produced by the system. It was concluded at this stage that the trouble was in the delay lines and pulse forming networks of the external Pockels cells control voltages, causing them to attain inconsistent and inadequate extinction levels, or in the Pockels cells themselves.

Meanwhile, UTRC had agreed to utilize double pulse holograms (51) to determine the modal deformation of the resonating disk and accordingly requested us to proceed to record double pulse interferograms for the test disk while in resonance.

7.3.2 Second Test Series: Even Probe Positions

The second test series was required for the following reasons: (a) sequential double-pulse or triple-pulse holograms recorded on the first test series were unacceptable due to Moire type fringes in interferograms, (b) AEDC NSMS data analysis had produced unsatisfactory results for two out of the three disk response modes, and (c) the occurrence of abrupt collapse of the disk response modes without gradual phase change muddled the UTRC single degree of freedom analysis method.

For this second test series, the linear dynamic characteristics of the test disk had been improved by installing a 2.25-inch-dia. x 0.11-inch-thick stiffener on each side of the disk in the hub area. Also wider spacing was used between the disk and the excitation magnets.

Test matrix objectives and test conditions for this second series remained the same - excitation magnets were

Figure 96. Triple Pulse Interferogram of the Disk with Split Fringes.

positioned on alternate sides of the disk on circles of 3.75 inches radius to excite a specific mode, and ISRL optical probes were positioned with angular spacings of 60, 40, and 30 degrees to measure the 2D, 3D, and 4D mode responses, respectively.

Test dates with run numbers and test conditions were provided in Table 35.

The first test in this series was with magnet gap spacing of 5/8 inch from the disk and with 25 μs for triple-pulse separation. Interferograms corresponding to Runs #1B and #2B contained an unresolvable number of fringes, indicating large displacements. The gap was increased to 3/4 inch in Runs #3B and #4B. AEDC NSMS on site data analysis by UTRC yielded no useful data because of high signal to noise ratios in the optical probe data. Threshold levels for their trigger device was altered, blade tips were refurbished, and the Argon laser output was trimmed. The subsequent test runs (#5B, #6B) were useful. Triple-pulse holography was pursued until now. Later a decision was made to discontinue triple-pulse efforts and record double-pulse holograms at resonance, before resonance, and after resonance. The off-resonance holograms would provide qualitative phase information as the disk transited through resonance.

Double pulse holograms were made for 4D (Runs 7B through 10B and 17B and 18B), for 3D (Runs 11B through 16B), and for 2D (Runs 19B through 22B) with a variety of exciter spacings and pulse separation times. Two data sets for every test condition, one at resonance and the other at off-resonance speed (usually at 3,000 rpm for ISRL and resonance speed without magnets for UTRC) were acquired. Tests were conducted at various magnet gap spacings from 9/16 to 15/16 inch to meet AEDC NSMS data range requirements.

7.3.2.1 AEDC Disk Spin Up and Spin Down Test

At the end of the standard test series that acquired response of the disk in its resonance modes, spin up and spin down tests were conducted for the AEDC NSMS one sensor method. Response amplitude of a disk accelerometer was monitored while the

TABLE 35
AEDC NSMS EVALUATION TESTS - SECOND TEST SERIES
ISRL DATA RECORDS
JULY 27 - AUGUST 5, 1988

Date	Run #	Mode	Magnet Gap (Inch)	RPM	Data Type	Remarks
7/27	1B	4D	5/8	3648	Resonance Speed	ISRL Data OK
	2B	4D		3000	Reference Speed	AEDC-No Data Holograms bad
7/28	3B	4D	3/4	3646	Resonance Speed	ISRL Data OK
	4B	4D		3000	Reference Speed	AEDC-No Data Holograms bad
7/29	5B	4D	3/4	3640	Resonance Speed	ISRL Data OK
	6B	4D		3000	Reference Speed	AEDC Data OK Holograms bad
8/1	7B	4D	5/8	3644	Resonance Speed	Good Data
	8B	4D		3000	Reference Speed	
8/2	9B	4D	5/8	3636	Lower Half Power Point Speed	Good Data
	10B	4D		3648	Upper Half Power Point Speed	
8/3	11B	3D	5/8	3642	Resonance Speed	
	12B	3D		3632	Lower Half Power Point Speed	Good Data
	13B	3D		3646	Upper Half Power Point Speed	
	14B	3D		3000	Reference Speed	
8/4	15B	3D	3/4	3633	Resonance Speed	Good Data
	16B	3D		3000	Reference Speed	
8/4	17B	4D	9/16	3642	Resonance Speed	Good Data
	18B	4D		3000	Reference Speed	
8/5	19B	2D	15/16	4063	Resonance Speed	Good Data
	20B	2D	15/16	4058	Near Resonance Speed	
	21B	2D		3000	Reference Speed	
	22B	2D		4058	Reference Speed Without Magnets	

218

disk transited through resonance. Amplitude changes due to speed change in steps of 1 rpm on either side of resonance were recorded for the 2D, 3D and 4D modes. Phase change while the disk went through resonant speed was observed by monitoring the accelerometer output signal as triggered by the 1PPR signal. A smooth phase change of nearly 90 degrees was observed for the 4D mode when the magnet gaps were 3/4 inch. This data set was not acquired during the first test series due to nonlinear behavior of the disk.

7.3.3   Third Test Series: Uneven Probe Positions

These tests were requested by the AEDC to verify the accuracy of an algorithm used by UTRC for uneven probe positions around the circumference of the bladed disk. Since large displacements were the prime concern, large excitation forces were achieved by placing the excitation magnets close to the disk.

After the test setup and data acquisition systems were prepared, 11 test runs as detailed in Table 36 were made on the following day. For each test, both the magnet and AEDC probe settings were changed to the desired positions, and the test disk was quickly spun up to its resonance. Data were concurrently recorded by the UDRI NSMS with its probes at 60, 40, and 30 degrees for the 2D, 3D, and 4D modes, respectively.

Holographic images for this test series were
not recorded due to the film transport shutter malfunctioning.

7.4.   MODE SHAPES OF ROTATING DISKS BY LASER INTERFEROMETRY

The double exposure laser interferometric technique was employed to record the mode shapes of the rotating disk. The least possible pulse gap of 10 microseconds between the two consecutive pulses was required to provide a minimum countable number of fringes on the surface of a vibrating bladed disk (52). Two sets of tests were conducted using the triple pulse ruby laser available ISRL. This technique provided quantitative interpretation of the interferometric fringes due to resonant vibrations of the test object (53) and served as a comparative tool for the Z-grid and plane-of-light sensor systems.

TABLE 36
AEDC NSMS EVALUATION TESTS – THIRD TEST SERIES
UNEVEN PROBE POSITIONS
AUGUST 24, 1988

Run #	Mode	Magnet Gap (Inch)	RPM	Data Type	Remarks
1C	4D	9/16	3648	Resonance Speed	ISRL and AEDC
2C	4D	9/16	3000	Reference Speed	Data Acquisition
3C	4D	9/16	3631	Resonance Speed	OK on ISRL
4C	3D	7/16	3600	Resonance Speed	No Data on AEDC
5C	3D	7/16	3000	Reference Speed 1	
6C	3D	No Magnets	3600	Reference Speed 2	
7C	4D	No Magnets	3631	Reference Speed 2 for Run 2C	
8C	2D	1/2	3000	Reference Speed 1	
9C	2D	1/2	4019	Resonance Speed 1	
10C	2D	1/2	4044	Resonance Speed 2	
11C	2D	No Magnets	4019	Reference Speed for Run 9C	

The double pulse interferometric method consists of comparing two consecutively recorded images of a vibrating disk rotating at a steady speed. The configuration of the optical setup used is illustrated in Figure 97. The rotational motion of the object was compensated by an image derotator, running exactly at half the speed of the object-disk. Circular polarization effects of the object beam were compensated by the addition of two quarter wave plates before and after the image derotator system. A 10-microsecond interval between two pulses of the ruby laser was achieved by a careful selection of appropriate voltage settings on the Q-Switch control of the power source of the laser and the
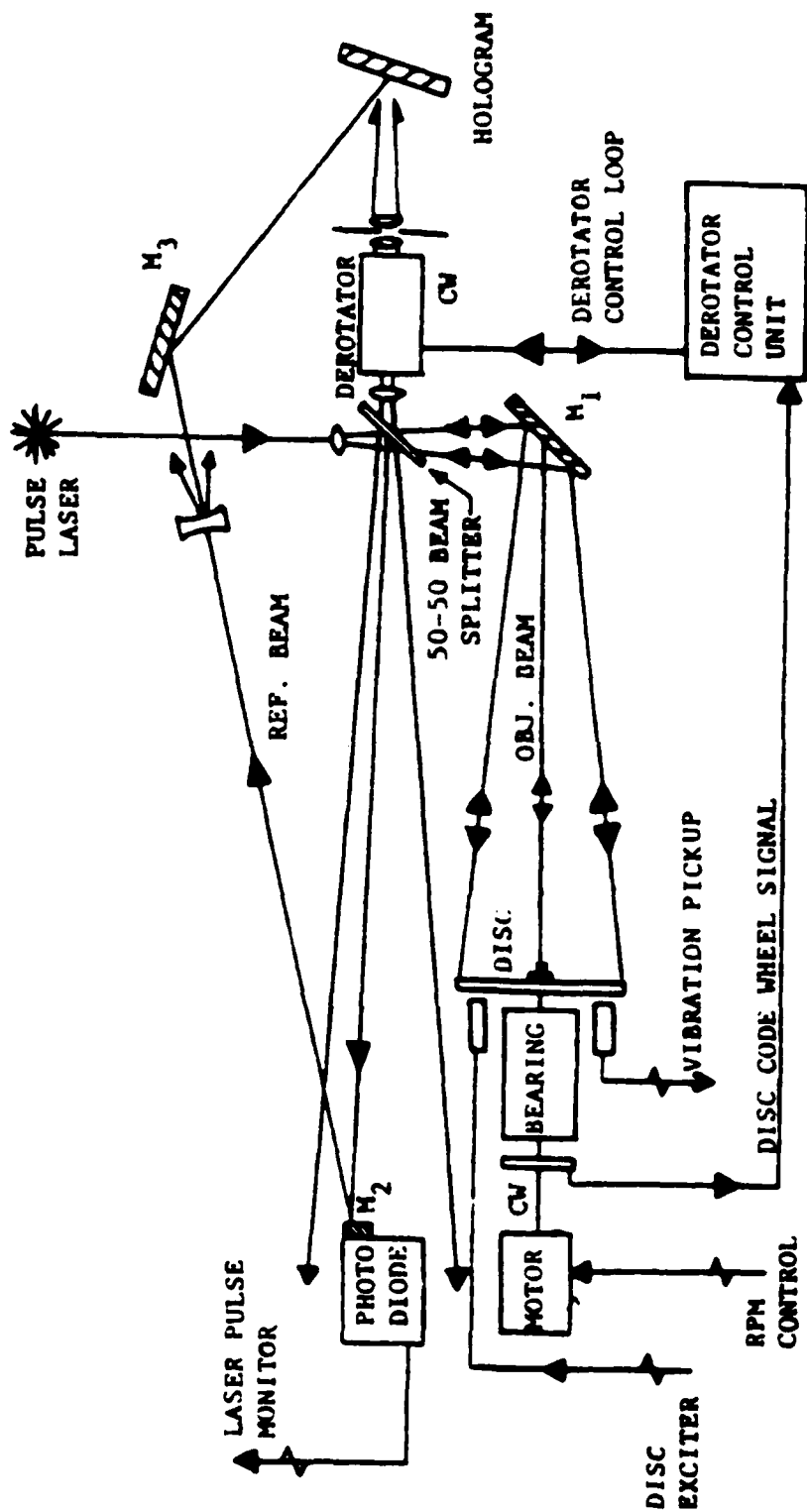
Figure 97. Optical Setup for Double Pulse Interferometry.

occurrence of double pulses was achieved by the instrumentation system, shown in Figure 98.

An important feature of the experiment was to initiate the first pulse of the laser at any point of time during a vibrating cycle of the bladed disk. An ideal point would be when a harmonically vibrating disk traverses the zero velocity point on the response cosine wave. For this purpose, a filtered acceleration signal was used as a reference, and a marker signal from the charge unit of the laser power supply was made to override the reference sine wave. It was possible to shift this marker to any point, and double pulse holographic images of the vibrating and rotating disk were made for marker positions of 45, 0, and 90 degrees on the response sine wave. This special control feature for initiating the first pulse of the ruby laser was achieved by the scheme shown in Figure 99. After the instrumentation was prepared, several diametral modes of the test disk at its critical speeds with different magnet gaps were recorded.

7.5 INTEGRATED Z-GRID - NSMS INSTRUMENTATION TESTS

The instrumentation ring, which supported dual Z-grid rings and three plane-of-light sensors, was mounted concentric with the 11-inch-diameter, 50-mil-thick test disk. The grid system source magnet and its counter weight were cemented to diametrically opposite blade tips, with a gap of 60 mils from the grid wires.

A series of tests were conducted using the integrated Z-grid - NSMS system to define integral vibrations of the test disk in 2D, 3D, and 4D modes.

Test runs and test conditions are summarized in Table 37.

The sequence for the integrated system tests consisted of:

(a) setting up the excitation magnets to excite a specific disk mode;

(b) positioning the optical probes at appropriate positions in the support ring;
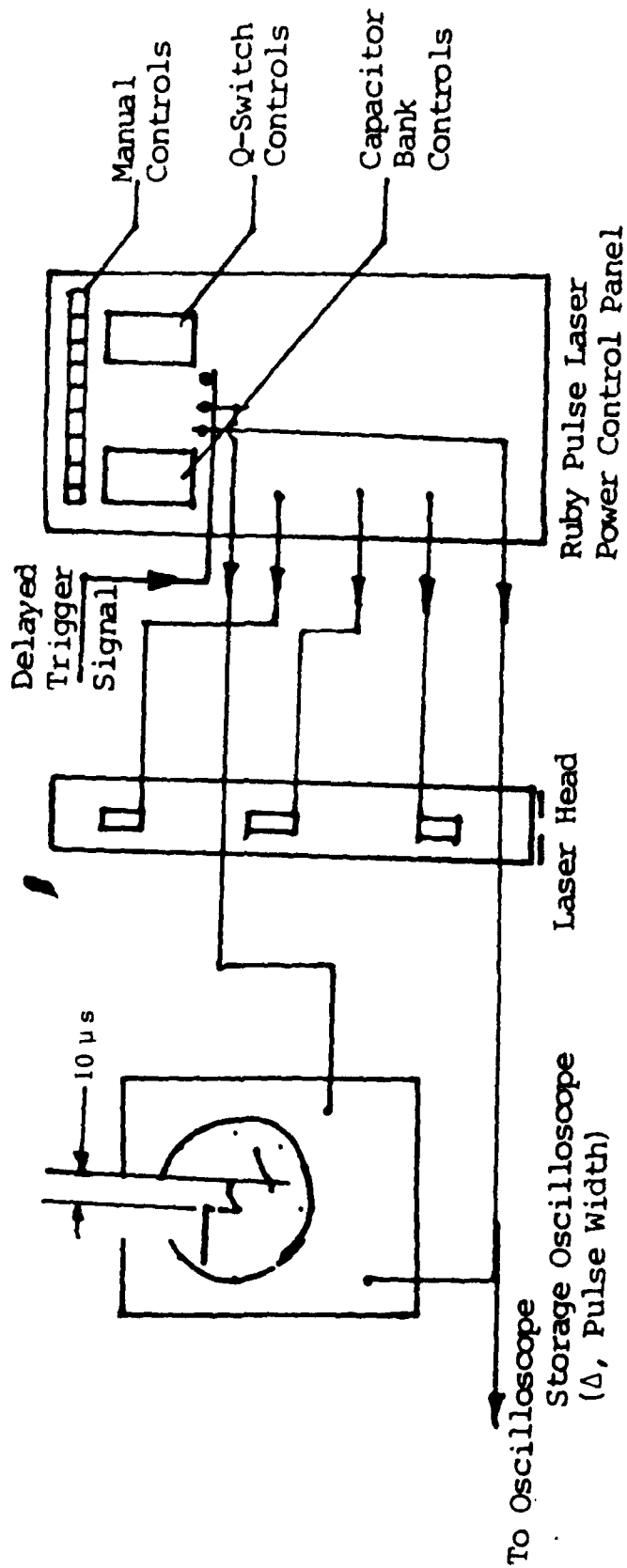
Figure 98. Double Pulse Settings for the Ruby Laser.

223

This marker can be set at
any point on Sine wave.

SA – Spectrum Analzer   KF – Kronhite Filler
CRO – Oscilloscope A_1, A_2 – Amplifiers
                               AC_1, AC_2 – Accelerometers
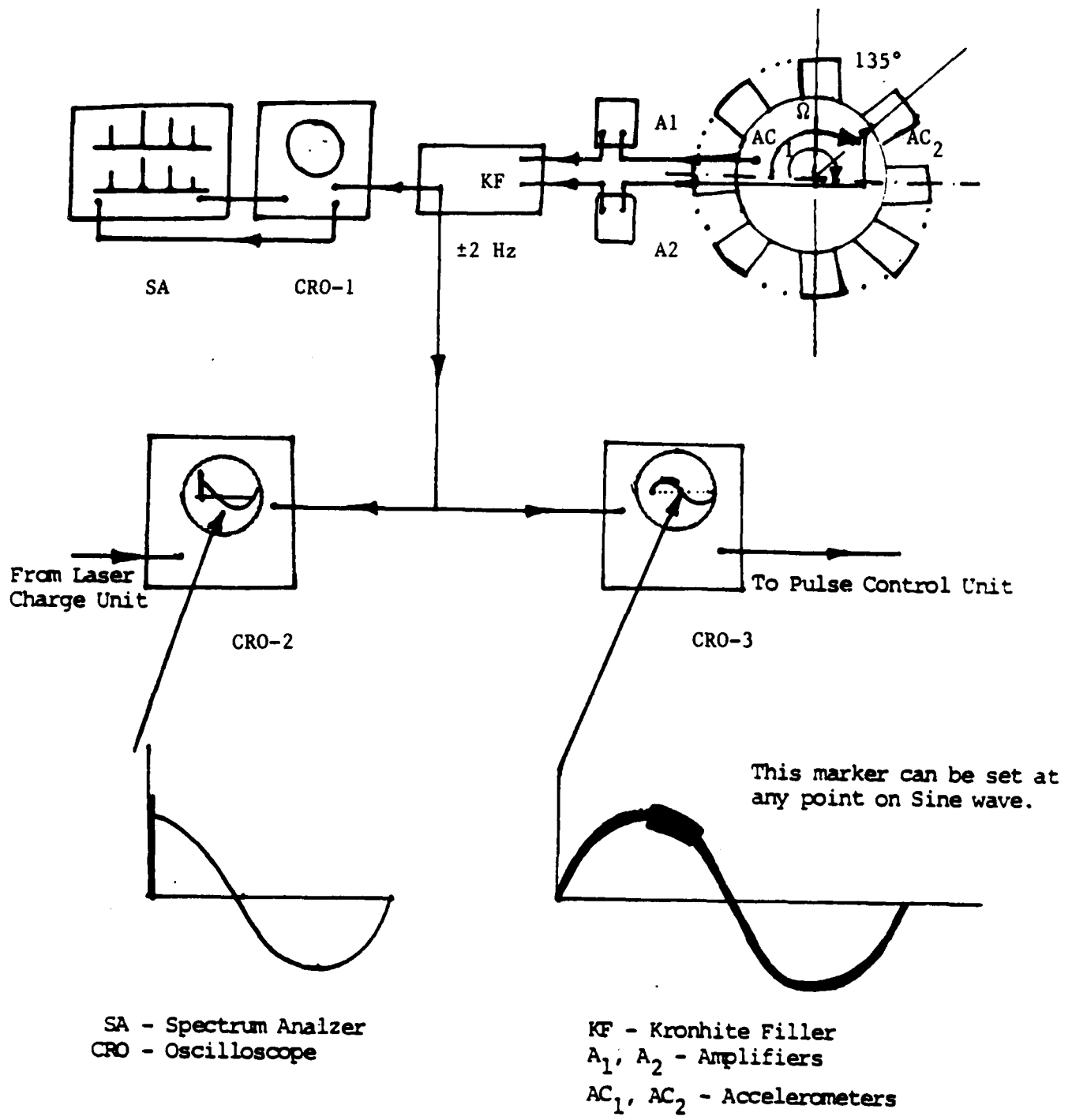
Figure 99.   Pulse Trigger Control and Display Instrumentation.

(c) ensuring the satisfactory functioning of optical and grid wire probes from histogram display; and

(d) recording a data set for each system.

When the disk was stabilized in its resonance, the plane-of-light sensors (ch. 2, 3, and 4) collected the blade deflection data. Also, an additional low response run of 3,000 rpm was recorded as reference data. Then, optical probes were disconnected from the signal conditioning unit and the two channels of the Z-grid system were connected to it as channels 3 and 4. A reference and resonance data set were recorded for the grid system under the same test conditions. The data were analyzed later on the VAX computer.

TABLE 37
THE INTEGRATED Z-GRID NSMS SYSTEM EVALUATION TESTS

Run #	Mode	Magnet Gap (Inch)	RPM	Data Type
17ZG	3D	3/4	3000	Reference Data for Z-Grid
18ZG	3D	3/4	3657	Resonance Data for Z-Grid
19ZO	3D	3/4	3657	Resonance Data for NSMS
20ZO	3D	3/4	3000	Reference Data for NSMS
21ZO	2D	15/16	4063	Resonance Data for NSMS
22ZO	2D	15/16	3000	Reference Data for NSMS
23ZG	2D	16/16	3000	Reference Data for Z-Grid
24ZG	2D	25/16	4063	Resonance Data for Z-Grid

Runs 21 through 24 were repeated as the magnetic tape data were not retrievable.

Run #	Mode	Magnet Gap (Inch)	RPM	Data Type
29ZO	4D	9/16	3646	Resonance Date for NSMS
30ZO	4D	9/16	3000	Reference Data for NSMS
31ZG	4D	9/16	3000	Reference Data for Z-Grid
32ZG	4D	9/16	3646	Resonance Data for Z-Grid

Runs 29 through 32 were repeated to reanalyze the data.

SECTION VIII
RESULTS AND DISCUSSION

This research and development program developed and implemented advanced finite element based deterministic and probabilistic methods to analytically predict the normal modes of flexible bladed disks. An instrumentation system using either a four plane-of-light and dual Z-grid measurement head was developed, and the blade tip deflections of a rotating bladed disk in backward traveling wave resonance were measured. Full-field double pulse interferometric method served as reference for comparing the blade-tip deflections.

8.1 COMPARISON OF NATURAL FREQUENCIES OF STATIC AND ROTATING DISKS

Two flexible disk natural frequencies were analytically predicted. SAP, MAGNA, PROTEC, and NASTRAN programs (the first three for static disks and the last for both static and rotating disk analysis) were used.

The zero speed normal mode data was first derived from static bench tests and compared with normal mode analysis results from the NASTRAN and the other finite element methods. All analytical methods had predicted double frequencies for perfectly axisymmetric or tuned circular bladed disks. Small errors in twin mode frequencies were essentially due to numerical computational errors in the eigenvalue extraction procedures. Of the existing eigenvalue extraction methods in NASTRAN, only the Fast Eigenvalue Extraction method (FEEM) yielded quick (less CPU time/mode for the same size problem) and reliable double modes compared to other methods. SAP and MAGNA analysis methods were slow compared to any of the NASTRAN methods for the same accuracy level. Note, however, that the Mindlin plate theory based PROTEC analysis produced analytical frequencies which were closer to the experimental values for static disks. A 12-bladed 12-inch-diameter, 62.5-mil-thick steel disk and a 38-bladed 11-in.-diameter, 50-mil-thick steel disk were analyzed, and their static frequencies are compared in Table 38. The agreement was better in the former than the latter because

the clamping area for the 11-inch diameter disk was over a larger surface area due to a hub slip ring. This resulted in a smaller active annulus area for the disk. The frequency discrepancy varied from 4 to 8 percent, and the errors in modal frequencies were essentially due to the simplistic assumption of infinite rigidity assumed for the multichannel slipring assembly for the 11-inch disk over a 2-inch diameter hub area. A large concentrated mass due to the slipring, near the disk rotational axis also lowered the natural frequencies of the static disk.

TABLE 38

COMPARISON OF STATIC DISKS RESONANCE FREQUENCIES

Mode	12 Bladed 12" Dia. 5/64" Thickness Disk		38-Bladed 11" Dia, 50-mil Thickness Disk with a 2" Dia. Hub Slip-Ring and 0.1" Hub Stiffness	
	Analytical	Experimental	Analytical	Experimental
1D	77	69	80.5	--
OC	92	85	83.9	--
2D	110	105	100.4	95
3D	200	194	165.1	150
4D	277	270	244.0	226

Resonances for rotating disks occur differently for different load types. Under harmonic excitation, standing waves as a result of the superposition of forward and backward traveling waves build up on spinning disk, and these waves travel around the disk with respect to the disk. For example, if a rotating disk was excited harmonically at the frequency, $p = \omega \pm n\Omega$, where ω was the disk resonance frequency, n was the nodal diameter number, Ω was the rotational speed, the + sign for the forward traveling wave and the - sign for the backward traveling wave, the disk will resonate at the frequency ω. This type of disk excitation was achieved by our freon-cooled electromagnets in vacuum. These resonances for the

227

12-inch disk were compared with the NASTRAN (Rigid Format 13) predicted frequencies and the comparison was good, Table 39.

TABLE 39

COMPARISON OF STATIC DISKS RESONANCE FREQUENCIES

| | 12-Bladed 12" Dia. 5/64" Thickness Disk at 4,000 rpm | |
Mode	Analytical	Experimental
1D	104	108
0C	110	117
2D	143	153
3D	226	227
4D	298	298

A 38-bladed disk was designed for the integral order vibration tests. The disk, in these tests was excited by a static force field. From the equation $p = \omega \pm n\Omega$, when the excitation frequency $p = 0$, i.e., a static force, $\omega = n\Omega$ and only the backward traveling waves would be present in the disk. These resonant waves travel at the same speed as the rotating disk. The speed Ω is also called the critical speed. Integral order waves were excited, measured, and compared. The resonances were monitored by accelerometers, piezocrystals and strain gages. Spin tests were conducted to establish the disk critical speeds and were observed to be dependent on the excitation force levels. A comparison of the critical speeds was provided only when the disk exhibited linear response; i.e., when the magnet gap was 9/16 inch or greater from the rotating disk surface. The analytical and experimental results are compared in Table 40. The measured critical frequencies for the second and third diametral modes provided good agreement with the analytical prediction. An error of 1.5 percent for the 2D, 3D, and 5.5 percent for the 4D mode was present. Low measured frequencies were possibly due to overestimation of centrifugal force effects for the disk with a slipring mass at the hub. The 1D

228

critical speed mode was not measured because the lower branch of the traveling wave would intersect the speed axis at a speed much higher than the design speed of the drive shaft system. We decided not to run the tests at these high rotational speeds.

TABLE 40

NATURAL FREQUENCIES (HZ) OF 38-BLADED DISK WITH 2.0-INCH-DIA. HUB SLIP RING AT ZERO RPM AND AT CRITICAL SPEED

| Mode	Zero Speed		Critical Frequencies (Speeds) in RPM	
	Analytical	Experimental	Analytical	Experimental
2D	100.4	95	132 (3950)	135 (4058)
3D	165.1	150	185 (3640)	184 (3670)
4D	244.6	226	260 (3900)	251 (3760)

8.2 MODE SHAPE ANALYSIS

Static disk mode shapes were first determined by the time average holographic method in which image exposure time exceeded the period of oscillation by a minimum factor of two. Good correlation between the predicted and measured modes was observed. Spatically orthogonal dual modes were identified for both test disks, but only one set of the analytical and experimental dual mode shapes of the 38-bladed disk are enclosed in Figures 100a and 100b.

For the mode shape definition of rotating disks, double pulse interferograms were recorded when the disk was in resonance. Interferograms of the disk in 2, 3, and 4D modes are shown in Figure 101. Figure 102 shows typical displacement patterns for the 3 and 4 diametral modes for two excitation cases, recorded in 10μs pulse separation time. The peak-to-peak vibration amplitude of the harmonic wave was derived by sine extrapolation of fringes. The increase in fringe number for a larger exposure time was evident and typical holograms for 2D mode for 10 and 15 μs pulse separation were shown in Figure 103.

229
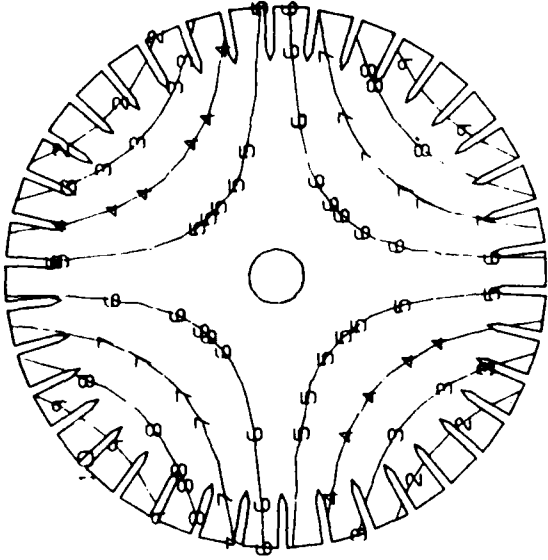
2D Mode – 84 Hz
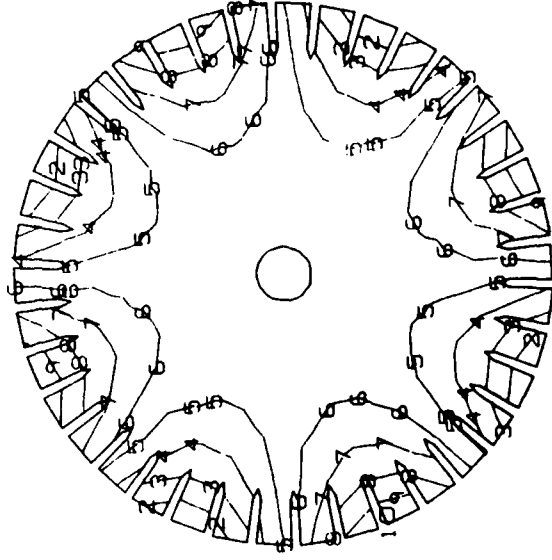
4D Mode – 244 Hz
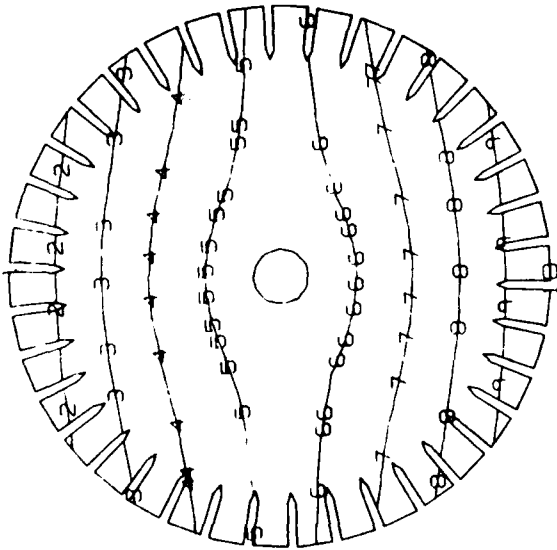
1D Mode – 58 Hz
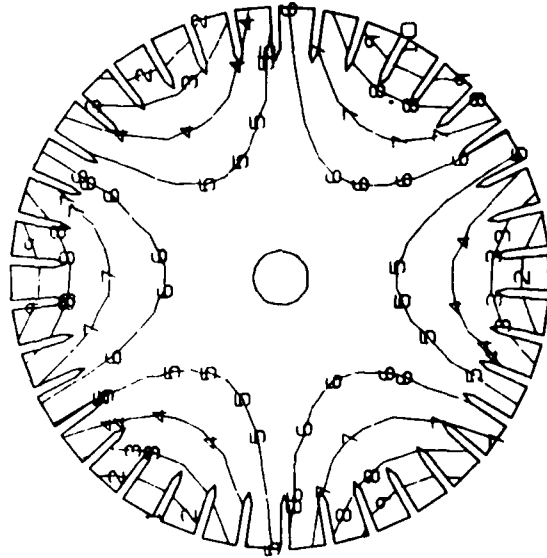
3D Mode – 162 Hz

Figure 100a. Analytical Mode Shapes of the Static Test Disk.
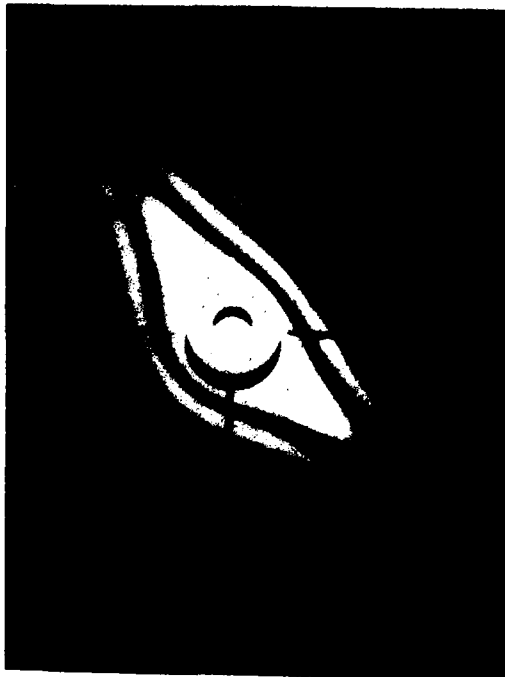
2D Mode – 87 Hz

4D Mode – 216 Hz

1D Mode – 65 Hz
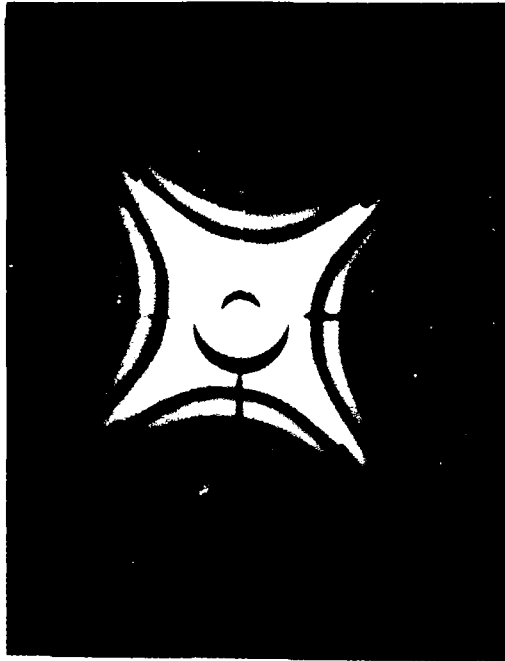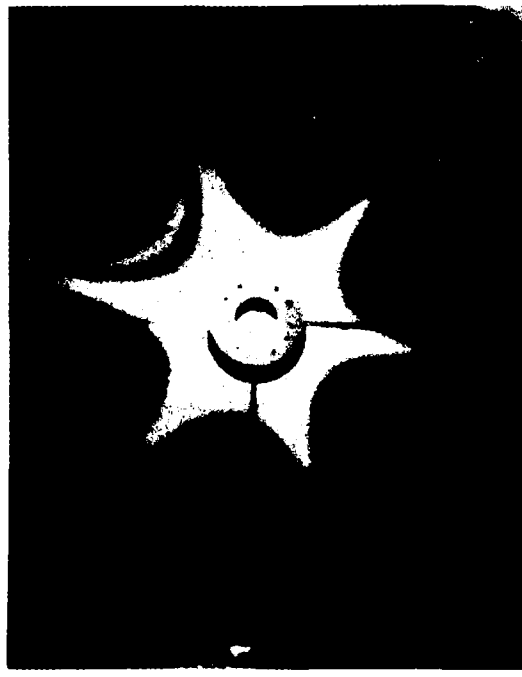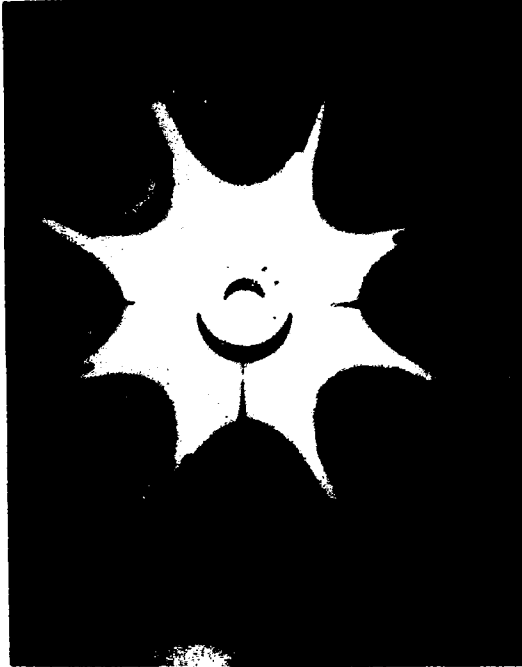
3D Mode – 150 Hz

Figure 100b. Experimental Mode Shapes of the Static Test Disk.
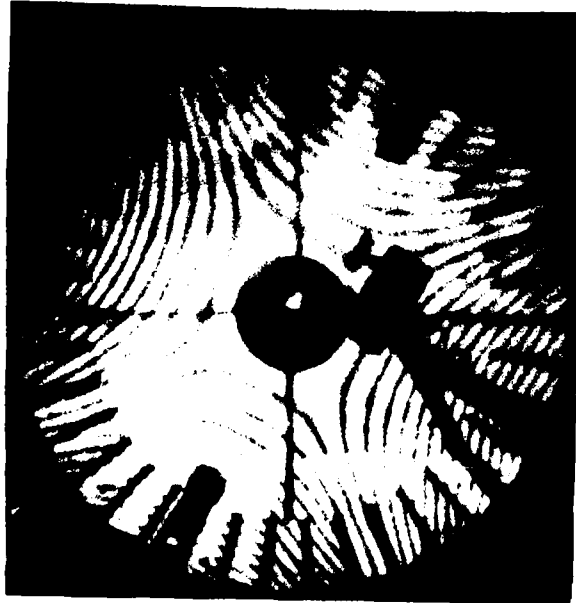
n	2D	3D	4D
N	4058	3642	3647
a	15/16	5/8	5/8
t	15	10	10
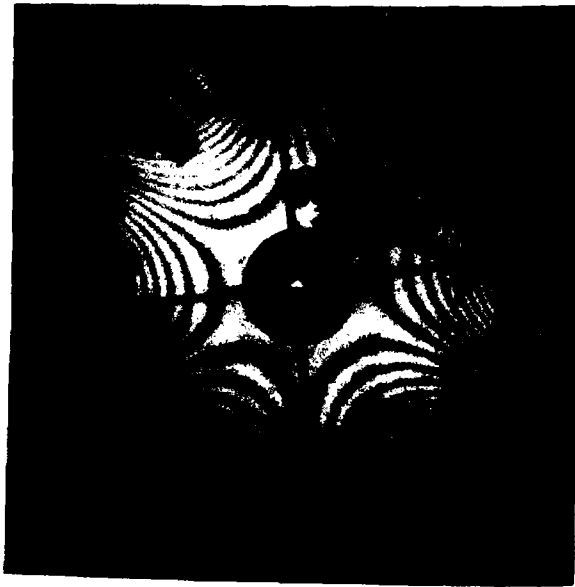
n = Mode   N = Critical Speed (RPM)
a = Magnet Gap (inch)   t = Pulse Separation (microseconds)

Figure 101. Interferograms for 2, 3, and 4D Modes of the Rotating Disk.
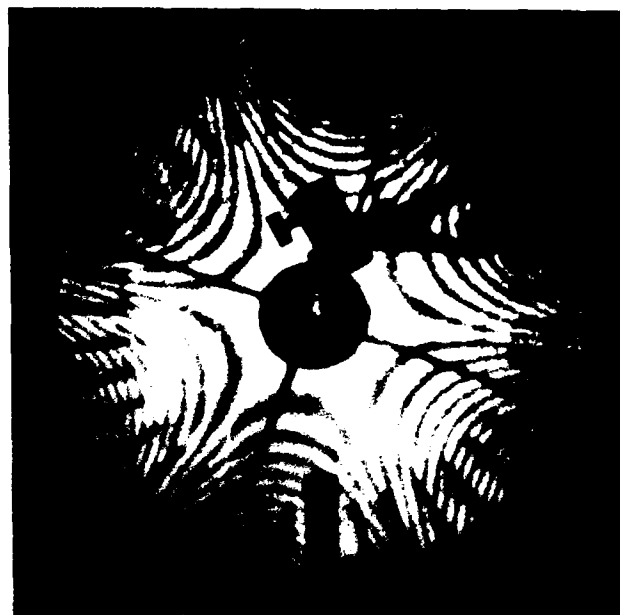
$\frac{5}{8}$ in., 3,642 rpm, 10 μs $\frac{3}{4}$ in., 3,633 rpm, 10 μs

3D MODE

$\frac{9}{16}$ in., 3,642 rpm, 7 μs $\frac{5}{8}$ in., 3,647 rpm, 10 μs

4D MODE

Figure 102.   Interferograms for the 3D and 4D Modes from Two
Excitation Force Levels.

233
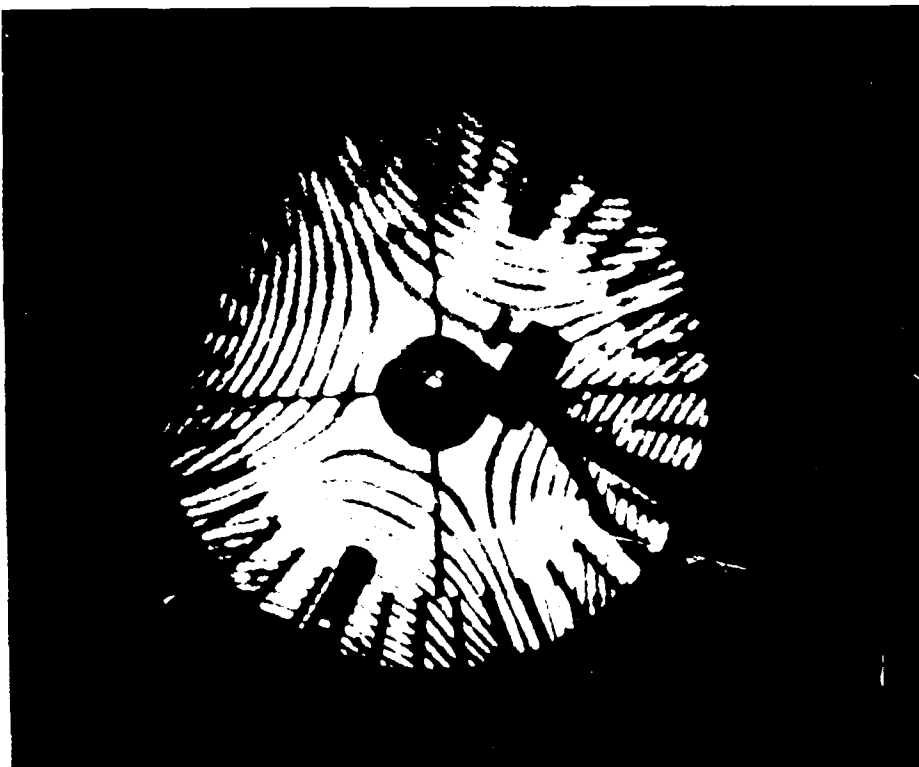
Figure 103. Interferograms for the 2D Mode for 10- and 15-μs Pulse Separation.

15μs

10μs

234

8.3 BLADE TIP DEFLECTIONS

Quantitative blade tip deflections of resonating disks were determined by AEDC and UDRI NSMS optical methods and compared with those from interferometric methods. Results from a limited Z-Grid test data were also analyzed.

8.3.1 The NSMS and Interferometric Methods

Maximum deflections at the blade tips were determined from (a) point-wise measurements from AEDC and UDRI NSMS-Systems, and from (b) wholefield interferogram data recorded when the disk had stabilized in resonance.

UDRI data analysis programs had determined the maximum blade tip deflections from the software generated time series and their spectral components for the 2,3, and 4D modes. Although a large number of time series and FFT plots (an approximate total of 110) were generated, only a few plots are included in this report for illustration. Figures 104a and 104b show the NSMS signals in time and frequency domains for the 3D mode in the large amplitude-first test series. Figures 105 through 107 show the time series and FFT components for the 2, 3, and 4D modes in second test series in which the test disk exhibited linear response. The plots for the third test series results are not presented in this report for want of space.

A summary of results analyzed by the UDRI NSMS data analysis software for the first, second, and third test series was provided in Tables 41, 42, and 43, respectively. In our analysis procedure, symmetrical arrays of blades were considered for 3 probe data. Software constructed time series data and FFT components of the data series yielded nearly identical peak-to-peak amplitude of vibrations for blade tips of the resonating test disk. The 2D, 3D, and 4D modes for all excitation test conditions were analyzed.

AEDC analysis yielded results for the first and second test series and a summary of test conditions and results are provided in Tables 44 and 45. No results were obtained for the third test

235
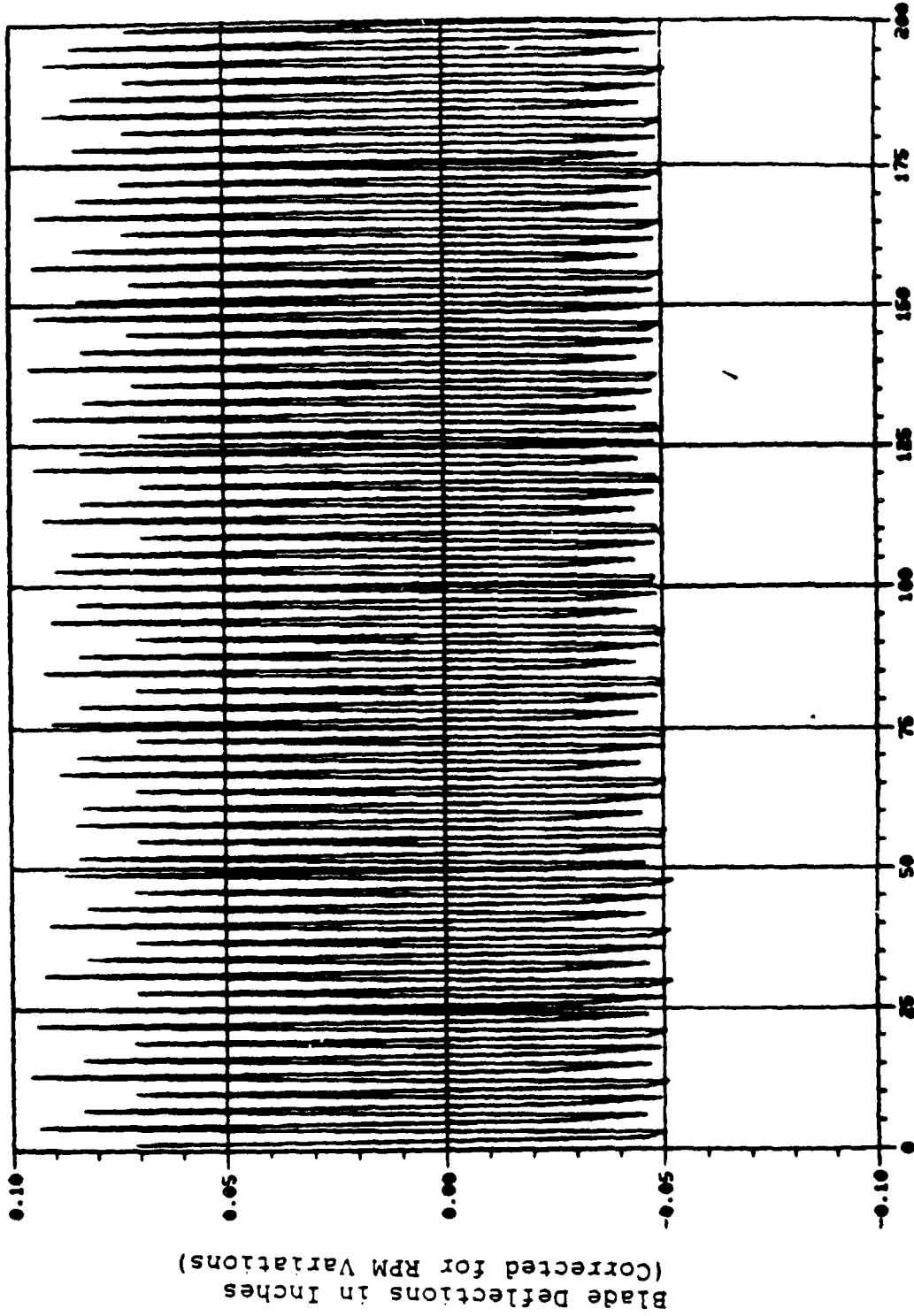
Figure 104a. Time Series Data for the 3D MODE - First Test Series.

236
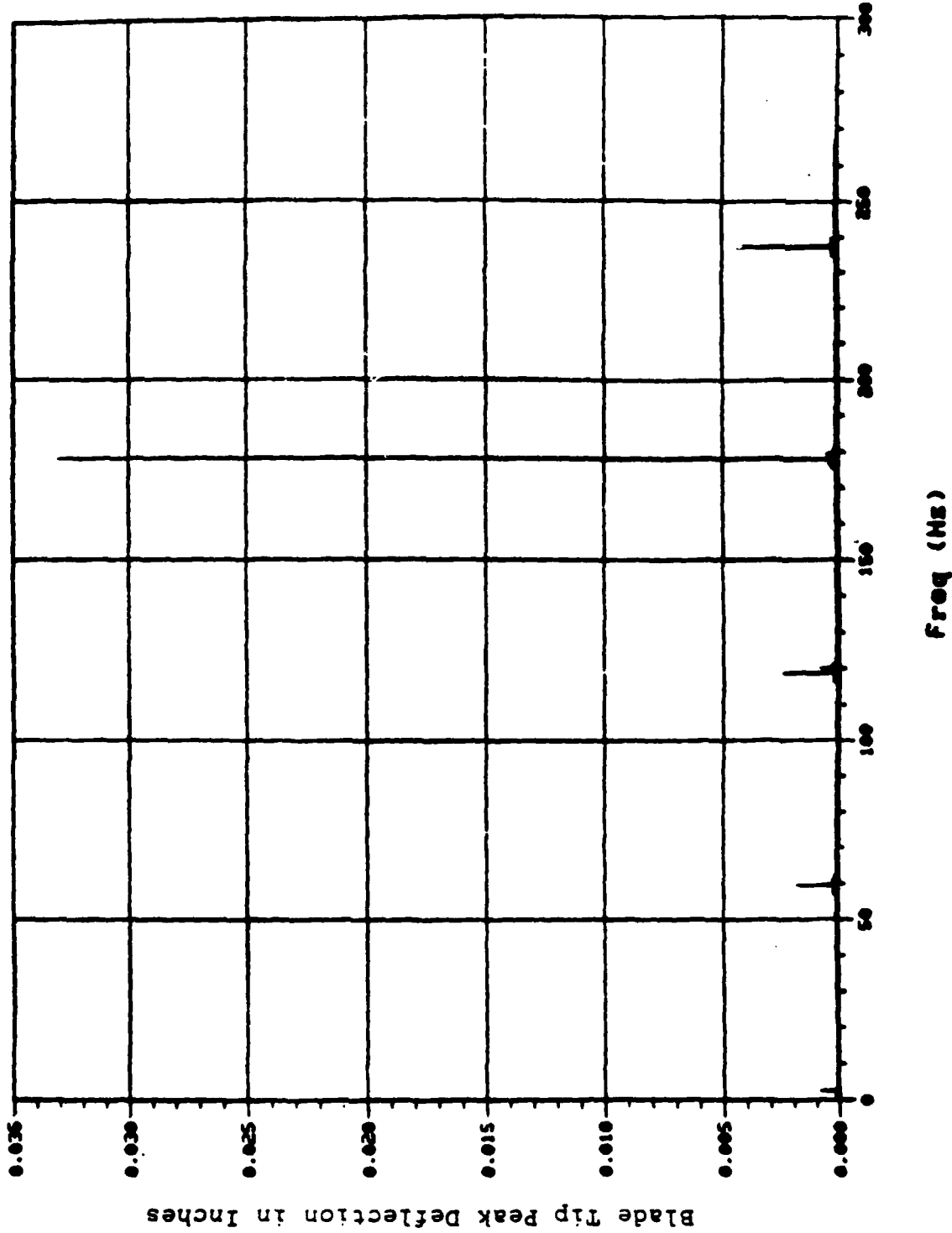
Figure 104b. Fourier Components for the 3D Mode - First Test Series.

237
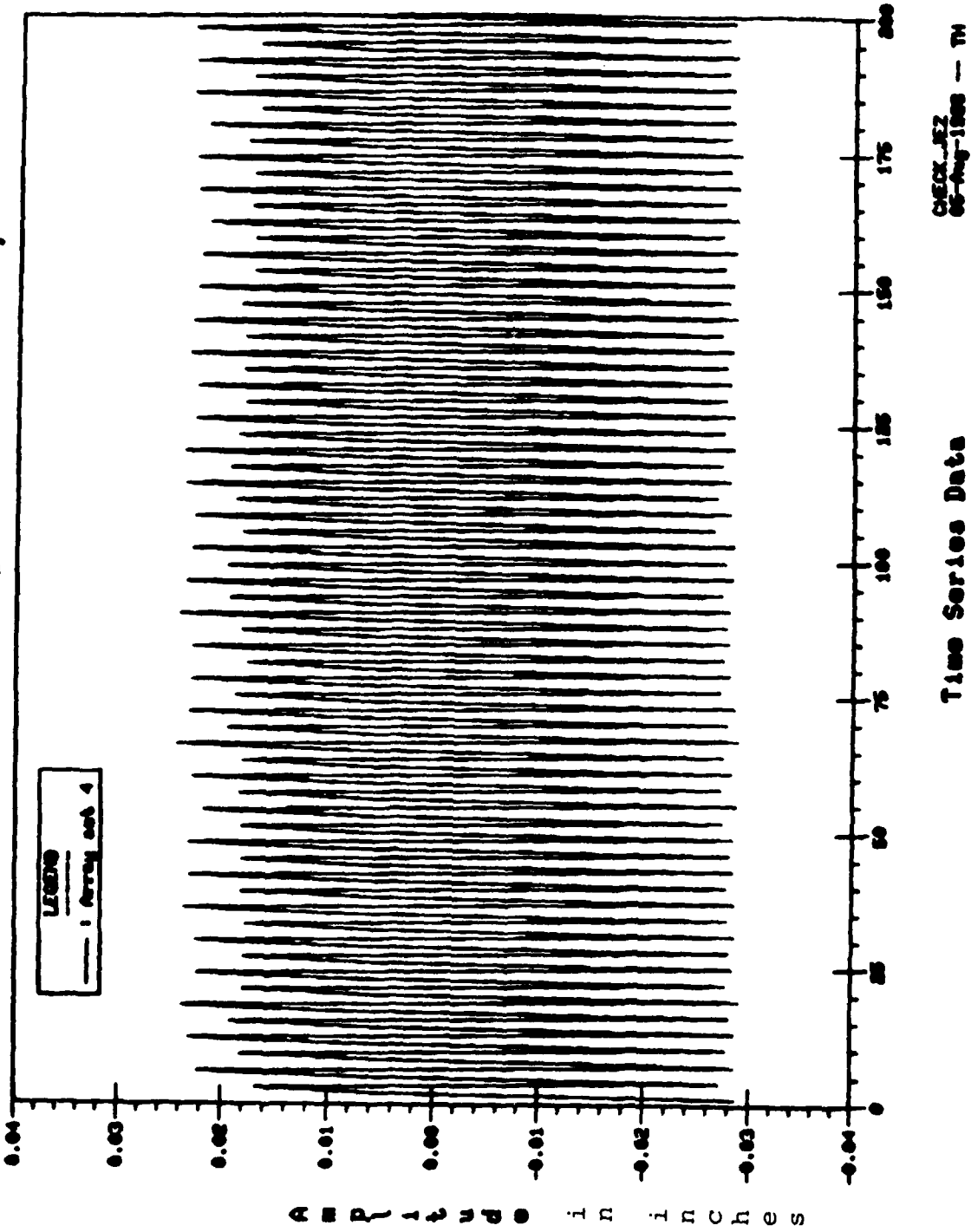
Figure 105a. Time-Series Data for the 2D Mode - Second Test Series.
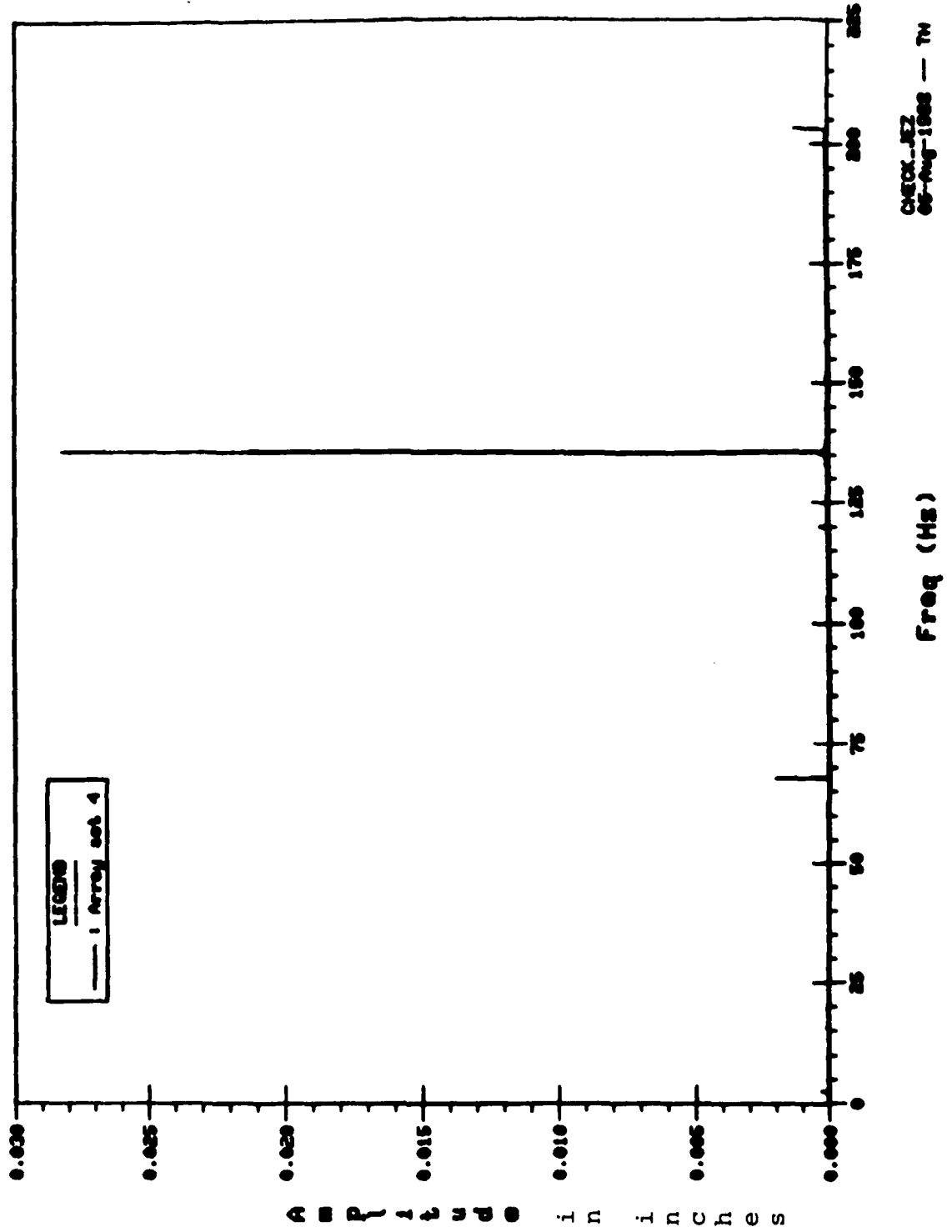
Figure 105b. Fourier Components for the 2D Mode - Second Test Series.

239
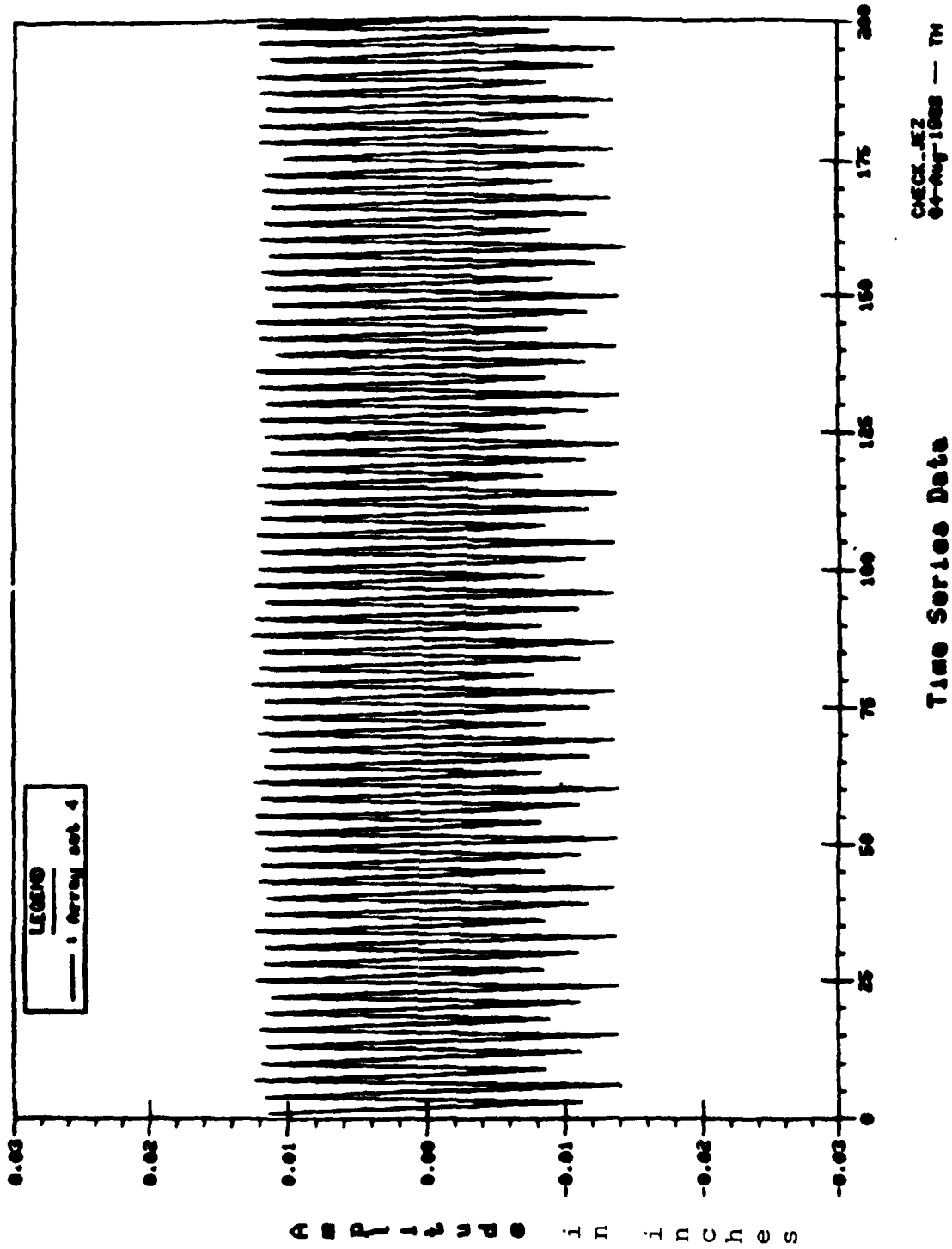
Figure 106a. Time-Series Data for the 3D Mode - Second Test Series.

Figure 106b. Fourier Components for the 3D Mode - Second Test Series.

Figure 107a. Time-Series Data for the 4D Mode – Second Test Series.

Run 18B/17B, 04-Aug-88, 4D at 3642 rpm
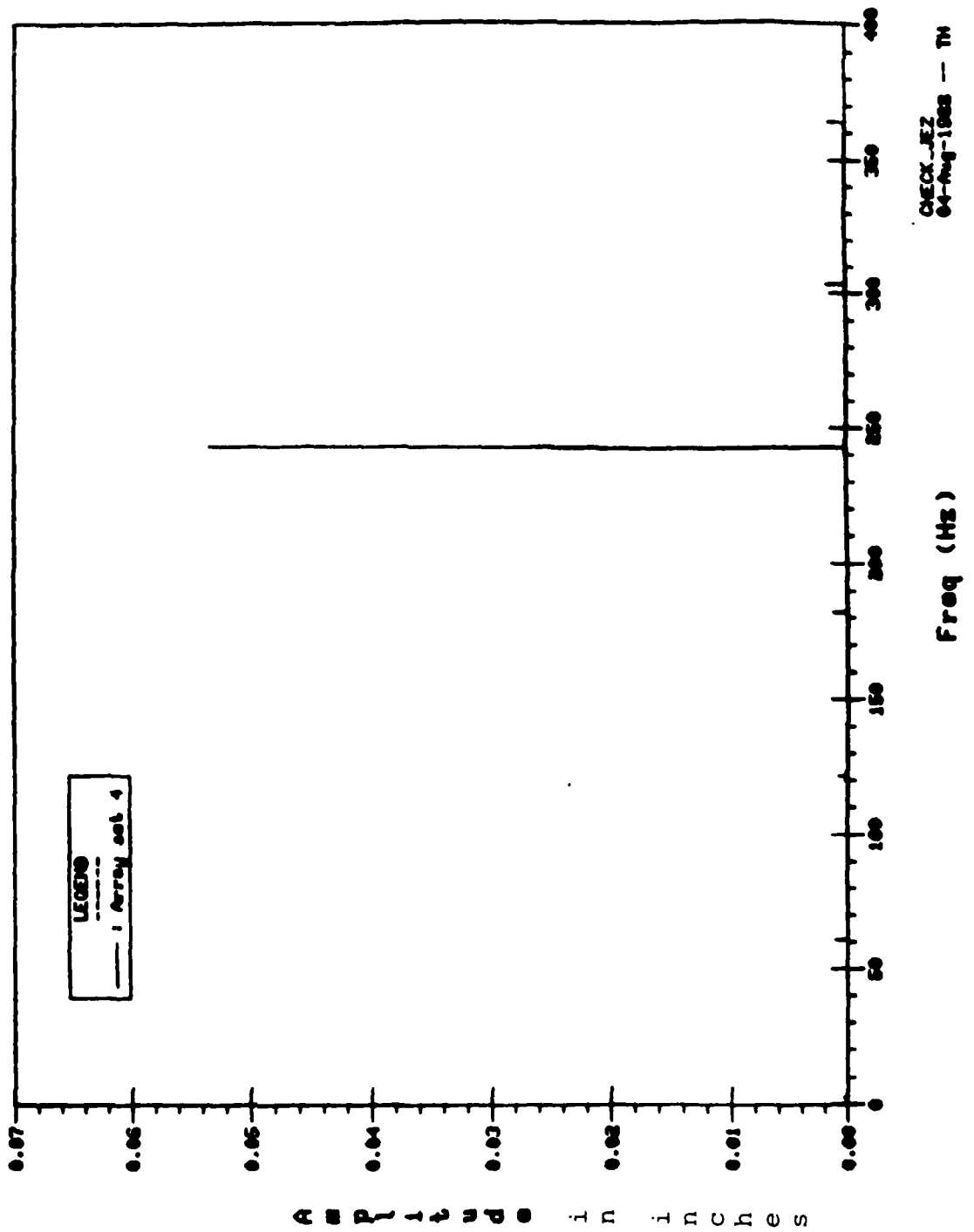
Figure 107b. Fourier Components for the 4D Mode – Second Test Series.

series because of a malfunction in the AEDC data acquisition
system. The first test series yielded large vibration amplitudes
because the excitation magnets were located close to the disk
surface. A comparison of the results from this test series is
provided in Table 46.

TABLE 41

BLADE TIP DEFLECTIONS (P-P)
CALCULATED FROM ISRL NSMS DATA
FOR THE FIRST TEST SERIES

Mode	Gap (in.)	Speed (rpm)	UDRI (p-p in mils)
3D	7/16	3720	110±2
3D	7/16	3560	52±2
3D	5/16	3732	160±4
2D	5/16	3970	No Data
2D	7/16	3780	176±5
4D	7/16	3630	62±2

TABLE 42

BLADE TIP DEFLECTIONS (P-P)
CALCULATED FROM ISRL NSMS DATA
FOR THE SECOND TEST SERIES

Res/Ref. Data Record	Resonance RPM	Magnet Gap (Inch)	Mode	Mils Defl. - P-P*
1B/2B	3648	5/8	4D	25.5 ± 3.1
3B/4B	3646	3/4	4D	15.1 ± 2.7
5B/6B	3640	3/4	4D	19.5 ± 1.3
7B/8B	3644	5/8	4D	22.4 ± 2.1
9B/8B	3636	5/8	4D	18.0 ± 3.7
10B/8B	3648	5/8	4D	25.5 ± 2.0
11B/14B	3642	5/8	3D	44.5 ± 2.6
12B/14B	3632	5/8	3D	34.7 ± 2.5
13B/14B	3646	5/8	3D	45.9 ± 2.5
15B/16B	3633	3/4	3D	27.8 ± 1.8
18B/17B	3642	9/16	4D	108.3 ± 2.3
19B/21B	4063	15/16	2D	53.1 ± 3.1
19B/22B	4063	15/16	2D	51.7 ± 1.6
20B/21B	4058	15/16	2D	33.3 ± 2.0
20B/22B	4058	15/16	2D	30.2 ± 1.9

*Deflection Values are the Mean and the Dispersion of Results from Four Data Reduction Runs Using Different Blade Array Sets for the Input Time History Data.

TABLE 43

BLADE TIP DEFLECTIONS CALCULATED FROM ISRL NSMS DATA
FOR THE THIRD TEST SERIES

Mode	Resonance Speed(rpm)	Gap (inch)	Peak-Peak Amplitude (mils)
4D	3631	9/16	30 ± 2
3D	3600	7/16	50 ± 3.0
2D	4019	1/2	38.3 ± 1.5
2D	4044	1/2	41.5 ± 0.5

The wholefield deflection patterns for the test disk were recorded by double pulse interferograms and the interferogram fringes were interpreted to determine maximum displacements at blade tips by the calculation procedure described in SECTION IV. Peak-to-peak amplitudes were evaluated based on pulse width separation time compared to the disk response frequency. AEDC and UDRI independently calculated blade tip displacements from the recorded interferograms, and these results are included in Table 47. A comparison of the optical and interferometric results in this table for selected test runs presents a range for blade deflections defined by counting the number of fringes in different sectors of the 2, 3, and 4D integral order mode shapes. Reasonable agreement was found between the AEDC and UDRI interferometric fringe analysis and between the interferometric and NSMS deflection data.

8.3.2 The Z-Grid System

The data acquired by the integrated Z-Grid and NSMS Systems described in Section VII.5 was analyzed and the results from tne 2, 3, and 4D modal deflection tests for selected excitation magnet spacings are summarized in Table 48. Similarity in the NSMS and Z-Grid time series data could be seen from Figures 108 and 109. Comparing the time series and the frequency

246

TABLE 44

UTRC NSMS FOUR-SENSOR ANALYSIS RESULTS - FIRST TEST SERIES

		TEST CONFIGURATION				RESULTS			
Run No.	Mux No.	Rotor Speed (rpm)	Excita- tion (E/O)	Magnet Gap (in.)	Sensor Spacing (deg)	Mode Order	Frequency (Hz)	Amplitude (mils p-p)	Phase Lag (deg)
5.8	2	3720	3	5/16	36.36.36	3	186.0	110	31
	3					3	186.0	108	32
	4					3	186.0	110	30
5.9	2	3720	3	5/16	36.36.36	3	186.0	110	31
	3					3	186.0	112	
	4					3	186.0	112	
6.2	2	3970	2	5/16	36.36.36	2	132.4	198	28
	3					2	132.3	196	
	4					2	132.4	200	
6.3	2	3970	2	5/16	36.36.36	2	132.3	196	29
	3					2	132.4	196	
	4					2	132.3	198	
6.8	2	3780	2	7/16	54.54.54	2	126.0	140	41
	3					2	126.0	140	
	4					2	126.0	160	
6.9	2	3780	2	7/16	54.54.54	2	126.0	130	41
	3					2	126.0	138	
	4					2	126.0	140	
7.3	2	3630	4	7/16	36.18.18	4	242.0	50	27
	3					4	242.0	44	
	4					4	242.0	50	
7.4	2	3630	4	7/16	38.18.18	4	242.0	50	27
	3					4	242.0	50	
	4					4	242.0	50	

TABLE 45

COMPARISON OF INTEGRAL ORDER TEST RESULTS – SECOND TEST SERIES

	TEST CONDITIONS				HOLOGRAM RESULTS				NSMS RESULTS				
RUN NUMBER	SENSOR SPACING(deg)	ROTOR SPEED (rpm)	EXCITATION E/O – M/GAP ("– inch)	RELATIVE DISP. FROM ACCEL	CASE No.	ENGINE ORDER	AMPLITUDE (mils p-p)	PHASE LAG (deg)	ANALYSIS TYPE	ENGINE ORDER	FREQUENCY (Hz)	AMPLITUDE (mils p-p)	PHASE LAG (deg)
19 5-19.21	54,54,54	4000-4080	2-15/16	0.83	NH				SDOF	2	135.1 R.	29	90
19.2	54,54,54	4069	2-15/16	0.77	4/5	2	23-28/41-46	125/111	4-SENSOR	2	135.6 R.	26-36	42
19.3	54,54,54	4063	2-15/16	0.65	1	2	30-32	100	4-SENSOR	ND	ND	ND	ND
19.4	54,54,54	4058	2-15/16	0.71	2	2	26-30	28	4-SENSOR	ND	ND	ND	ND
19.8	54,54,54	4048	2-15/16	0.68	3	2	19-24	133	4-SENSOR	ND	ND	ND	ND
19.17	54,54,54	4060	2-15/16	0.56					4-SENSOR	ND	ND	ND	ND
15.1	36,36,36	3642	3-5/8	1.00	14	3	48-50	67	4-SENSOR	3	182.1 R.	30-50	100
15.2	36,36,36	3642	3-5/8	0.98	NH				4-SENSOR	3	182.1 R.	30-50	93
15.3	36,36,36	3532	3-5/8	0.61	15	3	31-34	25	4-SENSOR	3	181.6 O/R.	20-36	72
15.4	36,36,36	3649	3-5/8	0.58	NH				4-SENSOR	3	182.4 O/R.	34-54	111
15.5	36,36,36	3646	3-5/8	0.81	16	3	48-52	79	4-SENSOR	3	182.3 O/R.	34-52	109
16 1-16.15	36,36,36	3600-3660	3-3/4	0.62	NH				SDOF	3	181.9 R	32	117
16.3	36,36,36	3625	3-3/4	0.40	6	3	24-26	31	4-SENSOR	3	181.3 O/R.	8-21	67
16.6	36,36,36	3633	3-3/4	0.60	7	3	29-31	65	4-SENSOR	3	181.7 R.	18-34	92
16.9	36,36,36	3637	3-3/4	0.60	8	3	29-33	85	4-SENSOR	3	181.9 O/R.	20-36	98
10 7-11.16	36,18,18	3560-3800	4-3/4	0.32	NH				SDOF	4	242.8 R	28	108
12.1	36,18,18	3644	4-5/8	0.60	17	4	30-34	95	4-SENSOR	4	243.0 R.	36-54	108
12.2	36,18,18	3636	4-5/8	0.37	18	4	25-29	46	4-SENSOR	ND	ND	ND	ND
12.3	36,18,18	3648	4-5/8	0.36	19	4	13-25	143	4-SENSOR	ND	ND	ND	ND
13 1-13.15	36,18,18	3560-3680	4-5/8	0.48	NH				SDOF	4	243.0 R.	43	108
17.3	36,18,18	3642	4-9/16	0.47	9/10	4	29-36/25-31	98/94	4-SENSOR	4	242.8 R.	34-46	118
18 1-16.16	36,18,18	3560-3700	4-9/16	0.47	NH				SDOF	4	242.7 R	47	100
18.4	36,18,18	3630	4-9/16	0.37	11	4	26-31	62	4-SENSOR	4	242.0 O/R.	30	107
16.10	36,18,18	3643	4-9/16	0.28	12	4	13-23	150	4-SENSOR	4	242.9 O/R.	24-34	140

ND – No Data, NH – No Hologram, R – Resonance, O/R – Off Resonance

248

RUN 15Z/16Z OPTIC 3D 7/16in. gap @ 3670/3000 rpm

Data Samples @ 3/Hz
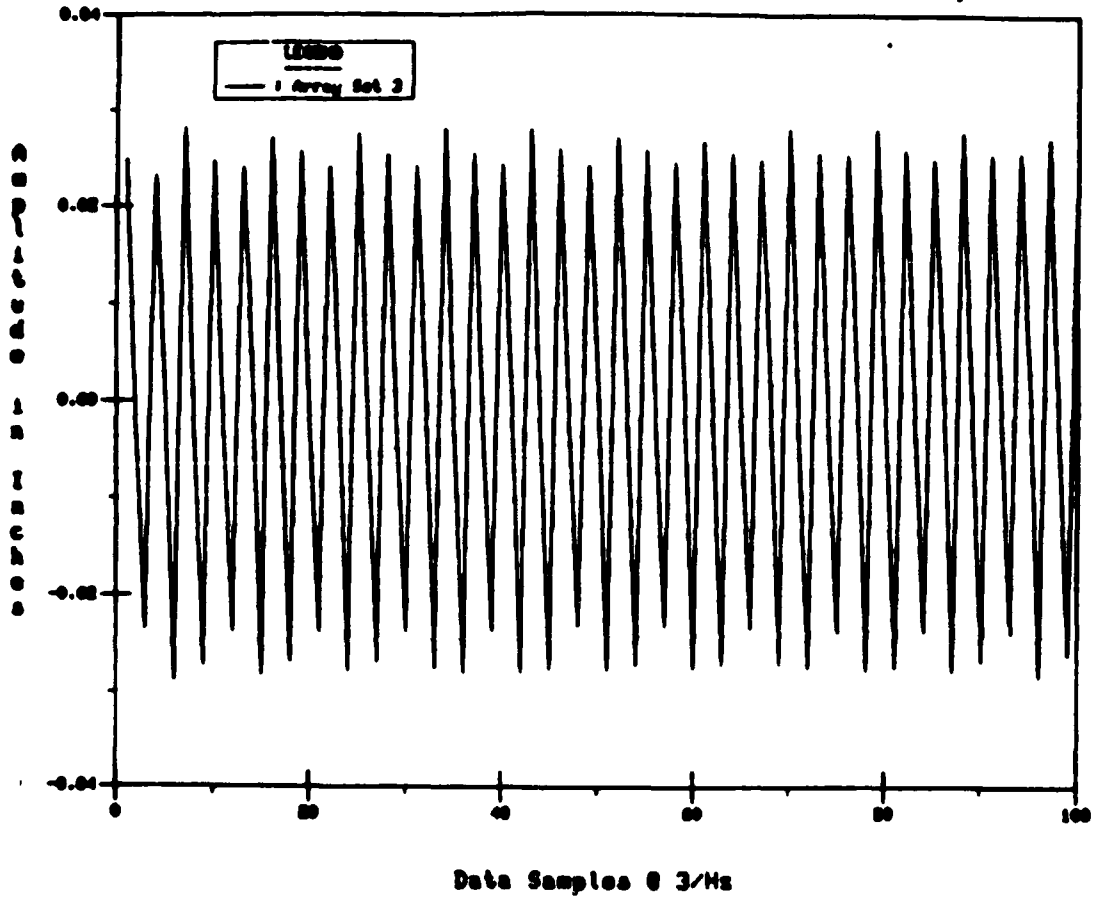
Figure 108. NSMS Time Series Data for a Sample Rate.
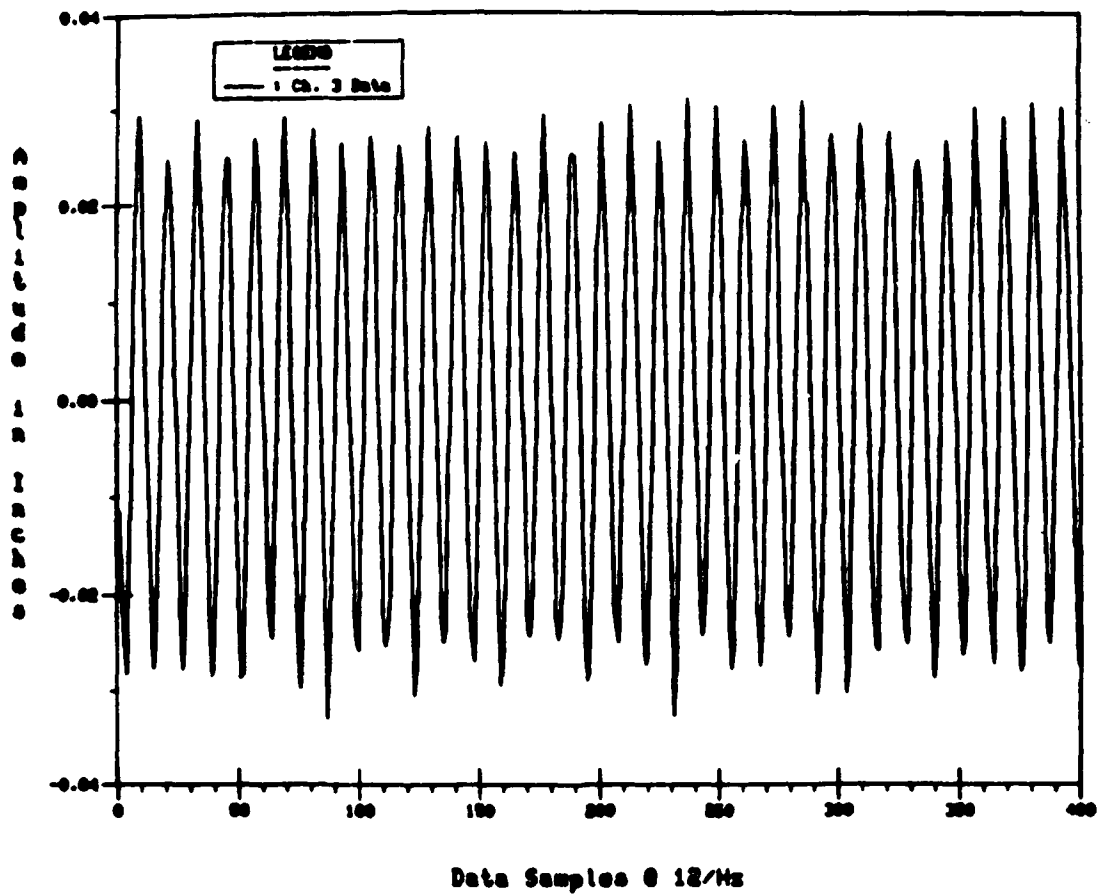
Figure 109. Z-Grid Time Series Data for the same Sample Rate.

TABLE 46

NSMS BLADE TIP DEFLECTION COMPARISON - FIRST TEST SERIES
(PEAK-TO-PEAK DEFLECTIONS IN MILS)

Mode	Gap (in)	Speed (rpm)	UDRI	UTRC
2D	5/16	3790	No Data	198-200
2D	7/16	3780	176±5	130-160
3D	5/16	3732	160±4	No Data
3D	7/16	3720	110±2	110-112
4D	7/16	3630	62±2	44-50

components of a specific mode, the Z-Grid measurement method often
yielded lower blade tip deflections than those from the NSMS
method. This would be possible if the source magnet was located
near the nodal diameter. Also the nonsymmetry of time series
indicated noise in the grid electronic circuits. Another
explanation for a lower disk response measurement by the Z-Grid
system, in general was the centrifugal stiffening effect of the
source magnet and its counterweight. Additional masses would
increase the disk stiffness from the relationship, the centrifugal
force, $f_c = (m_{magnet} + m_{counterweight})\ \omega^2 r$, where m was the mass, ω
was the angular speed, and r was the radial distance of the extra
mass from the spin axis.

UDRI had determined the axial and tangential displacement
components of the instrumented blade, using our digital Z-Grid

251

system. The time of arrival data from the two grid circuits were first corrected for speed changes and then summed and differenced to obtain tangential and axial components, respectively. This method of analysis was applied to the data run 13Z/14Z. The results from this analysis are shown in Figures 110 through 117. Figures 110 and 111 show segments of Z-grid time series data samples of channels 3 and 4 respectively. Figure 112 shows the sum of the channel 3 and 4 time series signals and represents the tangential motion of the instrumented blade. Nearly zero displacement was seen, and this correlated with the expected nearly zero tangential vibration of the flat-plate test disk. Figure 113 shows the time series of difference data from the two channels. Peak-to-peak vibration amplitude of 50 mil was shown for the axial vibration component. The Fourier components lent support to the analysis procedure. Figures 114 and 115 show the Fourier components of the channel 3 and 4 time series data, whereas Figures 116 and 117 show the spectral components of tangential and axial vibration from the sum and difference time series data, respectively. A zero displacement in Figure 116 and a half amplitude value of 25 mil seen in Figure 117 matched well with the respective time signals and also matched well with the NSMS measurements taken at the same test condition.

Further research will be required to understand the complete performance of the Z-grid system.

8.4 TRAVELING WAVE MODE SHAPE CHARACTERISTICS

For mode shape definition, holograms of the rotating disk in resonance were made. Two additional holograms, one at a lower speed and the other at a higher than critical speed were recorded to show the variation of the traveling wave position and amplitude with speed. Such changes in a 4D wave are shown in Figure 118. Similar changes in wave-travel are also noticed in Figure 119.

From the off-resonance records, a stationary displacement wave of the shape A cos $n\theta$ could easily be seen. The location of the nodal diameter with respect to the static magnets at speeds

252

Figure 110. Time History of the 3D Mode Response from Ch. 3 Z-Grid System.

253

Figure 111. Time History of the 3D Mode Response from Ch. 4 z-Grid System.

Figure 112. Tangential Vibration Component Due to the Sum of Ch. 3 and Ch. 4 Time Series Data.

Figure 113. Axial Vibration Component Due to the Difference of Ch. 3 and Ch. 4 Time Series Data.

Figure 114. Fourier Components of the Ch. 3 Z-Grid Data.

Figure 115. Fourier Components of the Ch. 4 Z-Grid Data.

Run 14Z/13Z, 10-Nov-88, 3D at 3670/3000 rpm

LEGEND

: Channels (3 + 4)

Amplitude in inches

0.030   0.025   0.020   0.015   0.010   0.005   0.000

0   25   50   75   100   125   150   175   200

Freq (Hz)

CHECK_JFC - RSD ALC VAX - TN
2-grid new/difference output
17-FEB-89 08:45:08
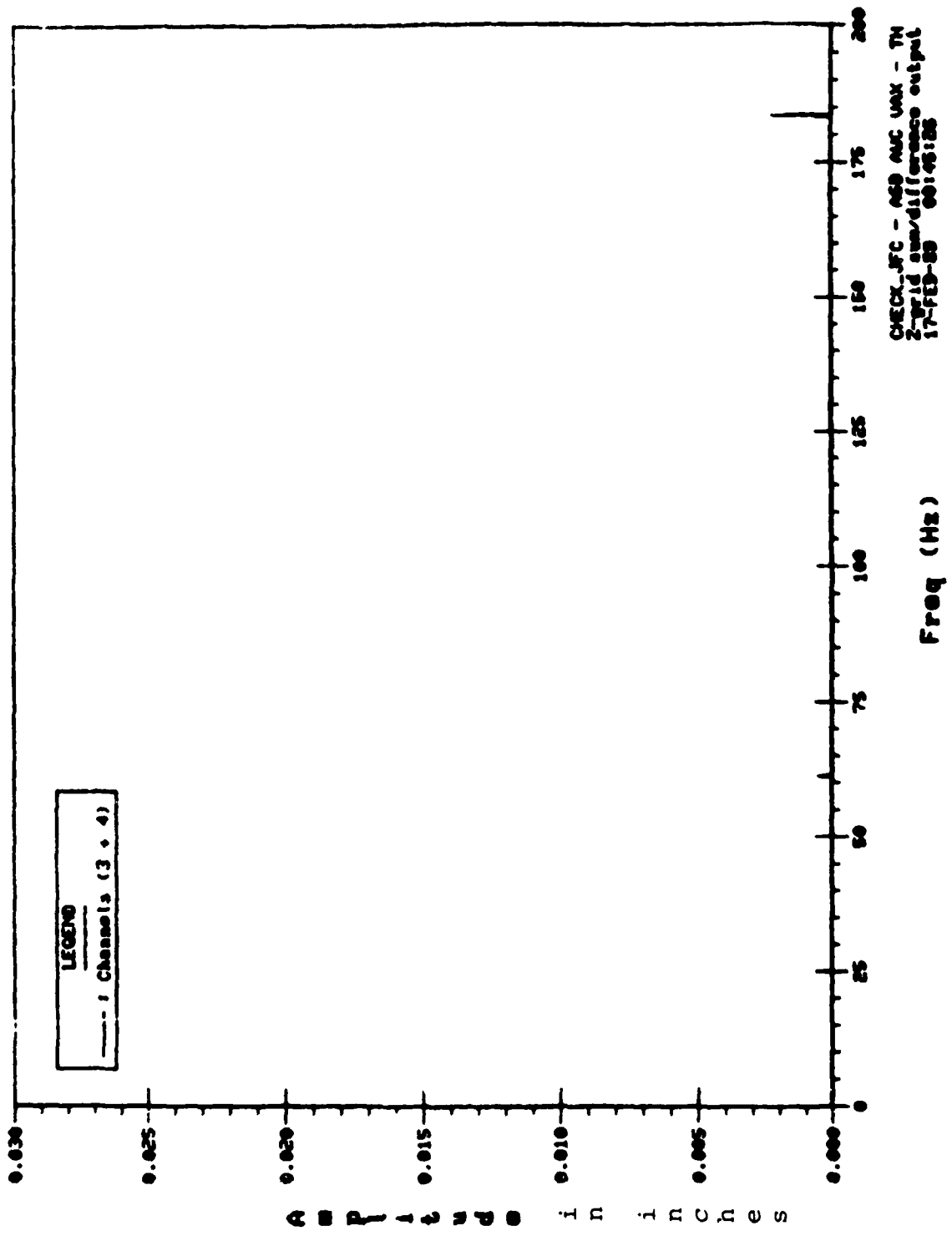
Figure 116. Fourier Components of the Tangential Vibration.
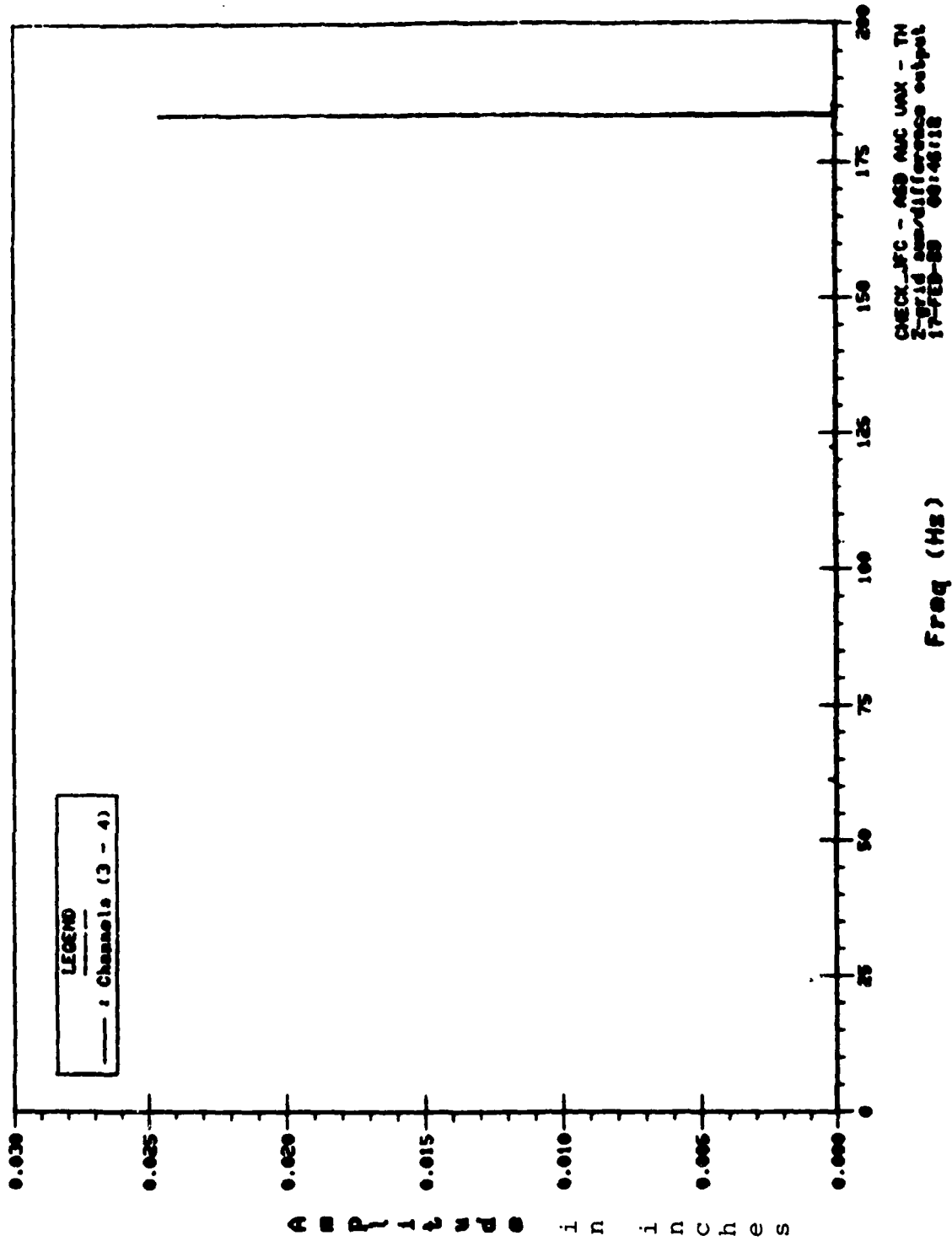
Figure 117. Fourier Components of the Axial Vibration.

Magnet

Nodal line
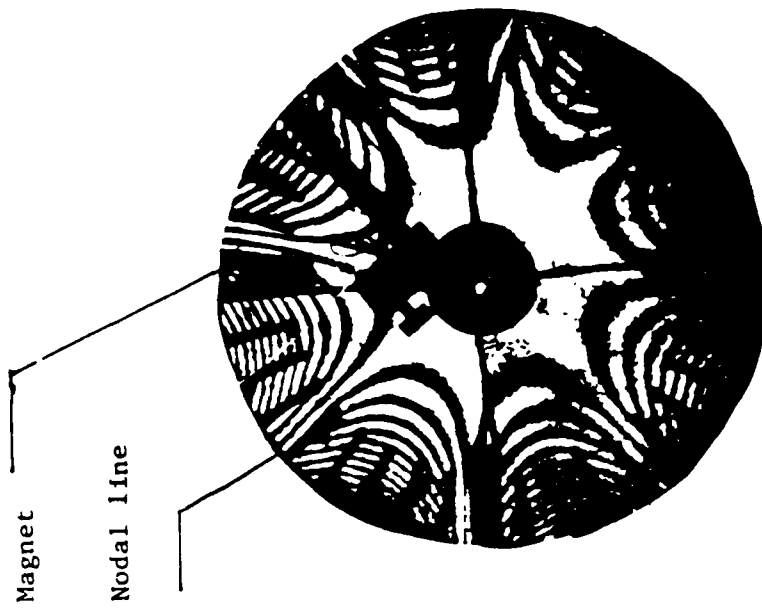
Before Resonance at 3640 RPM
Accelerometer Reading 0.049 V

Magnet

Nodal line
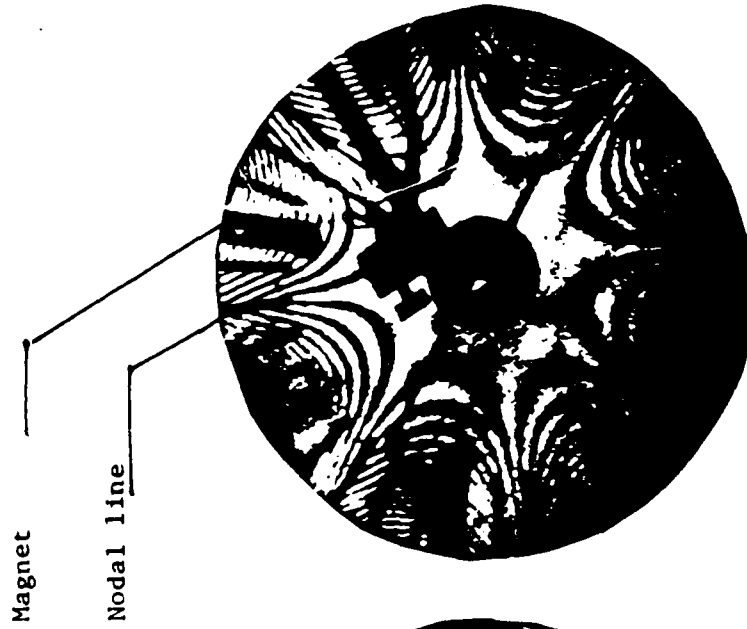
At Resonance at 3647 RPM
Accelerometer Reading 0.072 V

Magnet

Nodal line
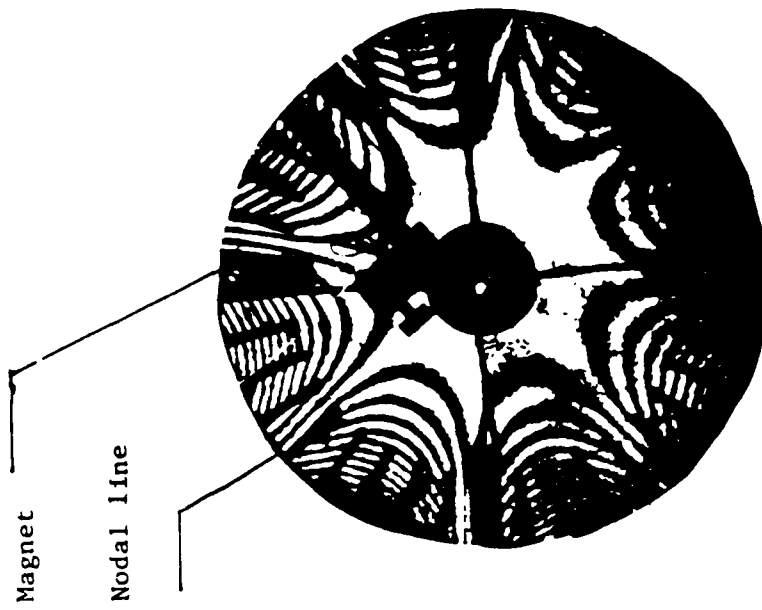
After Resonance at 3652 RPM
Accelerometer Reading 0.043 V

Figure 118. Traveling Wave Positions Before, At, and After Resonance for 4D Mode.

Figure 119. Traveling Wave Positions Before, At, and After Resonance for 3D Mode.
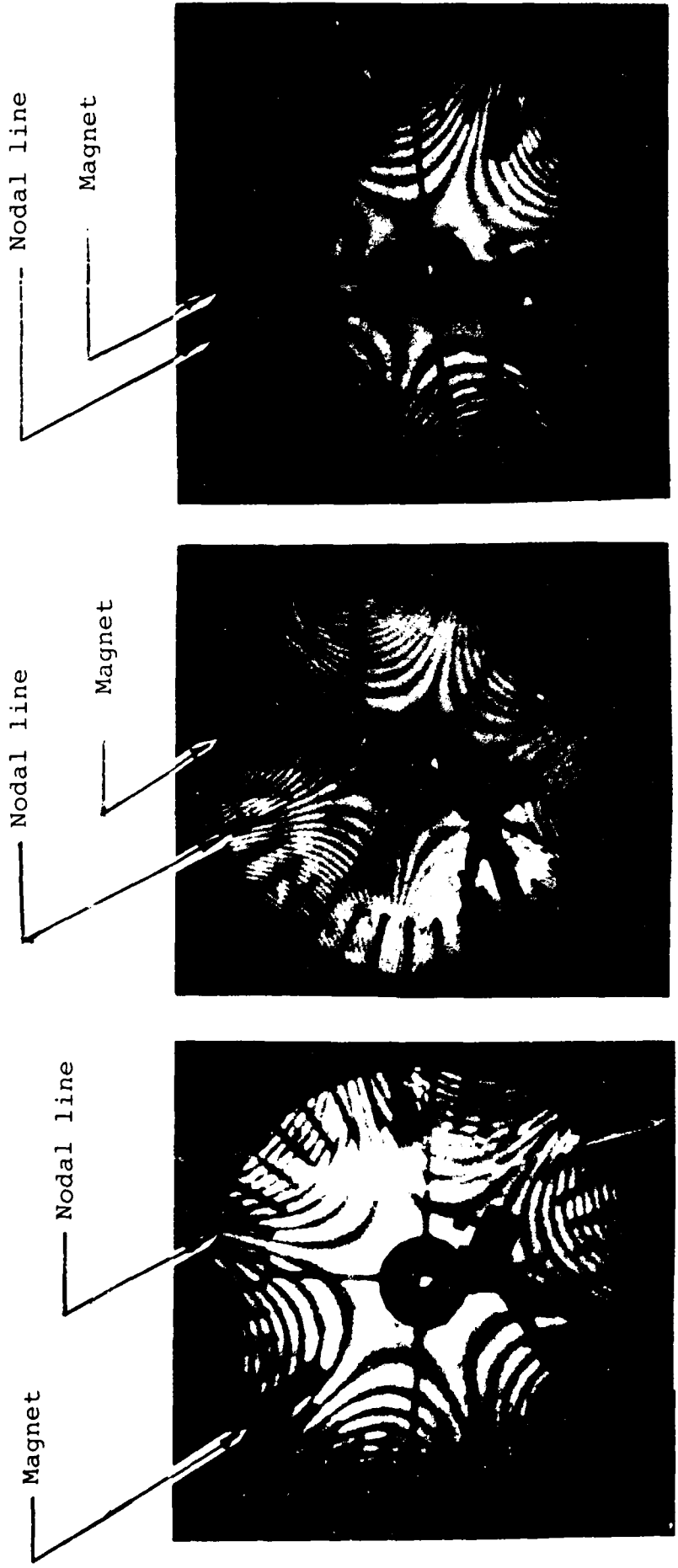
Before Resonance at 3,625 rpm   At Resonance at 3,633 rpm   After Resonance at 3,637 rpm

$\frac{3}{4}$ inch Gap, 10 μs

TABLE 47

NSMS AND LASER INTERFEROMETRY BLADE TIP DEFLECTION COMPARISONS: SECOND TEST SERIES

(Peak-to-Peak Deflections in mils)

Mode	Gap (in)	Speed (rpm)	UTRC Interfe-rometry	UTRC NSMS	UDRI Interfe-rometry	UDRI NSMS
2D	15/16	4063	23-28			
			30-32	No Data	24.8	51.7
	15/16		26-30		31.3	30.2
3D	5/8	3642	48-50	30-50		
	5/8		31-34	20-36	50.4	44.5
	5/8		48-52	34-54		
3D	3/4	3633	24-26	32		
			29-31	18-34	29.9	27.8
			29-33	20-36		
4D	5/8	3644	30-34	36-54		22.4
			25-29	No Data	33.2	
			13-25	No Data		
4D	9/16	3642	29-36	34-38	34.9	27.6
			25-31			

below and above resonance indicated the lead and lag phase angles of the force-wave relative to the response wave. When the disk was in resonance, the peak of the response wave was at $\pi/2$ relative to the excitation force.

Near resonance amplitude changes of the traveling wave with speed were illustrated in Figure 120. The wave build-up and decline effects were evident from the varying number of fringes in holographic mode shapes when the disk was below, at, and above the resonant speed. Fewer fringes were present in holograms made at the lower and upper half-power points of the resonance curve.

$\omega < \Omega$
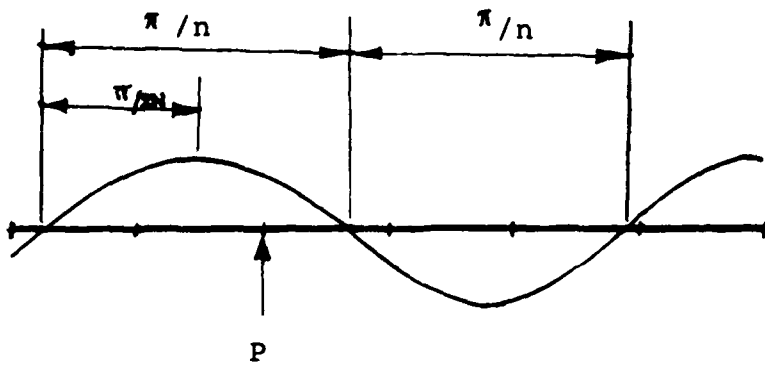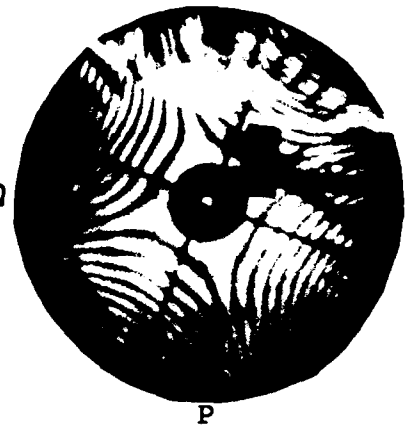
4,056 rpm, Amp = 12.5 fringes

$\omega = \Omega$
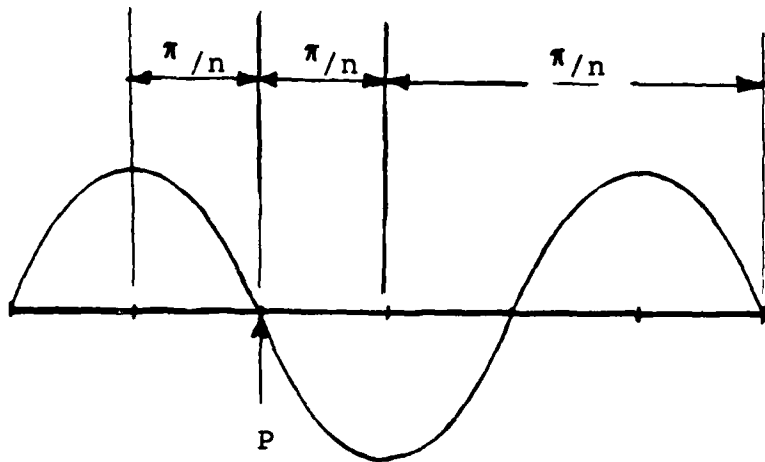
4,058 rpm, Amp = 14 fringes

$\omega > \Omega$
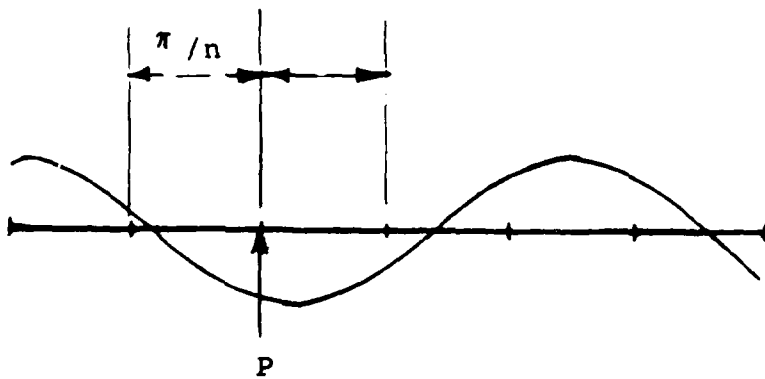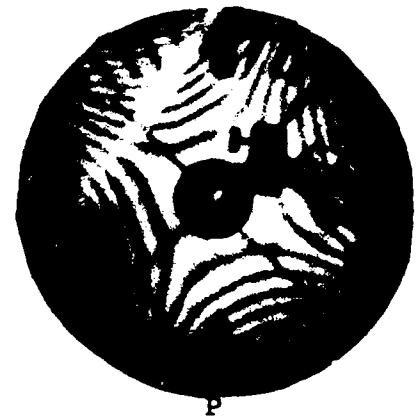
4,060 rpm, Amp = 9 fringes

Figure 120.   Resonant Wave Build-up with Speed - 2D Mode.

264

Maximum number of fringes at the resonant speed of 4,058 rpm for the 2D indicated maximum dynamic displacement for the disk. Also, maximum deflection occurred when the traveling wave node coincided with the excitation force location. The holographic mode shape records in Figures 118 through 120 seemed to indicate the opposite, but that was because the double pulse holographic technique recorded the nodes of the actual mode as antinodes in the image and vice versa. The force-response relationship of resonating bladed disks at critical speeds is further discussed in (54).

8.5 BLADE-TO-BLADE MISTUNING STUDIES

A perfect axisymmetric disk under symmetric load conditions will produce symmetrical modal response, but our test disk with several direct mounted motion sensing devices and their leadwires altered the disk stiffness locally and produced different blade responses.

The UDRI NSMS software was used to analyze the test run of August 3, 1988 and extract the blade-to-blade deflections. The details of this test and results were given in Table 49.

The routine NSMS data analysis procedure for the above test conditions yielded average blade deflections 35, 45, and 45 mils when the disk transited through resonance. The presence of harmonics other than the primary component was evident for the off-resonance conditions of the disk due to the participation from other modes. Blade deflections for the upper half power point were higher than those of resonance condition for the 3D mode but the phase change expected was not observed.

TABLE 48
BLADE TIP AMPLITUDES (MILS) COMPARISON
BY NSMS AND Z-GRID METHODS

Mode	Magnet Spacing (in.)	Critical Speed (RPM)	NSMS (p-p,mils)	Z-Grid (p-p,mils)
2D	1/2	4044	41.5	34.0 ± 3
	15/16	4058	30.2 ± 1.9	--
3D	7/16	3670	60 ± 1.0	58 ± 1
	3/4	3633	27.8 ± 1.8	--
4D	9/16	3631	30.1 ± 2	--
	5/8	3644	22.4	11 ± 1

To arrive at the average deflection of an array of blades, the NSMS data was rearranged and data values from several blades were used to construct a single time series, which was used in turn as an input for the FFT software analysis. The data for the four sets of symmetrically arranged blades was analyzed to produce the average deflection spectrums. Three such blade ordering schemes were already presented in Tables 27, 28, and 29 in SECTION VI.

266

TABLE 49

TEST DISK RESONANCE TEST CONDITIONS

Run #	Mode	Speed (rpm)	Gap (in.)	Data Acquired at	Average Deflections (p-p, mils)	
12B/14B	3D	3632	5/8	Lower half-power point	Array 1	32
					Array 2	37
					Array 3	37
					Array 4	31
11B/14B	3D	3642	5/8	Resonance	Array 1	44
					Array 2	47
					Array 3	47
					Array 4	46
13B/14B	3D	3646	5/8	Upper half-power point	Array 1	43
					Array 2	48
					Array 3	49
					Array 4	43

In the present study, data readings for each blade when the disk was in resonance were extracted. Each data value was corrected for speed variation and the statistical mean over 500 rotations calculated. The nonvibratory data at 3,000 rpm was similarly treated. The resonance data were then referenced with nonvibration data to get the number of counts for each of the blades. These counts were a direct measure of blade tip deflections. Histograms, the plot of number of counts versus blade numbers were then plotted. Figure 121, shows the blade-to-blade
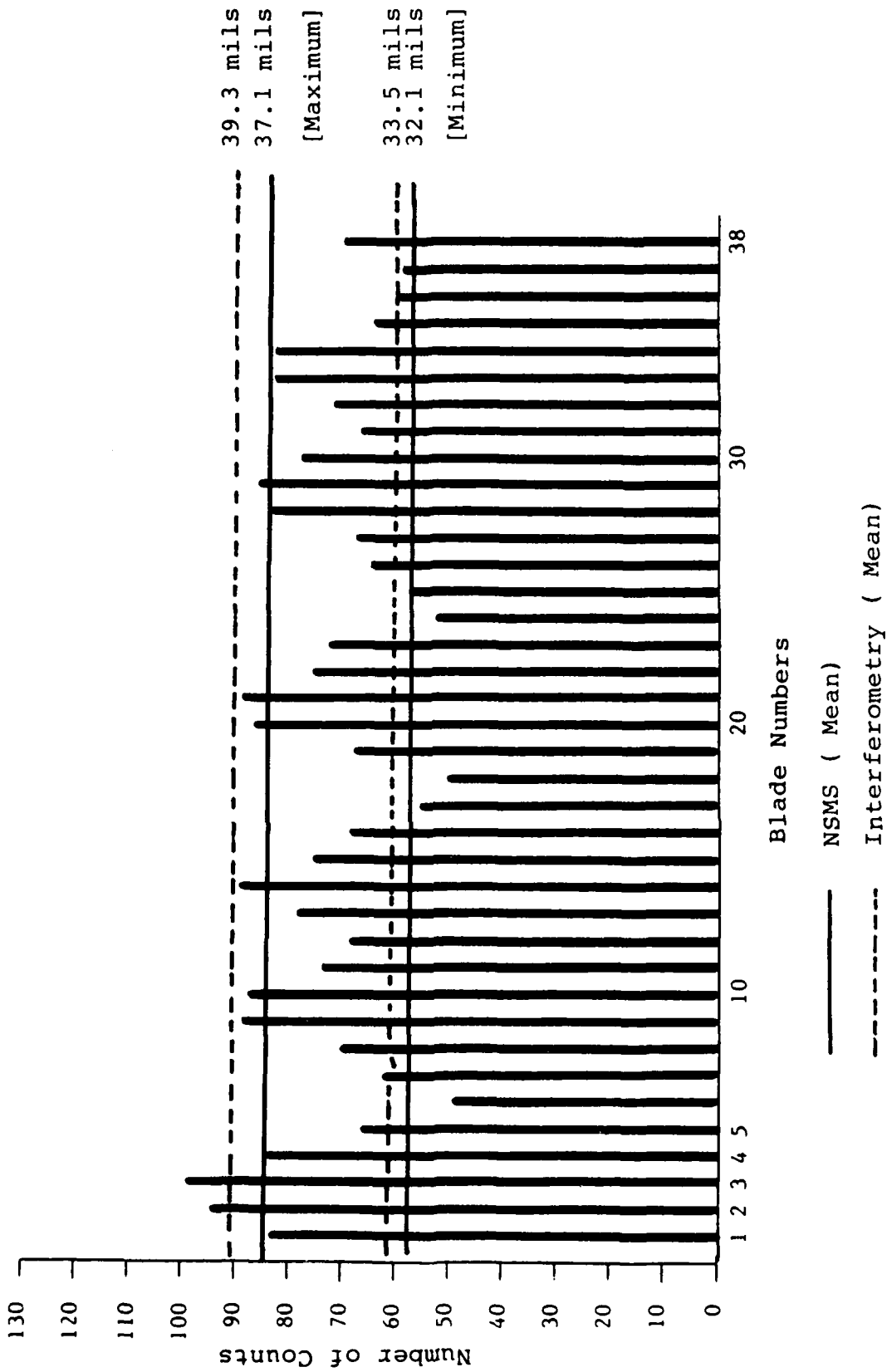
Figure 121. NSMS Determined Blade-to-Blade Deflection at 3,632 rpm.

deflections for the optical probe 2, when the disk was stabilized at the lower half-power point speed, 3,632 rpm. Similarly the Figure 122 shows resonant blade deflections at 3,642 rpm.

Fringe number differences in different sectors of a specific modal pattern were attributed to imperfection in the disk, that is, mistuning. Such asymmetric displacement patterns for the 2, 3, and 4D modes were recorded in our experiments. A typical modal asymmetric fringe pattern for 3D before and at resonance are shown in Figure 123. This behavior was evident in 3D and 4D resonant mode shapes of the disk shown in Figure 124. The offset effect seen in recorded mode shapes was due to the back and forth switching between two closely spaced resonant frequencies for different sectors of the disk. This was likely due to the variable stiffness and mass distributions of the instrumentation system installed to this very light test disk. Fringe muddling due to bias fringes was minimum at resonance speeds and a sample bias fringe hologram is shown in Figure 125.

8.6 NONLINEAR DYNAMICS

Tests were also conducted with various magnet spacings ranging from 1/2 to 1 inch to study the effect of excitation force on the dynamic response of the bladed disk. Amplitude changes due to speed increments in steps of 1 rpm on either side of resonance were recorded for the 2D, 3D, and 4D modes. A phase change of nearly 90 degrees as the disk passed through resonance was evident from Figures 126 and 127 for the 2D and 3D modes. A smooth phase change did not occur when the magnets were positioned closer than 9/16 inch. This was attributed to the nonlinearity of the disk. The nonlinear, hard spring response characteristic of the rotating bladed disk is presented in Figure 128.

269
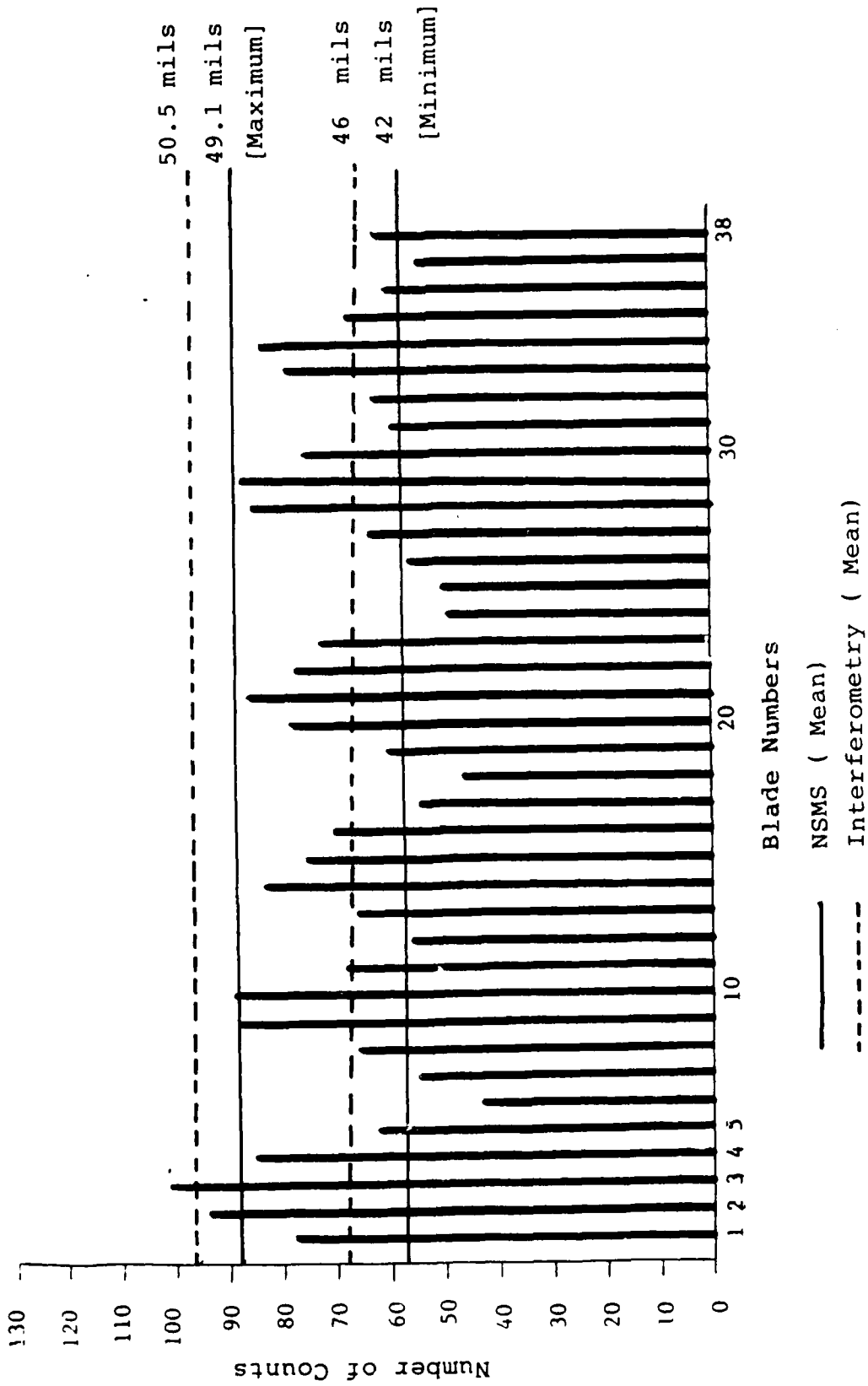
Figure 122. Blade-to-Blade Response of the Test Disk in 3D at 3,642 rpm.

270

AT 3,632 RPM

B_{31}

B_{24}

B_1

B_{19}

B_8

B_{13}
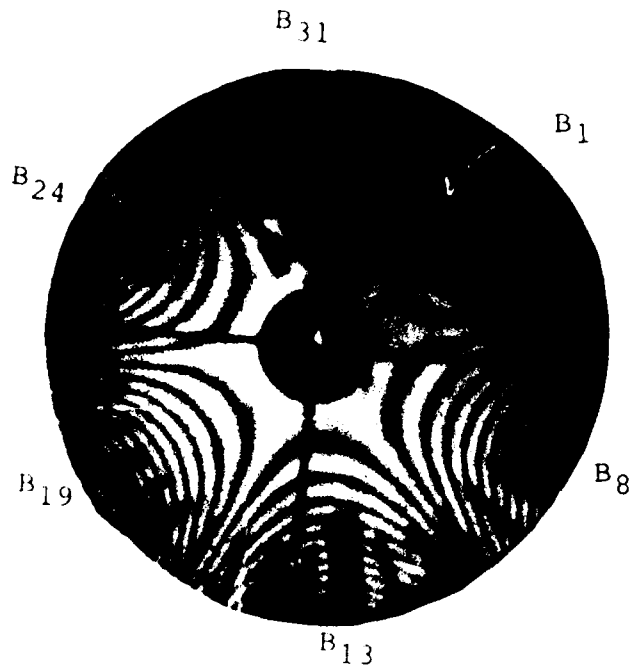
B_1, B_8, B_{13} – 39 mils

B_{19}, B_{24}, B_{31} – 33.5 mils

AT 3,642 RPM

B_{35}

B_5

B_{30}

B_{11}

B_{24}

B_{17}
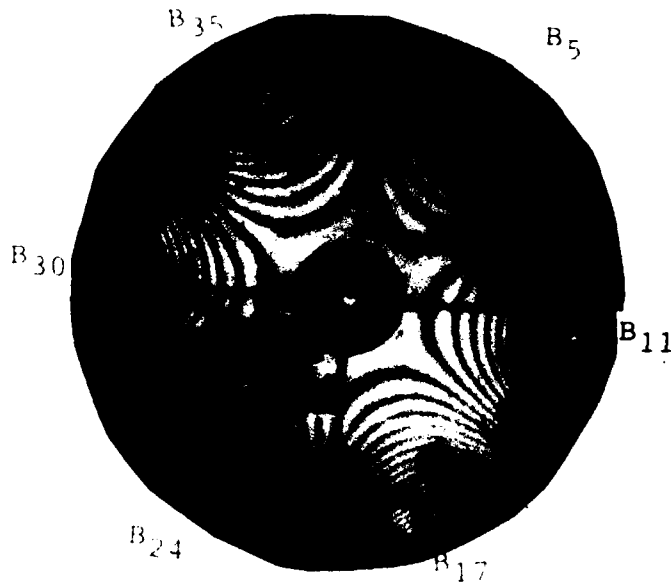
B_5, B_{11}, B_{17} – 50.5 mils

B_{24}, B_{30}, B_{35} – 46 mils

B_i – Blade Number   Deflection in mils

Figure 123.   Modal Asymmetry due to Disk Imperfection
at Two Speeds for 3D.

271
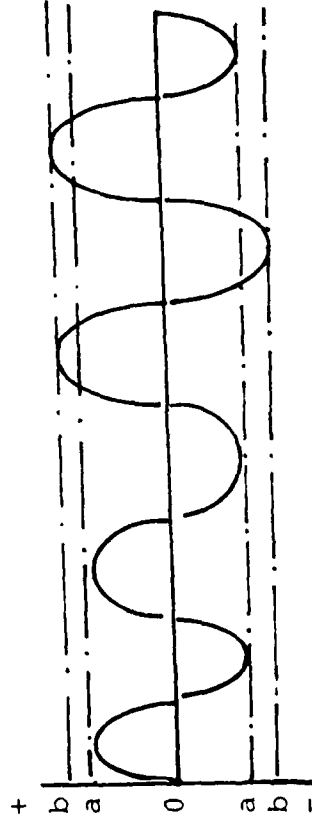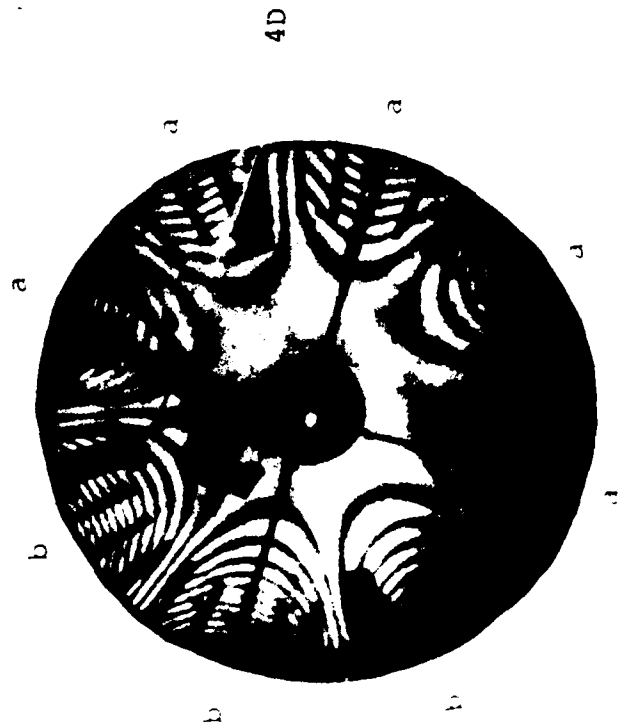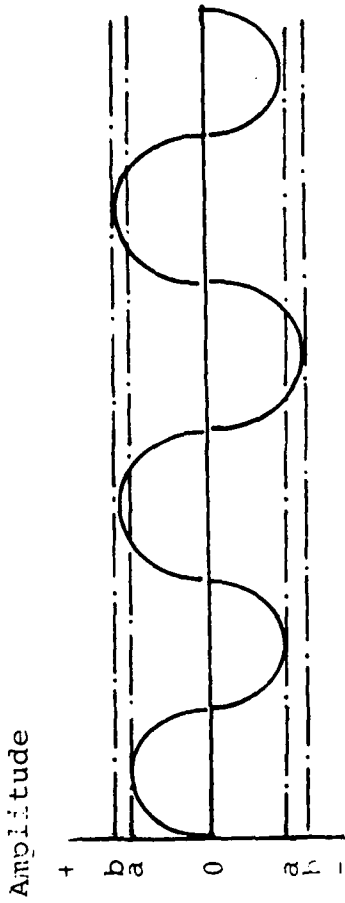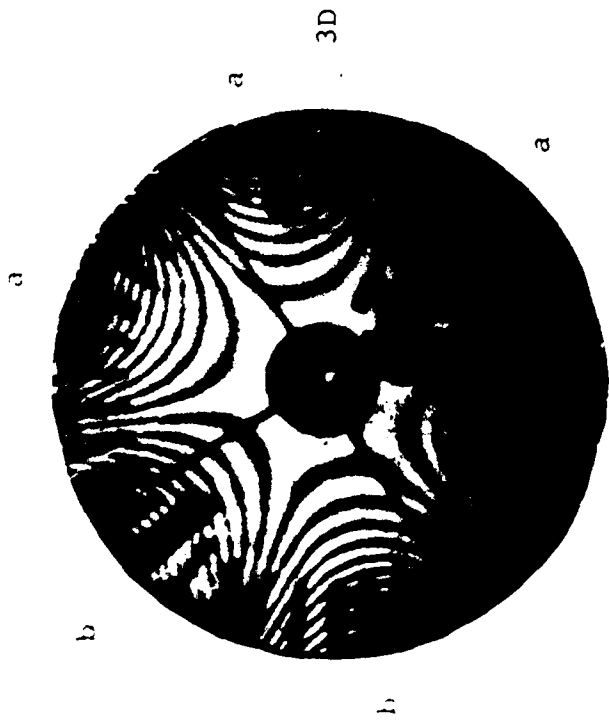
Figure 124. Blade-to-Blade Response of the Test Disk in 3D and 4D Modes.
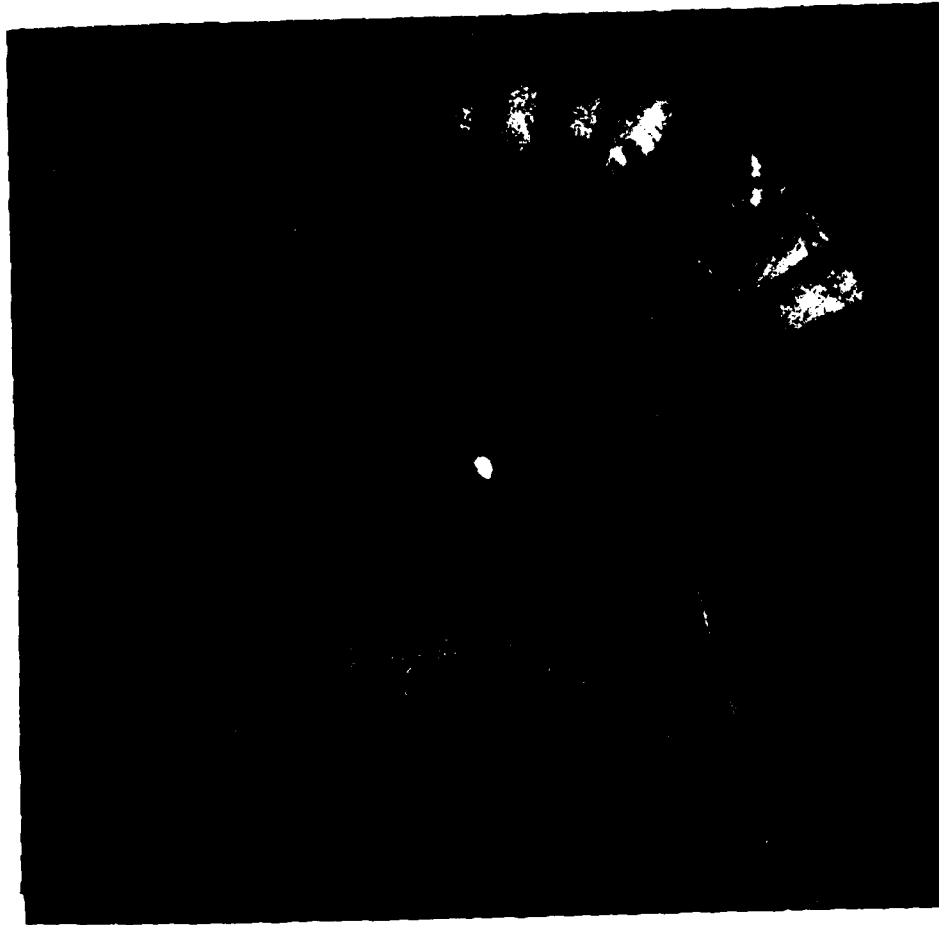
Figure 125. Double Pulse Bias Fringe Hologram
at 3,642 rpm.
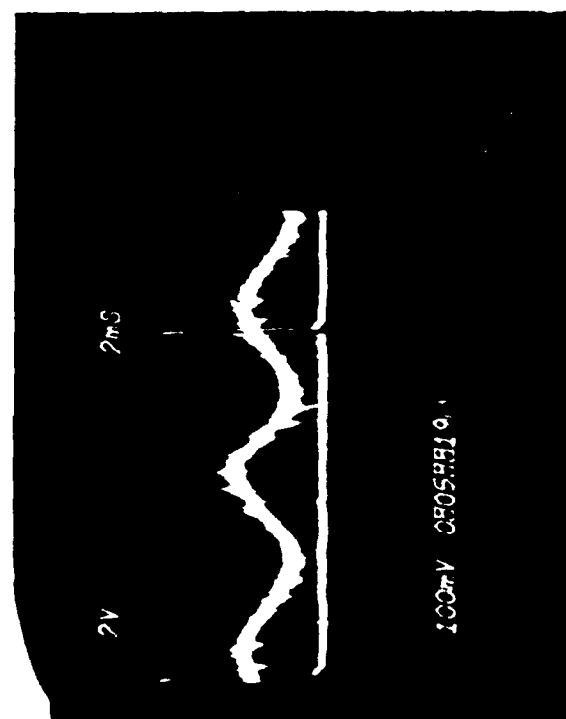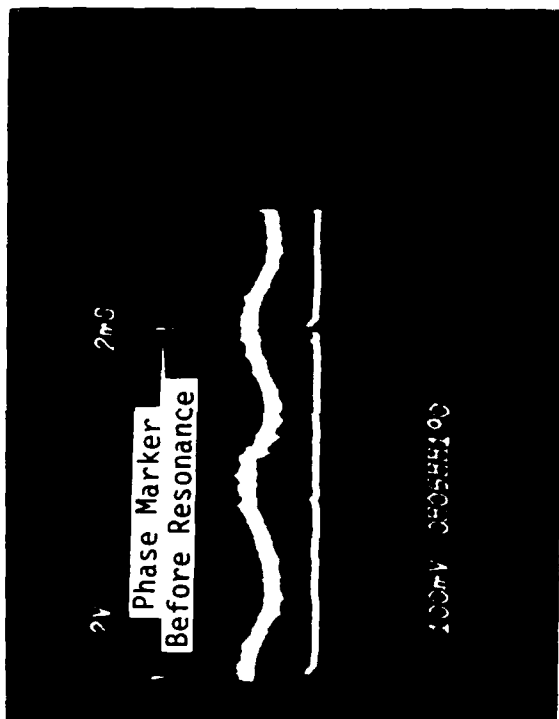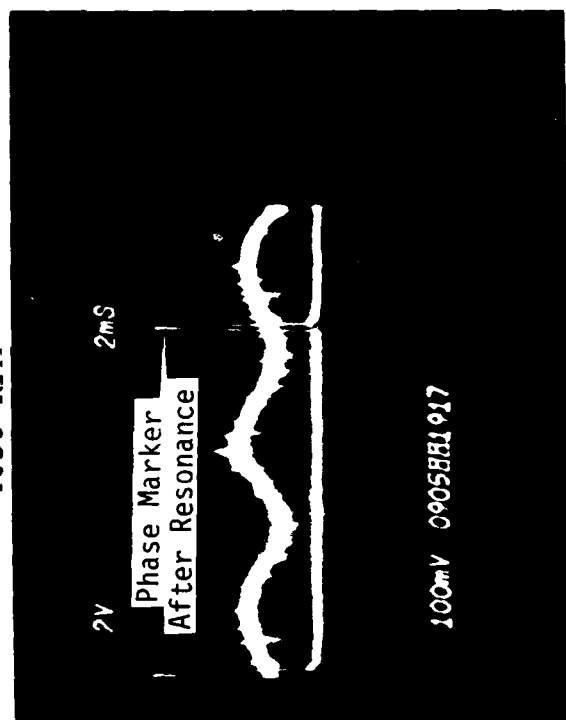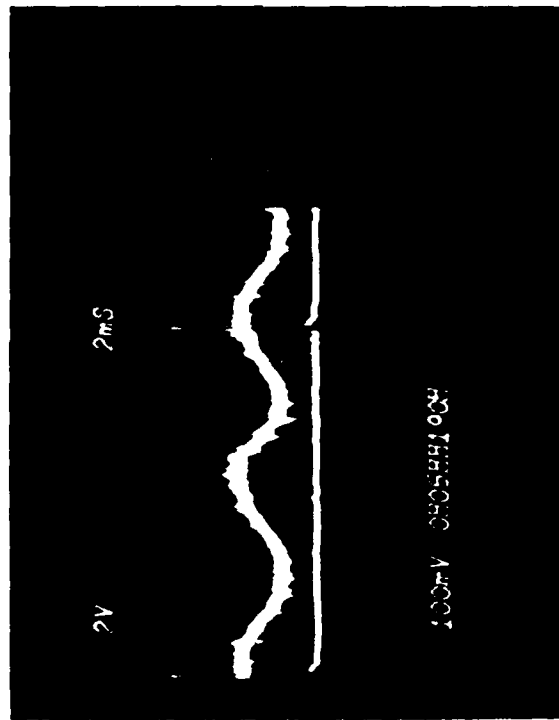
Figure 126. Phase Transition Diagram for 2D Mode.

274

Figure 127. Phase Transition Diagram for 3D Mode.
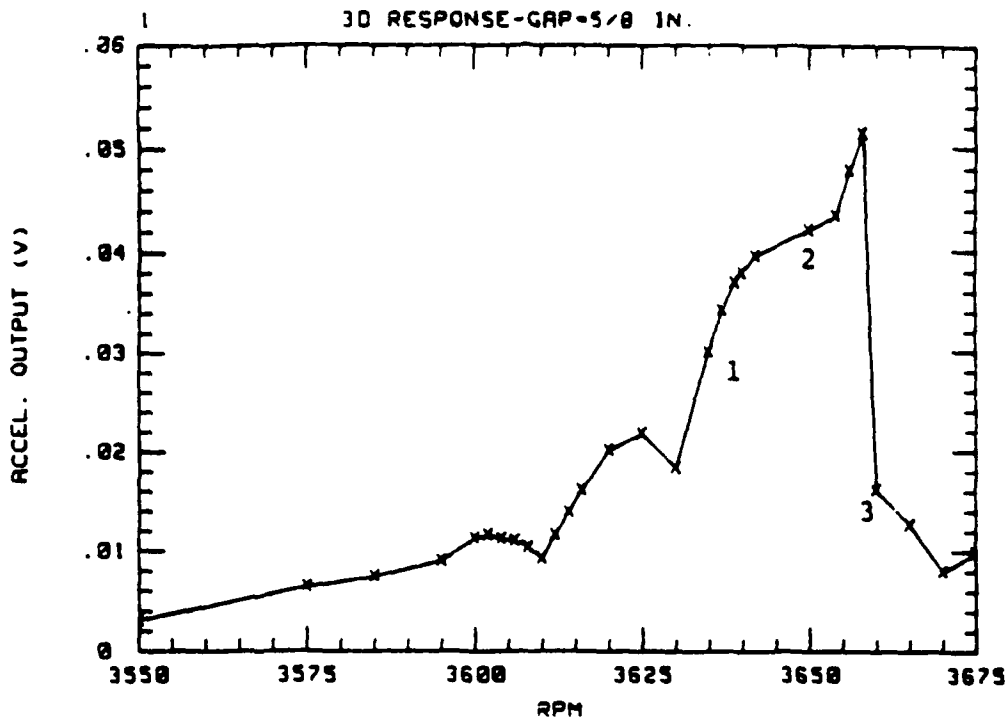
1. 3,635 rpm, Before Resonance
   Phase Marker on Trough of
   the Response Signal.
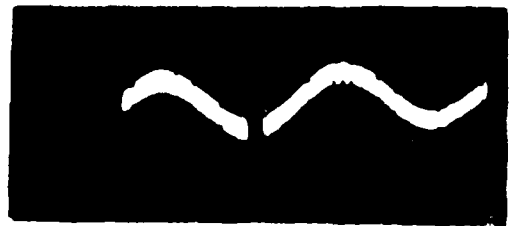
2. 3,650 rpm, Near Resonance
   Phase Marker Midway Between
   Trough and Crest of the
   Response Signal.
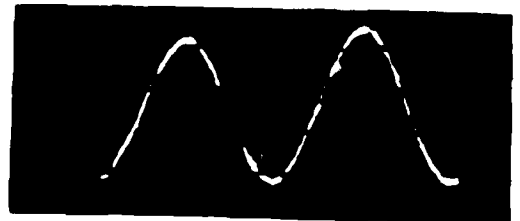
3. 3,660 rpm, After Resonance
   Phase Marker Near the
   Crest of the Response
   Signal.

275

NONLINEAR DISK RESPONSE CHARACTERISTICS
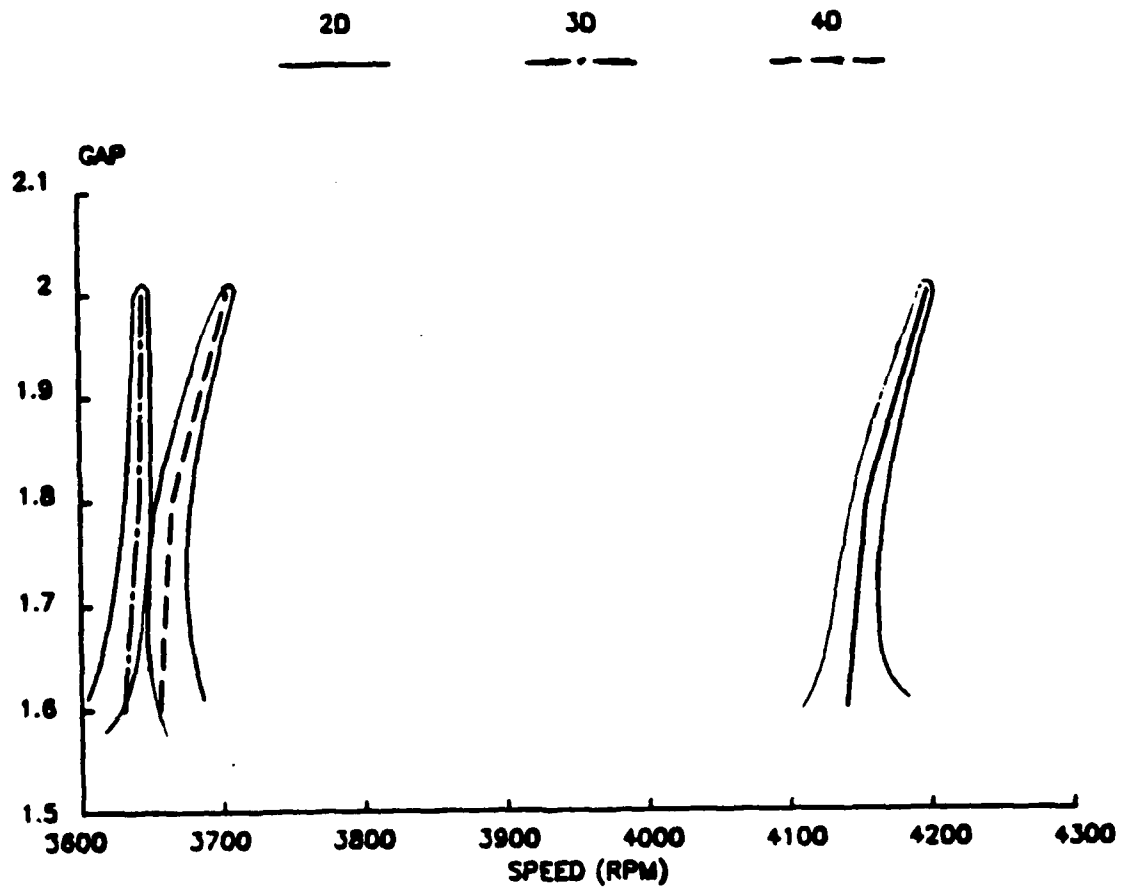
Figure 128.   Hard Spring Characteristics of Rotating
               Flexible Disk.

276

SECTION IX
CONCLUSIONS AND RECOMMENDATIONS

UDRI has concentrated its efforts to pursue the objectives of the proposed program for developing advanced analytical, experimental and instrumentation methods to characterize the dynamics of rotating turbine engine components. This research and development work performed during the period 1 September 1985 through 30 June 1989, has resulted in many accomplishments. Two nonintrusive instrumentation systems, one based on plane-of-light optical sensors and the other based on digital demodulation of twin gridwires were developed and demonstrated for rotating blade vibration measurements. Finite element based deterministic and probabilistic analysis methods were developed and used to analyze turbine engine components for vibrations. This section provides the conclusions from the program and offers some recommendations for future research.

9.1 CONCLUSIONS

The following conclusions are based upon the analytical and experimental investigation of turbine engine component dynamics.

9.1.1 NSMS Instrumentation

Four nonintrusive plane-of-light fiber optic sensors for blade tip deflection measurements of rotating bladed disks and the associated data acquisition, analysis, and display systems were developed, demonstrated and delivered to ISRL.

- This system is well suited for laboratory use and has an inexpensive white light source for illumination.

- Its fast turn around time allows the user to calculate test results, plan the next appropriate test condition and conduct the next test quickly.

- Stationary wave measurements on a 12-inch diameter disk using a single sensor provided accurate results.

277

- In a joint effort with AEDC (UTRC) on critical speed response measurements, the UDRI NSMS results compared well with those from the UTRC system. Our system provided results faster than the UTRC system.

- Fast rise time of 1 PPR trigger signal was achieved by the UDRI devised folded beam path.

- Noise in the digital data due to speed changes during each revolution was eliminated by a special UDRI developed algorithm which took these speed changes into account. This feature was not available with the AEDC System.

- The Data processing technique was suitably modified to capture the blade-to-blade vibratory response. This capability has potential for application in real turbine systems.

- Besides histograms, the UDRI system displays real-time data for five blades. This feature was unique to the UDRI NSMS.

9.1.2 *Z-Grid Instrumentation*

A novel 2-channel grid wire system was designed and tested for monitoring an instrumented blade tip vibrations of a rotating disk. This system was delivered to ISRL.

- The design of this system is unique. Demodulation was achieved by digital circuits unlike the analog methods used by Rolls Royce and G.E.

- The Z-grid signal conditioning units were integrated into the NSMS data acquisition system.

- The common data acquisition system for both Z-grid and NSMS was novel. However, it affected the system speed and stability.

- The Z-grid system was demonstrated in conjunction with the optical NSMS for rotating disk critical speed experiments. This system consistently gave lower blade tip deflections than the NSMS and interferometric methods.

278

- We recognized the need to vary the trigger signal delay time to compensate the speed and signal notch effects. This will hopefully increase the accuracy of measurements.

- A UDRI developed algorithm resolved successfully the grid data into tangential and axial deflection components.

- Comparing the NSMS and Z-Grid systems, the NSMS System provided data samples on all blades of the disk whereas the Z-Grid system provided data samples at a much higher rate on a single blade. The data sampling rate ratios for our optical and grid systems are 1:6, 1:4, and 1:3 for the 2D, 3D, and 4D modes respectively.

- Higher sampling rates are possible by increasing the number of probes in NSMS and decreasing the grid spacing in Z-Grid systems.

9.1.3 General Instrumentation Development

Some important developments in the mechanical, optical and electronic instrumentation which have furthered the experimental research at ISRL are:

- The UDRI designed 10-channel slip ring unit allowed test disks to rotate at higher spin rates than before. This direct mount design also eliminated downtime.

- For AEDC critical speed tests, UDRI provided a unique design for the multimagnet configurations to excite pure backward traveling waves in a rotating disk.

- The sine extrapolation equation for interpreting interferogram fringes for the full-field modal deflection definition has been explicitly derived. The user simply inputs the number of fringes and exposure time to determine the disk deflection topology.

- The Ruby laser has been repaired several times, and checked to establish double and triple pulse operation. Pulse width separations have been accurately determined by a digital storage oscilloscope.

279

- Pockels cells extinction ratios could not be determined for lack of suitable equipment which curtailed triple pulse interferometry implementation.

9.1.4 Analytical Research

Analytical techniques have been developed and used to understand the dynamic behavior of simple to complex turbine components. Some important developments were:

- Time and frequency domain forced response of rotating bladed disk assemblies with mass and stiffness asymmetry were explored. Amplitude and location of anti-nodal lines were significantly affected by mass distribution around the disk.

- Stiffness matrix singularities resulting from highly curved and twisted geometrics of advanced blade profiles were observed in the analysis. A procedure to suppress these singularities was developed and applied to low aspect ratio fan (LARF) blades and the results were compared with those of PW and G.E. A good correlation for all modes except one was observed.

- An integral bladed (Wennerstrom) disk was analytically modeled by PATRAN and analyzed by the NASTRAN cyclic symmetry feature for vibrations. Approximate equations to couple the interfacial displacements of the disk and blade was developed. Experimental and analytical results for non-rotating conditions, agreed well.

- Probabilistic finite element code (PROTEC) was developed to account for uncertainties in the element mass, geometry and material properties. This code has been successfully applied to analyze stress, frequency and deflection variances of the AEDC disk. The need to upgrade this code to account for centrifugal effects is recognized.

9.2 RECOMMENDATIONS

The following recommendations are offered to the Air Force. These are directly related to the current program and if implemented, will enhance the engine structural design technology.

■ In the present investigation, efforts were concentrated on the determination of one mode (cosine or sine wave) response of a bladed disk. It is recommended that the twin mode critical speed response investigation of a rotating disk be investigated so that the disk modal interpretation could be applicable to practical turbine disks.

■ The experiments conducted on the 38-bladed disk required testing within a specific frequency range which constrained the test specimen to a very flexible disk where nonlinear dynamic behavior was easily triggered. A stiff disk would be more stable over its entire critical speed range.

■ Stability characteristics of twin modes of vibrating disk and their interaction under a stationary system of forces are worth pursuing to define disk critical speeds.

■ Modal definition when flexible disks are near their resonance-speeds should be investigated in detail, since future designs suggest the use of lightweight flexible bladed disks for turbine engines.

■ Investigation on a realistic disk having both axial and tangential blade motions is needed to evaluate the measurement capability of NSMS methods.

■ Extension of the Z-Grid system application to monitor several blade tip deflections by sectored grids should be pursued.

■ The application of the NSMS test methods to actual compressor and turbine disks would be very desirable.

■ Upgrading the NSMS systems with several probes to completely define the deflection patterns of vibrating blades is required.

- The present systems monitor blade tip deflections, but a combined analytical and experimental approach to derive stress patterns for blade critical locations needs to be developed.

- Multiprobe and multigrid designs at leading and trailing edges will allow complete definition of flexural and torsional motions of turbine and compressor airfoils.

REFERENCES

1. M. J. Gutman, "Turbine Blade Data Acquisition System-Technical Reference Manual," WRDC-TR-89-2040, July 1989.

2. M. J. Gutman, "Turbine Blade Data Acquisition System-User's Guide," WRDC-TR-89-2041, July 1989.

3. M. J. Gutman, R. E. Blanchard, J. M. Aulds, A. L. Shoup, "Turbine Blade Data Acquisition System-Software Reference," WRDC-TR-89-2042, July 1989.

4. M. J. Gutman, R. E. Blanchard, J. M. Aulds, "Z-Grid Signal Conditioning System-User's Guide and Technical Reference," WRDC-TR-89-3043, July 1989.

5. R. A. Brockman, F. Y. Lung, and W. R. Braisted, "Probabilistic Finite Element Analysis of Dynamic Structural Response," AFWAL-TR-88-2149, March 1989.

6. M. Swaminadham and Robert J. Dominic, "Evaluating Plane-of-Light Noninterference Stress Measurement Systems for Measuring Bladed Disk Vibrations," UDR-TR-89-18, March 1989.

7. Thomas W. Held, "Data Analysis Guide for the Noncontacting Blade Deflection Measurement System," UDR-TR-89-31, March 1989.

8. R. A. Brockman, et. al., "MAGNA Part III - Post-Processor Manual," AFWAL-TR-82-3098, December 1982.

9. K. J. Bathe, E. L. Wilson and F. E. Peterson, "SAP IV - A Structural Analysis Program for Static and Dynamic Response of Linear Systems," April 1974.

10. The NASTRAN User's Manual, NASA-SP-222 (06), January 1983.

11. A. W. Leissa, Vibrations of Plates, Tables 2.5, 2.29 and 2.30, NASA-SP-160, 1969.

12. R. D. Blevins, Formulas for Natural Frequency and Mode Shape, Table 11.2(4), 1979.

13. V. Elchuri, and G. C. C. Smith, "Aeroelastic and Dynamic Finite Element Analysis of a Bladed Shrouded Disk," NASA-CR-159728, March 1980.

14. M. Swaminadham, W. A. Stange and J. D. Reed," Modal Response of a Rotating Bladed Disk Assembly," Proceedings 5th International Modal Analysis Conference, London, U.K., April 6-9, 1987.

15. S. L. Puterbaugh and A. L. Wennerstrom, "Structural Analysis of Transonic Compressor," AFWAL-TR-84-2052, October 1984.

16. Y. El-Aini, Pratt and Whitney Aircraft Company, "Review of the Stage Vibration Analysis," Private Communication, June 1985.

17. M. Swaminadham, "Stiffners Singularities in NASTRAN Analysis of Advanced Compressor Blade Vibrations," 13th Annual AIAA Minisymposium, University of Dayton, March 24, 1987.

18. _____, "CDC PATRAN-G Reference Manual," Control Data Corporation Publication Nos. 60459330 and 604549340, 1980.

19. M. Swaminadham, M. L. Soni, W. A. Stange and John D. Reed, "On Model Generation and Modal Analysis of Flexible Bladed Disk Assemblies," ASME Design Technology Conference, Boston, MA, September 1987.

20. R. H. McNeal, R. L. Harder, and J. B. Mason, "NASTRAN Cyclic Symmetry Capability," NASA TMX 2893, September 1973.

21. H. Benoraya and M. Rehak, "The Decomposition Method in Structural Dynamics," AIAA Paper 85-0685, 26th AIAA/ASME/ASCE/AHS Structural Dynamics & Materials Conferenace, 266-281, 1985.

22. F. S. Wong, "Stochastic Finite Element Analysis of a Vibrating String," J. Sound and Vibration, 96(4), 447-459, 1984.

23. W. K. Liu, T. Belytschko, and A. Mani, "Random Field Finite Elements," Int J. Numerical Methods in Engineering, 23, 1831-1845, 1986.

24. M. Shinozuka, "Simulation of Multivariate and Multidimensional Random Process," J. Acoustical Society of America, 49(1), Pt 2, 357-367, 1971.

25. R. A. Brockman, "Geometric Sensitivity Analysis with Isoparametric Finite Elements," Communications in Applied Numerical Methods, Vol. 3, 1-5, 1987.

26. R. A. Brockman and F. Y. Lung, "Sensitivity Analysis with Plate and Shell Finite Elements," to appear in Int. J. Numerical Methods in Engineering.

27. T. J. R. Hughes and T. E. Tezduyar, "Finite Elements Based Upon Mindlin Plate Theory with Particular Reference to the Four-node Bilinear Isoparametric Element," Journal Applied Mechanics, 48-587-596, 1987.

28. R. A. Brockman, "Dynamics of the Bilinear Mindlin Plate Element," Int. J. Numerical Methods in Engineering, Vol 24, 1-14, 1987.

29. R. E. Kielb, A. W. Leissa and J. C. MacBain, "Vibrations of Twisted Cantilever Plates-A Comparison of Theoretical Results," Int. J. Numerical Methods in Engineering, 21.1365-1380, 1985.

30. Hohenberg, Rudolph, "Detection and Study of Compressor Blade Vibration," Experimental Mechanics, pp 19A-24A, June 1967.

31. I. Ye. Zablotskiy, A. G. Zaslavskiy and R. A. Shipov," Experimental Determination of Vibration in Blade Rows When Flutter is Present in the Blades," FTD-4T-23-674-74, March 1974.

32. I. Ye. Zablotskiy, Yu, A. Korostelev and L. B. Svivlov, "Contactless Measuring of Vibrations in the Rotor Blades of Turbines," FTD-HT-23-673-74, April 1974.

33. W. C. Nieberding and J. L. Pollack, "Optical Determination of Blade Flutter," NASA TMX-73573, March 1977.

34. P. E. McCarty, and J. W. Thompson, Jr., "Development of a Non-Interference Technique for Measurement of Turbine Engine Compressor Blade Stress," AEDC-TR-79-78, June 1980.

35. P. E. McCarty, and J. W. Thompson, Jr., "Performance Evaluation of a Prototype Noninterference Technique for Measurement of Turbine Engine Compressor Blade Stress," AEDC-TR-80-5, October 1980.

36. H. Roth, "Vibration Measurements on Turbomachine Rotor Blades with Optical Probes," Proc. Symp. on Measurment Methods in Rotating Components of Turbomachinery, New Orleans, LA, March 10-13, 1980.

37. Endoh, M., et. al., "Noncontact Technique for Measurement of Rotating Blades," Proceedings 9th Annual Meeting of the Gas Turbine Society of Japan, pp. 111-116, 1981.

38. D. L. Camarata, R. M. Chi, M. D. Page and L. G. Puffer, "Conceptial Design of a Noninterference Stress Measurement System for Gas Turbine Engines," AEDC-TR-84-12, May 1984.

39. R. M. Chi, et. al., "Further Study of NSMS Theory and Data Processing Algorithms," UTRC Contract Report, R85-956905-R1, October 1985.

40. H. T. Jones, "Development of a Noninterference Technique for Measuring Turbine Engine Rotor Blade Stresses," AIAA Paper 85-1472, AIAA/SAE/ASME/ASEE 21st Joint Propulsion Conference, Monterey, CA, July 8-10, 1985.

41. H. T. Jones, "Performance Evaluation of a Noninterference Technique for Measuring Integral Order Vibrations of Turbine Engine Compressor Blades," AEDC-TR-84-21, June 1984.

42. R. M. Chi, et al., "Demonstration Testing of a Non-interference Stress Measurement System," UTRC Contract Final Report R87-957037-14F, July 1987.

43. J. M. Reschovsky, Private Communication, General Electric Research Center, Schnectady, NY, 1986.

44. H. Raby, "Rotor Blade Vibration Observed From the Casing," Conference on Methods on Transmitting Signals from Rotating Plant, CERL, Leathanhead, England, June 25-26, 1970.

45. M. Swaminadham, J. D. Reed and W. A. Stange, "Noncontact Blade Deflection Measurement Systems for Rotating Bladed Disks," ISA Paper 89-0046, Instrument Society of America Conference, Orlando, FL, May 1-4, 1989.

46. S. A. Tobias and R. N. Arnold, "The Influence of Dynamical Imperfection on the Vibration of Rotating Disks," Proceedings, Institution of Mechanical Engineers, Vol. 171, pp. 669-690, 1959.

47. D. J. Ewins, "Vibration Characteristics of Bladed Disk Assemblies," J. Mech. Engineering Science, Vol. 15, No. 3, pp. 165-186, 1973.

48. D. J. Ewins, "The Effects of Detuning Upon the Forced Vibrations of Bladed Disks," J. Sound and Vibration, Vol. 9(1), pp. 65-79, 1969.

49. A. V. Srinivasan, "Vibrations of Bladed-Disk Assemblies - A Selected Survey," J. Vibrations, Acoustics, Stress and Reliability 106, pp 165-168, 1984.

50. J. C. MacBain, W. A. Stange and K. G. Harding, "Analysis of Rotating Structures Using Image Derotation with Multiple Pulsed Lasers and Moire Techniques," Optical Engineering, 21(3), 474-477, May-June 1982.

51. K. A. Stetson, "The Use of an Image Derotator on Hologram Interferometry and Speckle Photography of Rotating Objects," Experimental Mechanics, Vol. 18, pp. 67-73, 1978.

52. J. C. MacBain, J. E. Horner, W. A. Stange and J. S. Ogg, "Vibration Analysis of a Spinning Disk Using Image-Derotated Holographic Interferometry," Experimental Mechanics, Vol. 19, pp. 17-22, 1979.

53. R. Aprahamian and D. A. Evenson, "Application of Holography to Vibrations, Transient Response, and Wave Propagation," NASA CR-1671, 1970.

54. M. Swaminadham and R. J. Dominic, "Measurement of the Critical Speed Response of Turbine Disks," to appear in the Proceedings, ASME Vibrations Conference, Montreal, Canada, September 17-20, 1989.